Channel Waveguide Lasers and Amplifiers in Single-Crystalline Ytterbium-Doped Potassium Double Tungstates

Dimitri Geskus

2011

Channel Waveguide Lasers and Amplifiers in Single-Crystalline Ytterbium-Doped Potassium Double Tungstates   D.Geskus

CHANNEL WAVEGUIDE LASERS AND AMPLIFIERS IN SINGLE-CRYSTALLINE YTTERBIUM-DOPED POTASSIUM DOUBLE TUNGSTATES

Dimitri Geskus

Members of the dissertation Committee:

Prof. dr.	M. Pollnau	University of Twente (promotor)
dr.	K. Wörhoff	University of Twente (promotor)
Prof. dr.	K. -J. Boller	University of Twente
dr.	P. W. H. Pinkse	University of Twente
dr.	U. Griebner	Max-Born Institute (Berlin, Germany)
Prof.	A. C. Tropper	University of Southampton, (Southampton, United Kingdom)
Prof. dr.	C. Fallnich	Westfälische Wilhelms-Universität Münster (Münster, Germany)
Prof. dr. ir.	A.J. Mouthaan	University of Twente (chairman and secretary)

MESA+
INSTITUTE FOR NANOTECHNOLOGY

UNIVERSITY OF TWENTE.

NWO
Netherlands Organisation for Scientific Research

This thesis was printed by Wöhrmann Print Service, The Netherlands.

Cover picture: Low magnification optical micrograph of partly overgrown channel waveguide structures in KYW. The channel structures, that have been etched in the substrate (right hand side) and active layer (partly visible in center of at the bottom of the micrograph), are covered by a thick layer of pure KYW (left hand side). The spine of the booklet shows the polished endface of the device. The spots originate from of the guided light when illuminated from the opposite side.

CHANNEL WAVEGUIDE LASERS AND AMPLIFIERS IN SINGLE-CRYSTALLINE
YTTERBIUM-DOPED POTASSIUM DOUBLE TUNGSTATES

PROEFSCHRIFT

ter verkrijging van
de graad van doctor aan de Universiteit Twente,
op gezag van de rector magnificus,
prof. Dr. H. Brinksma,
volgens besluit van het College voor Promoties
in het openbaar te verdedigen
op woensdag 16 november 2011 om 14:45 uur

door

Dimitri Geskus

geboren op 19 november 1979
te Hardenberg

Dit proefschrift is goedgekeurd door:

| Prof. dr. | M. Pollnau | (promotor) |
| dr. | K. Wörhoff | (promotor) |

Contents

Abstract

In the coming years, many applications in photonics will take advantage of miniaturization by on-chip integration of optical components, this might be for biomolecule detection and manipulation, optical coherence tomography, Raman spectroscopy, trace-gas detection, atom spectroscopy, optical clocks, optical computing, data communication, or laser beam steering, to name a few. In most applications, high-performance integrated lasers are required that provide high output power [lee02] and efficiency [sie10], excellent beam quality, broad wavelength selectivity [bra10] and tunability, ultrashort pulses [pud08], ultra-narrow bandwidth [ber10], or ultra-low heat generation, potentially by applying a low-cost, straight-forward fabrication process [yan10].

The potassium double tungstates $KGd(WO_4)_2$, $KY(WO_4)_2$, and $KLu(WO_4)_2$ are excellent candidates for solid-state lasers, see ref. [pol07] and references therein, because of their high refractive index of ~2.0-2.1 [kam01], the large transition cross-sections of rare earth ions doped into these hosts [kul97], a long inter-ionic distance of ~0.5 nm that allows for large doping concentrations without lifetime quenching [pet05] and a reasonably large thermal conductivity of ~3.3 W m^{-1} K^{-1} [sol96]. These advantages have been exploited to demonstrate thin-disk lasers [riv08], broadly tunable [jac07] and high-energy ultrashort-pulse lasers [majo09, pek10], low quantum defect lasers [jac08], as well as planar [rom06, riv07, bain09] and channel [bai09] waveguide lasers.

In this work the technology of Gd^{3+} and Lu^{3+} co-doped $KY(WO_4)_2$:Yb^{3+} thin films grown onto pure $KY(WO_4)_2$ substrates by liquid phase epitaxy is explored. The co-doping enables lattice matching of the grown layer with the substrate and enhances the refractive index difference between the grown layer and the undoped $KY(WO_4)_2$ substrate [gar07, bol09]. This technology enabled the demonstration of waveguide lasers with tight pump and laser mode confinement, resulting in excellent slope efficiencies in Yb^{3+}-doped planar and microstructured channel waveguide lasers of 82.3% and 72%, respectively.

Fabrication of double tungstate microstructured channel waveguides with further enhanced refractive index contrast of 1.5×10^{-2} by completely interchanging the Y^{3+} component of the $KY(WO_4)_2$ host material with Gd^{3+}, Lu^{3+}, and Yb^{3+} doping allows for the demonstration of a laser with an output power of 418 mW at 1023 nm and slope efficiency of 71% versus launched pump power. In addition, in two other resonator configurations these channels showed broad tunability of the laser wavelength from 980 to 1045 nm as well as a low quantum defect of 0.7% when pumping at 973 nm and lasing at 980 nm, thereby minimizing heat dissipation in the device. Laser operation at 980 nm is achieved in an open cavity configuration, which allows for optimal extraction of the laser power, resulting in a total extracted emission of 650 mW. Moreover, laser emission has been demonstrated by an on-chip resonator structure fabricated using a similar material composition of the waveguide and a deep Bragg-reflector milled by a focused ion beam through the complete waveguide structure [ay11] which is similar to the approach demonstrated in a semiconductor gain material [doc10].

Micro-chip optical active devices, currently developed in the well established semiconductor gain material platform, can be possibly being fabricated in the discussed rare earth ion doped material platform. This is highlighted by the last outcome of this project; demonstrating similar modal gain compared to state of the art semiconductor waveguide amplifiers of nearly 1000 dB/cm. To obtain this remarkable result the developed technology is used for the fabrication of nearly 50% Yb^{3+}-doped channel waveguide structures. This result is beyond the common expectation, as rare earth ions are regarded as impurities providing low gain.
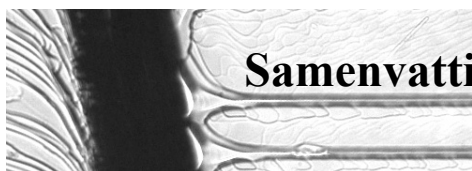
Samenvatting

De miniaturisatie en integratie van optische componenten op een enkele chip zullen in de toekomst voordelig zijn voor veel toepassingen zoals; biomolecuul detectie en manipulatie, optisch coherente tomografie, Raman spectroscopie, detectie van gassporen, atoom spectroscopie, optische klokken, optische computers, optische datacommunicatie, laserbundel sturing, etc. Echter, voor de meeste toepassingen zijn geïntegreerde laserbronnen met hoge prestaties nodig en, afhankelijk van de applicatie, voldoen aan verschillende eisen. Vele bronnen met specifieke eigenschappen zoals het hebben van een groot uitgangsvermogen [lee02] hoge efficiëntie [sie10], excellente bundelkwaliteit, emissie over een groot golflengtegebied [bra10], afstemming over een groot golflengtegebied, ultra korte pulsen [pud08] of een ultra smalle bandbreedte [ber10], en potentieel tegen lage kosten te fabriceren met behulp van eenvoudige fabricatieprocessen [yan10] zijn reeds ontwikkeld.

Kristallijn kalium wolframoxides $KGd(WO_4)_2$, $KY(WO_4)_2$, en $KLu(WO_4)_2$ zijn uitstekende kandidaten voor vaste stof lasers, zoals beschreven in ref. [pol07] en de referenties daarin. De hoge brekingsindex van dit materiaal van ongeveer 2-2.1 [kam01] en de grote transitie cross-secties van zeldzame aarde ionen gedoteerd in dit gastmateriaal [kul97] dragen bij aan een sterke interactie tussen het licht en de optisch actieve zeldzame aarde ionen. De (meestal ongewenste) interactie tussen de optisch actieve ionen is sterk gerelateerd aan de onderlinge afstand en reduceert de levensduur van de aangeslagen toestand van het individuele ion. Omdat de minimale afstand tussen de ionen gefixeerd is door het kristalrooster, welke relatief groot is (~0.5 nm), kan men in tegenstelling tot in andere gastmaterialen, grote doping concentraties toestaan zonder excessieve interactie tussen de ionen. Hierdoor blijft de verkorting van de levensduur van de aangeslagen zeldzame aarde ionen in dit gastmateriaal beperkt [pet05]. Daarnaast ondersteunt de redelijke grote thermische geleiding van ~3.3 $Wm^{-1}K^{-1}$[so96] het maken van hoogvermogens toepassingen. Het ontginnen van deze positieve materiaaleigenschappen heeft in het verleden al geleid tot demonstraties van thin disk lasers [riv08], brede tuning range [jac07] hoogvermogens korte puls lasers [majo09, pek10], klein kwantum defect [jac08], en zowel planaire [rom06, riv07, bain09] als kanaal [bai09] golfgeleider lasers.

Voor dit werk zijn er lagen van $KY(WO_4)_2$ ge-co-doteerd met Gd^{3+}, Lu^{3+} en Yb^{3+} ionen, gegroeid op pure $KY(WO_4)_2$ substraten door middel van liquid phase epitaxi. De Gd^{3+}, Lu^{3+} en Yb^{3+} ionen binden zich op de plaats van de Y^{3+} ionen door deze te vervangen. Het Yb^{3+} ion is het optisch actieve ion en daarom essentieel voor de werking van de laser. De Gd^{3+}, Lu^{3+}-ionen zijn optisch passief en dragen niet bij aan de laser processen. Alle drie ionen veranderen de afmetingen van het kristalrooster, wanneer deze in het gastkristal gedoteerd worden, hierbij hebben de optisch passieve Lu^{3+} en Gd^{3+} ionen een tegengestelde werking op het kristal rooster door het respectievelijk te verkleinen of te vergroten. Hierdoor is het mogelijk de afmetingen van het kristalrooster te ontwerpen en dit gelijk te maken aan dat van het substraat. Met deze methode is het mogelijk om sterk gedoteerde defectvrije kristallagen epitaxiaal te groeien op de pure $KY(WO_4)_2$ substraten. Omdat de Gd^{3+}, Lu^{3+} en Yb^{3+} ionen

een grotere elektronendichtheid hebben dan het Y^{3+} ion, dat ze vervangen, wordt de brekingsindex van het gedoteerde materiaal verhoogd ten opzichte van het niet gedoteerde substraatmateriaal. Dit brekingsindexcontrast tussen de gedoteerde laag en het pure $KY(WO_4)_2$ substraat is essentieel voor de geleiding van licht in de gegroeide laag, dat de basis is voor de golfgeleider. Hoewel de optisch actieve Yb^{3+} ionen reeds de brekingsindex van het materiaal verhogen, is hiervan de concentratie normaliter niet hoger dan 10% om fabricatie van defectvrije lagen te kunnen garanderen en optimale laser eigenschappen te verkrijgen. Door de laag te co-doteren met de optisch inactieve Gd^{3+} en Lu^{3+} ionen wordt de dubbele rol, de optisch actieve rol en de brekingsindex verhogende rol, van de Yb^{3+} ionen ontkoppeld. Het verhoogde brekingsindexcontrast tussen de golfgeleider en het substraat in ge-co-doteerde golfgeleiders zorgt voor een sterke concentratie van het licht in de golfgeleider, wat resulteerde in demonstratie van planaire en kanaalgolfgeleider lasers met respectievelijk 82.3% en 72% slope efficiëntie.

Door de Y^{3+} component van het $KY(WO_4)_2$ gastmateriaal compleet te vervangen met optisch passieve Gd^{3+}, Lu^{3+} en optisch actieve Yb^{3+} ionen is het brekingsindexcontrast tussen de actieve laag en het substraat verder verhoogt tot 1.5×10^{-2}. In dit materiaal is een microkanaal golfgeleider laser gedemonstreerd met een emissie van 418 mW bij een golflengte van 1025 nm en slope efficiëntie van 71% versus geabsorbeerd pomp vermogen. Daarnaast is er door de resonator aan te passen een brede golflengte tuning van de emissie golflengte over een bereik van 980 tot 1045 nm. Hierbij kon het kwantumdefect, d.w.z. het relatieve verschil tussen de pomp- en de emissiegolflengte, geminimaliseerd worden tot 0.7%. Een klein kwantumdefect is gunstig voor hoogvermogens toepassingen, omdat er onder deze omstandigheden een minimale hoeveelheid vermogen in het kristal gedissipeerd wordt. In dit experiment was de golflengte van de pomp 973 nm en de golflengte van de laseremissie 980 nm.

In een ander experiment is getracht zoveel mogelijk vermogen uit de laserresonator te ontrekken, door geen spiegels te monteren op de uiteinden van de golfgeleider en werd de resonator gevormd tussen de gepolijste uiteinden van de golfgeleider zelf, welke een Fresnel reflectie hebben van 11%. In deze open resonator configuratie is een totaal uitgangsvermogen van 650 mW behaald bij een golflengte van 980 nm. Tevens is er laseremissie gedemonstreerd bij een on-chip resonator. Deze on-chip resonator is gemaakt door de kanaalgolfgeleiders op nano-schaal met regelmaat volledig te onderbreken, waardoor er zgn. Bragg structuren ontstaan in de actieve golfgeleider. De nano-onderbrekingen zijn aangebracht door het lokaal te bombarderen met een gefocusseerde ionenbundel [ay11] deze fabricatiemethode heeft veel gelijkenis met technologie die toegepast wordt in halfgeleidertechnologie, waarin extreem grote optische versterking gehaald wordt en waardoor compacte laser structuren kunnen worden gerealiseerd [doc10].

De competitie tussen zeldzame aarde ionen gedoteerd dielectrisch optisch versterker materialen en de ver ontwikkelde halfgeleidertechnologie is echter tot op heden zelden aan de orde geweest. Dit is te wijten aan de gelimiteerde dopingconcentratie van zeldzame aarde ionen, door parasitaire interactie tussen de optisch actieve zeldzame aarde ionen met elkaar. De zeldzame aarde ionen worden in het algemeen beschouwd als kleine verontreinigingen van het gastmateriaal. Hierdoor wordt er enkel een kleine optische versterking geleverd. Echter, door de eerder benoemde unieke eigenschappen van het $KY(WO_4)_2$ gastmateriaal

blijft deze interactie minimaal, en in combinatie met het Yb^{3+} ion, dat slechts 2 energieniveaus heeft, zijn de parasitaire processen tot een minimum beperkt. Deze voordelen leidden tot het laatst behaalde resultaat binnen dit project. Het opzienbarende bij dit laatste experiment is dat er bijna 50% Yb^{3+} dotering is toegepast, waardoor er bijna 1000 dB/cm optische versterking is behaald en daarmee Gd^{3+}, Lu^{3+} en Yb^{3+} ge-co-doteerd $KY(WO_4)_2$ op gelijk niveau komt met state-of-the-art halfgeleider optische versterkers.

1   Introduction

This thesis concerns the development of optically active devices in single-crystalline ytterbium-doped potassium double tungstates, which has been performed at the Integrated Optical MicroSystems (IOMS) group of the University of Twente. The IOMS group is a member of the MESA+ Institute for Nanotechnology. The MESA+ Institute is one of the largest nanotechnology research institutes in the world. Its clean room facility provides an excellent environment for the development of micro- and nano-scaled devices. In this research environment the IOMS group develops both passive and active optical integrated devices. Some recent key research activities of this group concern: On-chip Raman spectroscopy [ism11] and optical coherence tomography [ack11], multicolor DNA analysis in an optofluidic chip [don10], calculation tools for integrated optics [ham] and optically active devices like waveguide amplifiers and lasers in Al_2O_3:Er^{3+} [bra11] with ultra-narrow linewidth [ber10] and demonstration of the first continuous-wave laser operation of a Nd-doped polymer channel waveguide [gri11, yan10].

1.1.   Integrated optics

The development of optical telecommunication started with large bandwidth, long distance data haul, using fiber optics. It now enters our houses, providing high speed internet and making the copper data cables redundant by replacing the connections for telephone, internet, and providing high quality digital television. This indicates the trend towards short distance optical communication, finally linking processors with each other. This development towards miniaturization of optical devices shows great similarities with the developed field of electronics, resulting in optical integrated circuitry. Many basic functions are required in an optical circuit. Besides miniature optical waveguides for directing light on the chip, optical sources for producing light, amplifiers for compensating signal losses, detectors for converting the signal into the electrical domain, modulators, combiners/splitters, filters and switches are required. These functions can be divided into passive devices (those that simply direct and manipulate light without, in principle, generating or destroying photons) and active devices (those that emit or amplify light or convert light energy to electrical energy).

Optical amplifiers and laser sources are fabricated in various material platforms, based on semiconductors, dyes and rare earth doped material. Table 1.1 shows a few material platforms and the optical gain achieved in micro-sized structures in these materials.

Table 1.1. List of commonly used optically active material platforms.

	Material		Wavelength (µm)	Modal gain (dB/cm)
Semiconductors	InGaAsP bulk		1.50-1.55	1032 [leu00]
				775-1192 [dou94]
	AlInGaAs/InP MQW (multi quantum well)		1.28	220 [koo01]
	VCSOA`s (Vertical cavity semiconductor optical amplifiers)	InGaAsP/InP	1.31	13650 [bjo03]
		AlInGaAs/InP	~1.5	13250 [bjo04]
		InGaAsP/InP	~1.5	10480 [col05]
	InGaAs/AlGaAsP-InP		1.55	250 [nag10]
	GaAs/AlGaAs QW (quantum well)		0.83	300 [sto01]
	Strained InGaAs/AlGaAs QW		0.98	266 [sto01]
	Organic semi-conductors	F8BT/Dow Red-F	0.66	775 [goo05]
		MEH-PPV	0.63	290 [ama06]
Laser Dyes	$OC_1C_{10}PPV$		0.60	44 [law02]
	Poly (9,9-dioctyfluorene) PFO		0.466	318 [lam03]
	PM650 in PMMA		0.616	385 [lam03]
Rare earths	Er (8wt%)-Yb (12wt%) co-doped phosphate glass		1.534	13.6 [pat04]
	Nd-complex-doped polymer		1.064	5.7 [yang10]
	$KGd_{0.447}Lu_{0.078} (WO_4)_2:(0.475)Yb^{3+}$		0.9806	935 [this work]

The highest gain is found among the semiconductor material platforms where the absolute peak modal gain, above 10000 dB/cm, is found for vertical-cavity semiconductor optical amplifiers (VCSOAs). The VCSOAs combine a perfect modal overlap with the high gain thin film layers. In addition the overlap of the optical field is enhanced by the resonant effect of the cavity configuration. However the interpretation of the vertical emitter gain media by defining a gain coefficient (dB/cm) is not completely appropriate and gain per QW is recommended [blo00], here the gain coefficients' are used to ease the comparison between the different gain media. The other semiconductor optical amplifier (SOA) configurations solely rely on index guiding of the light in waveguide configurations, resulting in a fairly low modal overlap with the sub-nanometer thick film(s) gain material. Moreover no resonant enhancement of overlap is exploited in such configurations, resulting in modal gain of about 1000 dB/cm. The modal overlap is larger in optical amplifiers based on laser dye materials; however the material gain of this material is significantly lower. Commonly, the rare earth doped materials have fairly low gain of a few dB/cm, however in this work we demonstrate by appropriate choice of host material and extremely large doping concentration a large gain of 935 dB/cm, which is comparable to state of the art semiconductor waveguide devices.

1.2. Lasers

Sunlight is responsible for many energy resources on earth and yet its power seems to be hidden compared to the force of wind and streaming water. It is the electromagnetic property of light causing the interaction of light with matter. The energy of light is transformed when it is absorbed in a material, developing heat in most cases. However the energy can also interact with a material, such that it is reemitted in another form. In 1917 Albert Einstein developed the hypotheses that besides absorption of light also stimulated emission could occur, resulting in amplification of light [ein17]. This interaction between light and matter

resulted in the theory of light amplification by stimulated emission of radiation (Laser) [sch58]. Soon the first working optical laser based on this theory was demonstrated by Maiman in 1960 [mai60]. The few photons from Maiman`s laser did not convince everyone directly, but the idea of powerful lasers was directly adopted by James Bond movies in 1964 [ham64].

A laser is based on a fairly simple principle; it is nothing more than an optical gain medium, with a closed feedback loop. The feedback loop makes the amplifier oscillate at a specific frequency; an acoustical version is found when holding a microphone close to the loudspeaker, resulting in a nice hum.

Light and matter interact with each other via the electrons of the material; in solids the electrons are bound to the material by the protons in the nuclei of the atoms. The interaction between the positively charged nucleus of an atom or ion and the negatively charged electrons results in discrete shells in which the electrons orbit around the nucleus of the atom. To promote an electron from an inner to an outer shell requires energy, and energy is released during the opposite transition.

The trivalent rare earth ions are characterized by electron transitions that take place in the 4f shell. The 4f shell is closer to the center than the shells having larger main quantum numbers 5s, 5p and 6s so that the electrons in the 4f shell are shielded from the environment by the electrons in the outer shells. Due to this shielding by the outer electron shells, the discrete energy transitions corresponding to the electron transitions in the 4f shell of rare earth ions is hardly affected by the host material in which the rare earth ions are doped [sil04].

The working principle of a laser in an optically active material can best be explained by four-level laser operation, involving the transition of an ion between 4 energy levels. Here the ion can be excited to a higher energy level (in this example referred as the upper pump level) by absorption of a pump photon followed by a rapid nonradiative relaxation to the upper laser level. From this upper laser level the ion can relax to its lower laser level by emitting a photon. This relaxation transition can also be triggered or stimulated by another photon, at this concurrency the properties of the incoming photon, such as its directionality, phase and wavelength, will be copied to the emitted photon resulting in an amplification of the incident photon. The ion will then rapidly decay from the lower laser level to the ground level. The 4-level laser process is depicted in Fig. 1.1.
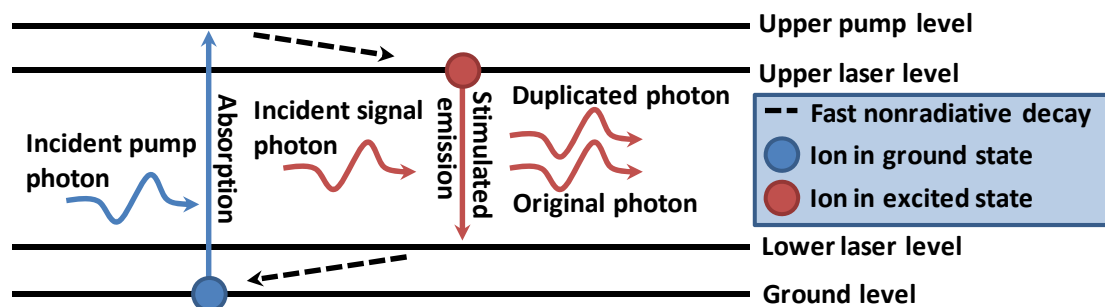
Fig. 1.1. Schematic representation of laser processes in 4-level laser materials. Starting with a stimulated absorption process in which an ion is promoted to the pump level when absorbing a pump photon. Followed by a rapid decay to the upper laser level, waiting for a signal photon that stimulates the decay of the ion to the lower laser level while emitting a photon with the same properties of the incident signal photon. After the stimulated emission the ion rapidly decays from its lower laser level to ground level.

The advantageous properties of laser light compared to ordinary light are its spatial and spectral coherence. The spatial coherence is responsible for the directionality, making it possible to propagate a light beam over large distances without large divergence and allows for tight focusing of the light. Spatial coherence plays an important role in many high power applications, such as welding and machining of various materials like steel. High precision laser sources are used in the biomedical applications such as surgery and eye treatments.

The spectral coherence of laser light denotes the single wavelength of the light and the phase relation of this light wave over large distances. The spectral coherence property makes laser light suitable for applications such as interferometric sensing, nonlinear optics, optical metrology and high resolution (laser interference) lithography.

1.3. $KY(WO_4)_2$ as host material for Yb^{3+} ions towards integrated optically active devices

The advantage of monoclinic double tungstates is that they strongly enhance the emission and absorption cross-sections of the optically active ytterbium (Yb^{3+}) ions doped into these materials, as compared to other host materials. In this work Yb^{3+}-doped single-crystalline layers composed from the monoclinic double tungstates $KGd(WO_4)_2$ (KGdW), $KLu(WO_4)_2$ (KLuW) and $KY(WO_4)_2$ (KYW) are grown onto pure KYW substrates. The peak absorption wavelength of KYW:Yb^{3+} is found around 981 nm, which allows efficient diode pumping of the laser [lag03, maj09]. The broad emission spectrum, stretching over a wavelength range of 925-1050 nm allows generation of ultrashort pulses and low quantum defect laser operation. These advantages have thoroughly been investigated and KYW:Yb^{3+} has proven its laser potential in bulk configurations concerning high efficiency [kule97], emission tunability [jac08] and generation of short pulses [majo09, pek10]. The large emission cross-sections at wavelength range from 990 to 1040 nm and the sharp peak found at 980 nm which can be accessed when pumped at shorter wavelengths of the Yb^{3+} ions doped into the KYW host provides large optical gain. This large optical gain allows laser oscillation in cavities with large outcoupling efficiencies, which is an advantage to overcome the large roundtrip losses of ~10% in waveguide lasers compared to a typical the roundtrip loss of ~0.5% observed in bulk lasers, and makes it possible to develop small, efficient and powerful laser devices in this material platform. The challenge of fabrication of microchip waveguide lasers in KYW is mainly caused by the crystalline character of this material, which does not allow growth of thin films on silicon substrates, forcing to use non trivial bonding methods [rivi08]. This creates a tough competition with most of the semiconductor laser platforms, of which the fabrication technology is well developed. However, the advantages of Yb^{3+} doped KYW like the long excitation lifetime and broad emission bandwidth makes it highly interesting for development of integrated optically active devices that exploit these properties, like in on-chip generation of ultrashort pulses.

1.4.   Outline of this thesis

Chapter 2 discusses the advantageous properties of the monoclinic double tungstates as host materials for rare earth ion doped solid state lasers. It also provides the fabrication flow from

the growth of active layers of co-doped monoclinic double tungstates onto pure KYW substrates towards planar waveguides using polishing, and the structural characterization of the produced crystalline films.

In chapter 3 the spectroscopy of the co-doped crystals is analyzed and discussed, since no spectroscopic data is available in the literature for the used composite materials. The spectroscopy of the pure crystals is combined with respect to the compositions of the co-doped crystals. This convoluted spectroscopic information is proposed to be used for the design and analysis of optically active devices demonstrated in these composite crystals. Experimentally obtained spectroscopic data of the composite material confirm the proposed convolution of spectroscopic data. In addition healthy laser properties of the composite crystals are confirmed by various characterizations of the developed co-doped material, and highly efficient laser performance of a planar waveguide is presented.

Chapter 4 concerns the wandered route towards microstructured channel waveguides, and discusses the tested approaches using dry etching techniques to fabricate these microstructured channels that form the basis for the following chapters.

Chapter 5 presents the performance of microstructured channel waveguide lasers in co-doped double tungstates. The structures provide highly efficient lasers having a low pump threshold, high slope efficiencies and large output powers. Also the demonstration of a wide tuning range, low quantum defect and zero-phonon line lasing is presented.

In chapter 6 a first successful approach towards on-chip laser devices is presented, based on deeply milled grating structures in the channel waveguide devices using focused ion beam milling.

In chapter 7 co-doped potassium double tungstate channel waveguides open the competition with well developed, state of the art semiconductor gain materials, by demonstration of an ultra high optical gain of 935 dB/cm.

Collaborations

1. Advanced Photonics Laboratory, Institute of Imaging and Applied Optics, Ecole Polytechnique Fédérale de Lausanne, Switzerland.
2. Laboratory of Inorganic Chemistry, Department of Chemistry and Applied Biosciences, ETH Zurich, Switzerland.
3. Optoelectronics Research Centre, University of Southampton, United Kingdom.
4. Low Temperature Division, MESA$^+$ Institute for Nanotechnology, University of Twente.

Funding

1. NWO Vici Grant "Integrated optical structures: From active thin films to micro/nanocavities to ultrashort-pulse lasers" (2006-2011).
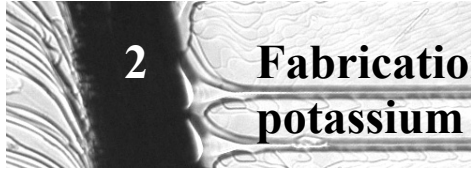
2   Fabrication of planar waveguides in co-doped potassium double tungstates

The unique property of the family of monoclinic double tungstates, especially $KGd(WO_4)_2$, $KY(WO_4)_2$, and $KLu(WO_4)_2$, to strongly enhance the absorption and emission cross sections of optically active rare-earth ions doped into these host materials is widely recognized, see ref. [pol07] and references therein. The enhanced peak absorption cross-section near 980 nm of $KYW:Yb^{3+}$ is up to 15 times larger than the peak absorption lines at 940 nm and 970 nm of the well established laser material $Y_3Al_5O_{12}:Yb^{3+}$ ($YAG:Yb^{3+}$) at room temperature [liu07]. When combining this large absorption cross-section with very large Yb^{3+} doping concentrations, reaching the stoichiometric structure $KYb(WO_4)_2$ [pujo02], the pump absorption length near 980 nm reduces to less than 20 μm. Also the quantum defect resulting from the difference between pump and laser photon energy can become very small in Yb^{3+}-doped double tungstates [klo03], making them excellent candidates for bulk [kul97, lag99], thin-disk [riv08], and waveguide [riv07, rom06, bain09] lasers.

But besides these spectroscopic aspects, other important aspects play a key role in the field of general integration of optical devices. The refractive index contrast of an optical waveguide with its environment is in direct relation to the confinement of the light that can be achieved. A larger refractive index contrast allows design of waveguides with smaller lateral dimensions and results in a better confinement of light. This chapter discusses the fabrication of co-doped active waveguides. The co-doping serves to enhance the confinement of light, resulting in efficient laser performance of planar waveguides having low laser thresholds. Growth of the active layers by liquid phase epitaxy is conducted by Dr. Shanmugam Aravazhi using the in-house growth facility.

2.1.   Monoclinic potassium double tungstates

Potassium yttrium double tungstate, $KY(WO_4)_2$ (KYW), belongs to the double tungstate family having the general formula $AT(WO_4)_2$, where A is a monovalent alkali-metal cation and T a trivalent metal or rare-earth cation. The large variety of possible substitutions leads to non-equivalent crystalline structures and very different properties. This work will focus on a selective group of potassium double tungstates: $KGd(WO_4)_2$ (KGdW), $KLu(WO_4)_2$ (KLuW), $KYb(WO_4)_2$ (KYbW), and KYW, all having the same monoclinic structure which makes them compatible with each other. Taking the slight differences of the unit cell sizes into account, it is possible to grow single-crystalline composite layers using the aforementioned building blocks (KGdW, KLuW, KYbW and KYW) on pure KYW substrates, hence allowing one to design the optical properties, such as absorption length and refractive index of the optically active layer.

2.1.1. *Crystal structure*

The basic crystal structure of KYW was described by Borisov and Klevtsova for the first time in 1968 [bor68]. KYW exhibits two different crystal structures; A high temperature tetragonal structure (called β-KYW), and a low temperature monoclinic structure (called α-

KYW). The β-KYW has a melting temperature of about 1080°C; the transition temperature between the β-KYW and α-KYW structures is found below the melting temperature at about 1010-1025°C [kle68, gal98, kam01]. This makes the β-KYW structure unstable at room temperature. KYW crystallizes in the stable monoclinic crystal structure α-KYW at temperatures below the temperature of the phase transition.

Three different coordinate systems are commonly used to describe the crystal structure. 1) The Schönflies coordinate system is recommended by the International Crystallographic Union as the standard setting. 2) The Hermann-Mauguin coordinate system is more intuitive, because its parameters, including the monoclinic angle β ≈ 94°, correlate better with the morphology of grown KYW crystals, therefore it is sometimes used for crystal orientation during spectroscopic characterization. However, to fabricate optical devices, spectroscopic characterization with respect to the orientation of the optical axes of this birefringent material is preferred. Since the orientation of the optical axes does not coincide with the orientation of the crystal axes, a third coordinate system describes the orientation of the optical axis. All three coordinate systems are drawn on a picture of a *b*-cut KYW substrate with an overgrown film in Fig. 2.1.
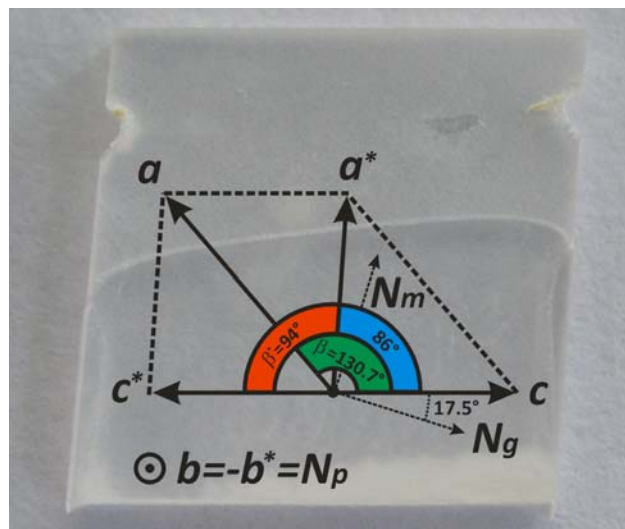
Fig. 2.1. Orientation of crystallographic axes of the KYW crystal structure according to the Schönflies coordinate system (without asterisk) and the Hermann-Mauguin coordinate system (with asterisk). In addition the optical indicatrix is shown. The crystal on the background has an overgrown layer on the lower part. The two indentions are made to fix the substrate to the platinum wire that holds the substrate that is partially dipped into the solution during LPE growth.

The unit cell parameters of the various monoclinic double tungstates used in this work are listed in Table 2.1.

Table 2.1. Lattice parameters according to the Schönflies coordinate system.

Material	a [Å]	b [Å]	c [Å]	β [°]	T [K]	Note	Ref.
KGdW	10.652(4)	10.374(6)	7.582(2)	130.80(2)	-		[puj06] [pujol01]
KGdW	10.6890(6)	10.4438(5)	7.6036(4)	130.771(3)	298	*	[sil07] [pujo01]
KLuW	10.576(7)	10.214(7)	7.487(2)	130.68(4)	293		[puj06]
KLuW	10.5898(5)	10.2362(5)	7.4962(3)	130.7445(2)	298	*	[puj06]
KYbW	10.590(4)	10.290(6)	7.478(2)	130.70(2)	-		[puj06]
KYbW	10.6003(12)	10.2673(12)	7.5066(8)	130.766(6)	298	*	[pujo01]
KYW	10.6313(4)	10.3452(6)	7.5547(2)	130.752(2)	298	*	[sil08] [pujo01]

[*]**These lattice constants have all been measured at the same temperature of 298 K, therefore this dataset is selected to predict the lattice constants of composite crystalline layers.**

The given unit cell parameters or lattice constants are used in this work to design the lattice constants of composite crystalline layers. To accurately predict the lattice constants of each composite crystal it is important to use values from the literature that have been measured at the same temperature. The deviation of the lattice constants is significant due to thermal expansion, as can be seen for the values given for KLuW consecutively measured using the same method at 2 different temperatures with only 5 degrees of difference.

The linear thermal expansion coefficients α of the potassium double tungstates related to this work are given in Table 2.2. Here α is defined as the slopes of the linear relationship between $(\Delta L/L)$ and temperature working in the different crystallographic directions along the a, b and c crystallographic axes [chu93].

Table. 2.2 Linear thermal expansion coefficients of the potassium double tungstates related to this work.

Compound	α [a] 10^{-6} K^{-1}	α [b] 10^{-6} K^{-1}	α [c] 10^{-6} K^{-1}	Ref.
KGdW	13.6	2.8	22.8	[puj99]
KLuW	10.6	3.35	16.3	[puj06]
KYbW	10.5	2.6	16.3	[puj99]
KYW	11.0	1.9	17.8	[puj99, kam01]

The minimum distance between neighboring Y sites is important, because it affects the probability of energy transfer between the dopant ions. For KYW the minimum Y-Y distance is 0.406(3) nm [kry02]. For stoichiometric KYbW the shortest Yb-Yb distance is 0.4049(2) nm [puj01]. This minimum distance between two trivalent ions is larger compared to other host materials like stoichiometric YbAG having an inter ionic distance between Yb-Yb of 0.366 nm [pen11], hence keeping the energy transfer relatively low.

2.1.2. *Optical properties*

The anisotropic crystal structure of the monoclinic potassium double tungstates is responsible for the birefringent property of the material. The direction of the optical axes with respect to the crystal orientation is given in Fig. 2.1. The N_p optical axis is parallel to the b crystallographic axis. The two other optical axes N_m and N_g are oriented in the a-c

crystallographic plane. N_g is the traditional labeling of the optical direction with the highest refractive index n_g of the optical indicatrix, N_m has the intermediate refractive index n_m, and N_p has the smallest refractive index n_p. The wavelength-dependent refractive indices of KYW can be approximated by the Sellmeier dispersion formula. Commonly, experimental data on refractive indices of a material at various wavelengths is fit to the Sellmeier equation with the Sellmeier coefficients as fitting parameters. Here various versions of the Sellmeier equation are used. The Sellmeier coefficients found in the literature and their corresponding form of the Sellmeier equation used to fit the experimental data in those publications are given in Table 2.3.

Table 2.3. Sellmeier coefficients for KGdW, KLuW, KYbW and KYW.

$E\|$	A	B	C	D	Used Sellmeier equation
KGdW, wavelength range 0.35-1.5 µm [pujo99]					
N_g	1.3867	0.6573	0.028907	-0.0002913	
N_m	1.5437	0.4541	0.035687	-0.0021567	$n(\lambda) = A + \dfrac{B\lambda^2}{\lambda^2 - C} + D\lambda^2$
N_p	1.5344	0.4360	0.034663	-0.0020999	
KLuW, wavelength range 0.41-1.2 µm [puj06]					
N_g	3.58334	0.73512	0.071289	-0.02953	
N_m	3.36989	0.74309	0.068607	-0.04331	$n(\lambda) = \sqrt{A + \dfrac{B\lambda^2}{\lambda^2 - C} + D\lambda^2}$
N_p	3.21749	0.75382	0.062830	-0.05076	
KYbW, wavelength range 0.45-1.5 µm [pujo02]					
N_g	3.28412	0.9921	0.064648	-0.01936	
N_m	3.17884	0.91624	0.062936	-0.00485	$n(\lambda) = \sqrt{A + \dfrac{B\lambda^2}{\lambda^2 - C} + D\lambda^2}$
N_p	3.06172	0.88655	0.056920	-0.02286	
KYW, wavelength range 0.405-1.064 µm [kam01]					
N_g	1	3.1278346	0.02608613		
N_m	1	2.9568303	0.02534002		$n(\lambda) = \sqrt{A + \dfrac{B\lambda^2}{\lambda^2 - C}}$
N_p	1	2.8134935	0.02338012		

The Sellmeier equations and the given coefficients are used to calculate the refractive indices of the various crystals. The refractive indices of the various crystals for the polarization $E\|N_m$, which corresponds to TE polarization for the optical experiments performed in this thesis, are shown in Fig. 2.2. This polarization exhibits the largest emission and absorption cross-sections. The refractive index of any material is related to the electron density of the material: larger electron densities provide larger refractive indices. The electron density of the material increases due to Gd^{3+}, Lu^{3+}, and Yb^{3+} ions replacing the Y^{3+} ions, resulting in slightly larger refractive index of the doped material.
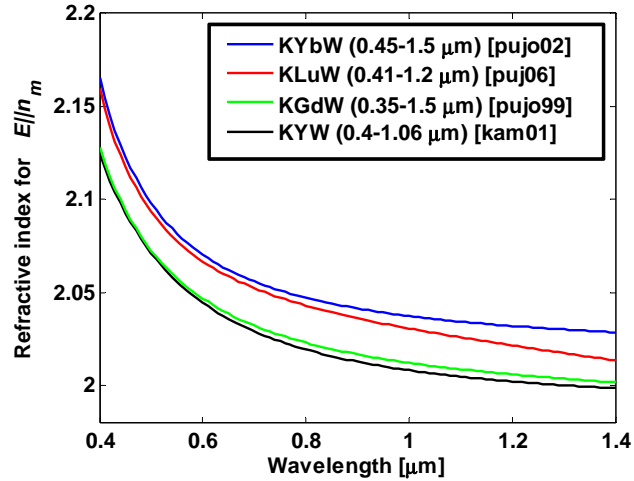
Fig. 2.2. The calculated refractive index for *E∥Nm* of KYbW, KLuW, KGdW, and KYW host material using the Sellmeier equations and coefficients given in Table 2.3.

Pure KYW has the lowest refractive index compared to pure KGdW or KLuW. Therefore, to achieve the highest contrast between doped layer and substrate, KYW should be used as the substrate. Due to the similar ionic radii of Yb^{3+} and Lu^{3+}, the smallest lattice mismatch is obtained, when growing $KLuW:Yb^{3+}$ layers onto KLuW substrates, which allows the growth of heavily Yb^{3+}-doped layers [pet07]. Thin-disk laser applications benefit from these high dopant concentrations [gri05], but the low refractive index contrast obtained in $KLuW:Yb^{3+}$ layers onto KLuW substrates is less suitable for waveguide laser devices.

The UV cutoff wavelength of KYW is near 320 nm, which corresponds to an optical band gap of 3.83 eV. The transparency window of KYW crystals extends up to 5400 nm, shown in Fig. 2.3.
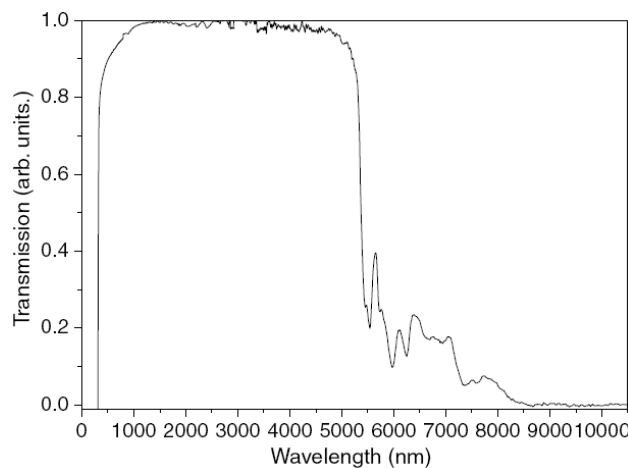
Fig. 2.3. Measured transparency of a 0.2 mm thin KYW sample cut parallel to the *a-c* plane. The transparency window extends from 350 nm to 5400 nm [mat06]

2.1.3. Synthesis

Single-crystalline material of high quality can best be obtained by layer-by-layer growth. Liquid phase epitaxy (LPE) is a layer-by-layer growth process and relies on self-orienting growth of crystalline material from liquid solute. Direct growth of monoclinic potassium

double tungstate crystals from the melt (i.e. not using a solvent) in standard Czochralski growth is impossible due to the crystal phase transition at ~1025°C mentioned in section 2.2.1, below its melting temperature at 1080°C [kam01]. During this transition the crystal becomes unstable and disintegrates. Therefore monoclinic potassium double tungstate crystals have to be grown from a solution to decrease the nucleation temperature below the transition point. By properly decreasing the temperature of the solution, the solution becomes supersaturated, resulting in nucleation of the solute on a seeding crystal.

The $K_2W_2O_7$ solvent was used for the first time by Van Uitert and Soden in 1961 to produce rare earth doped KYW crystals for different resonance and emission studies [uit61]. Later on, Klevtsov and Kozeeva [kle69] grew a series of stoichiometric compositions of KYW, and of KYW with Y replaced with various lanthanides ranging from Ce to Lu, from a stoichiometric mixture of K_2WO_4 and WO_3 corresponding to the $K_2W_2O_7$ composition. The major advantage of the $K_2W_2O_7$ solvent is the absence of foreign ions and the low melting temperature of 619°C [gue70] which allows crystal growth at temperatures between 900 and 950°C, depending on the concentration of the solute in the solvent as given by the solubility curve of KYW in the $K_2W_2O_7$ solvent in Fig. 2.4.
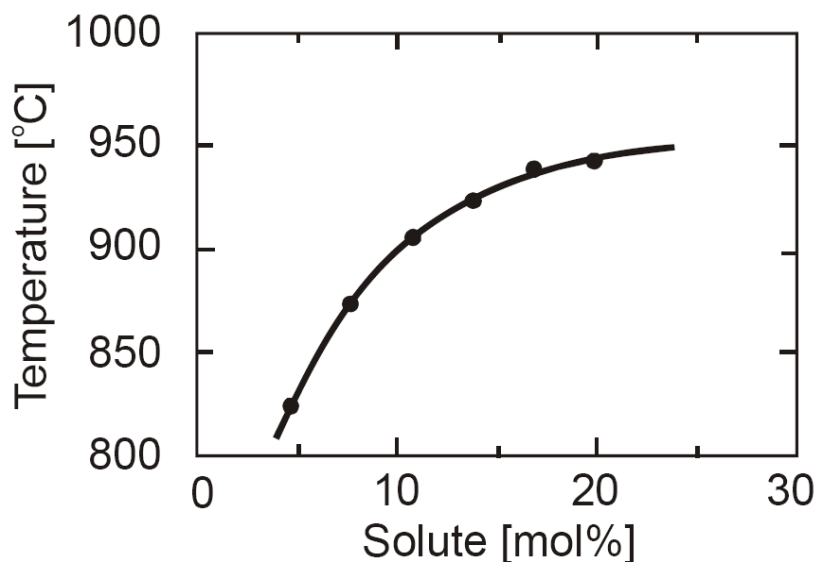
Fig. 2.4. Solubility curve of KYW in the $K_2W_2O_7$ solvent [puj99].

2.2.   Growth of doped layers onto undoped substrates

For fabrication of bulk crystals a seeding crystal is introduced into the solute to initiate the growth. Since the seed as well as the resulting crystal are both of the same material this method is also referred as homo-epitaxial growth. In this work undoped, 1 mm thick KYW crystals with laser-grade polished (010) faces were used as substrates on which rare earth doped KYW thin films were grown. Since the grown layer is not of the same material as the substrate, this method is referred as hetero-epitaxial growth. The substrates were fixed to a platinum wire and vertically introduced into the $K_2W_2O_7$ solution. The used solute/solvent ratio was rare earth doped KYW: 10.5 mol% and $K_2W_2O_7$: 89.5 mol%. The actual growth was performed at a low level of super saturation in the temperature range of 920-925°C. The

substrate was only partially immersed into the solution. Complete immersion is not desired, since overgrowth of the platinum wire disturbs the growth process, resulting in fractured layers. In addition, the non-overgrown surface of the substrate was used for orientation of the sample during polishing of the grown layer. An in-house developed, computer controlled LPE furnace was used to ensure reproducible layer growth. Fully automatic growth routines are developed, controlling the substrate rotation, growth duration, growth temperature, heating and cooling rates. A schematic representation of the used oven is given in Fig. 2.5.
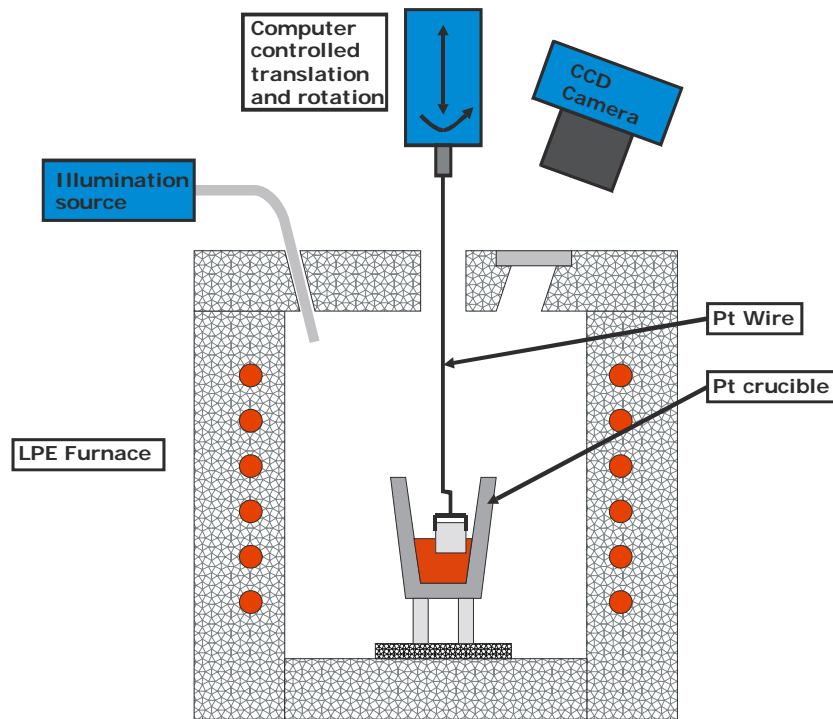
Fig. 2.5. Schematic of LPE furnace

The synthesis of heavily doped KYW layers at lower temperatures is preferred in order to decrease the thermal stress in the layers caused by the unequal thermal expansion coefficients of the substrate and the doped layer, as depicted in Table 2.2. Since the layers are commonly grown onto *b*-cut samples the thermally induced stress, which builds up during the cooling of the sample after the growth of the layer, works in the *a-c* crystallographic plane. Dr. Yaroslav Romanyuk studied growth of thin layers of KYW:Yb^{3+} onto KYW substrates at growth temperatures as low as 520°C using the NaCl–KCl–CsCl solvent in order to minimize this thermally induced stress [roma04]. He previously used this approach for LPE growth of Mn^{6+}-doped sulfates, molybdates, and tungstates of Ca, Sr, and Ba [rom04]. However, he found that using the NaCl–KCl–CsCl solvent for growth of heavily rare earth doped KYW layers onto pure KYW substrates is complicated by the formation of parasitic phases and pronounced 3D island nucleation, limiting the maximum layer thickness to approx. 10 μm [rom05]. Nevertheless, in this way he managed to grow thin layers that led to the demonstration of the first optical waveguide in a double tungstate [roma04]. Much better layer quality, allowing demonstration of the first highly efficient waveguide laser in a double tungstate [rom06], is obtained using the $K_2W_2O_7$ solvent for the layer growth.

The advantage of singly doped waveguides is obviously the fairly simple growth of crack free active layers having low doping concentrations below 3%. However, the lattice matching condition between the rare earth doped film and pure substrate cannot be fulfilled at larger doping concentrations, resulting in fractured layers [mat72]. Moreover, the Yb^{3+} doping has to simultaneously fulfill two purposes: it provides a higher refractive index to the guiding layer due to its larger electron density compared to the yttrium ion it replaces; in addition, it is responsible for the absorption and stimulated emission of light, which is of vital importance for the design of optically active devices such as lasers. Due to this concentration restriction, the obtained refractive index contrast with the substrate is typically a few times 10^{-4}, resulting in a waveguide thickness of roughly 20 μm for optimal single-mode laser performance. Fabrication of channel waveguides in this singly-doped composition using etching has been demonstrated [pol07], but no lasing has been attempted. However, ultrafast-laser-inscribed, large-size channels [bor07] have led to the demonstration of channel waveguide lasers [bai09].

2.3. Liquid phase epitaxy of Gd^{3+}, Lu^{3+} co-doped layers

Fabrication of heavily rare earth doped KYW layers onto pure KYW substrates is enabled by carefully choosing the amounts of Gd^{3+}, Lu^{3+}, Yb^{3+} and Y^{3+} in the $K_2W_2O_7$ solvent, enabling growth of a composite single-crystalline layers. The energy levels of both, Lu^{3+} (filled $4f$ shell) and Gd^{3+} (half-filled $4f$ shell) are in the deep UV regime, making them optically inert for laser applications at wavelengths around 1 μm.

The refractive index of the co-doped material is increased by co-doping of the active layer with optically inert Lu^{3+}, due its larger electron density compared to the Y^{3+} ion it replaces in the KYW host material. Therefore co-doping of the active layer with large concentrations of Lu^{3+} eliminates the need of Yb^{3+} doping for ensuring a sufficiently high refractive index contrast, since the enhanced refractive index contrast with the substrate is mostly determined by the large quantity of Lu^{3+}, as depicted in Fig. 2.2.

In addition Gd^{3+} doping is introduced to fulfill the lattice-matching condition between the composite material and the substrate, which is required for epitaxial growth of crack free co-doped layers onto pure KYW substrates. The lattice constants of KYbW and KLuW are smaller compared to the lattice constants of the KYW substrate and the lattice constants of KGdW is larger compared to the lattice constants of the KYW substrate, as depicted in Table 2.1. To design the lattice constants of the grown co-doped layer, the lattice constants of the grown $KY_{1-x-y}Gd_xLu_y(WO_4)_2:Yb^{3+}$ composite layer is assumed to be the weighted average of the lattice constants of the stoichiometric compositions KYW, KGdW, KLuW and KYbW. Growth of heavily doped, lattice matched, single-crystalline layers can be obtained when carefully balancing the composition of the grown layer in order to fulfill the lattice matching condition [fer99]. High refractive index contrast channel waveguides in Gd^{3+}, Lu^{3+} co-doped KYW:Yb^{3+} were first demonstrated by Dr. Florent Gardillou [gar07]. The approach lattice matching by co-doping of the grown layer has also been successful when using pulsed laser deposition instead of LPE and resulted in successful growth Neodymium or Erbium doped $(Gd, Lu)_2O_3$ layers onto Y_2O_3 substrates in which channel waveguide lasing was demonstrated [kah08, kah09, gun08].

2.4. Designing an active waveguide

In the co-doped material it is possible to design the refractive index contrast of the waveguide by adjusting the Gd^{3+}, Lu^{3+}, Yb^{3+} and Y^{3+} content, however to grow crack free layers the lattice constants of the grown layer have to match to the lattice constants of the substrate. To minimize the lattice mismatch between substrate and grown composite layer, the lattice constants of the composite layer are calculated as a weighted average of the lattice constants of the stoichiometric compositions; KGdW, KLuW, KYbW, and KYW, as given in Table 2.1. One can derive a rule of thumb for lattice matched layers on pure KYW substrates: when taking similar parts of Gd^{3+} and Lu^{3+} ions to replace the Y^{3+} ions, resulting in the $KY_{1-x-y}Gd_xLu_y(WO_4)_2$:$Yb^{3+}$ (with $x \approx y$) composition. The balanced mixing approach is visualized in Fig. 2.6. The rule of thumb for lattice matching is expanded for the introduction of the optically active Yb^{3+} ions, by replacing the Lu^{3+} ions.
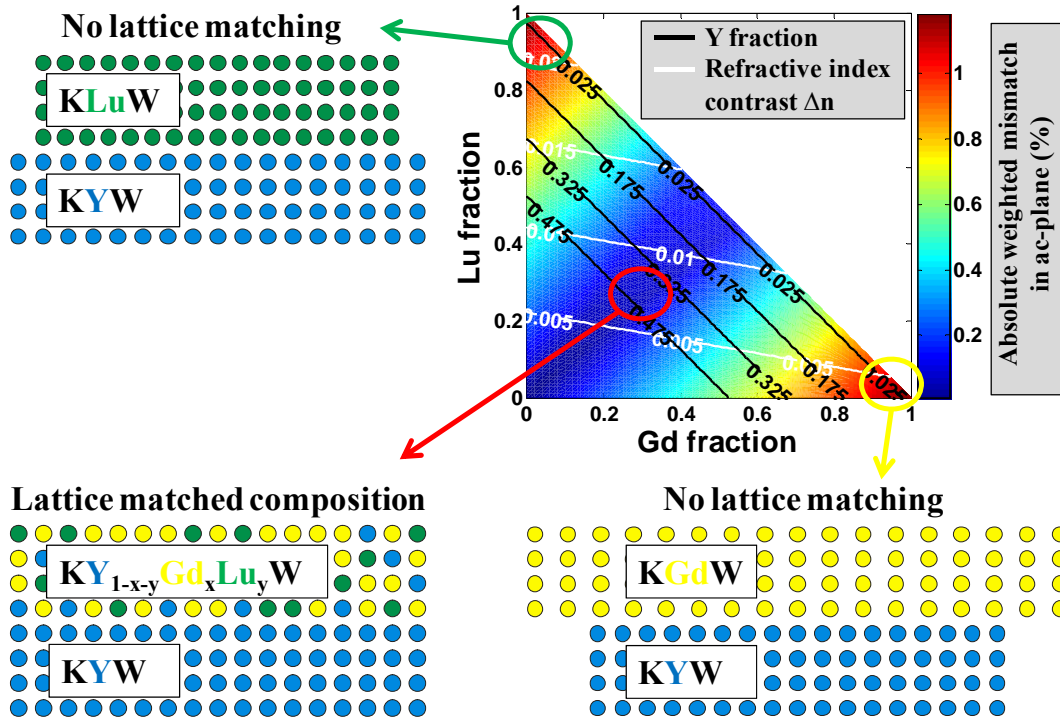
Fig. 2.6. Design of lattice matched thin films grown onto pure KYW substrates: This example visualizes the lattice mismatch between KLuW or KGdW films and KYW substrate when grown onto KYW substrates, indicated by the left-hand upper and right-hand lower schematic respectively. However, balanced introduction of Lu^{3+} and Gd^{3+} doping into the KYW film results provides lattice matched compositions as shown in the right-hand upper graph and left-hand lower schematic. In addition the refractive index contrast can be designed by adjusting the total doping concentration of the doped layer.

To estimate the composition of the layer having optimal lattice matching the lattice parameters of Table 2.1 are used to calculate the lattice constants (LC) in the *a-c* plane of various layer compositions. The sum of the absolute relative lattice mismatch (in %) between the substrate and the composite epitaxial layer for the *a* and *c* crystallographic axes should be minimized to achieve the optimum lattice matching. This sum to calculate this weighted mismatch between the layer and the substrate in % is given by:

$$Mismatch = \left[\left| \left(\frac{LC_{layer}^{a-axis}}{LC_{substrate}^{a-axis}} \right) - 1 \right| + \left| \left(\frac{LC_{layer}^{c-axis}}{LC_{substrate}^{c-axis}} \right) - 1 \right| \right] \cdot 100 \quad .$$

(2.1)

The lattice mismatch in the *ac*-plane of various layer compositions is visualized in Fig. 2.7 for layers having a $KGd_xLu_{1-x}(WO_4)_2:Yb^{3+}$ composition grown on a pure KYW substrate. Here the dark blue area indicates near-lattice-matched layer compositions when grown onto a pure KYW substrate.
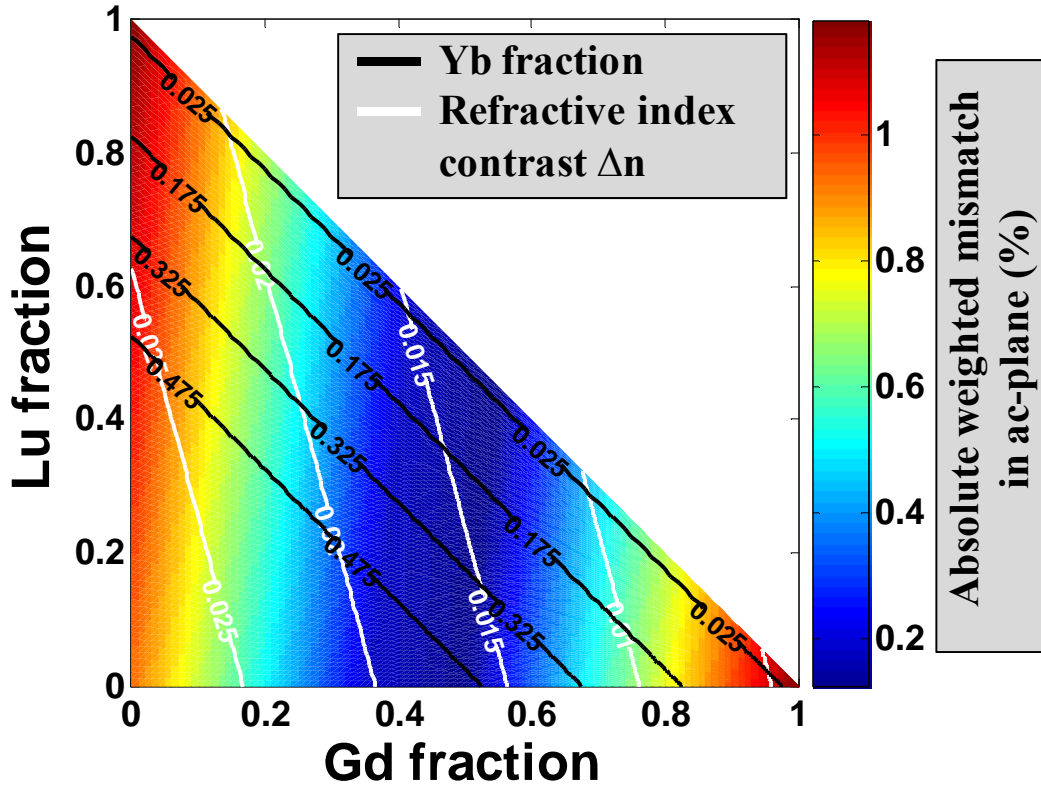
Fig. 2.7. A graphical representation of the weighted lattice mismatch in the *a-c* plane of a $KGd_xLu_{1-x}(WO_4)_2:Yb^{3+}$ composite layer having no Y^{3+} ions in its composition with respect to the KYW substrate. Here the lattice parameters, taken from Table 2.1., are used to calculate the weighted lattice mismatch in the *a-c* plane between the layer and substrate, according Eq. 2.1. The black lines represent the Yb^{3+} concentration and the white lines indicate the calculated refractive index contrast, according Eq. 2.2 and Eq. 2.3, with the substrate for $E||N_m$ polarized light at a wavelength of 1 μm using the data provided in Table 2.4.

The calculated refractive index contrast (Δn) for $E||N_m$ polarized light is indicated by the white lines in Fig. 2.7. The refractive index contrast is given by:

$$\Delta n = n_{layer} - n_{substrate}$$

(2.2)

Here the refractive index of the substrate ($n_{substrate}$) is equal to the refractive index of the used pure KYW. The refractive index of the layer (n_{layer}) is calculated using the relation,

$$n_{layer} = n_{KGdW}\mathrm{N}_{KGdW} + n_{KLuW}\mathrm{N}_{KLuW} + n_{KYbW}\mathrm{N}_{KYbW} + n_{KYW}\mathrm{N}_{KYW} ,$$ (2.3)

with N indicating the fractional concentrations of the components in the composite layer. The refractive indices used in this calculation are presented in Table 2.4.

Table 2.4. Refractive indices of the stoichiometric compositions of the monoclinic double tungstates, from which the composite layers are produced. The values are taken from Fig. 2.2, presenting the refractive indices of $E\|N_m$ at a wavelength of 1 μm.

Stoichiometric material	Refractive index of $E\|N_m$ at $\lambda = 1$ μm
KGdW	2.0124
KLuW	2.0309
KYbW	2.0376
KYW	2.0084

This table shows that when replacing the Y^{3+} ions of the KYW host by Gd^{3+}, Lu^{3+} or Yb^{3+} increases the refractive index contrast of the layer with the substrate. In this way the refractive index contrast between layer and substrate can be tuned up to $\sim 1.5 \times 10^{-2}$ for layers having the Y^{3+} ions completely replaced by Lu^{3+} and Gd^{3+} ions as depicted in Fig. 2.7.

2.5. Analysis of the layer structure and composition

A layer with a designed composition of $KY_{0.6}Gd_{0.13}Lu_{0.27}(WO_4)_2$:(1.7%)$Yb^{3+}$ was grown onto a *b*-oriented substrate [gar07]. The composition of the grown layer was determined by laser-ablation inductively-coupled plasma mass-spectrometry (LA-ICP-MS) [gun99]. The sample was ablated using a 193 nm ArF eximer laser (GeoLas M, Lambda Physik) with a fluence of 10 J/cm^2, a repetition rate of 1-5 Hz and creating crater diameters of ~ 60 μm. For analysis, the ablated material was transported within helium into an ICP-MS instrument (ELAN 6100 DRC +, Perkin Elmer). Quantitative analysis was carried out using NIST 610 glass as external calibration material and each sample was analyzed six times. This measurement was performed by K. Hametner from the Laboratory of Inorganic Chemistry, Department of Chemistry and Applied Biosciences, ETH Zurich. The results presented in Fig. 2.8 indicate that the composition of the grown layer is close to that of the initial solution and reveal that the segregation coefficients of all incorporated ions are close to unity.
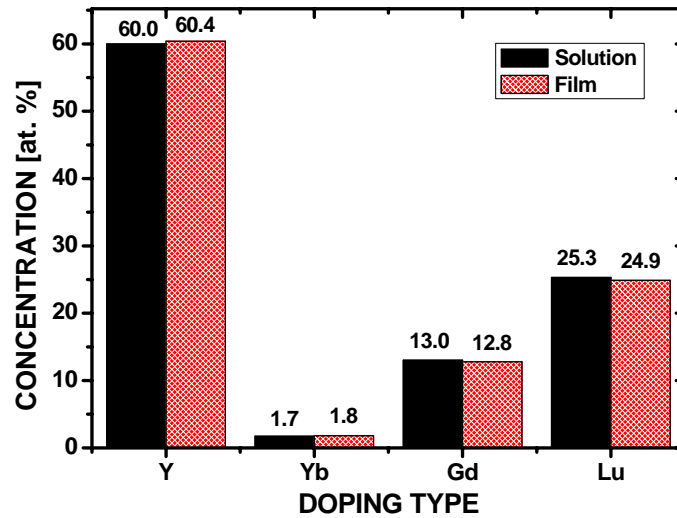
Fig. 2.8. Dopant concentrations in the solution and in the grown KY$_{0.6}$Gd$_{0.13}$Lu$_{0.27}$(WO$_4$)$_2$:(1.7%)Yb^{3+} layer as obtained from LA-ICP-MS measurements. The relative standard deviation of the determined concentration was < 1.3 %.

Co-doping a KYW layer with optically inert Gd^{3+} and Lu^{3+} ions introduces locally different environments to the active Yb^{3+} ions and may result in local lattice deformation, crystal defects, and increased levels of other optically active impurities. The influence of these undesired side-effects was investigated by X-ray diffraction (XRD), luminescence and lifetime measurements. The result of an XRD study is displayed in Fig. 2.9 and the 0-10-0 reflection is magnified in the inset. Although the measurement confirms the single-crystalline character of the grown layer, the full width at half maximum (FWHM) of the diffraction peak originating from the grown film is slightly larger (0.029°) compared to that of the undoped substrate peak (0.022°), which is due to the co-doping and to a certain extent also a result of the small thickness of the layer. The offset between the two diffracted peaks originates from the difference between the out-of-plane crystal lattice parameters of the film and the substrate.
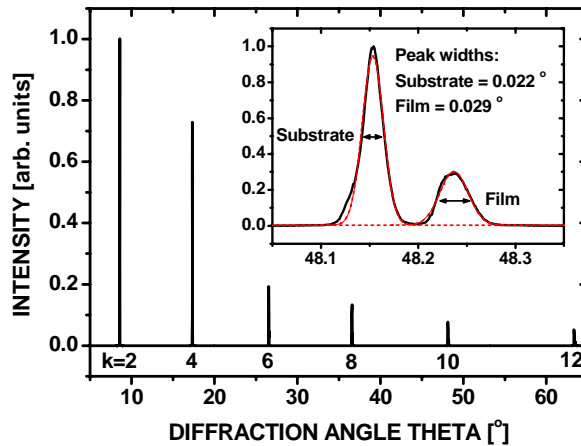
Fig. 2.9. XRD spectrum of a KY$_{0.6}$Gd$_{0.13}$Lu$_{0.27}$(WO$_4$)$_2$:(1.2%)Yb^{3+} layer grown onto an undoped KYW substrate showing the 0 k 0 reflections. An expanded view of the 0-10-0 Bragg diffraction together with the FWHM values derived for the film and the substrate are shown in the inset.

2.6.   Influence of refractive index contrast on mode confinement

The confinement of an optical mode in a waveguide strongly depends on the refractive index contrast between the waveguide and the cladding/substrate [kog90]. Modeling of the light confinement in the active waveguide region is performed using Phoenix FieldDesigner [pho] for various waveguide geometries having different refractive index contrasts. The refractive index contrast with respect to the pure KYW substrate of ~2% Yb^{3+} doped waveguides is approximately 7.5×10^{-4}. A contrast of nearly 1.5×10^{-2} is reached by replacing all of the Y^{3+} ions with Gd^{3+} and Lu^{3+} ions, as depicted in Fig. 2.6. At very large Yb^{3+} doping concentrations in the vicinity of 50%, the refractive index contrast has a maximum of 1.7×10^{-2}, as depicted in Fig. 2.7. Here, the trend of light confinement in the active region has been studied using air clad channel waveguide structures, of which the refractive index contrast of the waveguide material with respect to the substrate is varied. The refractive index contrast is varied from 7.5×10^{-4} up to 4×10^{-3}, in correspondence to the singly Yb^{3+} doped KYW waveguides, and in correspondence to first generation of Gd^{3+}, Lu^{3+} co-doped layers in having no complete replacement of the Y^{3+} ions by Gd^{3+} and Lu^{3+} ions, respectively.

The simulation entails 2-μm-deep etched, air-cladded channel waveguides, of which three parameters have been varied: the refractive index contrast of the layer with respect to the substrate, the layer thickness and channel width, as depicted in Fig. 2.10.
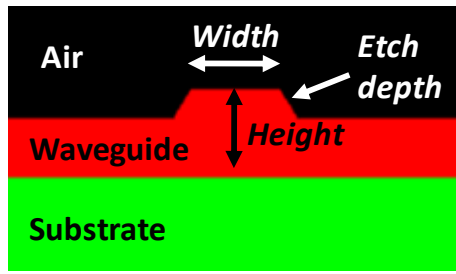
Fig. 2.10. Typical cross-section of waveguide design, to calculate the optimal waveguide properties using a mode solver.

Only single-mode solutions are taken into account when calculating the overlap of the laser mode with the gain medium below the etched ridge. The calculated overlap is presented in Fig. 2.11.
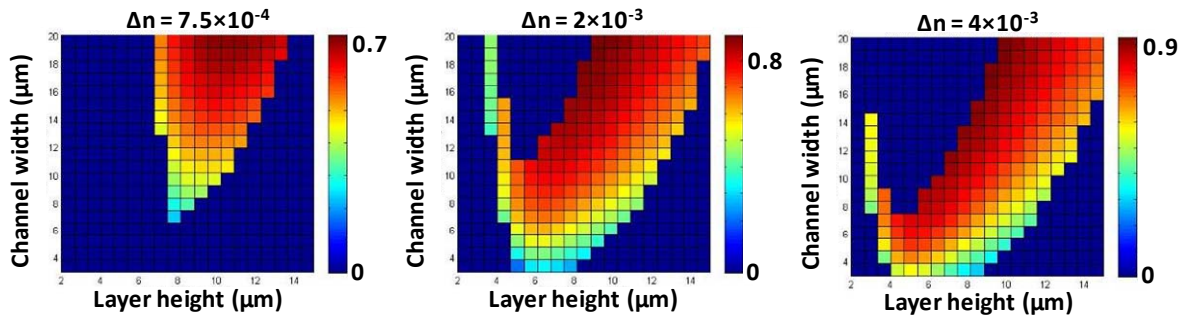
Fig. 2.11. Calculated mode overlap with the active region of the waveguide for various waveguide dimensions fabricated in materials with three different refractive index contrasts: 7.5×10^{-4}, 2×10^{-3}, and 4×10^{-3}. No solutions are calculated for waveguide dimensions corresponding to the dark blue area; these waveguide dimensions are either multimode or do not support a guided mode.

At low refractive index contrasts the mode tends to be large ($\sim 10 \times 20 \ \mu m^2$), and no advantage over a bulk design can be obtained, since the usually larger propagation loss observed in waveguide geometries negates the slightly positive effect of tighter mode confinement. A larger etch depth to improve the lateral confinement in this material does not improve the confinement, as the guided mode extends into the undoped substrate, resulting in a diminished interaction with the active layer. A layer of higher refractive index contrast is required, as it improves the confinement of the guided mode into the active region and allows smaller waveguide dimensions, making the fabrication of microstructured waveguides easier. The difference in mode-field diameter of the guided mode in channel structures in different refractive index contrast waveguides is nicely visualized in Fig. 2.12 [pol07], where the guided mode in deeply etched (up to 6 μm) channel-waveguide structures in KYW:Yb^{3+} and Gd^{3+}, Lu^{3+} co-doped KYW:Yb^{3+} layers grown on KYW substrates is compared.
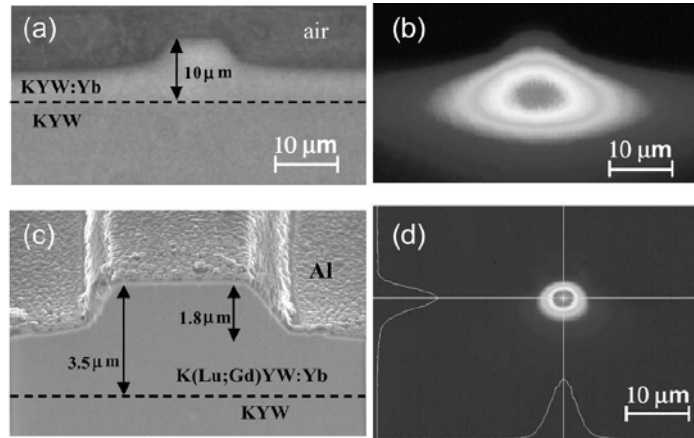
Fig. 2.12. End-face cross-section demonstrating the influence of enhancement of the refractive index contrast on the mode field [pol07], taken (a) with an optical microscope of a KYW:Yb^{3+} layer with low refractive index contrast, and (c) with a scanning electron microscope of a Lu^{3+}, Gd^{3+} co-doped KYW:Yb^{3+} layer with high refractive index contrast. Mode intensity profiles: (b) KYW:Yb^{3+}, (d) Lu^{3+}, Gd^{3+} co-doped KYW:Yb^{3+}.

An overlay of a pure KYW cladding is desired to improve the mode overlap with the active region, and ease polishing of the end-facets of the waveguide. Therefore, all laser results discussed in this thesis are based on buried waveguides.

2.7. Polishing

The time-consuming process of polishing is performed on all grown active layers, whereas the surface of passive overgrown layers remained as grown. The end-facets are also polished. One facet takes typically one day, including mounting and making the alignment. Polishing is by many people referred to as an art, but when performed a dozen times one can see a clear pattern: the origin of most errors introduced during polishing can be traced back. Some of the challenges when polishing a brittle material like KYW are discussed in this section.

2.7.1. Standard polishing routine

The topology of the grown crystals is not flat; normally the grown layer is much thicker near the edges than in the center of the sample. The non-uniformity of the thickness can be several tens of micrometers. Therefore, the treatment of the surface starts with a lapping step to level the surface topology.

The lapping and polishing recipe, depicted in Table 2.5., has been developed together with Logitech on a Logitech PM-5. Slight deviations from this recipe, i.e. varied processing duration, pressure applied, and rotation speeds may be required for different samples. At Logitech it has been demonstrated that the second fine lapping step could be skipped and compensated for by a slightly longer polishing step. Here the most successful process flow is discussed together with the most common errors.

Table 2.5. Polishing routine.

Step	Description	Fluid	Duration (minutes)	Disk RPM	Fork sweep	Pressure (g/cm²)
1	Fixation of sample on chuck	Quartz wax or Phthalate wax	30	--	--	--
2[*]	Conditioning of machine cast-iron lapping-disk	9 µm slurry	30	70	No	Standard load
3	Alignment of sample	--	5 – 20	--	--	--
4[*]	Coarse lapping	9 µm slurry	Up to desired result	5	No	200
5	Machine conditioning	3 µm slurry	30	70	No	Standard load
6	Fine lapping	3 µm slurry	Up to desired result	5	No	200
7	Machine conditioning	DI-Water	30	40	Yes	Standard load
8	Polishing	Struers (OP-U)	30 – 90	20	Yes	400

[*]**Process steps 2 and 4 are normally skipped for surface polishing.**

A slightly different treatment is required when processing the waveguide end-faces. Here the KYW sample is sandwiched between glass substrates to support the edge of the sample. The significant height difference of the glass/KYW substrates requires lapping by use of an abrasive having a coarse grain size. The lapping is performed in a cast iron lapping disk by use of Logitech silica carbide slurry having a grain size of 9 µm or 3 µm. The polishing step is performed on a polyurethane coated disk using Struers (OP-U) polishing emulsion. In between the processing steps both, the cast-iron lapping disk as well as the polyurethane polishing disk has to be conditioned to maintain their flatness.

To obtain the desired layer thickness, the layer is lapped down to a thickness of 5 µm thicker that the desired thickness. Typically 4 µm is removed during the polishing before a good quality is obtained; the last µm is removed by an extended polishing time. The removal rate is approximately 2 µm per hour depending on the applied processing pressure.

2.7.2. Sample preparation

For the purpose of surface polishing a sample is fixed on the chuck of the polishing jig by soft quartz wax having a melting temperature of approx 70°C, see Fig. 2.12.
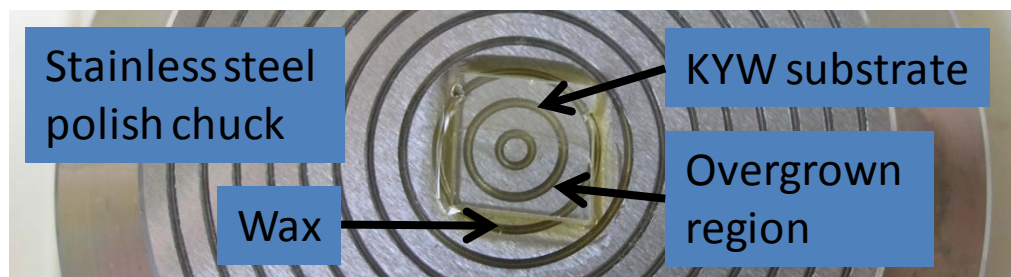
Fig. 2.12. Picture of sample mounted on polish chuck with use of quartz wax.

For end-face polishing, the sample has to be diced parallel to the orientation of the desired facet. This is performed using a high precision dicing saw from LoadPoint Ltd. using a

smooth F1230 diamond blade with a thickness of 30 μm. This dicing blade has a limited cutting depth of ~0.5 mm, which is sufficient to initiate a well-controlled fracture. A dicing saw blade from Thermocarbon Inc. (TC300), having a larger cut depth of 3 mm, is not suited for this purpose, as it provides a fairly rough finish of the facet, providing insufficient reflection for optical alignment with an autocollimator. Once the sample has the desired dimensions, the sample is cemented in between a stack of soda glass microscope slides using rigid, transparent wax (phthalate), having a melting temperature of 90°C. The stack is mounted in the sample holder, as shown in Fig. 2.13.
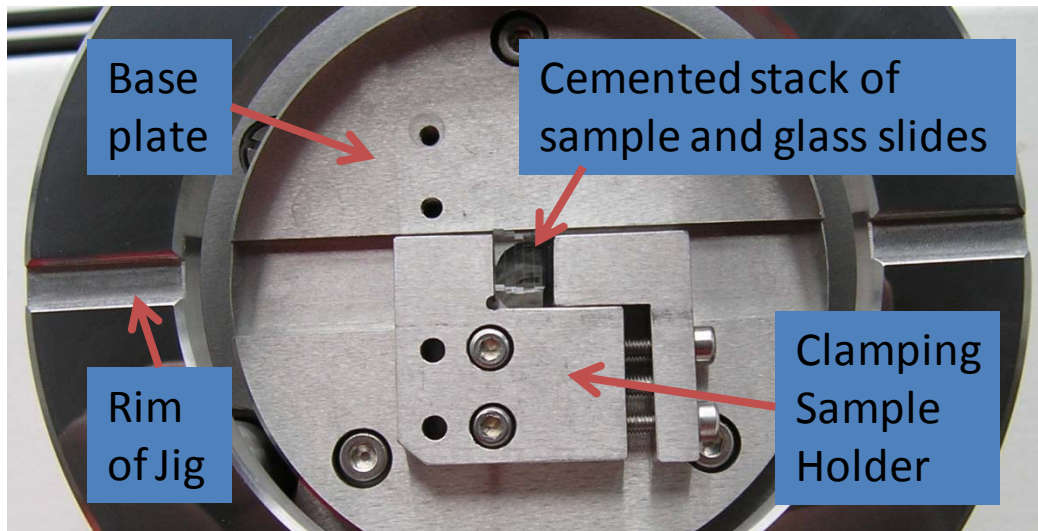
Fig. 2.13. Picture of samples mounted in sample holder for end-face polishing.

Roughly 1 mm^2 of the reflective, diced facet must be visible, i.e. clear from wax, for optical alignment with the autocollimator.

2.7.3. *Sample alignment using the autocollimator and setting of process pressure*

Once the sample holder is mounted into the polish jig, it can be aligned for parallel polishing of the surface with respect to the substrate orientation. For this alignment an autocollimator is used that exploits the reflection of the non-overgrown part of the substrate for orientation. In the same way the reflection of the diced facet is exploited for orientation of the sample prior to end-face polishing. The autocollimator has a specified alignment accuracy of 2 arc-seconds [log]. The jig presses the sample onto the lapping/polishing disk during processing. The contact force can be adjusted by changing the tension of the load spring of the jig. A balance is used to measure the contact force. The processing pressure is calculated by dividing the pre-set force by the sample area.

2.7.4. *Determination of layer thickness*

A Michelson interference microscope shown in Fig. 2.15 (a) is used to measure the thickness of the polished layers. The working principle of this microscope is based on the original principle used to measure motion of the planet earth through space [mic81]. In this optical instrument fringes are formed by combining the reflection from a reference flat (reference path) with the reflection coming from the surface of the investigated sample (measurement

path). A built-in interference filter at 550 nm is used to generate monochromatic light that is used as "ruler" providing a fringe line for each ½ wavelength optical path difference between the reference and sample arm. This means that the distance between each line in this instrument corresponds to 275 nm. The drawn example in Fig. 2.15 (b) shows a step shifting 4 fringes: this corresponds to a step height of 1.1 μm.

(a)   (b)
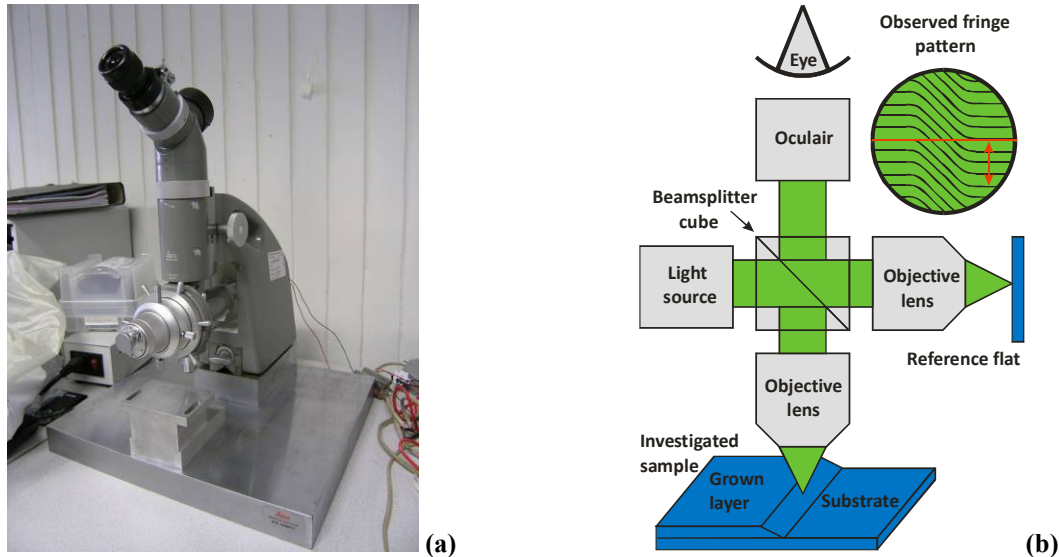
Fig. 2.15. (a) Picture and (b) schematic of the used profilometer, to measure the thickness of the grown layer by counting fringes as depicted by the red arrow in (b).

2.7.5. Obtained surface quality

To determine the flatness of the polished surface a Dektak profilometer has been used to measure the curvature of the surface, as shown in Fig. 2.16.
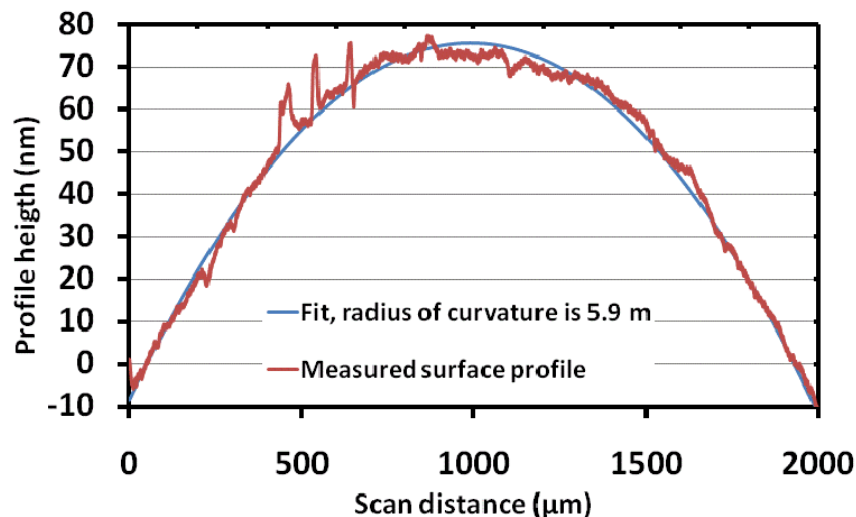
Fig. 2.16. Measured surface profile of in-house polished sample using a Dektak profilometer shown by the red line. The blue line gives the best fit with a radius of curvature of 5.9 meters. Dektak settings: 2.5 μm stylus, 5 mg scanning force.

The obtained curvature of 5.9 meters is slightly better than an earlier reported radius of 2.45

meters obtained on a Logitech CL40 Polishing machine [rom05]. The difference can be explained by the use of a different polishing machine.

An atomic force microscope (AFM) is used to compare the roughness of two substrates: one is polished by the supplier of crystals and the other is an in-house polished substrate. Only minor differences in surface roughness are observed, resulting in a measured surface roughness of about 1.5 nm root-mean-squared (RMS) for both samples.

Surface topology of an in-house polished substrate

Surface topology of a commercially polished substrate
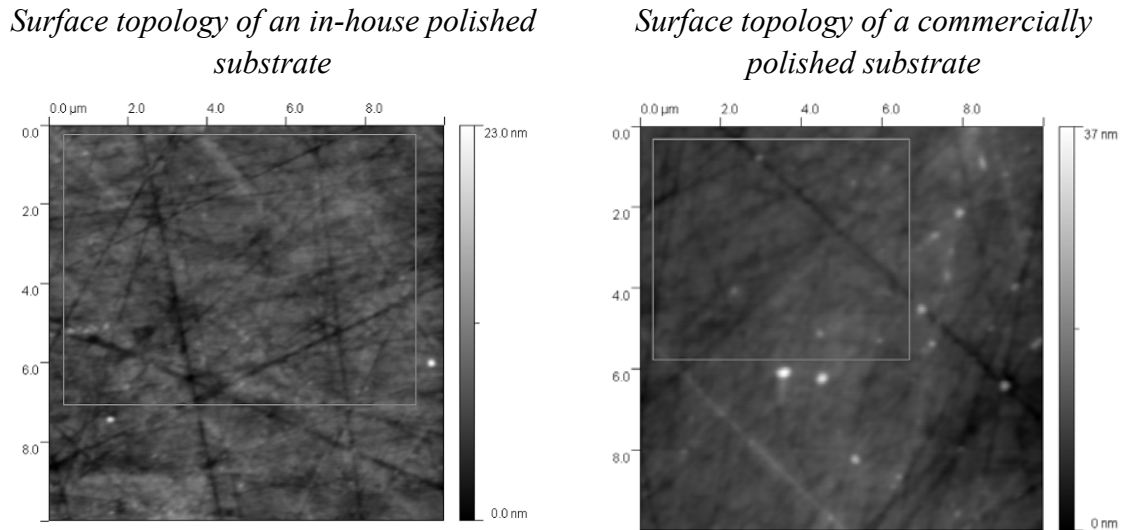
(a)

(b)

Analysis of selected area

RMS = 1.43 nm	RMS = 1.71 nm
Minimum = 0.32 nm	Minimum = 2.62 nm
Maximum = 13.2 nm	Maximum = 18.68 nm

Fig. 2.17. Comparison of the surface roughness between the surfaces of (a) an in-house polished KYW substrate and (b) the surface of a supplied KYW substrate, using AFM profile scans. The scans are performed by B. Mogulkoc from the TST group, having a scan speed of 0.7 Hz and a tip radius of 20 nm.

When comparing the obtained patterns from the AFM scans in Fig. 2.17, the surface topology of the purchased, commercially polished substrate appears to be a bit blurred. Most likely a chemical-mechanical polishing (CMP) procedure is used, washing out the scratches. The in-house polished surface has been polished only mechanically.

2.7.6. Obtained end-face quality

Edge-rounding effects at the polished end-faces should be kept to a minimum to reduce coupling losses to the waveguide [ger01], especially for air-cladded waveguides where any rounding of the edges directly affects the end-facet of the waveguide. The thickness of the wax layer between the sample and the glass slides must be as thin as possible in order to minimize rounding of the edges. This can be achieved by applying significant force on the stack at temperatures of 100°C for about 30 minutes. In this way thin wax layers can be achieved of ~1 μm thickness, as shown in Fig. 2.18.
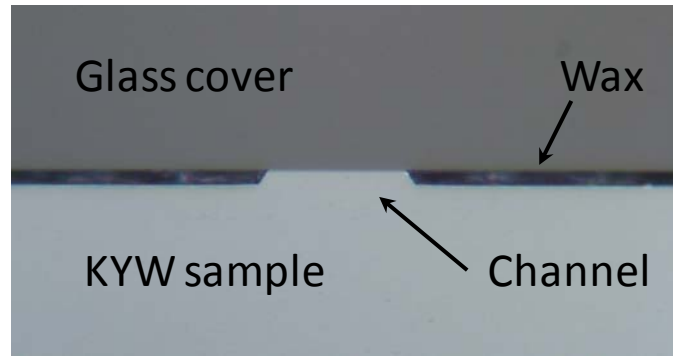
Fig. 2.18. Polished end-facet of an air cladded channel waveguide in KYW. Here the etch depth was approximately 1 μm. Since the top of the channel is in close contact with the glass cover, the wax layer is also around 1 μm thick.

Care has to be taken to apply the pressure in a gentle manner and large temperature fluctuations should be avoided, as otherwise the sample might crack by the induced stress. A typical cooling time from ~100°C to room temperature takes 30 minutes when removing the sample from the hotplate onto a wooden surface (e.g. the table). Cooling on a water-cooled aluminum chuck is not recommended.

Fig. 2.19. Visualization of rounding of the polished end-facet of a stack of three KYW samples. The fringes are formed between a glass cover slide that has been placed on top of the polished interface, hence these images are taken through this glass substrate, illuminated with green light.

Fig. 2.19 shows the polished facets of a stack of three KYW samples. Here the wax gap between the two top samples is roughly 1 μm. Towards the side the wax layer is significantly thicker and becomes clearly visible, as indicated by the arrow. The gap between the middle and lower samples is undefined, since the samples have only one side polished. The fringes are formed between a glass cover slide that has been placed on top of the polished interface; this image is taken through this glass substrate using green light. The image shows that the rounding of the edges near the wax gap is significant. In the center where the gap is only 1 μm, the deviation is roughly one fringe, i.e. ~250 nm, but at larger wax gaps the rounding of the edges rapidly increases. Therefore, it is of vital importance that during polishing of air cladded waveguides the gap should be minimal. This is an additional reason to develop buried waveguide structures by overgrowth of pure KYW onto the active waveguide. The overlay not only eases the end-face polishing, but in addition reduces the scattering losses, enhances the mode overlap with the active region and significantly enhances the optical damage threshold. Some polished buried waveguide end-facets are shown in Fig. 2.20.

(a)   **(b)**   **(c)**
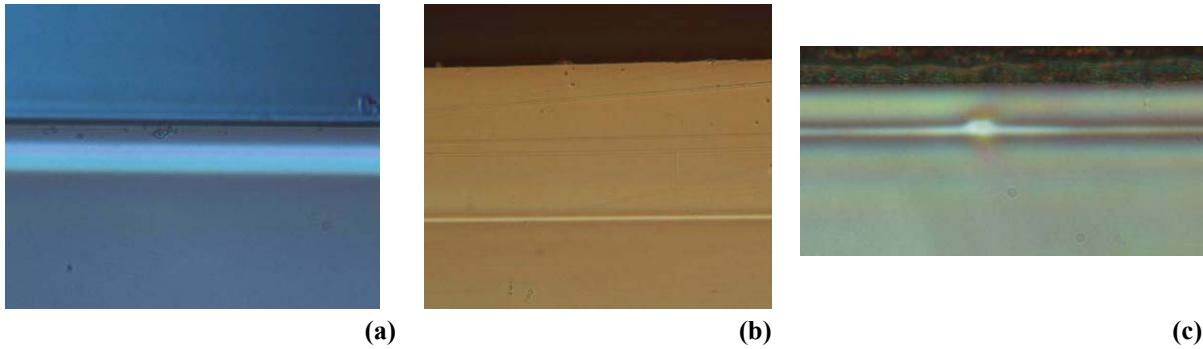
Fig. 2.20. Visualization of polished end-facets of (a) 4.3 μm (b) 1.2 μm and (c) ~2 μm thick buried waveguides using backside illumination. All images show from top to bottom: Air/wax – cladding layer – bright waveguide region – substrate. In images (a) and (b) dirt and damages are observed at the facets of the cladding, just above the important region of the waveguide facet.

2.7.7. *Polishing defects: "orange peel" topology*

The surface damage as depicted in Fig. 2.21 appears like the surface of an orange peel and can be easily observed by the naked eye when looking at the reflection of the surface.
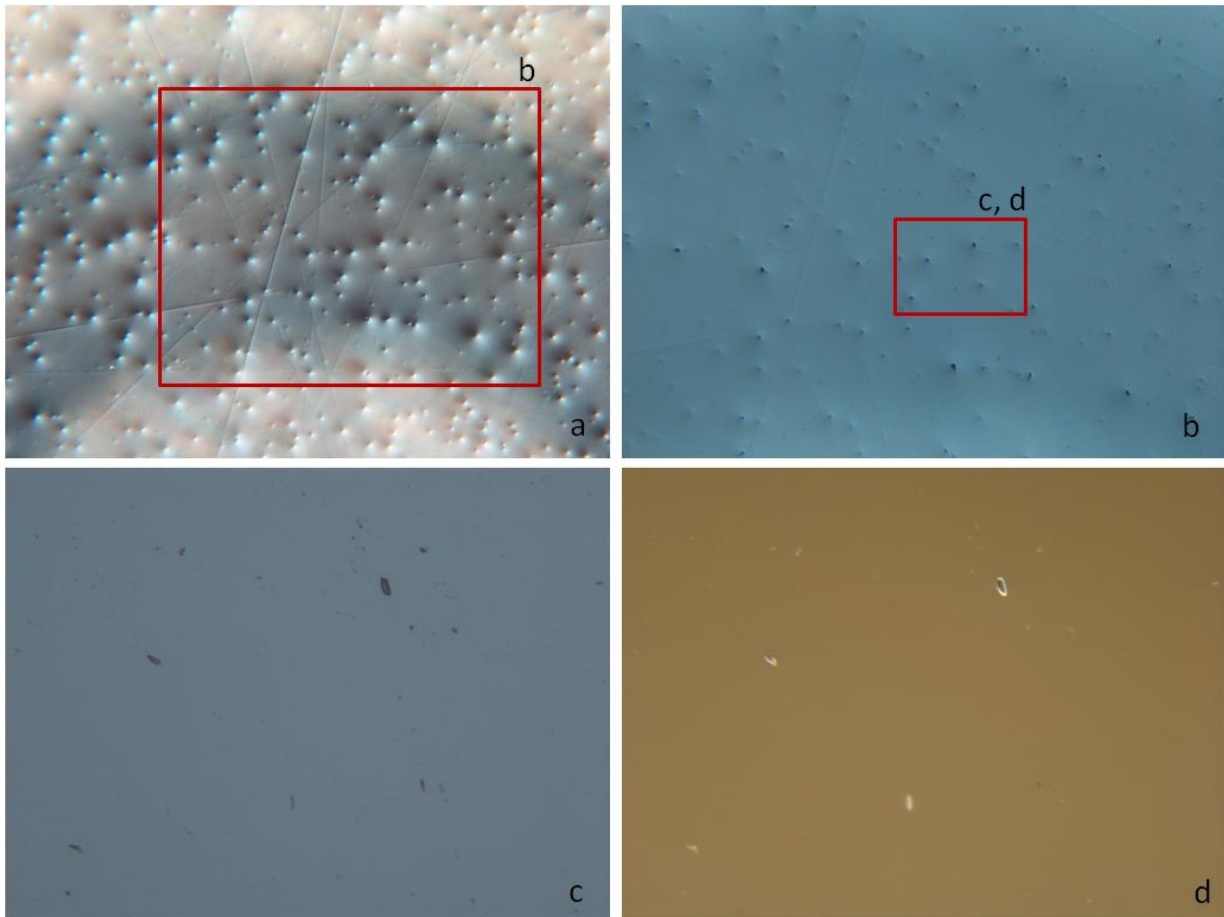
Fig. 2.21. Optical micrographs of orange peel topology. The craters and scratches are clearly visible under low magnification using an interference contrast microscope as is depicted by (a) and (b). At larger magnification (c) and (d) the voids in the surface are clearly resolved; here interference contrast mode and bright field mode are used, respectively.

These defects were only observed during the polishing step and were attributed to several causes during the polishing step. Several possible causes have been investigated, by changing the condition to sort out the underlying problem. The attempted solutions are listed in Table 2.6.

Table 2.6. List of tests to avoid "orange peel" topology polishing defects

Hypothetic cause of "orange peel" topology defects	Performed remedies
Poor hygiene of polishing machine	An additional shield is mounted above the machine
Inclusion of the $K_2W_2O_7$ solvent during the growth	This hypothesis is unlikely, since this has never been reported for this material
Too low PH value of polishing liquid, corrodes the surface	This is a common problem when polishing metals and can be solved by addition of ammonia to the polishing liquid
Undesired chemical etching of the surface	The chemical/mechanical polishing emulsion (Logitech SF1) has been changed to an only mechanical polishing emulsion (Struers OP-U)

In the long run all these precautions did not seem to have the desired effect. It appeared that the "orange peel" topology is caused during the lapping stage and only appears after polishing.

It appears that invisible micro-fractures can be formed when applying too large pressures during the lapping stage. During the final polishing step, these micro-fractures propagate, resulting in chipping of the surface. The development of the surface defects during polishing is depicted in Fig. 2.22.
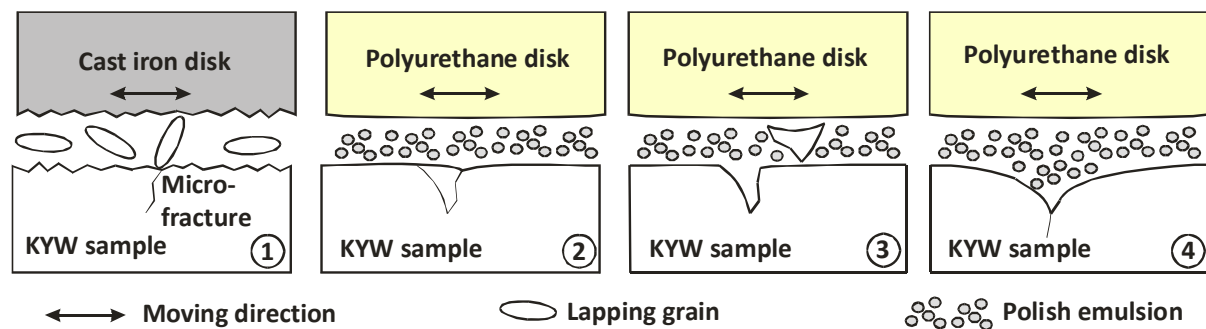
Fig. 2.22. Formation of surface defects during polishing caused by too much pressure. Invisible micro-fracturing occurs during the previous lapping step at too large pressures (1). The micro-fractures propagate (2) until chipping of surface occurs (3). After long polishing times > 1h the defects are not washed out; the micro-fractures seem to keep on propagating (4).

Besides the formation of craters, also severe scratches are observed in Fig. 2.21 (a) and (b); this occurs due to contamination of the polishing disk by chipped KYW particles. At larger magnification, see Figs. 2.21 (c) and (d), the voids of the chipped micro-fractures are clearly resolved. The images in Fig. 2.21 are taken from a sample that has been polished for over 1.5 hours. To rescue the sample used in Fig. 2.21, it has been lapped for one minute with 1 μm grain slurry at an extremely low pressure to remove the roughness. After 10 minutes of polishing only faint traces of the orange peel topology were observed. However, an additional 10 minutes of polishing resulted in a similar orange peel topology as initially observed. This

means that the chipping of the surface does not stop the propagation of the micro-fracture, as depicted in Fig. 2.22 (4). This means that the "orange peel" topology defect cannot be removed by longer polishing times. More detailed observation of the defects is shown in Fig. 2.23, using a scanning electron microscope (SEM).
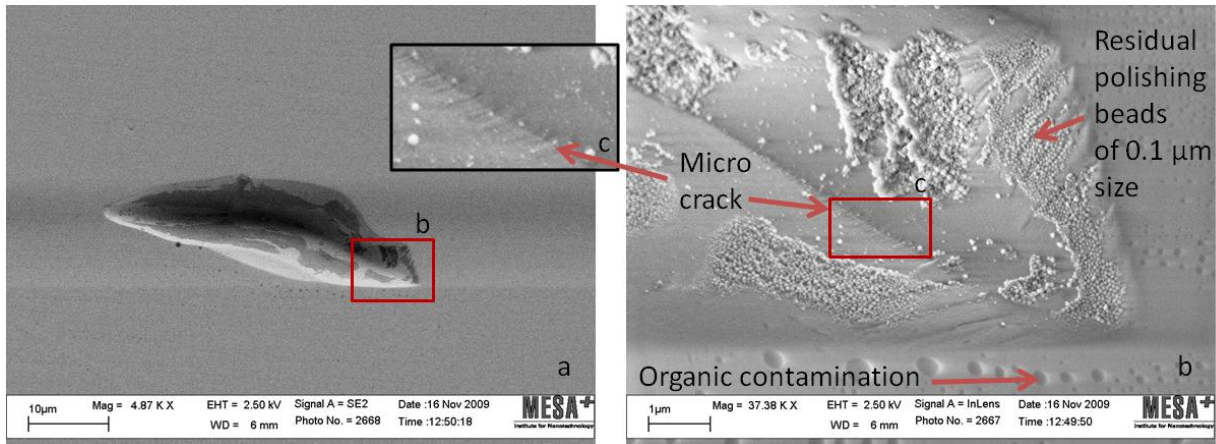
Fig. 2.23. Scanning electron micrograph of surface defect after polishing (a), and magnified (b, c) showing the micro-fracture. The size of the polishing beads is specified to be 0.1 μm that corresponds closely to the observed size. The organic contamination originates from the used wax and solvent to clean the sample, which can be removed by HNO₃-cleaning.

The SEM images reveal the hidden micro-fracture at its origin.

2.7.8. *Early detection and remedy of "orange peel" defects*

Formation of micro-fractures can indirectly be observed during the lapping stage. The pieces that chip off from the surface are usually somewhat larger compared to the grain size of the abrasive. These particles cause visible scratches in the sample which are more apparent on the rim of the polishing jig. The first action is to clean the whole machine to remove the contamination from the lapping disk, in combination with a reduced lapping pressure. Even at reduced pressures, chunks of material will chip off, caused by the already formed micro-fractures. A few cleaning/lapping cycles will usually result in less visible scratches on the jig. An indication of having no micro-fractures in the film anymore is found when all scratches on the rim of the jig have vanished (if there is still a film left). Ignoring these signals and proceeding to further polishing usually results in an orange peel topology.

Remarkably, this problem has never been observed during end-face polishing. Usually millimeters of material have to be removed during end-face polishing, which is done by cranking up the pressure and the RPM`s. During end-face polishing soda lime glass is used as sample support, since the hardness of KYW of around 4.5-5 on the Moh's scale [kam01] is close to that of soda lime glass, having a Mohs hardness of 5-6 [uqg]. It seems that the glass supports on both sides of the sample damp mechanical shocks, as the glass is more flexible compared to the brittle KYW. This mechanism prevents damage of the KYW crystal. Therefore, one could consider adding normal glass to the polish area, adjacent to the sample during surface polishing, to obtain the same positive effect. However, the disadvantage is that this significantly increases the process time, since two pieces of material never have the same

height/orientations, and requires long lapping times to level the interface of the sample with the surrounding glass.

2.8. Conclusions

By co-doping the optically active KYW:Yb^{3+} layers with large fractions of Gd^{3+} and Lu^{3+} ions it is possible to design the optical properties of the active waveguide, while maintaining the lattice matching condition. Here the refractive index contrast of the layer with respect to the pure KYW substrate can be designed up to 1.5×10^{-2}. In addition, large Yb^{3+}-doping concentrations of more than 50% can be reached under lattice matched condition using this approach. A model has been developed to calculate lattice matched compositions and provide the refractive index contrast of such layers with respect to the substrate.

High quality polishing of these active layers can be performed, having a surface roughness of about 1.5 nm rms. and a curvature of about 5.9 meters. Surface defects, caused by too large polishing pressures, have been analyzed. A solution to detect these defects in an early stage and avoid further damages is developed.

3   Towards Yb^{3+}-doped waveguide lasers in co-doped potassium double tungstates

This chapter discusses the spectroscopy of Yb^{3+} ions doped into monoclinic double tungstates. This choice of material provides many advantages such as large emission and absorption cross-sections, making it an excellent candidate for development of micro sized laser devices. However, no accurate spectroscopic data is available for the used composite crystalline host material; therefore a model is proposed, combining the available spectroscopic information of Yb^{3+} ions doped into stoichiometric crystal hosts that were used to make the composite host material in this work. This spectroscopic information was used in a spatially resolved rate equation model to design waveguide lasers. The work is complemented by demonstration of a highly efficient planar waveguide laser in a Gd^{3+}, Lu^{3+} co-doped KYW:Yb^{3+} host.

3.1.   Spectroscopy of rare earth ion doped potassium double tungstates

Rare earth ions are incorporated into the KYW host at its Y^{3+} site, thereby replacing the Y^{3+} ions. The stoichiometric compositions of a selective group of rare earth ions: Sm^{3+}, Eu^{3+}, Gd^{3+}, Tb^{3+}, Dy^{3+}, Ho^{3+}, Er^{3+}, Tm^{3+}, Yb^{3+} and Lu^{3+} ions all have the same monoclinic structure [kle96], hence allowing continuous solid solutions between KYW and the stoichiometric compositions using these doping types to create bulk crystals. The stoichiometric compositions KYbW [pujo02] and KErW [kam83] show unique laser properties. The extremely short absorption length of 13.3 μm at the absorption peak of 981 nm in KYbW is not only highly interesting for high power thin disk applications having an advantageous cooling mechanism [gie07], but also highlights the interest for micro-sized integrated optically active devices. The remaining rare earth ions La, Ce, Pr, Nd, and Pm crystallize in a tetragonal structure, which is different compared to the monoclinic structure of KYW, therefore only low doping concentrations up to 5% of these rare earth ions can be grown without affecting the monoclinic structure of KYW.
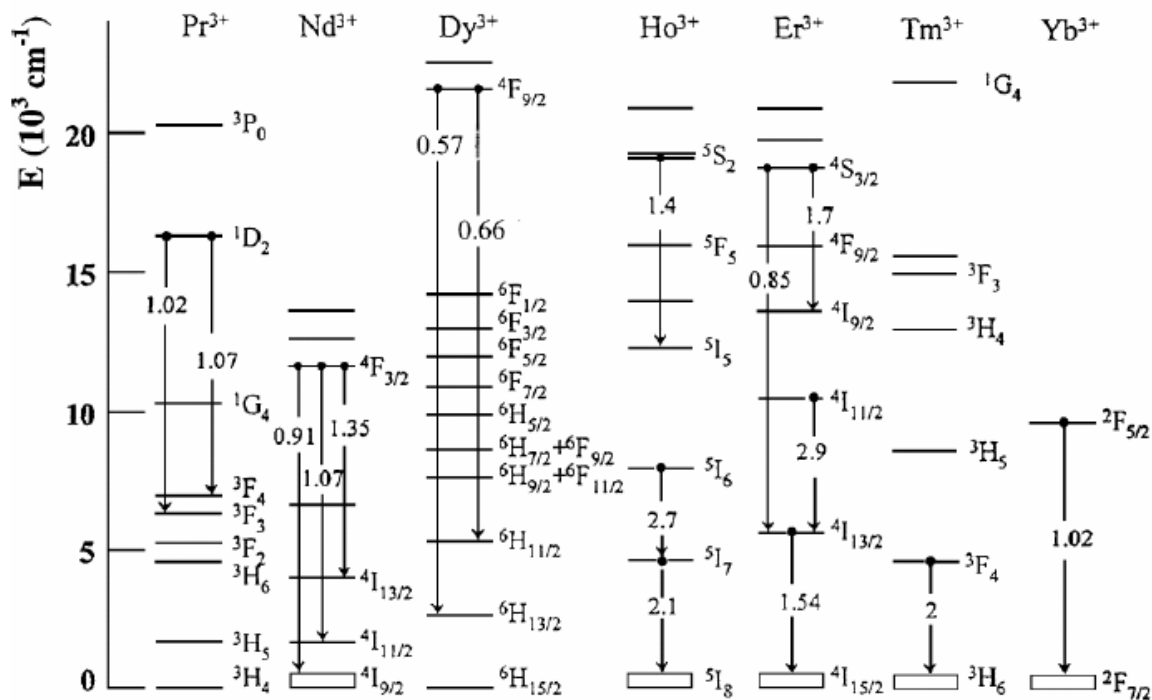
Fig. 3.1. Energy levels of rare earth ions used as active dopants for the KYW crystals. Some popular laser transitions are indicated by arrows with their transition wavelength in μm [kam02].

The energy level schemes for several rare earth ions in the KYW host, together with the indication of possible laser transitions and their corresponding wavelength are shown in Fig. 3.1. Generally, the positions of energy levels for the trivalent rare earth ions in KYW do not differ significantly from those in other oxide crystals [die63] because of the electronic shielding of the 4f sub-shell by the outer 5s and 5p sub-shells. One remarkable property of the Yb^{3+} ion is that it concerns a two energy level system, whereas the other ions have multiple energy levels. The advantage of such a configuration is that it lacks parasitic up-conversion processes. The two energy states, $^2F_{5/2}$ and $^2F_{7/2}$, are split due to the presence of the crystal field and Stark sub-levels are generated: three and four Stark sublevels for the $^2F_{5/2}$ and $^2F_{7/2}$ states, respectively. The energy level scheme of Yb^{3+} in the KYW host is shown in Fig. 3.2.
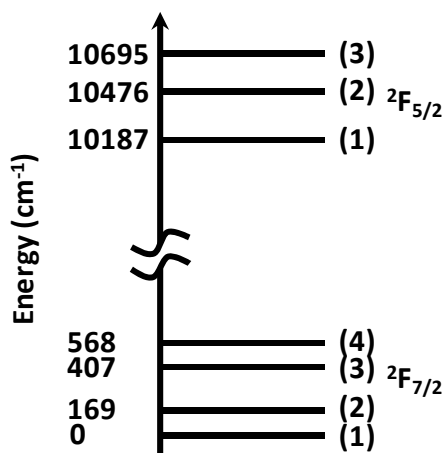
Fig. 3.2. Energy level scheme of the Yb^{3+} ion in the KYW host [kule97].

The Stark splitting is only a few hundred cm^{-1} and the partial population distribution f within a Stark multiplet obeys the Boltzmann distribution

$$f_i = \frac{\exp\left[(E_1 - E_i)/(k_b T)\right]}{\sum_i \left\{\exp\left[(E_1 - E_i)/(k_b T)\right]\right\}}.$$

(3.1)

Here, E_1 and E_i are the energies of the lowest and upper sub-levels, T is the temperature, and k_b is the Boltzmann constant. At $T = 300$ K, the partial populations of the ground $^2F_{7/2}$ and excited $^2F_{5/2}$ state are given in Table 3.1.

Table 3.1. Partial populations of the energy levels at T = 300 K of KYW:Yb^{3+} [kule97]

Energy level	Stark split level	Energy (cm^{-1})	Population @ 300K
$^2F_{5/2}$	2'	10695	6.5 %
	1'	10476	18.7 %
	0'	10187	74.8 %
$^2F_{7/2}$	3	568	4.0 %
	2	407	8.6 %
	1	169	26.9 %
	0	0	60.5 %

The main advantages of the crystalline host compared to amorphous host materials is its influence on the spectroscopic behavior of the Yb^{3+} ions doped into it. The strongly anisotropic crystal field enhances the absorption and emission cross-sections significantly for $E||N_m$ polarized light. In addition, the crystal field is equal for all ions; therefore, no inhomogeneous linewidth broadening is expected, resulting in narrow and strong transitions. Moreover, the large inter ionic distance, discussed in Subsection 2.1.1., strongly reduces parasitic inter-ionic interactions that lead to quenching of the excitation. In glass host materials the ionic distance is not fixed, and clustering of ions can occur at fairly low doping concentrations. The spectroscopic interaction between ions can negatively influence the laser related spectroscopy. Energy transfer processes between ions can cause migration of the energy to impurities, releasing the energy via non-radiative processes, effectively returning the ions to the ground state. Hence, an increased amount of ions is in the ground state and available for pump and signal light absorption, which can affect the laser performance [pol00]. These inter ionic distances are decisive in the phenomena of interactions between lanthanide ions. The interaction between the lanthanide ions has been investigated over many decades [ino65, kus73], however no evidence for significant adverse effects on the laser related spectroscopy in heavily doped KYW:Yb^{3+} crystals has been reported in the literature.

3.2. Spectroscopy of composite host material

A laser threshold analysis, performed on the last experiment concerning the zero-phonon line operation, revealed an unexplained discrepancy with the theoretically predicted behavior. Here basic laser theory, used in Subsection 5.4.3, predicted laser operation at the 1000 nm transition in open cavity configurations, while a very stable laser operation at the zero-

phonon line at 981 nm was found. Up to that moment the spectroscopic information concerning the emission and absorption cross-sections of KYW:Yb[3+] was taken from Kuleshov [kule97], but to explain the discrepancy with the experimental results an evaluation of the spectroscopic data provided by Kuleshov and the development of new spectroscopic data for the used composite host material was necessary. The emission and absorption lines of rare earth ions are influenced by the host material; this is the main reason why potassium double tungstates are selected as the host material, as they strongly enhance the absorption and emission cross-sections of rare earth ions doped into them. In this work a specific new spectroscopic footprint of the Yb[3+] ions is expected, since a new composition of host material was used. Luckily, the composition of the host material is based on four commonly used host materials, KGdW, KLuW, KYbW, and KYW that have similar spectroscopic properties. Here a weighted average of the literature values found for the four commonly used host materials is proposed to predict the spectroscopic footprint of the used composition. This approach resulted in a good prediction of the experimental observed laser wavelength.

3.2.1. Selection of reliable spectroscopic data for KYW:Yb[3+]

In the work of Kuleshov the absorption cross-section has been measured on a KYW:(5%)Yb[3+] crystal and the emission cross-section has been determined from the absorption cross-section using the reciprocal method [aul82], also called McCumber relation [cum64], given in Eq. 3.2.

$$\sigma_{SE}(\upsilon) = \sigma_{GSA}(\upsilon) \frac{Z_g}{Z_e} e^{\frac{E_{zl} - h\upsilon}{kT}} \qquad (3.2)$$

Here the partition functions of the ground state Z_g and excited state Z_e are equal to the degeneracies, d_k, of the two states at high temperatures, given by:

$$Z_k = \sum_k d_k e^{\frac{-E_k}{kT}} \qquad (3.3)$$

In ytterbium, each level has a degeneracy of two. The partition functions of the upper and lower states can then be calculated at room temperature. Using T = 300 K and with the Boltzmann constant, $k = 1.38065 \times 10^{-23}$ JK^{-1} Eq. 3.3 gives the values provided in Table 3.2.

Table 3.2. Evaluation of Eq. 3.3 at T=300 K, calculating the partition functions Z_e and Z_g of the ^{2}F$_{5/2}$ and ^{2}F$_{7/2}$ states, respectively, of Yb^{3+} ions doped into KYW.

Energy level	Stark split level	Energy (cm^{-1})	Relative energy E_k (cm^{-1})	$d_k e^{\frac{-E_k}{kT}}$	Partition function Z_k
^{2}F$_{5/2}$	2'	10695	508	0.1749	$Z_e = 2.6751$
	1'	10476	289	0.5001	
	0'	10187	0	2.0000	
^{2}F$_{7/2}$	3	568	568	0.1312	$Z_g = 3.3045$
	2	407	407	0.2840	
	1	169	169	0.8893	
	0	0	0	2.0000	

For the energy level structure of Yb^{3+} in KYW, the ratio of the partition functions $Z_g / Z_e = 1.2353$. Evaluation of the emission cross-section is performed using the provided absorption cross-section and reciprocal method taken from the work of Kuleshov. Fig. 3.3 depicts the obtained difference between the recalculated values using Eq. 3.2.
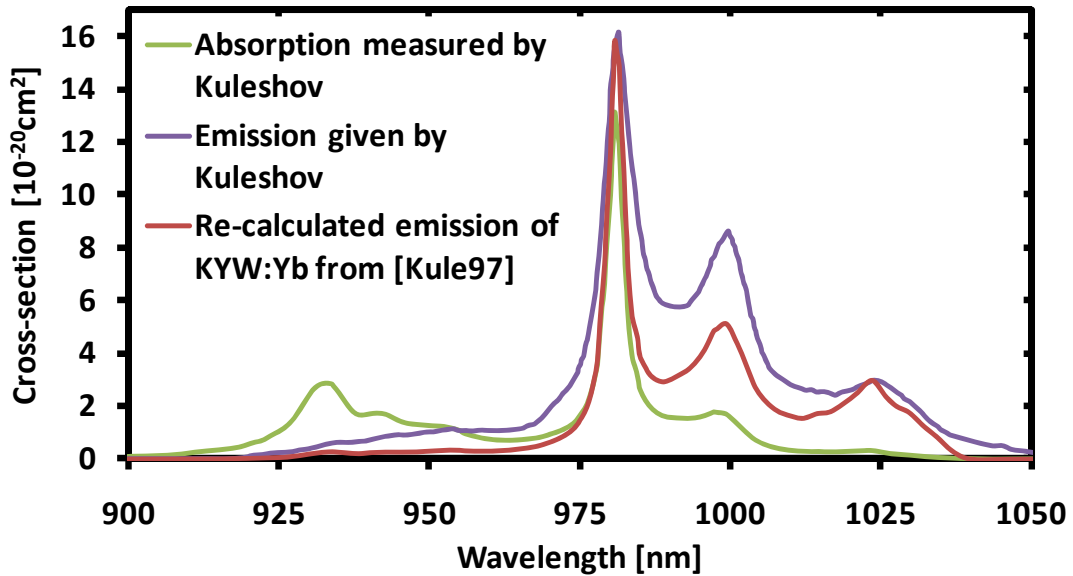
Fig. 3.3. Measured absorption cross-section and derived stimulated emission cross-section taken from [kule97] for KYW:Yb^{3+} with polarization $E\|a$*. Recalculating the stimulated emission cross-section from the given absorption cross-section reveals the overestimated value given by Kuleshov, especially around the 1000 nm region.

The re-derived emission cross-sections are significantly lower in specific wavelength regions compared to the values given in the article of Kuleshov. Especially the stimulated emission cross-section around the 1000 nm transition seems to be strongly overestimated by Kuleshov. A comparison of spectroscopic data of the same material, but taken from other sources found in the literature from Eksma [eks] and Liu [liu01] is presented in Fig. 3.4.
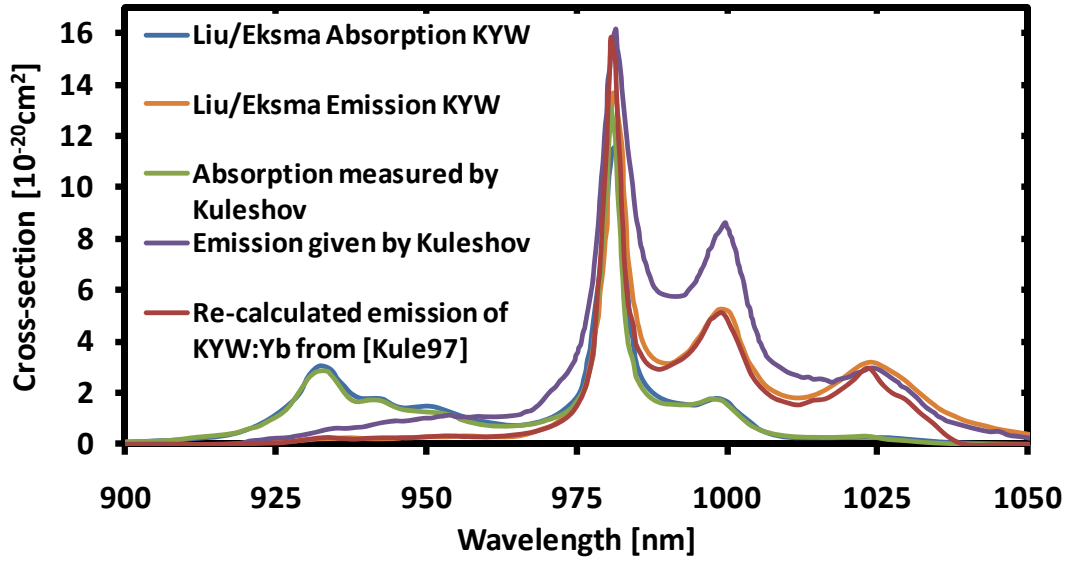
Fig. 3.4. Comparison of the Kuleshov data with other sources for KYW:Yb^{3+} with polarization $E||a*$.

No difference was found between the literature values provided by Liu and Eksma, therefore they are presented by only one single line. The data provided by Eksma serves a commercial purpose and is possibly taken from the scientific data provided by Liu. Comparison of the emission cross-sections of KYW:Yb^{3+} around the 1000 nm transition region confirms the overestimation of the emission cross-section by Kuleshov, but shows an excellent agreement for the absorption cross-section at that wavelength regime.

However, one major difference is found when comparing the height of the absorption peak at 981 from Kuleshov to the other data from Liu and Eksma. It is found that Kuleshov reports a larger absorption cross-section of 13.3×10^{-20} cm^2 at 981 nm compared to an absorption cross-section of 11.5×10^{-20} cm^2 found in the graph of Liu and Eksma. Strangely enough, Eksma reports a peak absorption cross-section of 13.3×10^{-20} cm^2 (identical to the value given by Kuleshov) in a separate table, right next to their graph that reveals the lower value for the peak absorption cross-section of 11.5×10^{-20} cm^2. It seems that Eksma tried to combine the best of both: Consistent emission and absorption spectra from Liu and detailed information about the peak emission and absorption from Kuleshov.

The article of Liu does not discuss the peak absorption line at 981 nm, as the work concerns laser experiments with polarization $E||b$ using a pump wavelength of 940 nm. The goal in Liu`s work is to access the broader emission band at wavelengths >981 nm for $E||b$ polarization, to allow generation of short pulses. The absorption spectrum reported by Liu was recorded on a 10% Yb^{3+}-doped KYW crystal with a length of 4 mm. Such a long and highly doped sample would nearly absorb all light at the absorption peak near 981 nm, makes it hard to determine the exact absorption coefficient as the detector noise is larger than the remaining signal noise. Liu used a spectrophotometer (Perkin-Elmer) in this experiment, which has typically a noise floor of about -50 dB [per]. Using the Lambert-Beer law,

$$A(dB) = 10 \cdot LOG\left(e^{-n\sigma l}\right), \tag{3.4}$$

to calculate the absorption (*A*) of the specific sample used by Liu gives a small signal absorption of about 146 dB at the absorption peak, see the calculation parameters in Table 3.3.

Table 3.3. Calculated peak absorption used in the absorption measurement of [liu01].

Analysis of Liu data for 10% Yb^{3+}-doped KYW using the Lambert-Beer law	
Doping concentration N	6.33×10^{20} cm^{-3}
Absorption cross-section σ	13.3×10^{-20} cm^2
Length l	0.4 cm
Absorption A	-146 dB

This explains the lower value of the peak absorption cross-section of 11.5×10^{-20} cm^2 in the graph of Liu compared to a value of 13.3×10^{-20} cm^2 reported by Kuleshov. Moreover, Kuleshov explicitly treats the measured value of the peak absorption at 981 nm in his work, hence the absorption data published by Kuleshov and the recalculated emission as discussed here were used for the estimation of gain (Chapter 7) and the analysis of lasing threshold for various outcoupling efficiencies (Subsection 5.4.3).

3.2.2. Combining spectroscopic data to approach the spectroscopy of composite hosts

The focus of this work concerns the development of optically active devices in the co-doped material; the co-doping of the material affects the spectroscopy of the Yb^{3+} ions doped into it. Therefore, the absorption spectra found in the literature for KGdW:Yb^{3+} [maj03], KLuW:Yb^{3+} [mat06], KYW:Yb^{3+} [kule97] and KYbW [pujo02] were used, together with their emission spectra calculated with the McCumber theory [cum64], to approximate the spectroscopic behavior of the composite material used in these experiments. The absorption and emission cross-sections of the composite KY$_{1-x-y}$Gd$_x$Lu$_y$(WO$_4$)$_2$:Yb^{3+} material were calculated by taking the weighted averages of the spectroscopic data of the Yb^{3+}-doped hosts KGdW, KLuW, KYW and the stoichiometric composition KYbW found in the literature.

There are a few reasons to call this an approximate method. Firstly, all our devices operate with polarization $E||N_m$, but for KYW:Yb^{3+} only spectroscopic data for $E||a*$ was found [kule97, liu01, eks]. The angular difference of 13.5° between those polarizations [bor68, kam01] will lead to some deviation of the spectroscopy as observed for the difference between the emission cross-sections of KGdW:Yb^{3+} for $E||a*$ [eks] and $E||N_m$ [bis05] shown in Fig. 3.5.
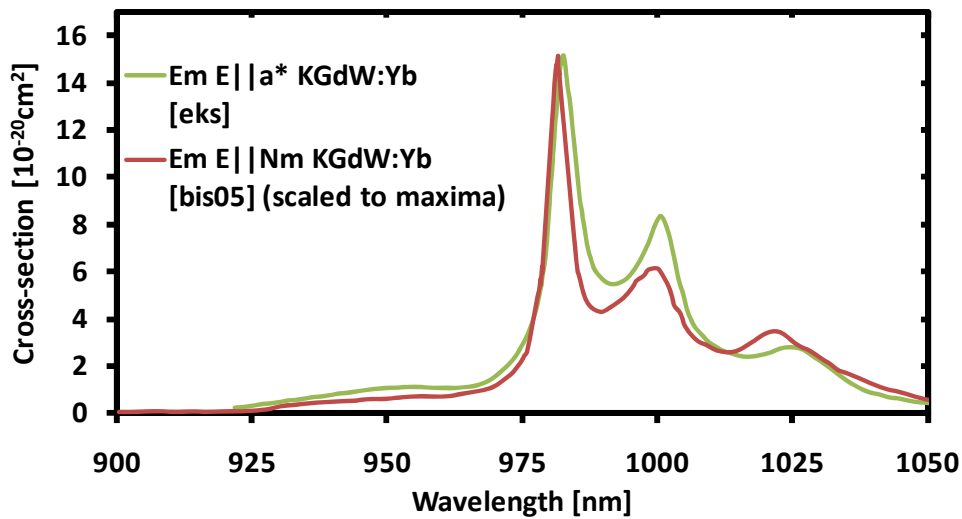
Fig. 3.5. Comparison of stimulated emission cross-section in KGdW:Yb^{3+} in polarization $E\|a*$ [eks] with measured fluorescence intensity for polarization $E\|N_m$ [bis05] (scaled to the maxima of the data from [eks]).

However, the spectroscopy is mostly used for the interpretation of gain (see Chapter 7) and lasing threshold analysis (Subsection 5.4.3) that concerns samples having the Y^{3+} component completely replaced by Gd^{3+}, Lu^{3+} and Yb^{3+}, hence not making use of the data from Kuleshov that concerns the $E\|a*$ polarization.

Another assumption is that the influence of the host material on the spectroscopy is linear, which has not been confirmed. However, the obtained spectroscopic features of the various host materials show great similarities; positions and magnitudes of the transition peaks are close to each other, except for the magnitude of the peak transition at 981 nm, which is not the same for all host materials, as shown in Fig. 3.6. The largest peak emission and absorption cross-sections at 981 nm are found for Yb^{3+}-doped KYW.

(a)
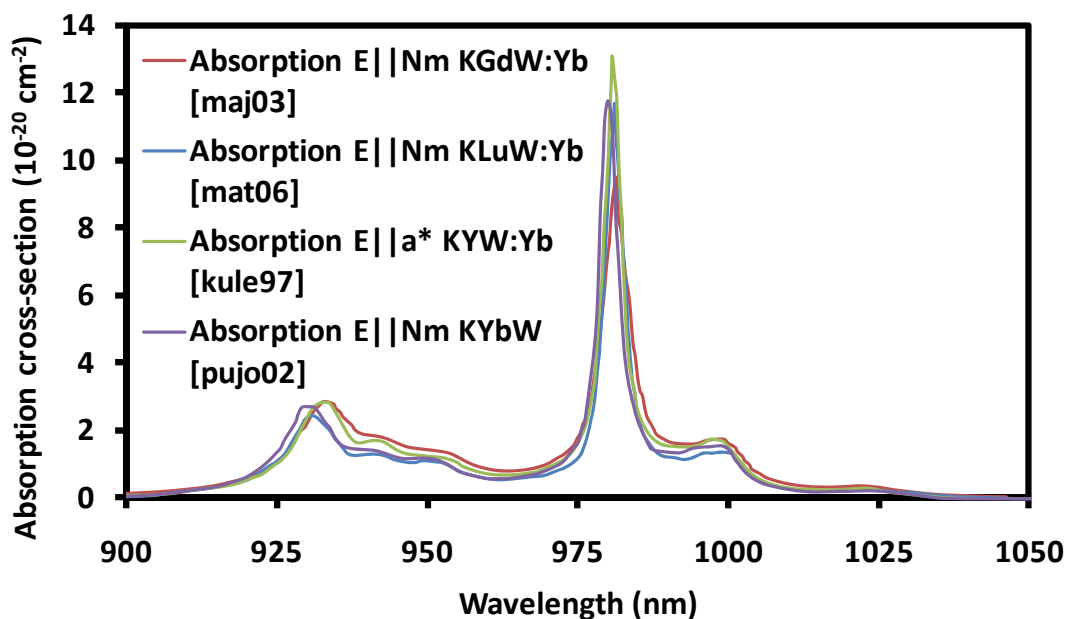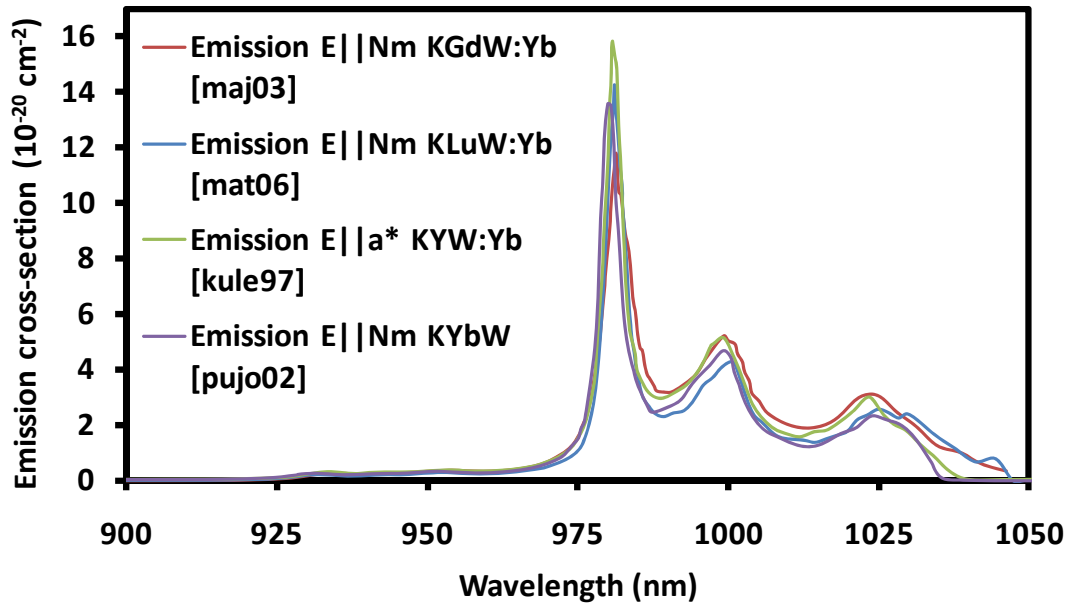
Fig. 3.6. (a) Absorption and (b) emission cross-sections of Yb^{3+} in the potassium double tungstate host materials of interest in this work.

3.2.3. Comparison of combined spectroscopy with the experimental luminescence

The emission spectra of KYW:(1.7%)Yb^{3+} and KY$_{0.60}$Gd$_{0.13}$Lu$_{0.27}$ (WO$_4$)$_2$:(1.7%)Yb layers are recorded for $E||N_m$. In this experiment the spontaneous emission for $E||N_m$ polarization was collected perpendicular to the surface using a liquid fiber having a polarization filter fixed to the collection end. The spectrum of the collected light is recorded using a spectrophotometer. The excitation wavelength was set to 932 nm and coupled into the waveguides from the waveguide end-face. A comparison is presented in Fig. 3.7 (a), showing the measured emission from the KYW:Yb^{3+} waveguide and the recalculated emission cross-sections taken from [kule97], and Fig. 3.7 (b) presents the measured spontaneous emission from the co-doped waveguide compared to the calculated emission spectra for a composite host material as described here. In both graphs the measured intensity spectra have been rescaled to the maximum value of the calculated literature values but have not been corrected for the detector response. The features of the curves in both graphs reveal a good agreement between the measured spontaneous emission and the proposed emission cross-section spectroscopy in this section.
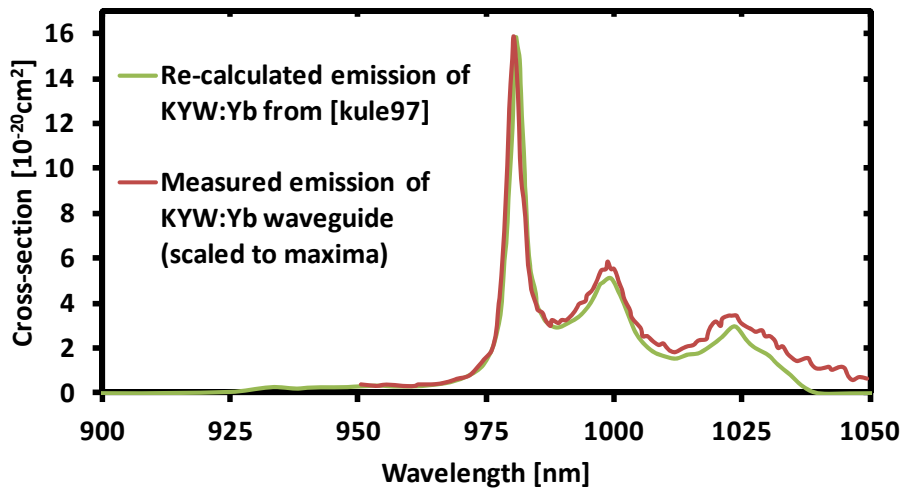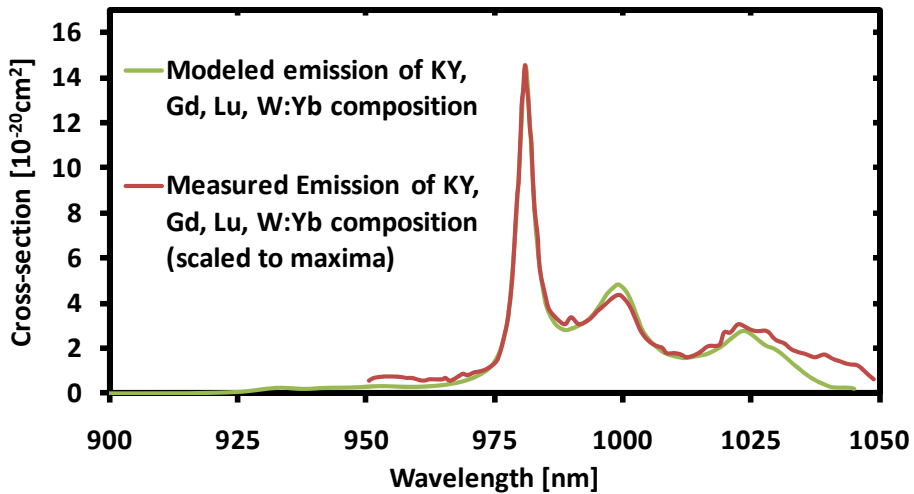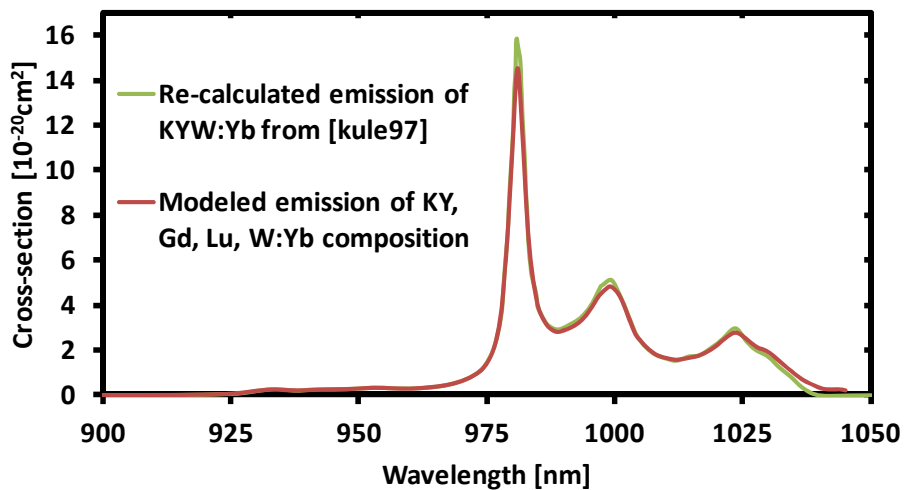
Fig. 3.7. (a) Comparison between measured spontaneous emission spectra from KYW:(1.7%)Yb^{3+} and re-estimated emission given by [kule97], and **(b)** comparison of measured spontaneous emission spectra from KY$_{0.60}$Gd$_{0.13}$Lu$_{0.27}$W:(1.7%)Yb^{3+} with the balanced composite emission from the various sources [maj03, mat06, kule97, puj02]. **(c)** Presented in green is the re-estimated emission given by [kule97] and the balanced composite emission of KY$_{0.60}$Gd$_{0.13}$Lu$_{0.27}$W:(1.7%)Yb^{3+}. The major difference is found at the peak emission cross-section at 981 nm.

In Fig. 3.7 (c) the difference between the re-estimated emission of KYW:Yb^{3+} given by [kule97] and the estimated emission for a composite material KY$_{0.60}$Gd$_{0.13}$Lu$_{0.27}$W:(1.7%)Yb^{3+} is presented. It reveals only minor differences between the two compositions, which is caused by a fairly low co-doping concentration of 40% in this specific case. The largest deviation between the emission cross-sections is found at its peak value near 981 nm. The differences are expected to be larger for compositions having no Y^{3+} in the host material.

3.2.4. Influence of co-doping on luminescent lifetime and luminescent spectra

When fitting the measured luminescence peaks at 981 nm of the KYW:(1.7%)Yb^{3+} and KY$_{0.60}$Gd$_{0.13}$Lu$_{0.27\%}$W:(1.7%)Yb^{3+} layers to a Lorentzian curve, this gives a FWHM of the emission peak at ~981 nm in the co-doped film of 3.8 nm (Fig. 3.8 (a)), which is slightly larger than the corresponding value of 3.6 nm obtained for the single-doped film (Fig. 3.8b).
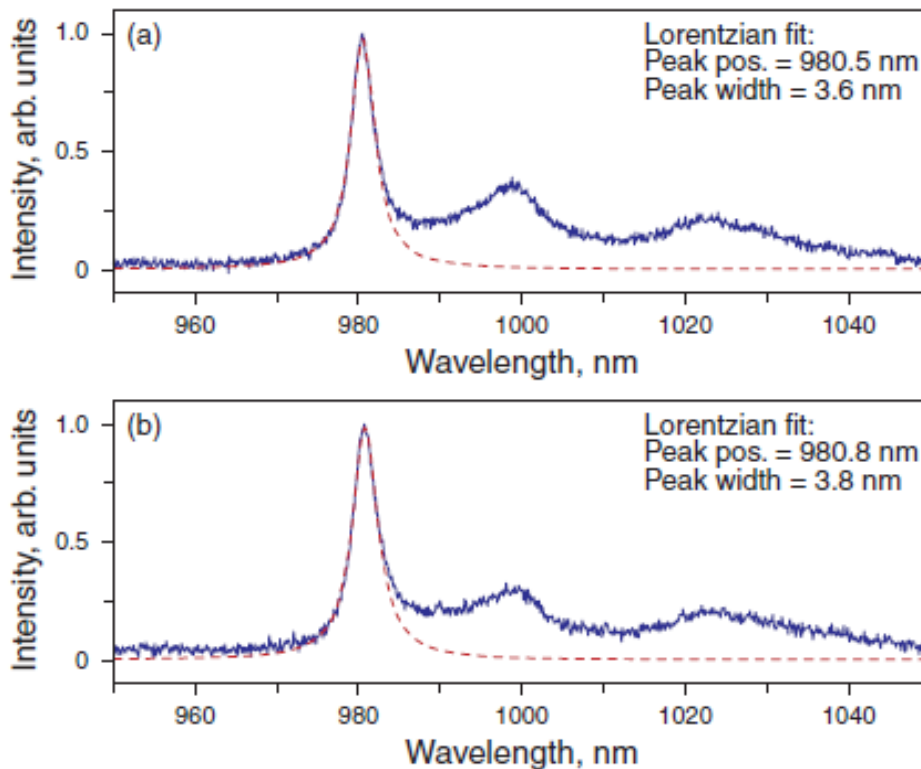
Fig. 3.8. Luminescence emission spectra from (a) a KYW:Yb^{3+}(1.7%) layer and (b) a KY$_{0.60}$Gd$_{0.13}$Lu$_{0.253}$W:(1.7%)Yb^{3+} layer. The dashed line is a Lorentzian fit of the main emission peak.

The influence of co-doping on the lifetime was measured by pumping the active layers with a switched diode laser operating at 976 nm. Luminescence light at 1040 nm was collected normal to the sample surface by a liquid fiber, diffracted by a monochromator and detected by an amplified InGaAs detector. Lifetime values of 260 μs and 267 μs were measured for the co-doped and the single-doped layers, respectively, see Fig. 3.9.
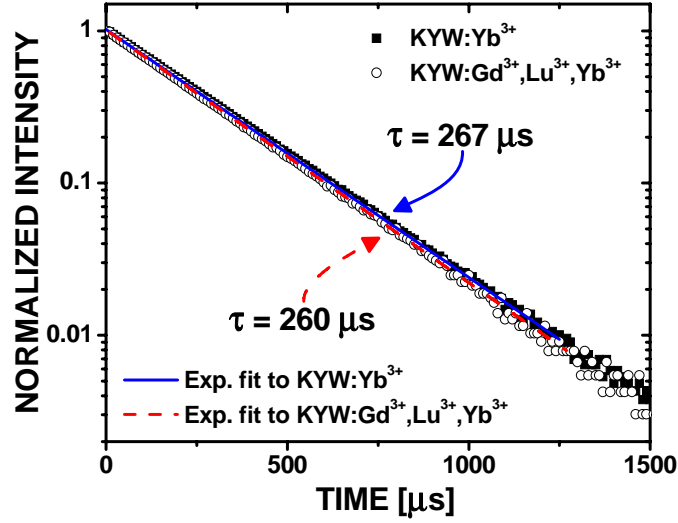
Fig. 3.9. Decay curves of the luminescence at 1040 nm in KYW:(2.4%)Yb^{3+} and KY$_{0.60}$Gd$_{0.13}$Lu$_{0.27}$W:(1.2%)Yb^{3+} films.

Both the shorter lifetime and broader emission linewidth are attributed to the co-doping, however, the small deviations detected in the co-doped layers indicate that incorporation of large percentages of Gd^{3+} and Lu^{3+} ions has no strong adverse effect on these laser-relevant spectroscopic properties of the fabricated layers.

3.3. Design and modeling of optical amplification

For the model proposed in this section an 2-level ytterbium-doped laser system is considered where the KY$_{1-x-y}$Gd$_x$Lu$_y$W:Yb^{3+} waveguide is pumped from one end. The Yb^{3+}-doped waveguide is described by rate equations which have been derived from the transitions between the two energy levels of the Yb^{3+} ions due to ion-light interactions:

$$\frac{dN_1(x,y,z)}{dt} = R_{01}(x,y,z)N_0(x,y,z) - R_{10}(x,y,z)N_1(x,y,z) \tag{3.5}$$

$$N_0(x,y,z) = N_T - N_1(x,y,z), \tag{3.6}$$

where N_0 and N_1 denote the concentrations of Yb^{3+} ions in the ^{2}F$_{7/2}$ ground level and the ^{2}F$_{5/2}$ excited level, on rate from the ground level to the excited level and from the excited level to the ground level respectively. The definitions of these respective rates are given by:

$$R_{01} = \frac{P_p(z)\phi_p(x,y)}{h\nu_p}\sigma_p^{abs} + \frac{P_l(z)\phi_l(x,y)}{h\nu_l}\sigma_l^{abs} \tag{3.7}$$

$$R_{10} = \frac{P_p(z)\phi_p(x,y)}{h\nu_p}\sigma_p^{em} + \frac{P_l(z)\phi_l(x,y)}{h\nu_l}\sigma_l^{em} + \frac{1}{\tau}. \tag{3.8}$$

Here P is the total optical power (forward and backward) at position z, ϕ is the normalized

transverse intensity distribution, such that $\iint\limits_{Area} \phi(x,y)dxdy = 1$. h is Planck's constant, v is the optical frequency, and τ is the lifetime of the excited level. Here σ are the effective cross-sections taken from spectroscopic data, in this work used the spectroscopic data depends on the composition of the host material as described in Section 3.2. The superscripts *abs* and *em* denote absorption and emission, while *p* and *l* subscripts denote pump and laser, respectively. During steady state operation the rate Eq. (3.5) should equal zero, so it follows from Eqs. 3.5 and 3.6 that

$$N_1(x,y,z) = N_T \frac{R_{01}}{R_{01}+R_{10}}.$$ (3.9)

The transverse normalized intensity distributions ϕ of the guided pump and laser modes were calculated with a commercial mode solver program (Phoenix FieldDesigner). An example is given in Fig. 3.10.
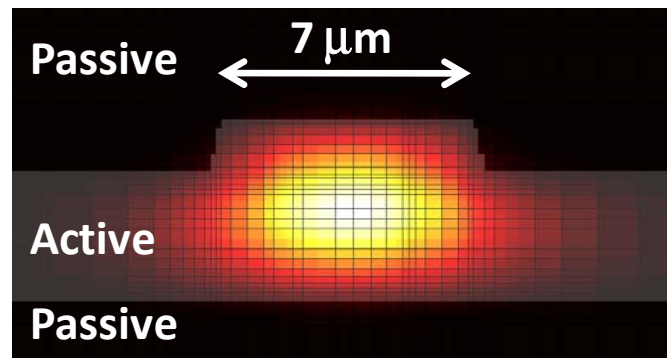
Fig. 3.10. Transverse mode and structural cross-section used as input for the rate equation model. The structural information (indicated in gray) of a typical waveguide laser was used in the Phoenix FieldDesigner software to calculate the shape of the guided fundamental mode. The shape of the guided mode, the discretization grid (dark lines) and the structural information is then exported and used as input for the rate equation model.

The Lambert–Beer law for absorption and stimulated emission of an optical signal at wavelength λ, propagating through a medium over a short length interval Δz, yields the following equation for our 2-level system:

$$P^{\pm}(z \pm \Delta z) = P^{\pm}(z)\exp\left(\left(\sigma^{em}(\lambda)N_1(x,y,z) - \sigma^{abs}(\lambda)N_0(x,y,z) - \alpha_{loss}\right)(\pm\Delta z)\right).$$ (3.10)

The positive and negative superscripts in Eq. (3.10) indicate the optical power travelling in the forward and backward directions, respectively, while α_{loss} denotes the propagation loss in the waveguide. The intracavity pump and laser powers are subjected to the following boundary conditions which are imposed by the resonator setup:

$$P_p^+(z=0) = P_{launched} + R_{1p}P_p^-(z=0)$$ (3.11)

$$P_l^+(z=0) = R_{1l}P_l^-(z=0) \tag{3.12}$$

where $P_{launched}$ is the pump power launched into the waveguide, R_1 is the power reflectivity[1] of the incoupling mirror at the pump and laser wavelengths as denoted by the subscripts p and l.

At the other end of the cavity of length L, generally both pump and laser light are reflected by the output mirror which has a power reflection R_2 such that

$$P_p^-(z=L) = R_{2p}P_p^+(z=L) \tag{3.13}$$

$$P_l^-(z=L) = R_{2l}P_l^+(z=L) \tag{3.14}$$

The local population densities were calculated from (3.6) and (3.9). By iterating (3.10) along the length of the resonator for the pump and laser powers with the boundary conditions (3.11)-(3.14), the emitted laser power was obtained from

$$P_{out} = (1 - R_{2l})P_l^+(z=L) \tag{3.15}$$

Arbitrary initial population densities obeying the relation given in Eq. 3.6 and intra-cavity optical powers lower that the launched pump power were chosen to initialize the simulation. The optical fields were iterated along the resonator, while the localized population densities were updated accordingly. These iterations were performed until the entire system converged to a steady state solution.

This same model was used to calculate the modal gain of waveguide structures by changing the calculation iteration such that only forward propagating light is taken into account until the entire system converges to a steady state solution. For calculations of modal gain the subscript l denoting laser related properties is replaced by the subscript s, denoting the signal related properties.

3.4. Planar waveguide laser

3.4.1. Experiment introduction

Room-temperature laser operation was investigated under continuous-wave Ti:Sapphire pumping at the Yb^{3+} absorption peak near 981 nm with pump polarization parallel to the N_m optical axis of the waveguide layer. Two cylindrical lenses were used to adapt the pump mode to the laser mode, resulting in a pump waist radius of ~30 μm in the horizontal direction formed by a $f = 4$ cm cylindrical lens, while optimal coupling to the waveguide in the vertical direction with a spot size of ~7 μm was obtained with a second cylindrical lens with $f = 1$ cm, as shown in the schematic in Fig. 3.11. The positions of both lenses were

---

[1] Here R_{1p} R_{1l}, R_{2p} and R_{2l} denoting the reflectivity of the mirrors, should not be confused with the earlier mentioned R_{01} and R_{10} denoting the excitation and relaxation rates respectively. The discrimination is made by using unique subscripts.

individually adjustable in the direction of the light propagation to ensure optimal laser performance.
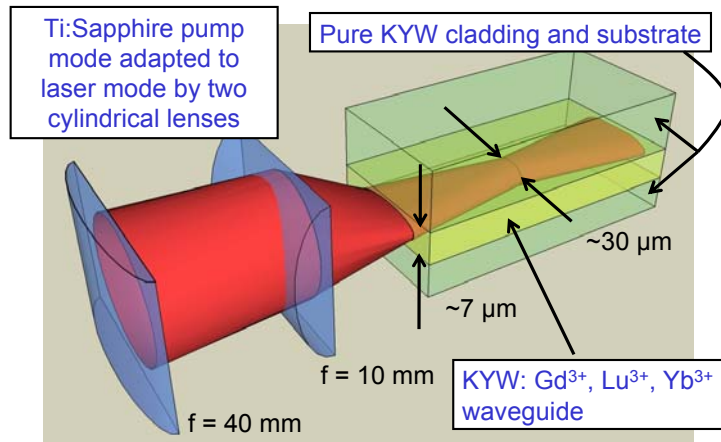
Fig. 3.11. Pump mode adaption by cylindrical mirrors

Before launching, the pump light passed through a mechanical chopper operating at a frequency of 33 Hz with a duty cycle of 50% to avoid any mirror or waveguide end-face damage by the pump irradiation. However, by removing the mechanical chopper the laser could also be operated under true continuous-wave conditions without observing any difference in the output characteristics. A reflective grating was used as dispersive element to separate the residual transmitted pump light from the laser emission, thus enabling measurement of both powers independently by a power meter, see Fig. 3.12.
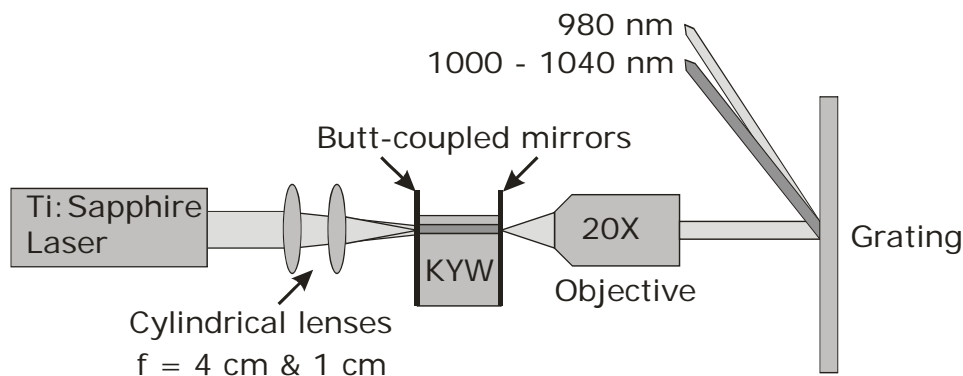
Fig. 3.12. Schematic of experimental setup used for the investigation of the $KY_{0.60}Gd_{0.13}Lu_{0.27}(WO_4)_2$:(1.2%)$Yb^{3+}$ planar waveguide lasers.

The absorbed pump power was estimated by subtracting the residual pump power outcoupled at the end-facet from the power coupled to the waveguide. The coupling efficiency of the incident pump light to the waveguide was measured in a separate experiment, in which the pump wavelength was tuned away from the absorption peak at 981 nm to the wavelength of 960 nm, assuming that the coupling efficiency is essentially the same at both wavelengths, while measuring the residual pump power at the other end-facet. Corrections were made for the material absorption at 960 nm by taking the overlap of the pump mode with the active

medium and the Yb^{3+} absorption at this wavelength into account. From this measurement an overall coupling efficiency, including the reflection at the incoupling surface, of 67% of the incident power to the waveguide was estimated.

At the laser wavelength of 1025 nm the incoupling mirror had a reflectivity of 99.8%, while for the outcoupling mirror transparencies of 1.7%, 5%, 10%, 20%, and 23% were tested. The mirrors were coupled to the end facet by fluorinated oil (Fluorinert FC-70). Fig. 3.13 (a) shows the laser output characteristics as a function of absorbed pump power. The highest slope efficiency of 82.3%, which represents the highest value yet reported for any dielectric waveguide laser to date, and a maximum extracted laser power of 195 mW, for an absorbed pump power of 280 mW, were obtained using the 23% outcoupling mirror. Further power scaling was not attempted in order to avoid potential damage of the in-coupling end-facet by the high pump intensity. The lowest laser threshold of 18 mW absorbed pump power obtained with the 1.7% outcoupling mirror represents a reduction by a factor of 2.2 compared to previous experiments [rom06, bain09] and highlights one of the advantages of the high optical confinement achieved by the enhanced refractive index contrast. The best laser performance in all cases was found for a laser wavelength of 1025 nm, although the emission wavelength could be varied from 1000 nm to 1042 nm by slightly changing the alignment, which was probably caused by etalon effects of the gaps between the mirrors and the waveguide end-facets. In all investigated configurations the laser emission had a highly elliptical Gaussian profile with FWHM of ~4.5 µm perpendicular and ~60 µm parallel to the waveguide plane (Fig. 3.13 (b)).
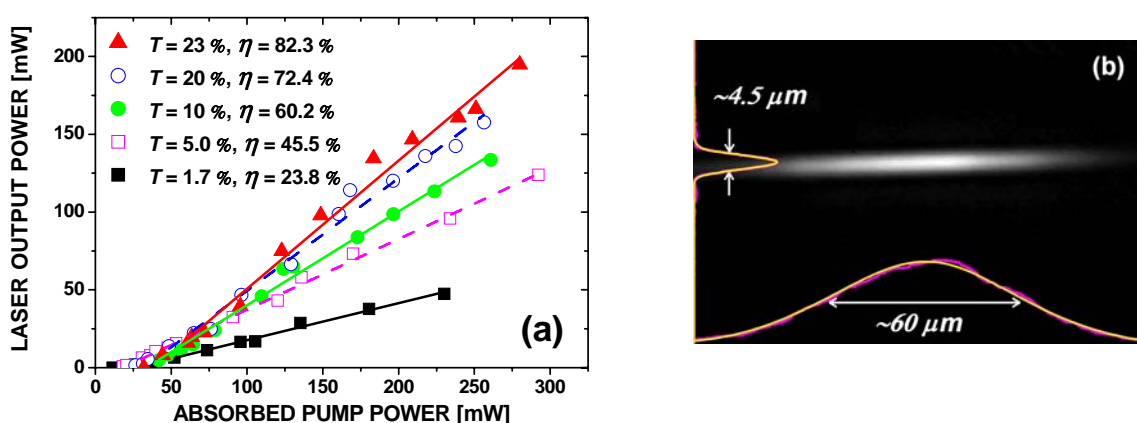
Fig. 3.13. (a) Laser output power as a function of absorbed pump power for various outcoupling mirror transmissions and (b) laser mode profile obtained from the $KY_{0.60}Gd_{0.13}Lu_{0.27}(WO_4)_2$:(1.2%)$Yb^{3+}$ planar waveguide.

3.4.2. Propagation loss of planar waveguide

Based on the theoretical behavior of lasers exhibiting reabsorption losses [ris88] the intracavity round-trip loss L and the laser efficiency parameter η_0 were derived by plotting the inverse of the measured slope efficiency η versus the inverse of the transparency T of the output mirror according to:

$$\eta = \eta_0 \frac{\ln(1-T)}{\ln[(1-L)\cdot(1-T)]} \quad \Rightarrow \quad \frac{1}{\eta} = \frac{1}{\eta_0} + \frac{-\ln(1-L)}{\eta_0}\cdot\frac{(-1)}{\ln(1-T)}. \qquad (3.16)$$

Eq. 3.16 represents a modified version of the corresponding expression for the slope efficiency η in [ris88], which avoids approximating the logarithmic function and allows a more accurate estimation of the round-trip loss for outcoupling mirrors with higher transmission values. The result based on laser performance obtained with the 1.7%, 5%, 10%, and 20% outcoupling mirrors is displayed in Fig. 3.14. A fairly high value of 4.4% was derived for the round-trip loss L compared to previous results [rom06, bain09]. This increased loss is attributed to the tighter confinement due to the smaller waveguide dimensions, which results in higher beam divergence at the waveguide end-facets and, consequently, higher losses at the gaps between end-facets and butt-coupled mirrors. The laser performance obtained with the 23% outcoupling mirror was not taken into account in this analysis, because the flatness of this mirror was better, resulting in a smaller gap between the end-face and the mirror and, thus, in lower intracavity round-trip loss and enhanced laser performance.
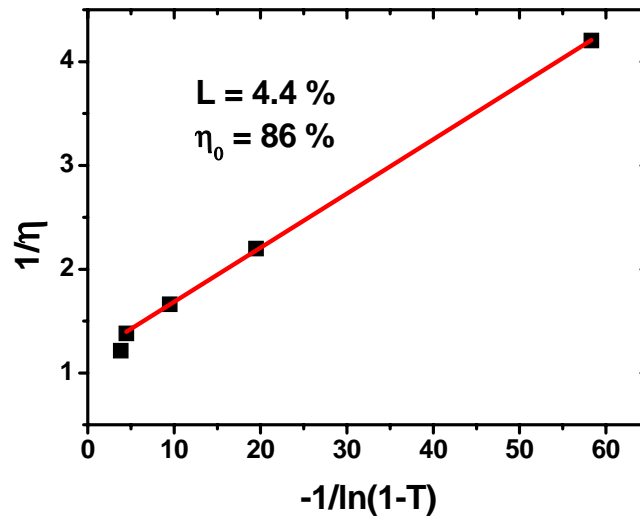
Fig. 3.14. Inverse slope efficiency (1/η) as a function of inverse logarithmic reflection (-1/ln(1-T)) of the outcoupling mirror. The solid line is a linear fit, based on values obtained with the outcoupling mirrors with transmission values of 1.7%, 5%, 10%, and 20% according to Eq. 3.16.

The laser efficiency parameter η_0 indicates the efficiency of the conversion of pump-light to laser light. This strongly depends on the overlap of the pump with the laser mode, reabsorption losses, and Stokes efficiency. The laser efficiency parameter η_0 is not affected by the intracavity roundtrip loss; it therefore indicates the upper limit of the laser efficiency in a lossless cavity. Due to an optimized overlap between pump and laser mode a high value of $\eta_0 = 86\%$ was calculated, which is 13% higher than a previously reported value [bain09]. The most efficient laser performance was obtained when choosing a slightly smaller waist size of the pump mode compared to the waist size of the laser mode, because the horizontal stability of the cavity relies on a pump-induced guiding effect, which increases with tighter

focusing the pump mode. However, a too small pump waist gives rise to stronger pump beam divergence and results in poorer mode overlap. This guiding effect has not been studied in detail, but one can imagine that the pump-induced guiding effect strongly depends on the size of the pump waist. In the vertical direction, the wings of the pump and laser mode propagate partially through the undoped substrate, thus decreasing the overall pump absorption (which does not affect η_0, because it is measured versus absorbed pump power), but also reducing the reabsorption of laser light. These effects may explain the rather efficient light conversion η_0.

A spatially resolved steady state rate equation simulation, described in Section 3.3, predicts even higher light conversion efficiency in channel waveguide structures. This simulation is based on a lossless channel waveguide with a waveguide cross-section as depicted in the inset of Fig. 5.11 (a) from Chapter 5, and with the other parameters given in Table 3.4 for a lasing wavelength of 1025 nm and $\alpha_{loss} = 0$. The resulting slope efficiency of this simulation of 94% represents the high light conversion efficiency η_0 for channel waveguide structures, being close to the Stokes efficiency of 96%. This high light conversion efficiency can be explained by the improved mode overlap and strong confinement of the light within the active region of such structures.

3.4.3. Planar waveguide lasing at the zero-phonon line

The ZPL of absorption and emission between two crystal-field multiplets is the transition involving the lowest Stark level of each multiplet. Due to the large Boltzmann population of this Stark level and the selection rules that apply to the individual transitions, the ZPL is often the transition with the largest effective absorption and emission cross-section. More details about channel waveguides lasing at the ZPL are given in Section 5.4.

In this experiment the same planar waveguide was used in a similar experimental setup. Here the excitation wavelength was changed to 932 nm and the cavity was formed by the Fresnel reflection of 11% at the pumped side of the waveguide and a mirror with 97% reflectivity at 980.8 nm coupled to the other end facet by fluorinated oil (Fluorinert FC-70). The emitted laser light was collected from the pumped side via a beam splitter placed into the pump beam line. A reflective grating was used to separate the laser emission from the residual pump light.

The laser oscillation was accidentally obtained during an optimization for maximal spontaneous emission, to obtain evidence of real laser oscillation and to be certain that no amplified spontaneous emission was observed the spectrum of the emission and the relaxation oscillations were recorded. The spectrum of laser emission from the planar waveguide (Fig. 3.15 (a)) was spectrally analyzed by a spectrometer (Jobin-Yvon iHR550) with a resolution of 0.1 nm.
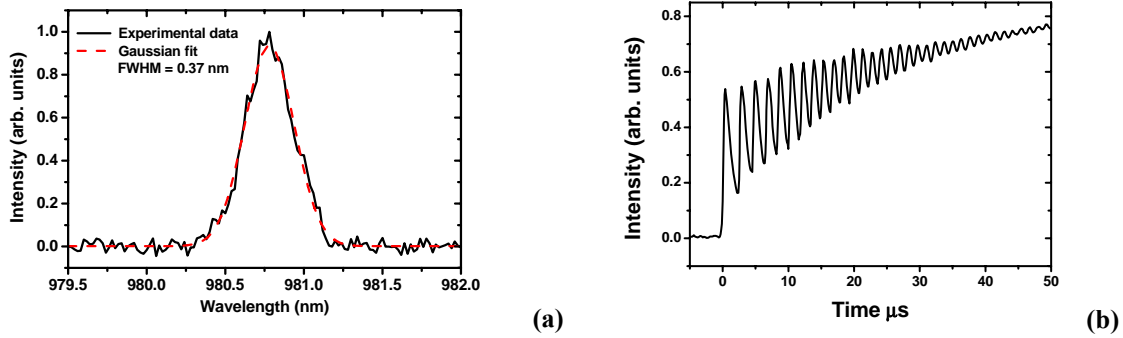
Fig. 3.15. (a) Spectrum of laser emission and (b) relaxation oscillations measured in a KY$_{0.60}$Gd$_{0.13}$Lu$_{0.27}$(WO$_4$)$_2$:(1.2%)Yb^{3+} planar waveguide laser oscillating at the ZPL.

The emission peak occurs at a wavelength of 980.8 nm. A Gaussian fit reveals a full width at half maximum of 0.37 nm. The recorded spectrum is not smooth; small peaks can distinguished in the envelope curve, this indicates multi mode laser operation. Relaxation oscillations or laser spiking is typically observed during the starting period of a laser, at this beginning phase the internal energy balance has not yet reached steady state laser oscillation. The relaxation oscillations, depicted in Fig. 3.15 (b), were recorded by an InGaAs detector in combination with a high speed amplifier (Femto DHPCA 100) and a digital oscilloscope (HP-Infinium) when switching to maximum pump power.

The best performances of both experiments with the slab waveguide when lasing at the ZPL and at a wavelength around 1025 nm, are presented by the dots in Fig. 3.16.
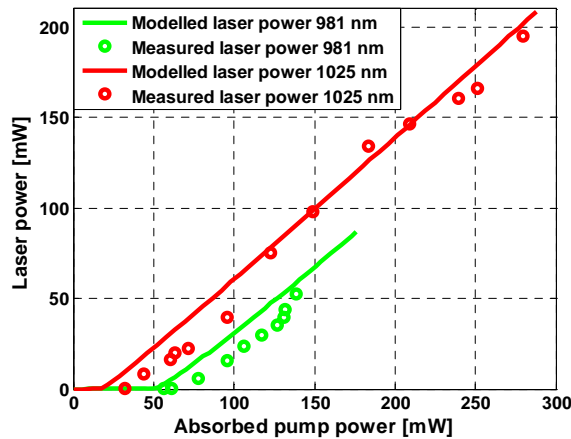
Fig. 3.16. Laser performance of the planar waveguide of KY$_{0.60}$Gd$_{0.13}$Lu$_{0.27}$(WO$_4$)$_2$:(1.2%)Yb^{3+}, operating at 980.8 nm (green) and 1025 nm (red). The dots indicate the experimental results and the continuous lines indicate the calculated values.

The laser performance at the ZPL of the planar waveguide reveals a fairly high laser threshold of 65 mW absorbed pump power owing to the open-cavity configuration. The slope efficiency was 71% versus absorbed pump power and the maximum output power 53 mW. In addition to the experimental data the outcome of the rate equation model is also provided in the same Fig. 3.16, indicated by continuous lines. The input data for this model are given in Table 3.4.

Table 3.4. Input parameters for the spatially resolved rate equation model to calculate the laser performance of slab waveguide lasers operating at 1025 nm and 981 nm.

Parameter	Normal lasing	ZPL
λ_p (nm)	981	932
λ_l (nm)	1025	981
σ_p^{em} (m^2)	14.6×10^{-24}	0.2×10^{-24}
σ_p^{abs} (m^2)	11.9×10^{-24}	2.7×10^{-24}
σ_l^{em} (m^2)	2.4×10^{-24}	14.6×10^{-24}
σ_l^{abs} (m^2)	0.2×10^{-24}	11.9×10^{-24}
R_{1l}	0.998	0.11
R_{1p}	0.11	0.11
R_{2l}	0.77	0.97
R_{2p}	0.77	0.83
α_{loss} (m^{-1})	4.5*	4.5*
Mode dimensions (μm^2)	4.5×60	4.5×60
N_T (m^{-3})	7.6×10^{25}	7.6×10^{25}
L (mm)	5	5
Δz (mm)	0.1	0.1

*Corresponding to a round trip loss of 4.4%**

The used steady state rate equation does not account for divergence of the pump and laser beam in the planar waveguide. However the experimental observations indicate a slightly smaller waist size of the pump mode, hence the divergence of the pump beam is also larger, resulting in a larger pump mode size at the end-faces of the waveguide compared to the size of the laser mode. This justifies the assumption of equal sized pump and laser modes as input parameter of the rate equation model. The outcome of the steady state rate equation model, indicated by continuous lines in Fig. 3.16, confirms the laser performance of both lasers at 1025 nm and 981 nm very accurately.

3.5. Conclusions

The developed method to approximate the spectroscopic absorption and emission cross-sections of composite host materials predicts the observed laser wavelengths in half open cavities, see Section 5.4.2. Modeling the emission wavelength of lasers having open cavities using the data provided by Kuleshov resulted in a predicted wavelength of 1000 nm, although emission at the zero phonon line (ZPL) of 981 nm is observed. The cause of the discrepancy between the observed lasing wavelength and predicted wavelength using the emission cross-section provided by Kuleshov is explained by the overestimated emission cross-section around 1000 nm given by Kuleshov and the difference between the spectroscopy of KYW:Yb^{3+} and KY$_{1-x-y}$Gd$_x$Lu$_y$W:Yb^{3+}. In addition a steady state rate equation model was developed. Using the spectroscopy of composite host materials in combination with the steady state rate equation model resulted in a good prediction of the laser performance of co-doped waveguide lasers.

The analysis of the luminescent spectra and lifetimes of Yb^{3+} ions in singly and co-doped host materials did not reveal any strong adverse effects on the laser relevant spectroscopic properties, when co-doping the KYW host material with large quantities of Gd^{3+} and Lu^{3+}.

The demonstration of lasers with low laser threshold of 18 mW, record-high slope efficiency

of up to 82.3%, and maximum output power of 195 mW in $KY_{1-x-y}Gd_xLu_yW:Yb^{3+}$ planar waveguides highlight the healthy laser properties of the Gd^{3+} and Lu^{3+} co-doped host material.
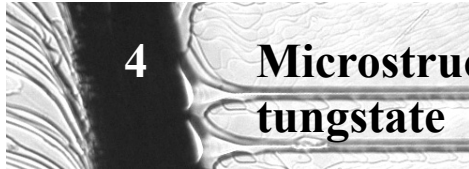
4   Microstructuring of potassium double tungstate

Several techniques have been explored in the past to fabricate channel waveguides in monoclinic double tungstates. Changing the refractive index of the host material by ion implanting was used to create planar waveguides in bulk crystals [bor05] and channel waveguides in thin layers, with a propagation loss of ~0.5 dB/cm in KYW [bor06]. Fabrication of femtosecond written channel waveguides was first demonstrated in [bor07]. The same approach resulted in a monolithic channel waveguide laser [bai09] with butt-coupled mirrors having a propagation loss of 1.9 dB/cm. These technologies all rely on changing of the refractive index of the host material, reaching only small refractive index contrasts. The fairly weak confinement of the light in the waveguide results in large mode field diameters of about 20 μm.

Other routes have been attempted to increase the refractive index contrast of the waveguide with its environment; epitaxial growth of channels through platinum and gold mask material [rom05] was not successful. However, micro-structured channels in thin films using dry etching techniques in fluorine chemistry and poly-silicon mask material resulted in promising waveguide structures having fairly large propagation losses of 3.2-5.5 dB/cm [pol07]. In this way Y junctions have been produced in high refractive index contrast layers, resulting in nicely confined light having modal width of ~ 5 μm as shown in Fig. 2.12 and improved propagation loss below 1 dB/cm [gar07]. Dry etching of fairly hard material like Ti:Sapphire has been demonstrated using plasma etching [kim03] and physical argon etching [gri03].

Chapter 3 of this thesis presents highly efficient lasing of Gd^{3+}, Lu^{3+} co-doped layers exhibiting an enhanced refractive index of the waveguide with respect to the pure KYW substrate and cladding material. This chapter discusses the development of an etch recipe to create smooth channel waveguide structures by etching ridges into the active planar waveguide layer. The enhanced refractive index contrast of Gd^{3+}, Lu^{3+} co-doped KYW with respect to the pure KYW substrate and cladding results in tightly confined guided modes in these channel waveguides. The challenge is to fabricate smooth channel structures to ensure efficient laser operation. Therefore the ridge structure is selected due to reduced interaction of the modal light with the sidewall roughness compared to rib waveguide structures, resulting in lower propagation losses. In addition ridge structures require a smaller etch depth compared to rib waveguide structures, which is another advantage regarding to the limited etch depths that can be obtained in KYW. Mode solver simulations using Phoenix FieldDesigner [pho] were used to optimize the lateral mode confinement of channel waveguides in the co-doped active layers. This resulted in a desired etch depth of 1-2 μm and channel widths around 2-10 μm for single mode waveguides. The obtained channel waveguides finally lead to demonstration of the first microstructured channel waveguide laser in KYW as discussed in Chapter 5. Another approach to obtain microstructured channel waveguide lasers by filling microstructured trenches in pure KYW substrates with optically active doped KYW was demonstrated shortly after [bol10].

4.1. Used dry etching systems

4.1.1. Reactive ion etching system

In a reactive ion etching (RIE) system, the etching process relies on generated highly reactive free radicals of aggressive etch gases. Chlorine and fluorine based gases are ionized using a radio frequency (RF) plasma generator and directed towards the substrate by applying a voltage difference between the plasma generator and the substrate. The free radicals impinge with a fairly large kinetic energy onto the substrate, ejecting atoms from the surface. This physical etching process or sputtering is assisted by the chemical property of the impinging radicals. The most preferred products of the chemical reactions are the volatile components that can be pumped away. It is desirable to have a certain amount of chemical etching to accelerate the etching process and obtain smoother sidewalls. In the available Oxford Plasmalab 100, shown in Fig. 4.1, various reactive gases can be used for generation of the plasma. In this work inert argon gas and a BCl_3/HBr gas mixture of ratio 5:2 are used in the Oxford Plasmalab 100. The substrate holder is at a fixed angle, with a helium backing to cool the substrate to a temperature around 0°C.
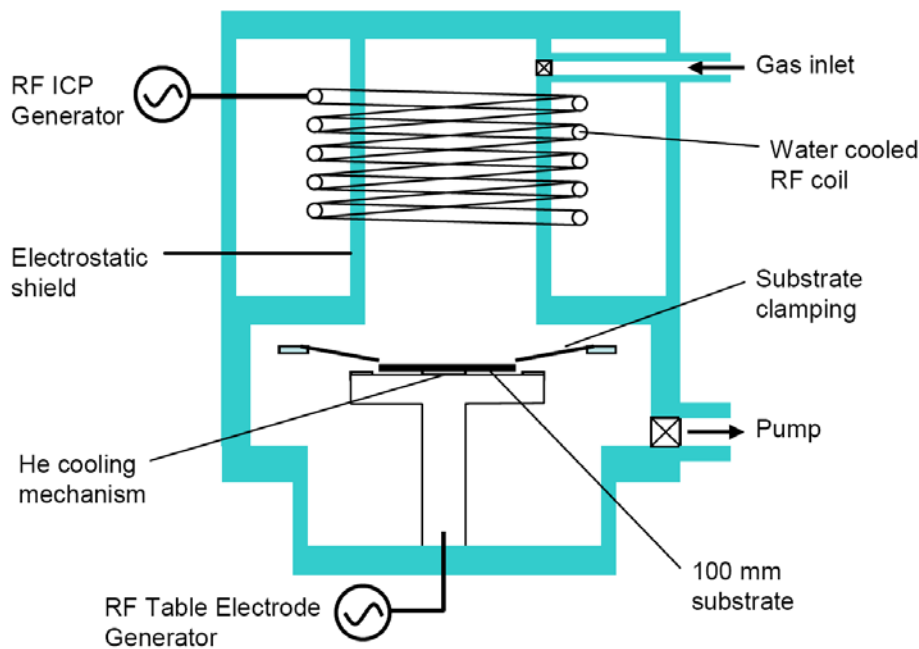

Fig. 4.1. Illustration of inductively coupled plasma RIE system. Schematic obtained from [bra09].

4.1.2. Ion beam etching system

In an ion beam etching (IBE) system, argon ions are extracted from the plasma by an extraction grid. The ions are accelerated by the acceleration grid, and finally neutralized by the neutralizer grid. A schematic of an IBE instrument is given in Fig. 4.2.
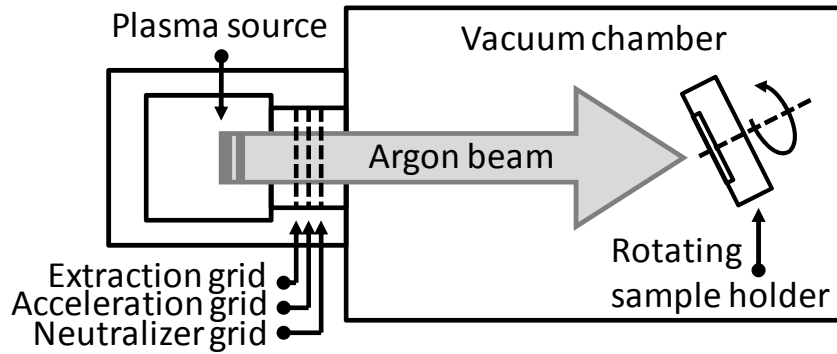
Fig. 4.2. Schematic of argon ion beam etcher.

This approach results in a highly directional, high energy neutral atom beam. The acceleration voltage, providing the kinetic energy to the ions, depends on the specification of the used instrument; in this work an acceleration voltage of 350 V is used. The main purpose of the high energy argon beam is to physically mill down the substrate, which is mounted on a tilted, rotating chuck. The tilt angle and the continuous rotation of the target improves the sidewall roughness as the angle of the impinging ions continuously changes with respect to the substrate. Here the angle of the tilt is set to 20° which corresponds to an optimal etch rate and feature shape for most materials according to [auc81, lee79]. As no chemistry is involved in the etching process, the etch rates of different materials are fairly similar. Therefore, an etch depth of 1 μm requires at least 1 μm of mask material.

Two different IBE instruments are available at the MESA$^+$ Institute; a home-made instrument (called the old IBE instrument) and a modern system (Oxford Ionfab 300plus). However, possible potassium contamination of the IBE systems may occur when etching KYW. This makes the systems incompatible with other etch processes. Therefore, etching of KYW was only allowed on the old IBE instrument, since it was amortized and not heavily used anymore.

In the old IBE instrument the plasma source is a penning source that ionizes the gas by an electrically heated tungsten filament. In this old system, the generated plasma is not very dense compared to the modern IBE system, having a RF plasma source. Therefore, the beam flux is small, resulting in a low etch rate compared to modern IBE systems, and compared to the used RIE system (described in Section 4.1.1). The advantage of the low beam flux is the lower thermal load of the sample, which is advantageous, as the used old IBE system has no actively cooled sample holder. The Oxford Ionfab 300plus provides much higher etch rates and is furnished with an cryogenically cooled chuck. In such an instrument, it is possible to work at a beam energy just above the etch threshold to permit removal of the material while minimizing ion implantation induced lattice defects, which would introduce additional optical propagation losses.

4.2. KYW etch recipe optimization

4.2.1. Etching of KYW by argon plasma in a reactive ion etching machine using Al$_2$O$_3$ mask material

Etching of aluminum oxide using a reactive gas mixture [BCl$_3$/HBr] has previously been

demonstrated as a suitable gas mixture for etching straight, vertical ridge structures with smooth side walls in sapphire (crystalline Al_2O_3) [jeo03,kim03]. In addition, a BCl_3/Cl_2 mixture was used to etch channel waveguides in Ti:Sapphire layers [cru02]. Moreover, microstructuring of amorphous aluminum oxide has been thoroughly investigated at IOMS by Dr. Jonathan Bradley [bra07, bra09]. He developed a recipe based on [BCl_3/HBr] to etch low loss channel waveguides in sputtered $Al_2O_3:Er^{3+}$ layers, resulting in various amplifier and laser devices, see [bra11] and references therein.
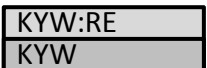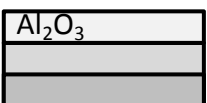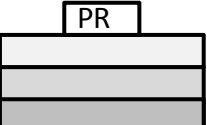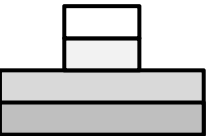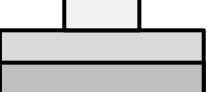
Due to the availability and in-house experience of this etching process, this recipe was selected for the first attempt. However, etching of Al_2O_3 by use of the reactive gas mixture [BCl_3/HBr] strongly relies on the chemical reactions taking place at the surface of the sample and on the volatility of the products. In KYW no volatile chemical products are expected using the reactive gas mixture [BCl_3/HBr]. Etching with this chemistry provided a slow etch rate of 4.1 nm/min in KYW (see Table 4.2), thereby confirming the chemically inert property of KYW to the [BCl_3/HBr] chemistry. Reactive ion etching of KYW using fluorine chemistry was extensively investigated by Dr. Camelia Borca, resulting in microstructured channel waveguides in KYW [bor06]. She employed photoresist, metal, and semiconductor masks that were deposited onto the KYW substrates using standard UV-photolithography methods. The best results were obtained with polysilicon masks. The etch rate in KYW was 35–40 nm/min. and ribs as deep as 6 μm were obtained in KYW:Yb^{3+} films of 10-μm thickness, as shown in Fig. 2.12. These channels had relatively high propagation losses of 5.5 dB/cm at 670 nm and 3.2 dB/cm at 981 nm [pol07]. Propagation loss below 1 dB/cm was obtained in channel waveguides having an etch depth of 1.8 μm [gar07].

Physical etching relies on milling of material by bombardment of highly energetic particles. Etch methods based on physical etching are not selective, i.e., similar etch rates are observed for most materials. The etch rates are only slightly affected by the hardness of the material. To create deeply etched structures using physical etching, it is therefore necessary to either find a very hard mask material or use a very thick mask. Here RF-sputtered Al_2O_3 having a microhardness of 18-20 GPa [sri07] is a suitable mask material, since it is harder than KYW. Using SiO_2 as mask material is less suited due to its lower hardness between 14.4-18 GPa [mem]. SiO_2 is assumed to have a similar hardness as soda lime glass, having a Mohs hardness of 5-6 [uqg]. This is only a little bit harder than the Mohs hardness of around 4.5-5 for KYW [kam01]. In addition, the use of Al_2O_3 as mask material is preferred due to the in-house available knowledge on deposition and machining of such layers for low loss optical waveguides [bra09, bra07].

For these experiments ~500 nm thick Al_2O_3 layers were sputtered on KYW. Channel structures were defined using photolithography (FujiFilm OiR 907/17 photoresist). The photoresist mask was then transferred into the Al_2O_3 layer using RIE with the [BCl_3/HBr] chemistry. After removal of the photoresist by an oxygen plasma cleaner, the RIE machine was used again, but now with argon gas to create an argon plasma for physical etching, since the etch rate of KYW is small in [BCl_3/HBr] chemistry. Here the substrate electrode RF power directs the argon plasma towards the substrate holder, hence providing the kinetic energy of the impinging ions. The etch rate and sidewall roughness are studied as a function of the substrate RF power. The recipe used for this study is summarized in Table 4.1.

Table 4.1. Process flow for etching of KYW using Al$_2$O$_3$ mask material

Layer structure	Description of process steps
KYW:RE KYW	Standard cleaning: ~10 minutes in wet HNO$_3$ (100%)
Al$_2$O$_3$	Sputter deposition of ~500 nm thick Al$_2$O$_3$ layer, using AJA ATC1500
PR	Lithography and development of FujiFilm OiR 907-17 Photoresist, using EVG 620 mask aligner
	Etching of Al$_2$O$_3$ mask, using Oxford Plasmalab 100 ICP RIE. Settings are for 70 nm/min. etch rate are [bra09, bra07]: • BCl$_3$/HBr Gas mixture of ratio 5:2 • Pressure of 12 mTorr, total gas flow of 35 sccm. • ICP power of 1750 W, RF substrate electrode power of 25 W
	Removal of Photoresist: ~30 minutes in Tepla 300E plasma etcher and ~10 minutes in wet HNO$_3$ 100%
	Argon etching, using Oxford Plasmalab 100 ICP RIE Applied RF substrate powers are: 25 W, 50 W, 100 W and 150 W • Argon gas • Pressure 19 mTorr, gas flow of 100 sccm. • ICP power of 1500 W

The etch rates for physical argon etching of both the KYW layer and the Al$_2$O$_3$ mask are measured using the SEM micrographs when etched at various RF substrate powers. The obtained etch rates are given in Table 4.2.

Table 4.2. Measured etch rates of Al_2O_3 and KYW using argon plasma at different RF powers. In addition, the measured etch rates of photoresist (PR) (FujiFilm OiR 907/17) and KYW using BCl_3/HBr chemistry, normally used to etch Al_2O_3, are given.

Etch Gas	Al_2O_3 mask thickness	Power [W]	Time [min.]	Etch depth[*] [nm]	KYW etch rate [nm/min.]	Al_2O_3 mask etch rate[*] [nm/min.]	Selectivity
Ar	482 nm	25	7	0	0	0.57	0
Ar	482 nm	50	7	97	13.9	19.7	0.71
Ar	482 nm	100	7	440	63	28.6	2.2
Ar	482 nm	150	7	588	84.0	31.3	2.68
Etch Gas	**PR mask thickness**	**Power [W]**	**Time [min.]**	**Etch depth[*] [nm]**	**KYW etch rate [nm/min.]**	**PR mask etch rate[*] [nm/min.]**	**Selectivity**
BCl_3/HBr	1.7 µm	25	5:20	22	4.1	51	0.08

[*]**Determined using SEM images given in Fig. 4.4.**

The effect of the RF substrate power on the etch rates of Al_2O_3, KYW and the etching selectivity, given by the division of the substrate etch rate by the etch rate of the mask material, are depicted in Fig. 4.3.
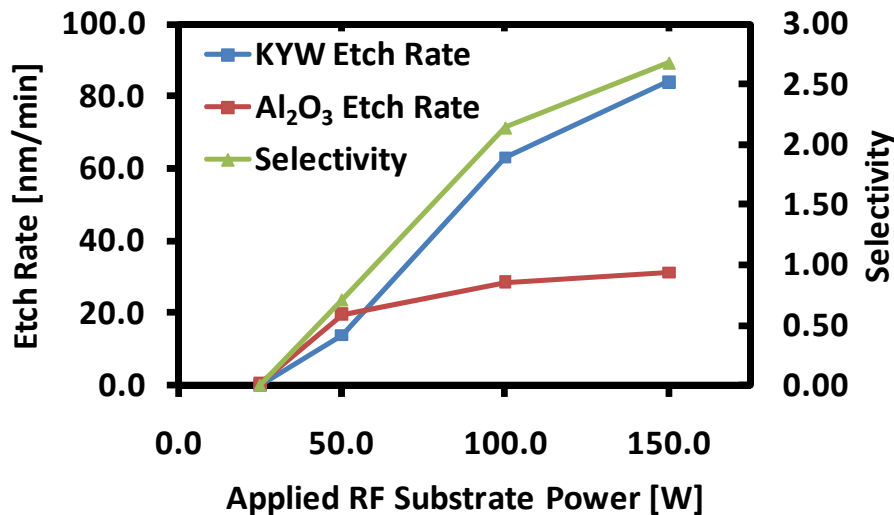
Fig. 4.3. Plot of etch rates and selectivity versus RF substrate power for KYW and the Al_2O_3 mask material in an argon plasma.

As the RF substrate power is increased (i.e., 100 W and 150 W), the selectivity increases. This is expected, because Al_2O_3 is harder than KYW. The best selectivity is obtained using the largest RF substrate power. Physical inspection of the etched structures is performed using a scanning electron microscope (SEM). The SEM micrograph images are shown in Fig. 4.4.

25 W

50 W

100 W

150 W
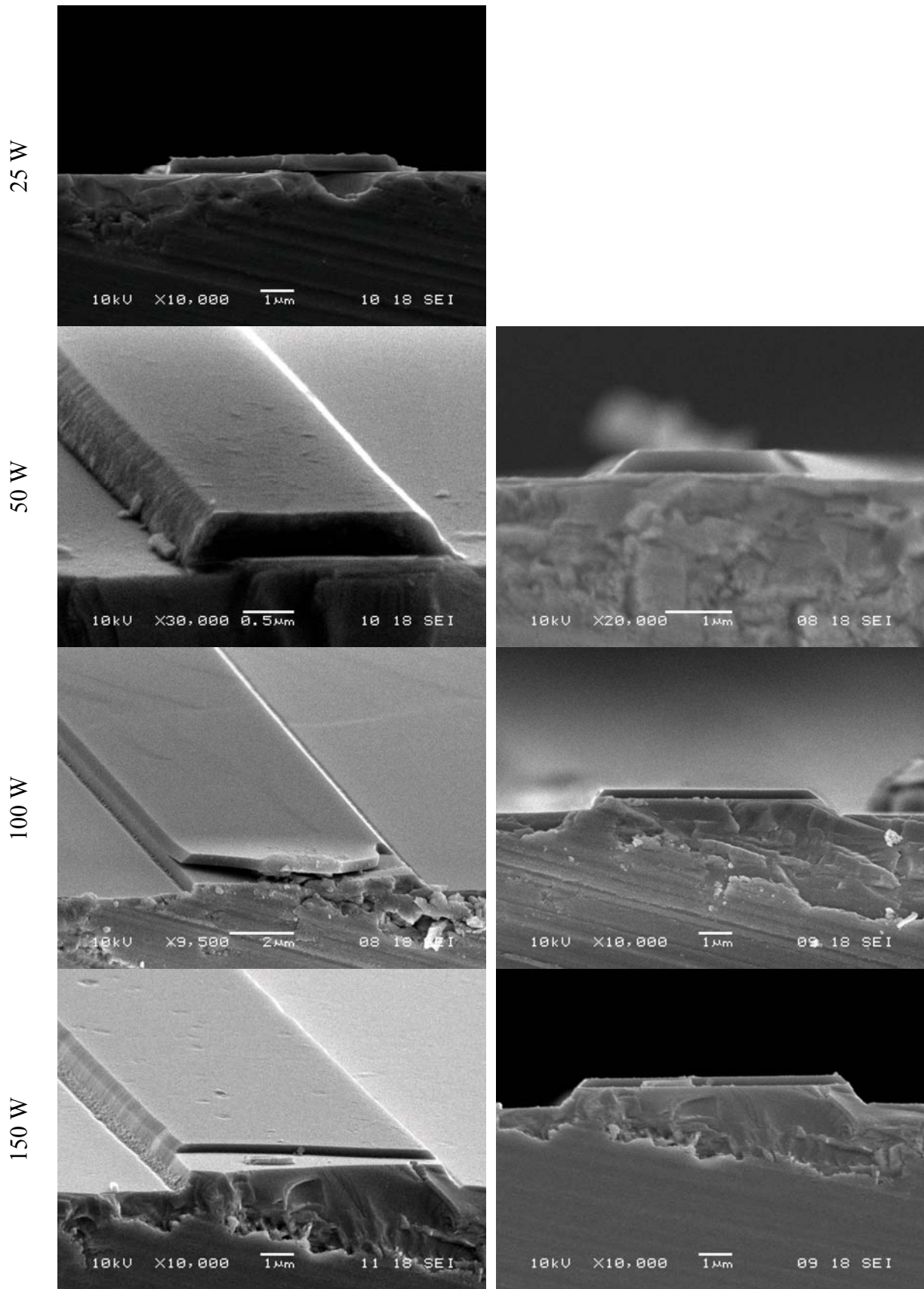
Fig. 4.4. SEM micrograph images of etched structures in KYW by argon plasma at various RF-powers in a RIE machine using Al$_2$O$_3$ mask material (not removed.)

The lowest sidewall roughness is obtained using an RF substrate power of 100 W. At larger powers the sidewall roughness seems to increase, as well as formation of deeper trenches next to the channel structures. The forming of this trench is typical for an RIE etching process [mad]. At lower power almost no trench is observed. The optimal substrate power is found to be 100 W based on the combination of good selectivity, significant etch rates and low sidewall roughness obtained using this setting.

4.2.2. Removal of the Al_2O_3 Mask

Due to material stress, the edges of the waveguides tend to chip off during end-face polishing. Therefore, the Al_2O_3 mask has to be removed prior to end-face polishing. In addition, fabrication of buried channels having an overlay of pure KYW grown on top of the Al_2O_3 mask by LPE is impossible, since the Al_2O_3 mask does not allow lattice matched single-crystalline growth, resulting in a fractured layer. No wet etching of KYW has been previously reported; therefore HF etchant (50%) was used to remove the remaining Al_2O_3 mask material of the best sample etched with a substrate power of 100 W. Fig. 4.5 shows the channel before and after this treatment. An increase of the sidewall roughness can be observed. It seems that the crystal structure which is damaged at the waveguide edges by the argon ion bombardment becomes more sensitive to the 50% HF, resulting in severely pronounced sidewall roughness.

(a)   **(b)**
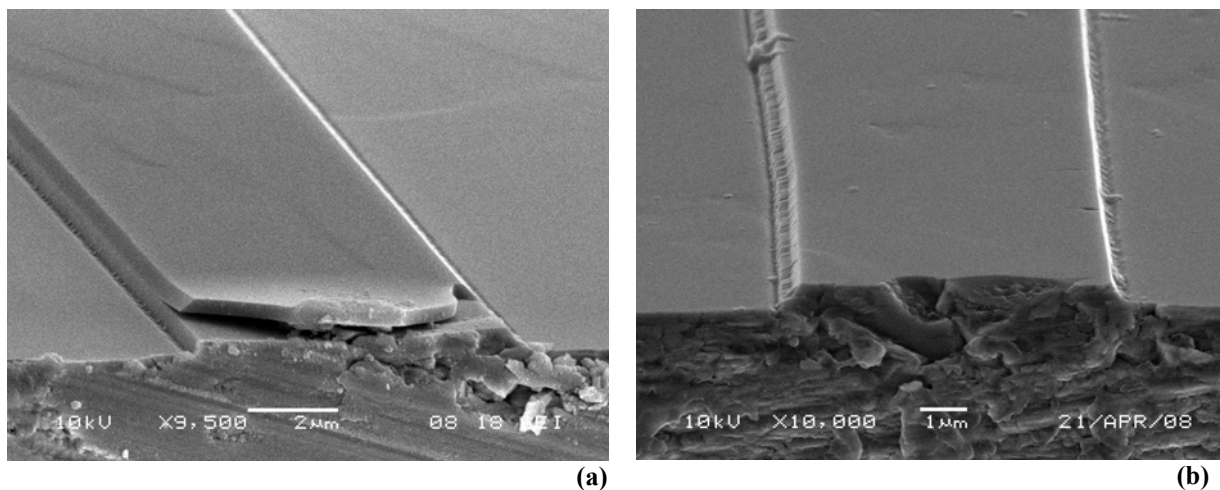
Fig. 4.5. Removal of Al_2O_3 mask using 50% HF (a) with mask and (b) after removal of mask, having an etch step of 440 nm.

In order to optimize the mask removal recipes, several KYW samples with an Al_2O_3 mask thickness of ~1 µm were prepared using the 100 W argon etch recipe. In order to obtain the targeted 2 µm ridge depth, a processing time of 31 minutes was selected. However the etch rate appeared to be a bit faster as measured earlier, resulting in an etch depth of ~2.2 µm. Faster etch rates can be explained by minute changes in etching conditions like substrate temperature and chamber pressure. To remove the residual Al_2O_3 mask various etchants were used. The etch rates of Al_2O_3 for the etchants used were measured using Al_2O_3 layers on Si substrates before using them on the structured KYW samples. The measured etch rates of Al_2O_3 are listed in Table 4.3.

Table 4.3. Measured etch rates of Al$_2$O$_3$ on Si substrate using an ellipsometer (Woollam)

Wet etchant	Time	Removed thickness	Removal rate
1% HF	20 min.	423 nm	21.2 nm/min.
Al etch at 60°C	16 min.	540 nm	33.8 nm/min.
Dry etch Al$_2$O$_3$ recipe, previously measured [bra09, bra07]			70 nm/min.

After removal of the residual Al$_2$O$_3$ mask by the selected etchants, a high resolution SEM is used to observe the sidewall roughness. The results of the mask removal test are presented in Fig. 4.6.

(a) Before mask removal

(b) Removal by RIE Al$_2$O$_3$ etch recipe for 17 minutes

(c) Removal by 1% HF for 46 minutes

(d) Removal by Al etch at 60°C for 30 minutes
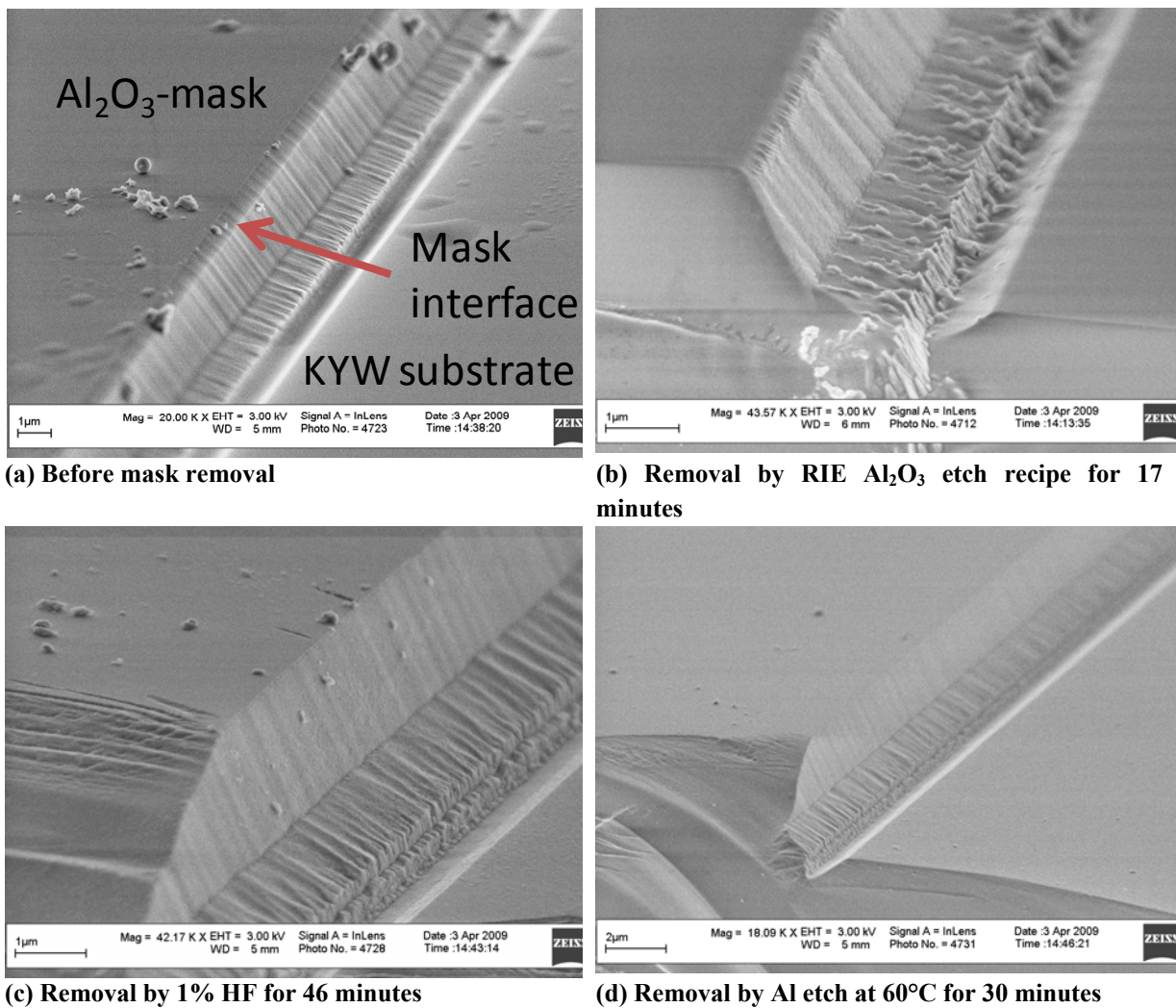
Fig. 4.6. SEM micrographs of 2.2 μm deeply etched channels fabricated using RIE (a) with residual Al$_2$O$_3$ mask, and (b) after removal of masking material using: RIE with Al$_2$O$_3$ recipe causing rounding of the top edges of the waveguide, and (c, d) using two wet etchants providing similar results exposing severe roughness at the bottom of the trench.
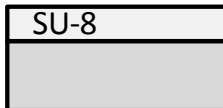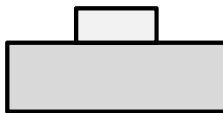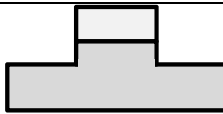
The sidewall roughness of the etched structure before mask removal (Fig. 4.6 (a)) appears to be more severe compared to the fairly smooth result depicted in Fig. 4.5 (a). The difference can partly be explained by the larger etch depth. Note that a little trench was already visible in Fig. 4.5 (a). In Fig. 4.6 (a) some traces of organic contamination fill the deepest trench.

The organic contamination originates most likely from residual vacuum grease that is used to mount the sample into the RIE machine. The organic contamination is fully removed by all etch methods, hence not visible after removal of the mask; see Fig. 4.6 (b-d). The sidewall roughness is almost equal for all Al_2O_3 etchants. In order to determine whether this roughness is acceptable for optical waveguide fabrication, the propagation losses were measured by means of a Fabry-Perot loss measurement, resulting in 7-15 dB/cm loss.

4.3. SU-8 reactive ion etching

Using SU-8 [mic] as mask material for physical etching tackles the issue from the other side, since large SU-8 mask heights of 5 μm can easily be obtained, circumventing the necessity of a hard mask material like Al_2O_3. SU-8 resist is a negative resist; this means that during lithography, the UV light initiates the polymerization reaction. Hence the illuminated areas remain, after dissolving the non-exposed area in an isopropanol bath. It has to be noted that the adhesion of the SU-8 mask to the surface is very weak, therefore gentle rinsing in an isopropanol bath and gentle blow-dying of the sample is recommended. The optimized process flow is given in Table 4.4.

Table 4.4. Process flow for optimization study of SU-8 photoresist on Si substrates using RIE etching

Layer structure	Description of process steps
Si	1.1 Standard cleaning: 10 minutes HNO_3 (100%) 1.2 Quick dump rinse (QDR) < 0.1 μs 1.3 Blow dry with nitrogen 1.4 Drybake: ~2 hours at 120ºC
SU-8	2.1 Spincoat SU-8/5 at 2000 RPM 2.2 Pre-bake: sample put on cold plate, freely ramped up to 95º, total time is 15 minutes
	3.1 Exposure (Flood mode, with manually placed mask. The hard contact mode crushes the sample): 16 seconds (optimized) 3.2 Post exposure bake: sample put on cold plate, freely ramped up to 80ºC, total time is 12 minutes 3.3 Development in PER600 bath (gentle!): 60 seconds (optimized) 3.4 Isopropanol bath rinse (gentle!) 3.5 Blow dry 15 cm distance (gentle!)
	4.1 Loading in Oxford Plasmalab 100 ICP RIE, sample mounted on Si-wafer by vacuum grease 4.2 KYW Ar-plasma etch recipe for 2 μm (~30 minutes)
	5.1 Resist strip: 10 minutes HNO_3 (100%) 5.2 QDR < 0.1 μs 5.3 Blow dry with nitrogen

An optimization study has been performed in order to achieve smooth structures when using SU-8 as mask material. The first test concerned the variation of the exposure time and development time. In a second test the post exposure bake temperature was varied. The optimization study has been performed on silicon substrates.

Here the exposure time was set to two values: 13 seconds and 16 seconds with a post exposure bake temperature of 80°C. The duration of development in PER600 was tested for 30, 40, 60, 90 seconds. An optical microscope was used to observe the shape of the structures after 30 minutes of RIE using an argon plasma. The residual resist cannot be removed by standard method using acetone. Removal of the mask using HNO_3 later on was successful for most cases, and performed during the second part of the optimization study (Section 4.3.2). The images taken by the microscope are presented in Fig. 4.7.
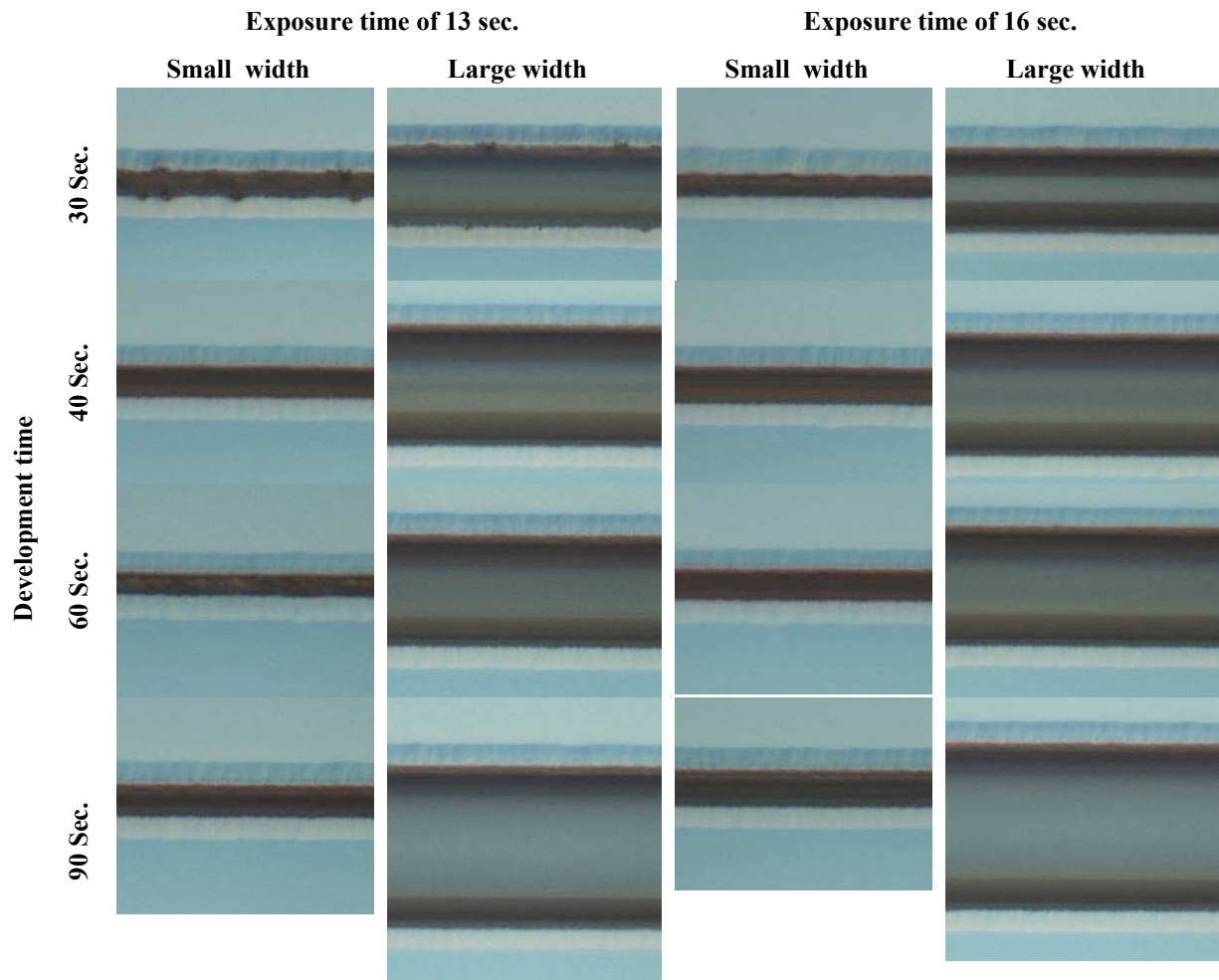
Fig. 4.7. Optical inspection of RIE etched structures using SU-8 as masking material, having different development times and exposure times. Note that the channel widths used in this experiment were not constant.

Analysis of the observed sidewall roughness reveals severe roughness when using short development durations of 30 seconds. At exposure times of 13 seconds with a development time of 60 seconds some delaminating effects are observed for the smaller features. Only minute differences are observed for the test range of 40-60 seconds development time and an exposure time of 16 seconds. An optimal structure was found for the recipe having an exposure time of 16 seconds and a development time of 60 seconds, and therefore selected for further investigation.

4.3.2. Optimization of SU-8 by variation of the post exposure bake temperature

The temperature during the post exposure bake, determines the degree of polymerization, and thus the glass temperature of the resist. An optimization study for the different temperature regimes have been performed, to find the optimal smoothness of the final etched structure.

In this test the post exposure bake temperatures of 60ºC, 80ºC, 100ºC and 120ºC, are tested using an exposure and development times of 16 and 60 seconds respectively.

SEM images, shown in Fig. 4.8, have been taken from the SU-8 structures, after etching of the channels using RIE and after the resist strip step using HNO_3 (100%).
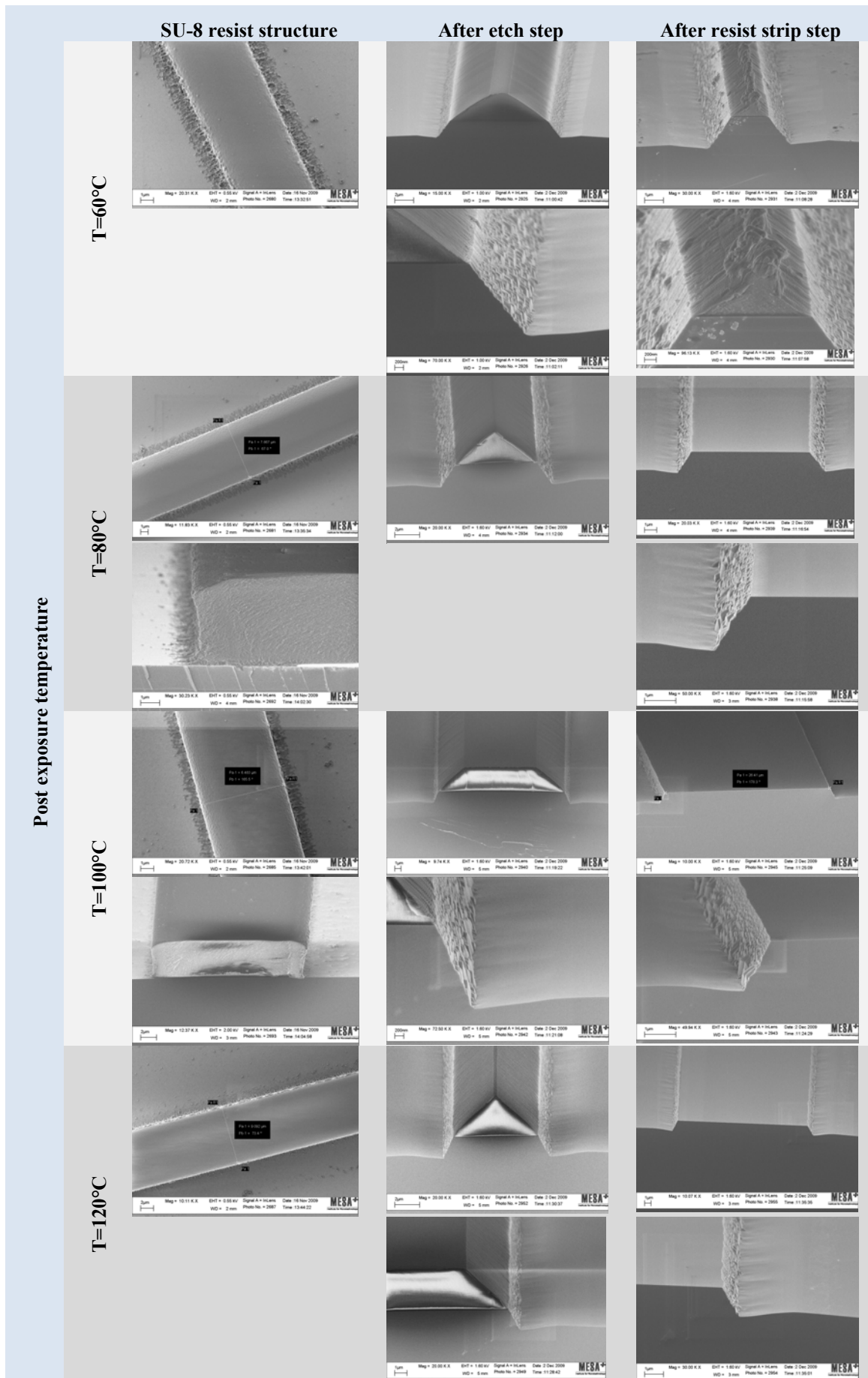
Fig. 4.8. RIE optimization study using SU-8 masking material for various post exposure temperatures.

From Fig. 4.8 it can be seen that all masks show a web-like structure at the feet of the SU-8 photoresist; this web is minimal at a post exposure bake temperature of 120°C. However, at these high temperatures of 100ºC and 120ºC the top edge of the final structure is not straight (most visible in 120ºC). It seems that a fairly large mask roughness is transferred into the substrate, resulting in a wavy edge of the top of the waveguide. At lower post-exposure temperatures this effect is reduced, this does not correlate with the observed web-structure which is more prominent at the lower post exposure bake temperatures. At the lowest post exposure temperature of 60ºC the residual resist is hard to remove. Therefore, the most promising results are expected using a post exposure bake temperature of 80ºC. However, the sidewall roughness of this process is still not convincing, the observed web-like structure of the SU-8 and the final roughness show that this route is not optimal. Etching using an ion beam etcher might improve the situation, as the direction of the impinging ions with respect to the substrate is continuously changed by rotation of the substrate holder. This might wash out the side-wall roughness.

4.4.　SU-8 ion beam etching

In the IBE machine, the substrate is placed at an angle and rotates continuously during processing. The roughness of the mask will be reduced by a washing/wiping effect of the continuously varying angle of incidence of the ion beam. In this test the best SU-8 recipe was used from the previous study. In addition, a test was made to remove the web-like structure of SU-8 photoresist by a cleaning step in an oxygen plasma at 200 W for 10 minutes prior to the IBE. The observed result is presented in Fig. 4.9.

With resist still on top   **After removal of the resist**

No oxygen cleaning

With oxygen cleaning

SU-8 mask

Redeposition
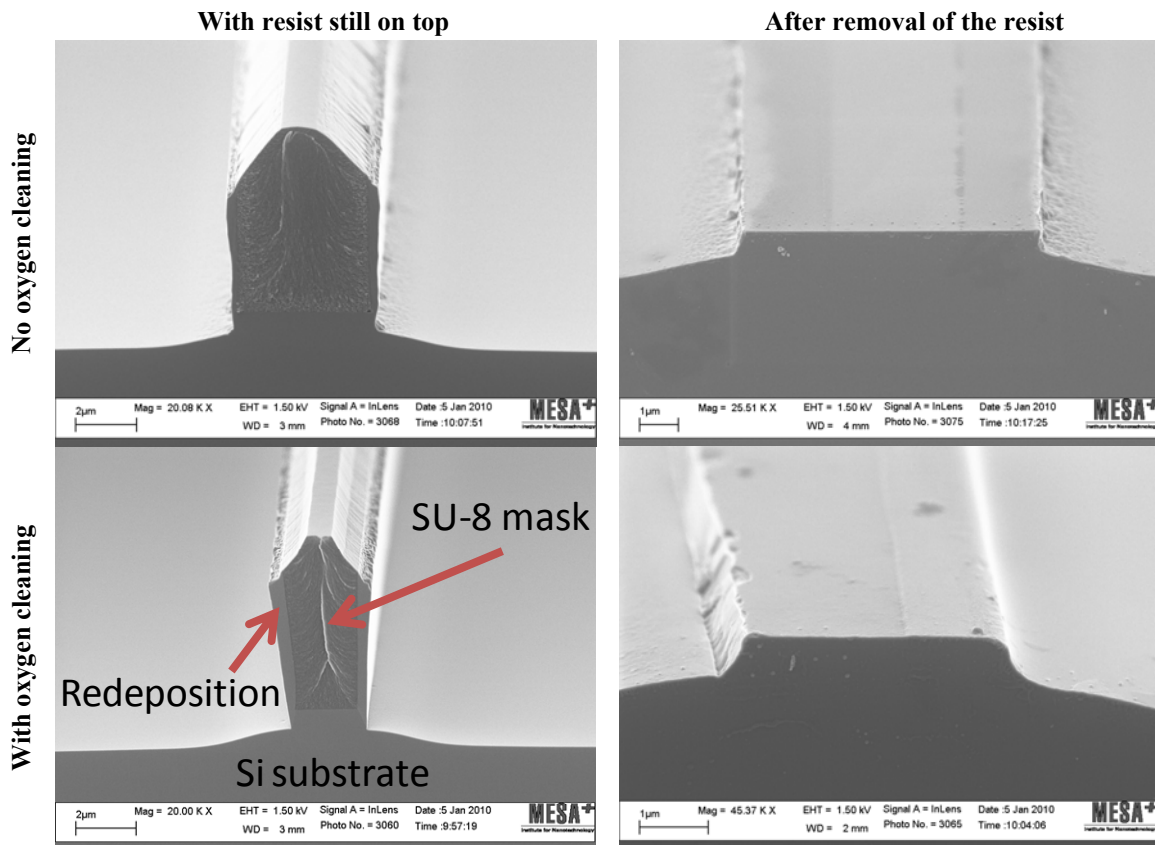
Si substrate

Fig. 4.9. Structures in Si, fabricated by IBE using SU-8 as mask material. The top 2 figures show additional roughness at the bottom of the substrate caused by SU-8 residuals. For the bottom 2 figures these SU-8 residuals have been removed by an O$_2$ cleaning step prior to the IBE processing. Both methods resulted in fairly rough sidewalls. Note that the widths of the displayed structures are not identical.
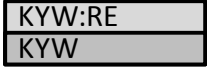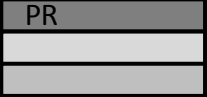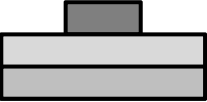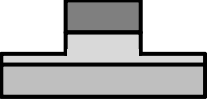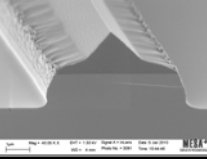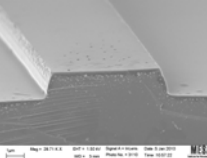
After removal of the web-like structure using the oxygen cleaning step, the sidewalls look promising before removal of the SU-8. However the large amounts of re-deposited material on the sides of the photoresist seem to chip of the edges of the final structures during the photoresist removal step, hence the roughness of the final result is still too large. The large amounts of re-deposition is typical for ion beam milling using thick masking materials, changing the shape of the mask, or reducing the height of the mask material can reduce the re-deposition effects significantly [lee79].

4.5. Photoresist (OiR 908/35) ion beam etching

The approach in this method was to make a very smooth mask using FujiFilm OiR 908/35 photoresist. This photoresist does not rely on a temperature dependent crosslink process and has a constant melting temperature/glass transition. After development of the photoresist mask, the mask was set to a temperature of 150ºC to reflow the photoresist mask material, resulting in very smooth resist patterns having a hemispherical shape due to the surface tension of the photoresist. The hemispherical shape of the photoresist reduces the negative effects of re-deposition of material at the sidewalls [lee79]. The disadvantage of the reflow step is that the specified thickness of 3.5 µm for the photoresist is not constant for all channel widths and that it affects the exact feature widths. The process flow for this test, presented in

Table 4.5, has been used to etch silicon and KYW.

Table 4.5. Flowchart for fabrication of channels in KYW using IBE

Layer structure	Description of process steps
KYW:RE KYW	1.1 Standard cleaning: 10 minutes in HNO_3 (100%) 1.2 Quick dump rinse (QDR) 1.3 Switch on oven: step 3.7
PR	2.1 De-hydration bake: 5 minutes @ 120°C[*] 2.2 HDMS Spin-coating: 20 seconds @ 4000 RPM 2.3 Photoresist (FujiFilm OiR 908/35): 20 seconds @ 4000 RPM, Start spinning directly after applying droplet, to minimize edge beads on back and front side of the sample 2.4 Pre-exposure-bake: 2 minutes @ 95°C 2.5 Degassing: 5 minutes
	3.1 Litho at EVG620 on flat chuck with blue tissue and additional pieces of glass to support mask. The mask is manually put in place along the optical axis[**] 3.2 Flood exposure: 10 seconds, delay 5 seconds 3.3 Degassing: 5 minutes 3.4 Post-exposure-bake: 1 minutes @ 120°C 3.5 Development: 30 sec + 25 seconds 3.6 Post-exposure-bake: 10 minutes @ 120°C 3.7 Reflow: 1 hour @ 150°C (oven)
	4.1 Fixation of samples on Si wafer using a little thermal conductive paste and kapton tape. 4.2 Ion beam etching, settings: • Process time: ~8 hours, (etch rate of KYW ~ 2.79 nm/min) • Acceleration voltage: 350 V • Beam current: 20 mA • Angle: ~20 degrees • Rotation: on
	5.1 Standard resist strip: 10 minutes in HNO_3 (100%) 5.2 Quick dump rinse (QDR)

[*]**No fracturing of samples has been observed when putting the samples directly on a hotplate at 120°C (300°C is not possible).**

[**]**A red LED (bicycle tail light) is used to align the sample along the optical axis using crossed polarizer sheets. A separate test demonstrated that the LED light has no effect on the development of the photoresist.**

During the etch tests the etch rates of the various materials have been measured, they are presented in Table 4.6.

Table 4.6. Measured etch rates of various materials using the IBE.

Material	Etch rates in ion beam etcher
Silicon	2.4 nm/min
Photo resist (FujiFilm OiR 908/35)	2.8 nm/min
KYW	2.79 nm/min

The measured etch rates confirm the almost equal etch rates for the various materials, as expected for physical etching methods. Etching of both KYW and Si did result in fairly smooth structures, as shown in Fig. 4.10. Especially etching of Si reveals that the reflow of the resist provides a very smooth surface of the resist, the roughness of the sidewalls only caused by the crystalline structure of the material, which is hard to avoid.
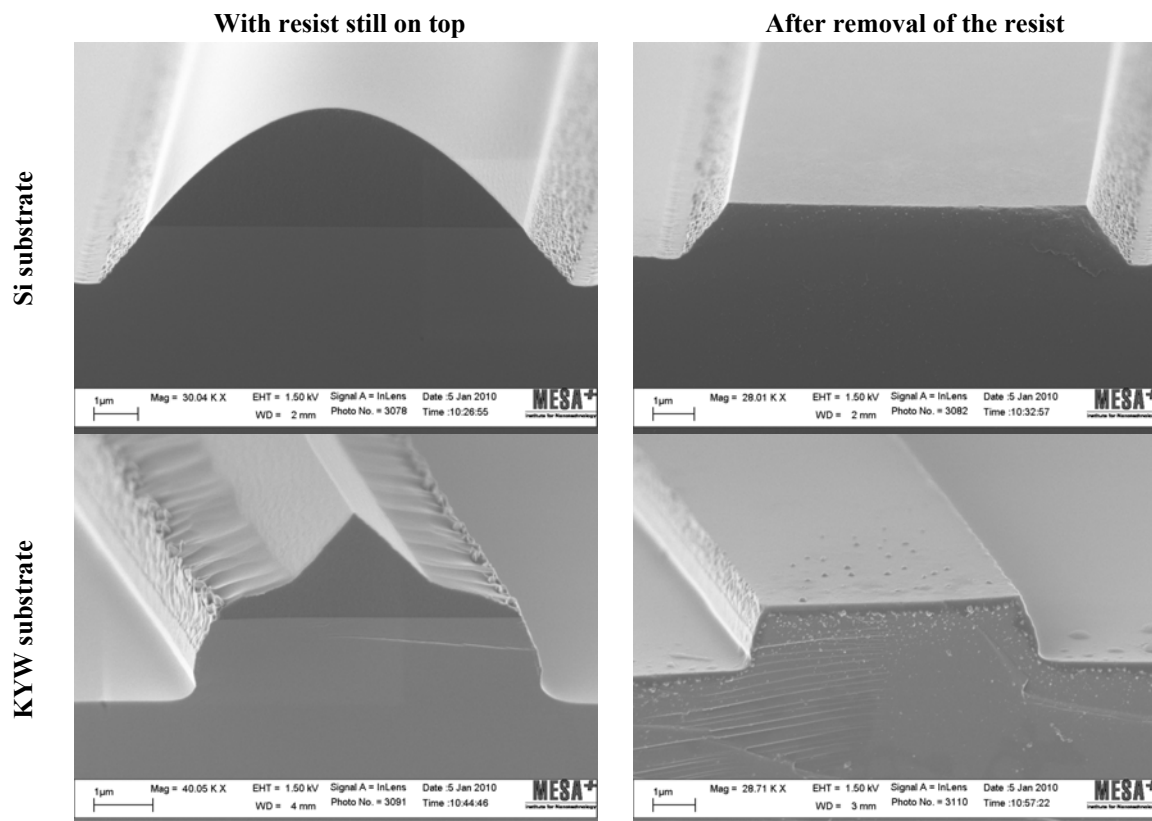
Fig. 4.10. IBE Etched structures in Si using 908/35 masking material.

The observed difference of the sidewall angle is related to the angular etch dependence of the used photoresist and the substrate material [lee79]. However, the sidewall roughness and shape of the photoresist when processing KYW are not understood. Possible explanations are: material re-deposition, surface temperature and adhesion. A significant difference in surface temperature compared to the silicon substrate is expected by a much weaker thermal conductivity of the KYW. The observed effect might be explained by the larger surface temperature that allows a reflow of the photoresist during processing combined with a difference in surface tension and continuous re-deposition. However the overall result using this process looks promising, providing structures with an etch depth of 1.4 μm. It must be noted that when the photoresist layer is too thin, the rough top of the photoresist profile gets

transferred into the KYW substrate [mog79]. This typically occurs at small waveguide dimensions as shown in Fig. 4.11.

2.5 µm ◄—————— Width of mask design ————► 7.5 µm
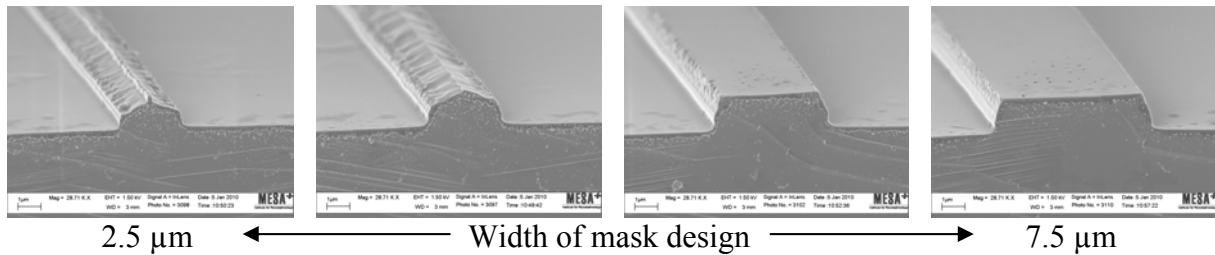
Fig. 4.11. Transfer of the roughness of the photoresist into the substrate at smaller waveguide widths.

The transfer of mask roughness, caused by too thin mask thickness, therefore restricts the feature width to a minimum of approximately 5 µm.

4.6.   Conclusions

Various etch methods were tested and evaluated. Using RIE and a hard Al_2O_3 mask material resulted in shallow etched structures with low roughness, however the increased sidewall roughness obtained at larger etch depths and after mask removal resulted in unacceptable propagation losses of 7-15 dB/cm. Using SU-8 as mask material did not improve the sidewall roughness. Therefore IBE was tested using SU-8 mask material; here the sidewall roughness seemed to be improved, especially after an oxygen cleaning step to improve the initial roughness of the SU-8 mask. However, the fairly large re-deposition of material on the sidewalls hid significant roughness that revealed after removal of the mask. In addition the re-deposited layer seemed to damage the channel structure during removal.

The most promising results were obtained using standard photo resist (FujiFilm OiR 908/35) as mask material and IBE to transfer the mask structure into KYW. This recipe resulted in smooth waveguide structures having widths larger than 5 µm and an etch depth up to 1.4 µm. This process was selected for the fabrication of channel waveguides in thin films of Yb^{3+} doped double tungstates, forming the basis of channel waveguide laser devices in this crystalline material.

Wall of remarkable structures
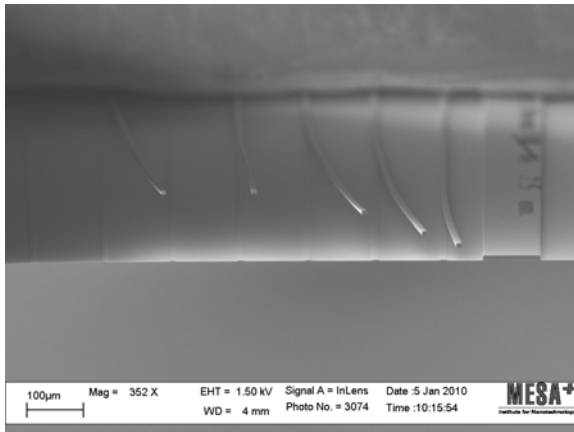
Happy SU-8: Due to the weak adhesion of the SU-8 photoresist with the substrate, the feet of the SU-8 photoresist start to dance after cleaving of the sample. The music is produced by playing the micro snares of SU-8 using a Dektak profilometer.
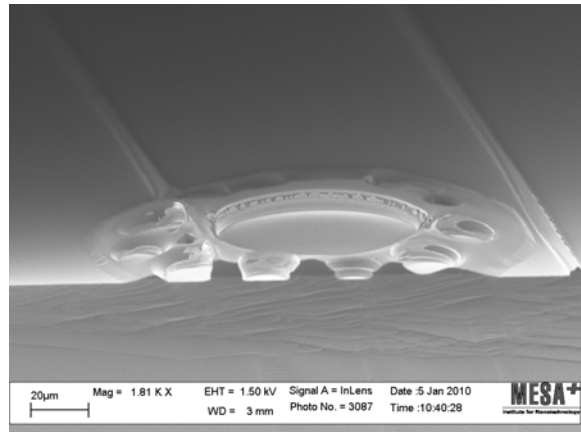
Micro UFO: Air bubbles in the photoresist and other contamination make the nicest features. This might be a landed microbe-vessel, observed during winter-times. Note: no mouth caps are used in the cleanroom.
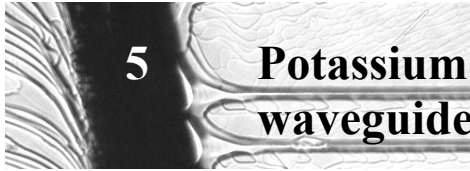
5   Potassium double tungstate channel waveguide lasers

The demonstration of micro-sized laser devices in double tungstate host materials is brought to a higher level, as presented in this chapter. The larger refractive index contrast with the substrate obtained in the Gd^{3+}, Lu^{3+}, co-doped KYW:Yb host material allows for smaller waveguide dimensions and revealed no adverse effects on the laser related spectroscopic properties of the Yb^{3+} ions, as demonstrated in Section 3.4. Here the developed etch procedure discussed in Section 4.5 is applied to fabricate channel waveguides of $KY_{1-x-y}Gd_xLu_y(WO_4)_2:Yb^{3+}$. The resulting buried channel waveguide structures provide lateral confinement of the light, driving the light intensity in the actively doped waveguides to high levels. The remarkable laser performance obtained from these channel waveguides is caused by the excellent confinement of pump and laser light, which allows efficient excitation of the active ions.

Due to the strong light confinement very low laser thresholds of 4.5 mW were achieved and reflections as low as the Fresnel reflection (11% per facet) on either side of the waveguide were still sufficient to commence laser oscillation in the waveguides. The large outcoupling degrees provides efficient extraction of laser light of up to 76% slope efficiency versus absorbed pump power and large output powers up to 650 mW. In addition, laser operation with large tuning range and small quantum defect was demonstrated in these channel waveguides.

5.1.   General device fabrication and preparation

The devices used in these experiments have all been fabricated in-house using the developed technology concerning LPE growth, polishing and etching. Firstly, the active layers were grown and polished as described in Chapter 2. Ridge waveguides were etched along the N_g optical axis into these active layers using IBE, providing a typical etch depth of 1.4 μm, according to the developed recipe presented in Section 4.5. In order to ease polishing of the end-facet, reduce propagation losses and improve the mode overlap with the active waveguide, a pure KYW overlay was grown onto these ridge waveguides using LPE. The end-facets of the samples were polished perpendicular to the buried channels, i.e. parallel to the N_m optical axis. Dielectric mirrors were butt-coupled to the waveguide end-facets by use of fluorinated oils (Fluka or 3M Fluorinert FC70), such that a monolithic cavity along the N_g optical axis was formed. For these experiments samples were prepared having different material compositions of the active layer. The ridge height and device length was different for each sample.

5.2.   Channel waveguide laser using butt-coupled mirrors

5.2.1. Experiment

This section discusses the laser performance of a buried channel waveguide of $KY_{0.4}Gd_{0.433}Lu_{0.167}(WO_4)_2:(1.7\%)Yb^{3+}$. Several experiments have been performed on a 1.4

μm deep etched ridge waveguide with a width of 7 μm and a thickness of 2.4 μm. This device is referred as sample A. The ridge waveguide is oriented along the N_g optical axis and 7.5 mm long cavities with various outcoupling efficiencies were formed by butt-coupling mirror substrates to the polished end-facets using a fluorinated oil (Fluka) with a refractive index of 1.58. A scanning electron microscopy (SEM) picture of such a ridge waveguide is shown in Fig. 5.1.
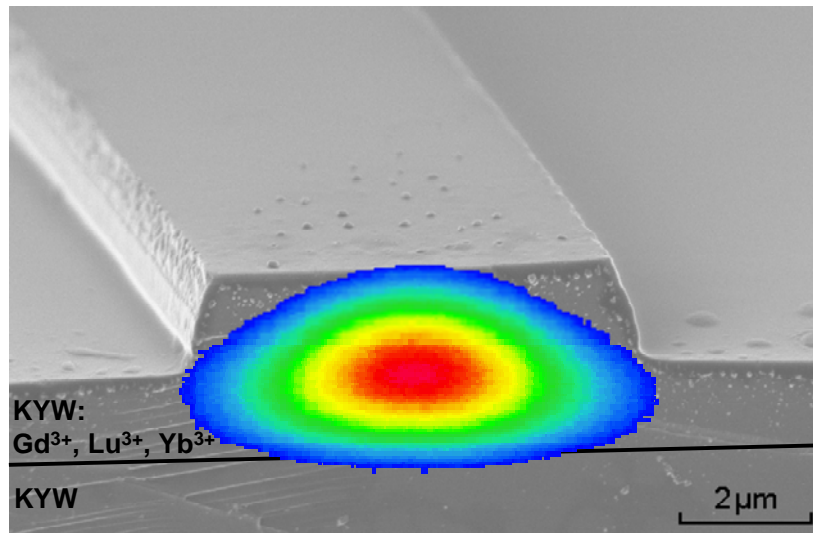
Fig. 5.1. SEM micrograph of a microstructured channel waveguide before overgrowth, with a color projection of a measured mode profile of the laser emission.

Pump light from a continuous-wave Ti:Sapphire laser operating at a wavelength of 981 nm, at the Yb^{3+} absorption peak in KYW, was coupled with polarization parallel to the N_m optical axis into the channel waveguide by a ×16 microscope objective with a numerical aperture (N.A.) of 0.32. Residual transmitted pump light and laser light were coupled out at the other waveguide end by a ×20, N.A. = 0.4 microscope objective.
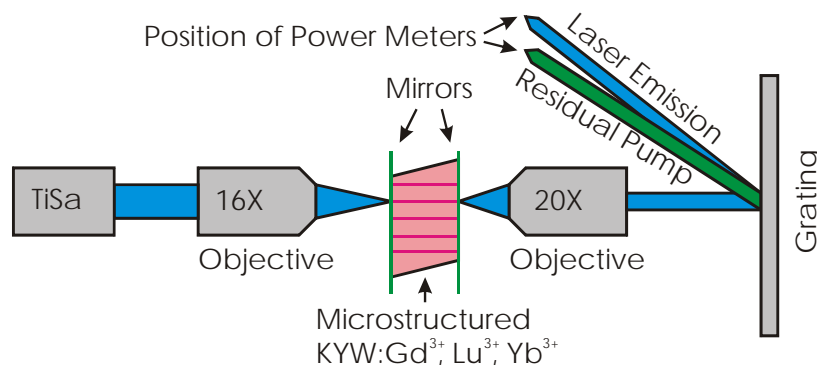
Fig. 5.2. Schematic of experimental setup used for characterization of the channel waveguide lasers.

A reflective grating was used as a dispersive element to separate the residual transmitted pump light from the laser emission. A schematic of the setup is shown in Fig. 5.2.

5.2.2. *Laser performance*

At the laser wavelength near 1028 nm the incoupling mirror had a reflectivity of 99.8%, while for the outcoupling mirror transparencies of 2%, 5%, 10% and 23% were tested. Fig. 5.3 shows the laser output power as a function of launched pump power. For the smallest outcoupling efficiency of 2%, laser oscillation commenced at a launched pump power as low as 4.5 mW. The laser threshold increased to a value of 5.5 mW for the largest outcoupling efficiency of 23%. Due to the low threshold which clamped the excitation of the upper laser level to a rather low excitation density, resulting in only a small fraction of ground-state bleaching, as well as the rather long waveguide length approx. 99% of the launched pump power was absorbed in the channel. Slope efficiencies of 11%, 23%, 53% and 62% versus launched pump power and maximum extracted laser powers of 13 mW, 24 mW, 61 mW and 76 mW were obtained for 2%, 5%, 10% and 23% output coupling, respectively.
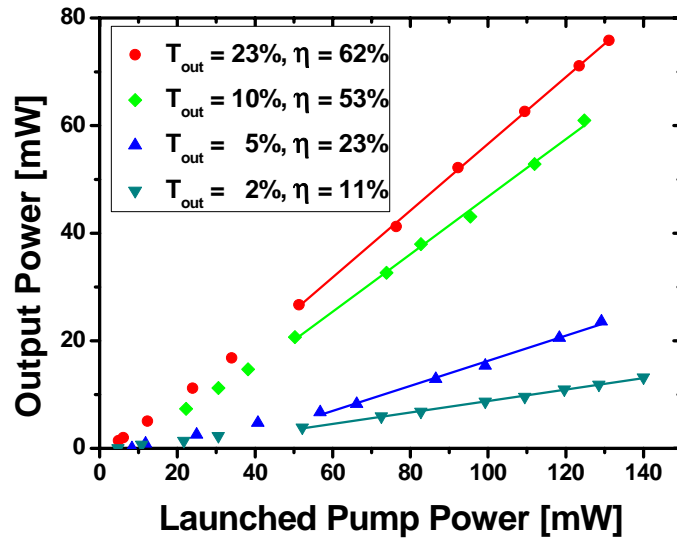
Fig. 5.3. Measured output power of a $KY_{0.4}Gd_{0.433}Lu_{0.167}(WO_4)_2$:(1.7%)$Yb^{3+}$ buried channel waveguide (sample A) as a function of launched pump power (approximately 99% of the launched pump power was absorbed) for different transmission values T_{out} of the outcoupling mirror.

An image of the near-field mode profile of the laser emission was recorded by a CCD-camera (Moticam) using the available ×20 objective lens and the reflective grating to separate the laser emission from the residual pump light. The recorded mode profile is depicted in the overlay of Fig. 5.1 to show the strong light confinement in the ridge waveguide. Fig. 5.4 depicts the Gaussian fit of the intensity profile in both, horizontal and vertical directions, providing a beam size (e^{-2}) of 4.8 × 2.1 μm^2.
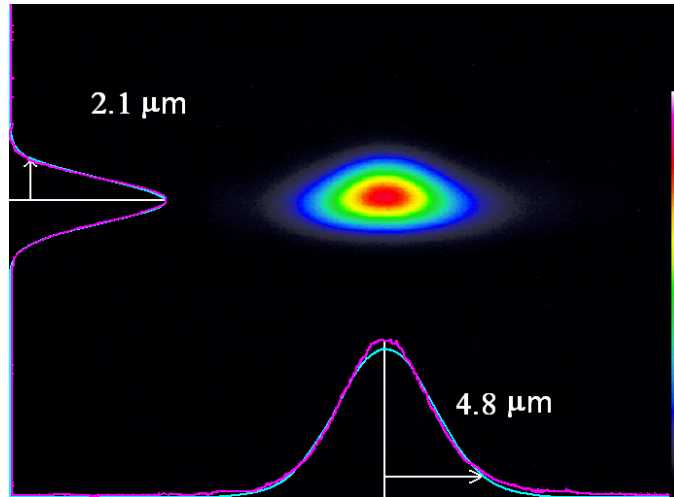
Fig. 5.4. Measured mode profile of the laser emission of sample A.

According to simulations with mode solver software (Phoenix FieldDesigner [pho]), the tested waveguide of 7 μm width supports 2 propagating modes; hence we assume that the laser output is transverse multi-mode. The ridge waveguide geometry causes the triangular shape of the guided mode. An intracavity roundtrip loss of 11% is derived, when analyzing the obtained slope efficiencies versus output coupling according to the theory for laser devices exhibiting reabsorption [ris88], as discussed earlier in Section 3.4.2. However, using the linear form of Eq. 3.16 does not provide a reliable fit to the measured data, due to a lower experimental accuracy, caused by a more critical coupling of the mirrors to the end-facets of the channel waveguides as compared to the planar waveguide laser experiments. Therefore, the non-linear form (left hand relation of Eq. 3.16) and the predicted internal efficiency of η_0 = 94% for this channel waveguide configuration (Section 3.4.2) is used to estimate the roundtrip loss. The result is presented in Fig. 5.5.
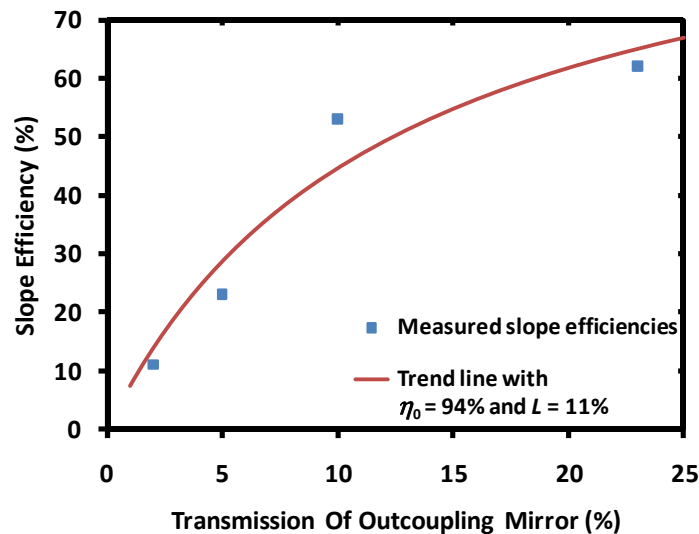
Fig. 5.5. Slope efficiency as a function of transmission of the outcoupling mirror. The solid line is a fit based on values obtained with the outcoupling mirrors with transmission values of 2%, 5%, 10% and 23% according to the left hand relation of Eq. 3.16. Here a fixed value for η_0 = 94% was used, resulting in a roundtrip loss of L = 11%.

This value includes the waveguide propagation losses and losses occurring due to butt-coupling of the mirror substrates to the end-facets. Therefore, the value of 11%, equaling 0.34 dB/cm, is the upper limit for the propagation loss at 1028 nm in the microstructured channel waveguide.

5.3. Tweaking the emission: High-power, broadly tunable and low quantum defect KGd$_x$Lu$_{1-x}$(WO$_4$)$_2$:Yb^{3+} channel waveguide lasers

5.3.1. Sample fabrication

The composition of the active layer was designed with Y completely replaced by the co-dopants Gd^{3+}, Lu^{3+} and Yb^{3+} to provide a maximum refractive index difference of 1.5×10^{-2} between layer and substrate. The composition of the buried ridge waveguide was KGd$_{0.49}$Lu$_{0.51}$(WO$_4$)$_2$:(2.5%)Yb^{3+}, having a thickness of 5 μm and a width of 7 μm and it supports only the fundamental mode around 1 μm. The cavity length was 6.6 mm. This device is referred as sample B.

5.3.2. Extraction of 418 mW at 1023 nm from a channel waveguide laser

The sample was placed on an aluminum mount without active cooling, indicating possible further power scaling by actively cooling of the sample. Pump light at 980.6 nm from a broadly tunable Ti:Sapphire laser was end-coupled by a ×16 microscope objective into the waveguide. The light outcoupled at the other end of the waveguide was collimated by a ×20 microscope objective. A reflective grating was used to separate the residual transmitted pump power from the laser emission and the laser light was directed to a powermeter or a spectrometer. At the input side a dielectric mirror with a high transmission of $T = 96\%$ for the pump light and a high reflectivity of $R = 99.8\%$ for the laser light was directly butt-coupled to the end-facet with fluorinated oil (Fluorinert FC70). An outcoupling mirror with $T_{out} = 70\%$ at 1023 nm was attached to the other side. A schematic of the experimental setup is shown in Fig. 5.6 (a). We obtained a maximum laser output power of 418 mW at 1023 nm, limited only by the available pump power, with a slope efficiency of 71% versus launched pump power, see Fig. 5.6 (b). The threshold was 40 mW. Almost no residual pump light was observed at the output, as 99% of the launched pump power was absorbed in the slightly too long waveguide.
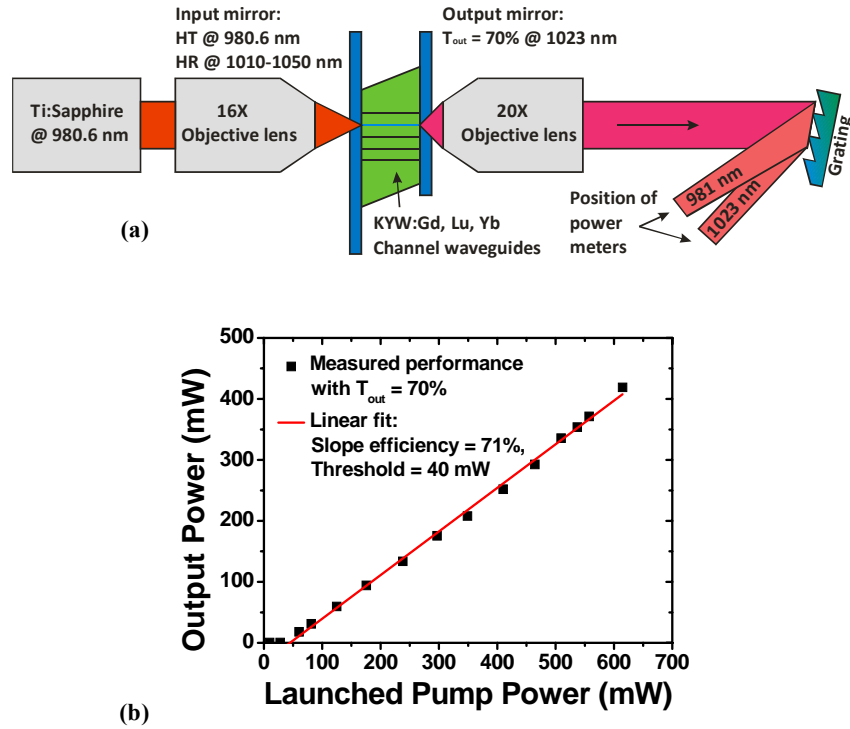
Fig. 5.6. (a) Schematic of experimental setup for high laser output power; (b) input-output curve of the KGd$_{0.49}$Lu$_{0.51}$(WO$_4$)$_2$:(2.5%)Yb^{3+} channel waveguide laser (sample B) pumped at 980.6 nm and lasing at 1023 nm.

5.3.3. Tuning the emission wavelength

To achieve broad wavelength tunability of the laser output, an incoupling mirror with ~99.8% reflectivity from 980 nm to 1050 nm was attached to the incoupling side. The transmission of this mirror steeply increased below 932 nm, hence a short pump wavelength of 930 nm was chosen. The outcoupling mirror was removed and the cavity extended by collimating the output with a ×20 microscope objective and directing it onto a grating (576 l/mm, blazed at 23.5°) such that the first order diffraction is redirected into the cavity (i.e. Littrow configuration). Hence a strongly wavelength-selective feedback is provided by the grating. A schematic of the experimental setup is shown in Fig. 5.7 (a).
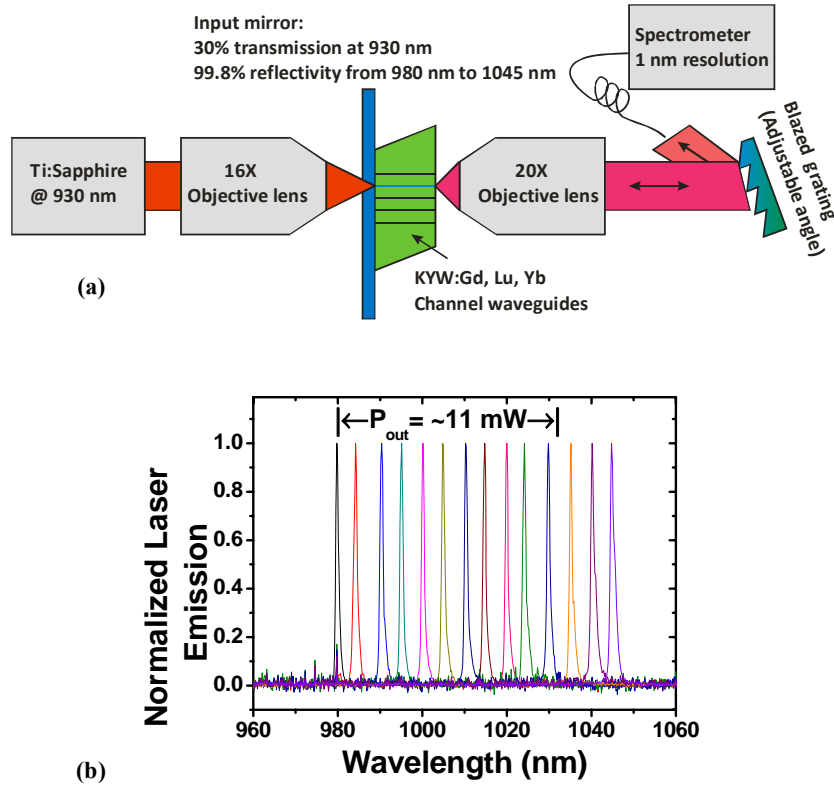
Fig. 5.7. (a) Schematic of experimental setup for tuning the laser emission by extension of the cavity with a reflective grating in Littrow configuration; (b) measured emission spectra under pumping at 930 nm when changing the angle of the reflective grating.

By rotation of the grating the emission wavelength could be continuously tuned from 980 nm to 1045 nm, see Fig. 5.7 (b). With 120 mW of launched pump power at 930 nm, output powers of approximately 11 mW were measured from the 2nd order of the grating in the wavelength range 980-1033 nm. The emission dropped gradually when tuning the laser to 1045 nm, followed by operation at 980 nm when further rotating the grating. The intracavity loss in this experiment is estimated to be up to 50% due to non-optimal optical elements; therefore, the threshold is high and the slope efficiency small. An even larger tuning range, extended towards longer wavelengths, is expected in cavities with lower loss [jac08].

5.3.4. *Small quantum defect of 0.7%*

In a third experiment, laser operation with a record-low quantum defect was demonstrated. The mirror at the incoupling side was removed and a mirror with a reflectivity of 97% at 980 nm was butt-coupled to the other waveguide end. In this situation, laser emission at a wavelength of 980 nm was extracted from the pumped side. The experimental setup is shown in Fig. 5.8 (a). Remarkably, the laser continuously oscillated at 980 nm while tuning the excitation wavelength from 910 nm to 973 nm. The spectrum in the latter pump-wavelength setting is displayed in Fig. 5.8 (b), resulting in a record-low quantum defect of only 0.7%. Low quantum defect laser operation is of special interest for the development of high power laser devices, since it provides minimal heat dissipation in the device.
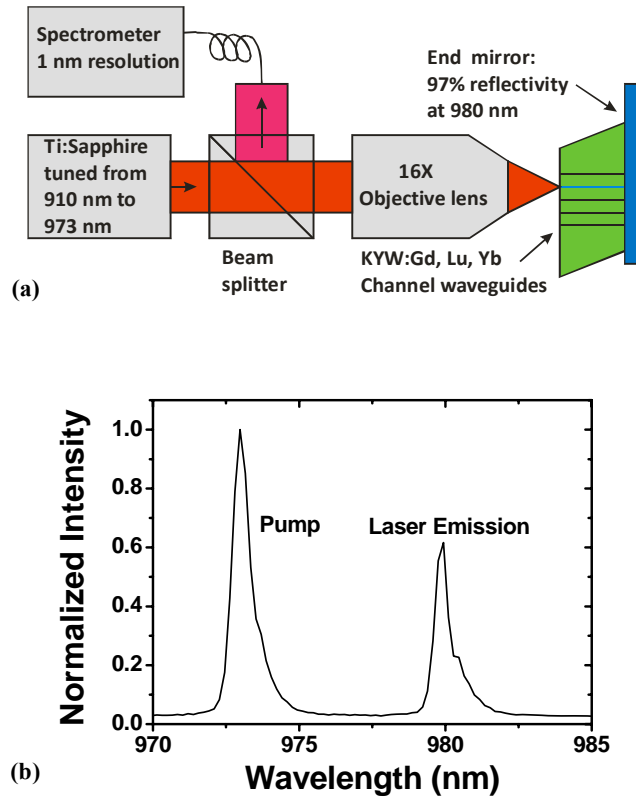
Fig. 5.8. **(a) Schematic of experimental setup for the demonstration of low quantum defect lasing. (b) Recorded spectrum during lasing with the smallest attained quantum defect.**

5.4. Highly efficient channel waveguide laser at the zero-phonon line of Yb^{3+}

5.4.1. *Sample fabrication*

For these experiments both sample A and B were used, having a waveguide length of 7.0 mm (re-polished from 7.5 mm after previous investigations when lasing at 1028 nm, see Section 5.2) and 6.6 mm, respectively.

5.4.2. *Introduction to zero-phonon line lasing*

The ZPL of absorption and emission between two crystal-field multiplets is the transition involving the lowest Stark level of each multiplet. Due to the large Boltzmann population of this Stark level and the selection rules that apply to the individual transitions, the ZPL is often the transition with the largest effective absorption and emission cross-section. Fig. 5.9 (a) shows the energy level scheme, indicating the relevant transitions and Fig. 5.9 (b) shows the absorption and emission spectra of $KY_{0.40}Gd_{0.433}Lu_{0.167}(WO_4)_2{:}(1.7\%)Yb^{3+}$ with the dominant ZPL at 981 nm.
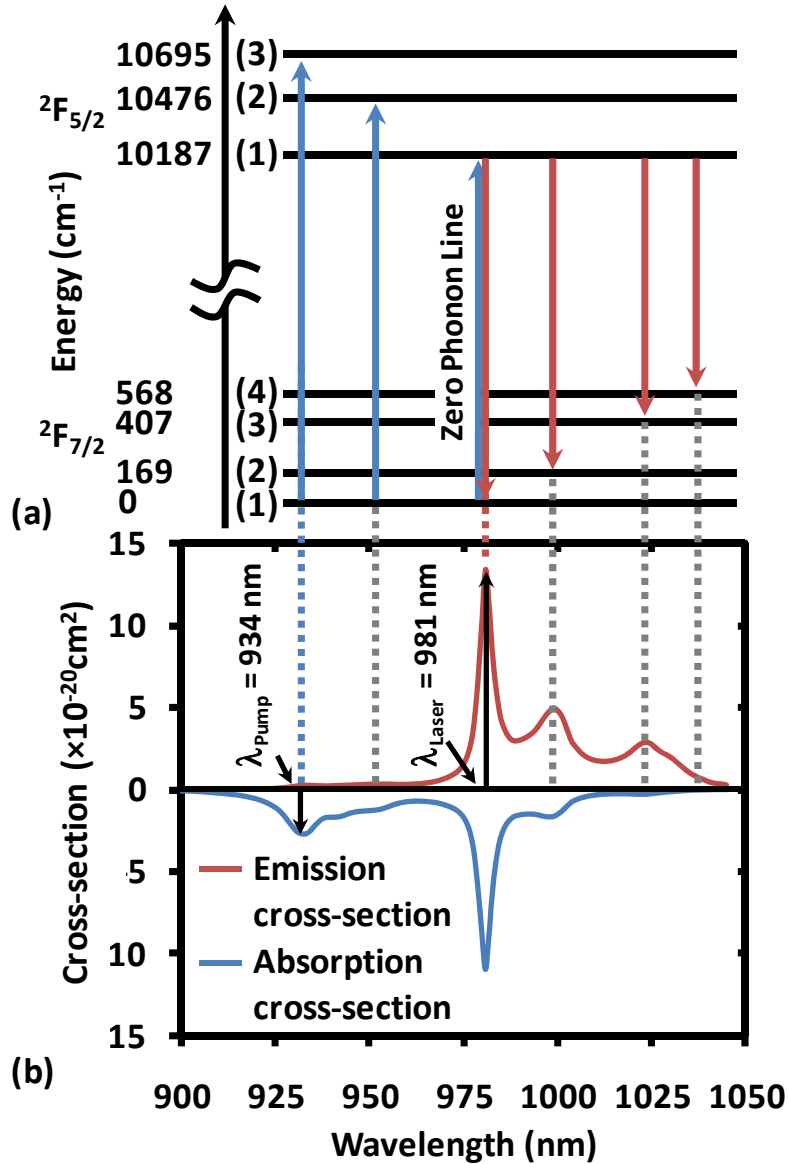
Fig. 5.9. (a) Yb^{3+} $^2F_{5/2}$ and $^2F_{7/2}$ electronic multiplets with Stark-level energies in KY(WO$_4$)$_2$ and transitions from the lowest, highly populated Stark level of each multiplet [kule97]. (b) Corresponding transition wavelengths within the emission and absorption cross-section spectra of KY$_{0.40}$Gd$_{0.433}$Lu$_{0.167}$(WO$_4$)$_2$:(1.7%)Yb^{3+} in correspondence to the composition of sample A, as discussed in Section 3.2.

5.4.3. Analysis of laser threshold for different transitions

While an ideal four-level laser would naturally operate on the ZPL, because the highest emission cross-section provides the lowest laser threshold, typical three-level laser transitions, such as the Nd^{3+} 0.9 µm, Yb^{3+} 1 µm, Er^{3+} 1.5 µm, Tm^{3+} 1.9 µm, Ho^{3+} 2.1 µm and Dy^{3+} 3 µm transitions, usually operate at longer wavelengths because of the strong reabsorption at the ZPL. However, with decreasing reflection $R_{out} = R_1R_2$ of the two cavity mirrors, the laser shifts toward shorter wavelengths and can ultimately oscillate on the ZPL [dal11]. This shift of laser wavelength can be examined by deducing the threshold excitation density N_2 from the round-trip equation for the intra-cavity photon number in ground-state lasers:

$$(1-2\alpha\ell)R_{out}\exp\left\{2\ell\Gamma\left[b_{2i}N_2-b_{1j}(N_d-N_2)\right]\sigma_{2i\leftrightarrow1j}\right\}=1$$

$$\Rightarrow N_2=\frac{-\ln\left[(1-2\alpha\ell)R_{out}\right]/\left(2\ell\Gamma\sigma_{2i\rightarrow1j}\right)+b_{1j}N_d}{\left(b_{2i}+b_{1j}\right)}.\qquad(5.1)$$

When making the threshold analysis for these devices it appeared that the emission cross-sections for KYW:Yb^{3+} given in [kule97] did not confirm the observed behavior. Further investigations revealed overestimated emission cross-section provided in this reference. Using the same methodology proposed by Kuleshov et al. to interpret their measured absorption cross-sections resulted in reliable data, showing great similarities with the data presented by [liu01]. In this work, lasing of a composite host material based on KY(WO$_4$)$_2$, KGd(WO$_4$)$_2$, KLu(WO$_4$)$_2$ and KYb(WO$_4$)$_2$, is demonstrated. The emission and absorption spectra of the stoichiometric compositions have been convoluted to predict the resulting spectroscopic features as accurately as possible. The details of this method to predict the spectroscopy composite host material is discussed in Section 3.2. The parameters used to estimate the laser threshold are given in Table 5.1.

Table 5.1. Data used to estimate the threshold excitation densities of the emission lines indicated in Fig. 5.9 (a) in the investigated KY$_{0.40}$Gd$_{0.433}$Lu$_{0.167}$(WO$_4$)$_2$:(1.7%)Yb^{3+} channel waveguide.

Quantity	Parameter	Value
Dopant concentration	N_d	1.08×10^{20} cm^{-3}
Mode overlap with active waveguide geometry	Γ	0.82
Waveguide length	ℓ	0.66 cm
Propagation loss	α	0.34 dB/cm
Boltzmann factors at 300 K	b_{21}	0.748
	b_{14}	0.040
	b_{13}	0.086
	b_{12}	0.269
	b_{11}	0.605
Effective emission cross-sections from Fig. 5.9 (b)	$\sigma_{21\leftrightarrow14}\times b_{21}$	1.34×10^{-19} cm^2
	$\sigma_{21\leftrightarrow13}\times b_{21}$	0.50×10^{-19} cm^2
	$\sigma_{21\leftrightarrow12}\times b_{21}$	0.29×10^{-19} cm^2
	$\sigma_{21\leftrightarrow11}\times b_{21}$	0.05×10^{-19} cm^2

For transitions with small cross-sections, the first term in the nominator becomes relevant and the threshold increases drastically with increasing R_{out}, while for the ZPL with its large cross-section the threshold is only weakly influenced by R_{out}. For the four emission transitions indicated in Fig. 5.9 (a), the corresponding threshold excitation densities N_2, estimated from Eq. (5.1) with the values given in Table 5.1, change in such way that the laser wavelength shifts from 1025 nm at low R_{out} to the ZPL at high R_{out} (Fig. 5.10). Nevertheless, only by intense pumping at shorter wavelengths one can achieve the high excitation densities of >50% required to operate a laser at the ZPL (Fig. 5.10), as has been observed experimentally in KY(WO$_4$)$_2$:Yb^{3+} bulk crystals [bou05].
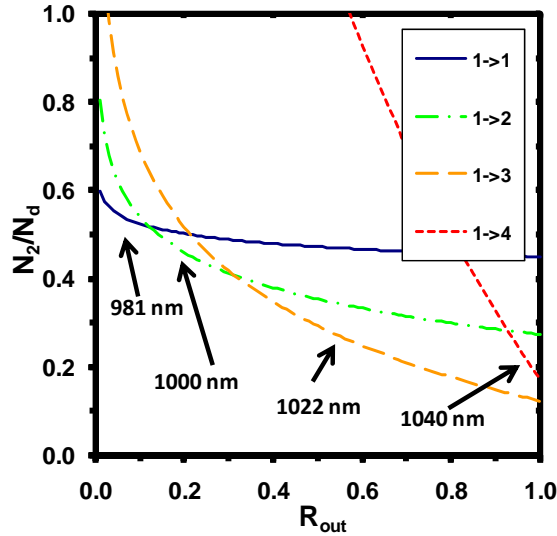
Fig. 5.10. Relative threshold excitation densities of the emission lines indicated in Fig. 5.9 (a) in the investigated $KY_{0.40}Gd_{0.433}Lu_{0.167}(WO_4)_2:(1.7\%)Yb^{3+}$ channel waveguide of sample A as a function of R_{out}, estimated from Eq. 5.1 and the values given in Table 5.1.

5.4.4. *Zero-phonon line lasers in the literature*

The attractiveness of lasing at the ZPL becomes apparent in integrated waveguides. Firstly, like in ZPL fiber lasers [ros08], the required high inversion can easily be achieved due to the strong pump light confinement and, consequently, high pump intensity. Secondly, the large gain obtained in this regime can establish threshold inversion in cavities with low reflectivity, such as waveguides with integrated, short Bragg gratings (see Chapter 6), ring cavities with integrated directional couplers [bra10], cavities with one open waveguide end [kuh09], or entirely mirror-less cavities based solely on the Fresnel reflection at both waveguide end-facets [sie10, bol10]. Thirdly, while the propagation losses in integrated waveguides are typically high and contribute a significant fraction to the total cavity losses, the low R_{out} required to operate the laser at the ZPL increases the fraction of useful cavity losses, thereby enhancing the slope efficiency. By exploiting the latter fact, we demonstrated waveguide lasing with a slope efficiency of 76% versus absorbed pump power, which to the best of our knowledge, represents the highest slope efficiency reported for any rare earth ion doped microstructured channel waveguide laser to date.

5.4.5. *Experimental setup*

The waveguides were end-pumped by a continuous-wave Ti:Sapphire laser operating at ~934 nm with its polarization parallel to the N_m axis. The pump laser was chopped with a 50% duty cycle at a frequency of 200 Hz. Pump light was coupled into the channel waveguide with a ×16 objective lens with a numerical aperture (N.A.) of 0.32. With a variable beam expander in the pump-beam line the pump mode was adapted to the slightly lower N.A. of the channel waveguides. By use of mode-solver software (Phoenix FieldDesigner [pho]) a coupling efficiency of 88% and 82% (without Fresnel reflection) was calculated for the pump light, of which ~62% and ~80% was absorbed in sample A and B, respectively. The waveguide geometries and calculated [pho] fundamental laser modes are presented in the insets of Fig. 5.11. Besides, sample A supports propagation of a weakly confined higher-order laser mode.

The cavity of sample A was formed by the 11% Fresnel reflection at the pumped waveguide end-facet and a mirror with 97% reflectivity at 981 nm butt-coupled to the other end-facet by fluorinated oil (Fluorinert FC-70). The emitted laser light was collected from the pumped end via a beam splitter placed into the pump beam. A reflective grating was used to separate the laser emission from residual pump light. The cavity of sample B was formed by the Fresnel reflections from both waveguide end-facets. Here, the emitted light was monitored only from the non-pumped end-facet in order to launch the maximum available pump power. The measured emitted power was multiplied by a factor of two to account for emission from the pumped side. This is a conservative estimation, since counter-propagating laser light is more efficiently amplified than co-propagating laser light.
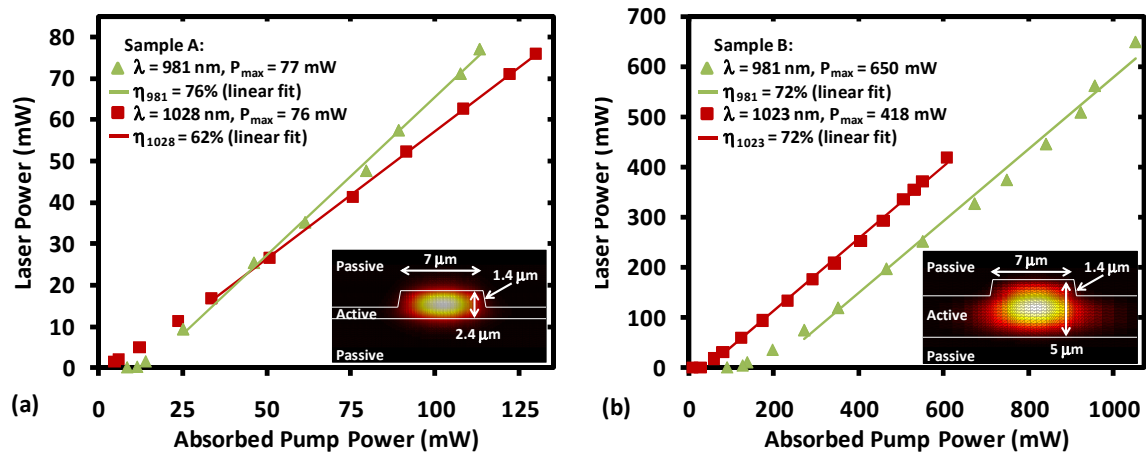
Fig. 5.11. Measured power characteristics of the waveguide laser devices based on (a) sample A and (b) sample B. The insets show the modeled fundamental-mode profiles in these structures.

5.4.6. Laser performance

The measured laser performance at the ZPL, displayed as green triangles in Fig. 5.11 (a, b), reveals slope efficiencies of 76% and 72% (green solid lines) versus absorbed pump power and maximum output powers of 77 mW and 650 mW for sample A and B, respectively. The laser emission spectrum from sample B was analyzed by a spectrometer (Jobin-Yvon iHR550) with a resolution of 0.11 nm. The emission peak occurs at a wavelength of 981 nm with a width of 0.5 nm, see Fig. 5.12.
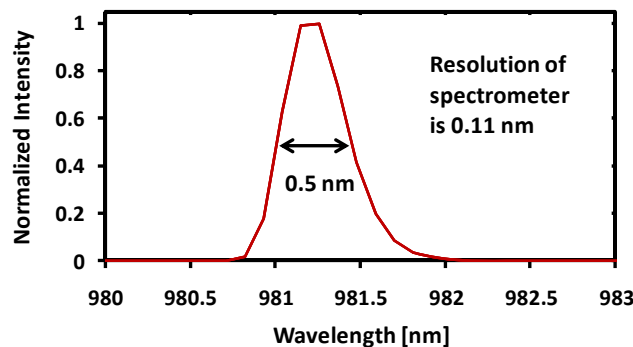
Fig. 5.12. Measured laser emission spectrum of sample B, obtained by a spectrometer (Jobin-Yvon iHR550) with a resolution of 0.11 nm. The emission peak occurs at a wavelength of 981.2 nm with a width of 0.5 nm.

Despite the stronger reabsorption, similar or larger slope efficiencies are obtained at the ZPL compared to laser performance of the samples at longer wavelengths (Fig. 5.11, red squares). This is mainly caused by the large outcoupling efficiency. The latter experiments were performed by pumping at 981 nm, using butt-coupled mirrors on both waveguide ends with reflectivities of 99.8% and 77% at 1028 nm (sample A) or 99.8% and 30% at 1023 nm (sample B), resulting in slope efficiencies of 62% and 71%, respectively.

5.5. Conclusions

Demonstration of the first microstructured double tungstate channel waveguide laser, discussed in Section 5.2, reveals the advantages of excellent control over the lateral waveguide dimensions. This lateral confinement of pump and laser mode, in combination with the high absorption and emission cross-sections present in Yb^{3+}-doped double tungstates, makes it an attractive high-gain laser, resulting in low laser thresholds down to 4.5 mW and large slope efficiencies up to 62% versus launched pump power. From this laser performance an upper limit of the propagation loss in the channel waveguide structure of 0.34 dB/cm is estimated. The refractive index difference between layer and substrate is even further enhanced to 1.5×10^{-2} by complete replacement of the Y^{3+} component by Gd^{3+} and Lu^{3+} ions, in Section 5.3. Here the full potential of the waveguide is explored, revealing a slope efficiency of 71% versus launched pump power and a maximum output power of 418 mW at 1023 nm. In addition, the emission wavelength was tuned over a wavelength range of 65 nm from 980-1045 nm using an external grating, hence demonstrating a large fraction of the extremely large emission bandwidth supported by the Yb^{3+} doping. This large bandwidth, combined with a short cavity length and very high laser intensity oscillating in the waveguide, makes this device an excellent candidate for high-repetition-rate ultrashort-pulse generation on a chip.

Moreover, tuning of the pump wavelength towards the laser wavelength in an half-open cavity configuration resulted in demonstration of a low quantum defect of 0.7%, which is of great interest for the development of high power lasers.

When replacing a large part of the Lu^{3+} ions with Yb^{3+} ions of almost the same ionic radius in the active layer, the absorption length at 980 nm can be reduced to much less than 100 μm, allowing one to move from a single-mode-diode end-pumping to a diode-array side-pumping configuration. Such a side-pumped scheme, combined with the ultra-low quantum defect and accordingly small heat generation, promises to be a great step forward toward efficient integrated waveguide lasers emitting large single-mode output powers far beyond 1 W. In addition, integrated distributed feedback (DFB) waveguide lasers without active wavelength stabilization have recently produced a linewidth of 1.7 kHz at 3 mW of output power [ber10]. The linewidth narrows linearly as the laser power increases, hence the output power obtained in this work would bring about a DFB laser with an ultra-narrow linewidth in the range of 10-20 Hz. The minimal thermal load is also of great advantage for the wavelength stability of such ultra-narrow linewidth lasers.

The large gain found at the ZPL around 980 nm when pumped at shorter wavelengths of about 930 nm, presented in Section 5.4, resulted in laser oscillation at 981.2 nm in partly and fully open cavities. These large outcoupling efficiencies reduce the adverse influence of the fairly large intracavity propagation loss on the laser performance. This resulted in a large

slope efficiency of 76% and a total extracted laser power of 650 mW.
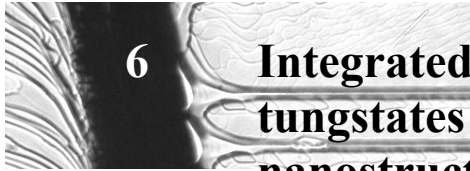
6   Integrated lasers in crystalline double tungstates with focused-ion-beam nanostructured photonic cavities

Deeply etched Bragg gratings were fabricated by focused ion beam (FIB) milling in $KGd_xLu_{1-x}(WO_4)_2:Yb^{3+}$ to obtain photonic cavity structures. By optimizing parameters such as dose per area, dwell time and pixel resolution the re-deposition effects were minimized and grating structures more than 4 μm in depth with an improved sidewall angle of ~5° were achieved. Fabry-Perot micro cavities were defined and used to assess the optical performance of the grating structures at ~1530 nm. An on-chip integrated laser cavity at ~980 nm was achieved by defining a FIB reflective grating and FIB polished waveguide end-facet. With this cavity, an on-chip integrated waveguide laser in crystalline potassium double tungstate was demonstrated.

The idea for the fabrication of deeply FIB-milled Bragg grating structures cross-sectioning the complete thickness of the active waveguide was picked up after attending a presentation about on-chip resonators in using deeply etched distributed Bragg reflectors (DBR) in semiconductor optical amplifiers (SOA) given by Dr. Boudewijn Docter, which was later published in [doc10]. This project to obtain deeply FIB-milled Bragg grating structures in $KGd_xLu_{1-x}(WO_4)_2:Yb^{3+}$ waveguides was then lead by Dr. Feridun Ay, who conducted the simulations to obtain optimal FIB structures, measured the cavity loss and guided the FIB optimization study that was carried out by Ion Iñurrategui, Dr. Vishwas Gadgil and Henk van Wolferen.

6.1.   Introduction

The increasing interest in patterning materials at the nano-scale provides major challenges, but also stimulates the development of innovative techniques and technologies. Focused ion beam (FIB) milling has been used for more than a decade in the microelectronics industry. The attractiveness of this method in the area of photonics has only recently been recognized [rei98, ger05, hop07]. The main motivation for applying this technology stems from the need for nanostructuring materials or material combinations that are hard to etch by use of more conventional methods such as those based on e-beam lithography or holography. Moreover, in comparison to other technologies for nanofabrication, FIB has the advantage of enabling fast prototyping, thereby considerably reducing the design-fabrication-characterization cycle time.

For miniaturization and full integration of such technologies, the development of high-quality micro- and nanostructuring processes is required. 1D and 2D photonic crystal structures have been extensively investigated for manipulating light and enabling densely integrated circuits. To date, most implementations of micro- and nanostructuring have been realized by a combination of specifically optimized processes of electron-beam lithography and reactive ion etching (RIE) [oka96, bog04, pru07]. Chapter 4 presents the obtained microstructures using both RIE and IBE in combination with standard lithography, however this technology does not allow for accurate fabrication of sub μm sized features with etch depths up to 5 μm

which is required for fabrication of the on-chip optical resonators devices discussed in this chapter. The increasing variety of materials used in photonic applications has created a growing demand for a material-independent nano-patterning tool. FIB milling is emerging as such an alternative method for nano-structuring in photonics, as it involves physical removal of a material by a beam of ions, hence making the method adaptable to almost any material system. FIB has already been applied to defining photonic components in several materials such as Si and Si_3N_4 [ger05, hop07].

This chapter reports about the utilization and optimization of the FIB technique for the fabrication of grating structures for integrated photonic devices in a double tungstate channel waveguide. An optimization study for achieving a sufficient grating aspect ratio in $KGd_xLu_{1-x}(WO_4)_2:Yb^{3+}$ by controlling the re-deposition of material during the milling process is presented. Finally, we investigate the optical performance characteristics of the fabricated grating structures and demonstrate a functional on-chip laser device.

6.2. Experimental

$KGd_{0.491}Lu_{0.509}(WO_4)_2:(2.5\%)Yb^{3+}$ layers were grown by liquid phase epitaxy onto undoped, (010)-orientated, laser-grade polished KYW substrates (see Section 2.2). This composition has no Y^{3+} in the active waveguide and provides a maximal refractive index difference between guiding layer and substrate of $\sim 1.5 \times 10^{-2}$ (see Section 2.4). The maximal index contrast minimizes the size of the mode field and the waveguide thickness hence reducing required etch depth for complete cross-sectioning of the waveguide using FIB etching. As indicated in Fig. 6.1, the active film thickness was $t = 1.92$ μm, etched down by a depth of $h = 1.2$ μm using Ar^+ milling according the etch recipe provided in Section 4.5. The resulting ridge waveguides were aligned along the N_g optical axis of the material and had widths of about 6 μm. Finally, a 1-μm-thick Si_3N_4 film was deposited by plasma-enhanced chemical vapor deposition as a top cladding layer to increase the overlap of the optical mode with the active waveguide region.
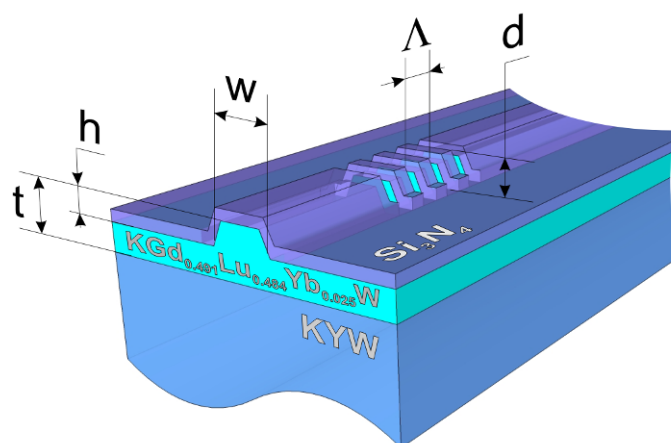
Fig. 6.1. Schematic of the $KGd_xLu_{1-x}(WO_4)_2:Yb^{3+}$ channel waveguide and grating structure geometries. A waveguide of thickness t is etched to depth h, resulting in waveguides with width w. The grating period and milling depth are indicated as Λ and d, respectively.

6.2.1. General focused-ion-beam milling settings

The grating structures on $KGd_xLu_{1-x}(WO_4)_2$:Yb^{3+} channel waveguides were realized using a FEI Nova 600 dual beam FIB machine. The acceleration voltage for the Ga^+ ion source was set to 30 kV. The milling current was varied between 93 pA and 280 pA during the experiments. The gratings were milled using a predefined mask file (stream file) that contains milling time, pixel information, and pixel sequence for the desired geometry. The milling parameters were optimized in order to achieve optimum nanostructuring. Control of the stationary time of the ion beam on each pixel, i.e. dwell time, and the number of repetitive passes for the whole pattern, i.e. number of loops, is critical. The dose per area, defined by the total current dwell time averaged over the milled area, was monitored to account for the re-deposition effects. Finally, to avoid charging of the structures a Pd/Au layer with a thickness ranging from 30 to 100 nm was sputtered on top of the Si_3N_4 cladding layer.

6.2.2. Cross-sectioning

In order to analyze the effect of milling parameters on the sub-µm grating structures, the technique for creating cross-sections of the milled structures was optimized. The cross-sectioning was done in situ using the same FIB machine that produced the grating structure. The optimized method started with local FIB-induced deposition of a Pt layer on top of the region of interest in order to prevent re-deposition when milling the cross-section and to provide a contrast for scanning electron microscopy (SEM) imaging. The next step involved milling a large-area hole with a sloped angle to avoid long milling times. Finally, a line-by-line scan (termed cleaning cross-section) was applied at a lower current (typically 28 pA) to facilitate a high contrast image, as depicted in Fig. 6.2. Analysis of the cross-sectional profile of the grating structures was performed by use of SEM available in the same machine.
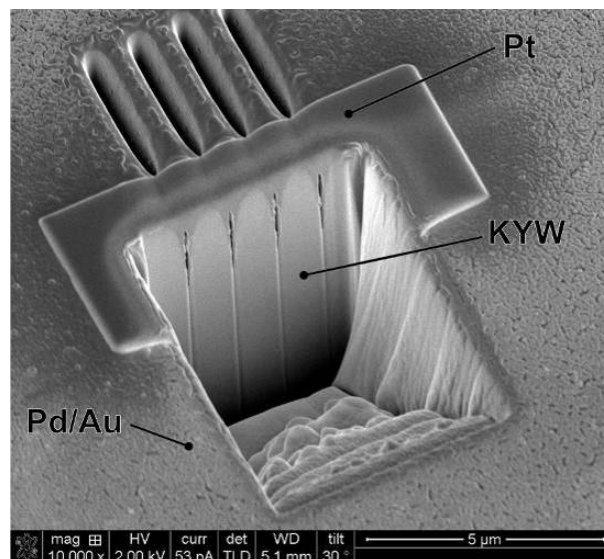
Fig. 6.2. Example of a SEM cross-sectional imaging procedure used to assess the milling quality of Bragg gratings in KYW.

6.3. Focused-ion-beam milling optimization

6.3.1. Requirements of the grating structures

Deep gratings of several micrometers depth are necessary for fully etching through the whole waveguide cross-section to obtain the required effective refractive index contrast. Deep grating structures enable a better overlap between the optical mode and the active layer. Furthermore, a smaller number of periods are required to obtain the same amount of light reflection in the grating.

Realization of straight grating sidewalls is the other important aspect of the milling process. Straight sidewalls are desired for minimizing the out-of-plane losses [kra96]. Both, large depth and straight sidewalls demand for a good control over the re-deposition of material taking place during the milling process.
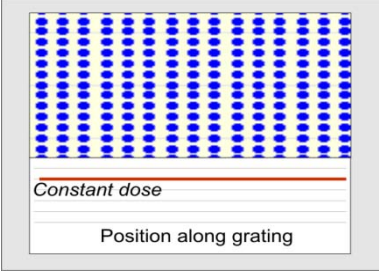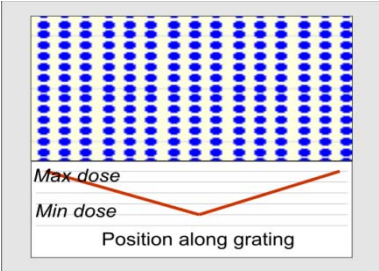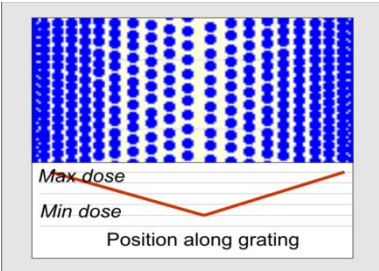
Phoenix Opto Designer and Phoenix Field Designer [pho] were used to simulate the optical performance of gratings and determine the optimum grating dimensions for the fabricated $KGd_xLu_{1-x}(WO_4)_2:Yb^{3+}$ channel waveguides. The milled grating structures targeted the realization of third-order gratings. Two different grating periods of 0.89 and 1.22 µm, each with a total length of ~4.48 µm, were defined for testing at wavelengths around 0.98 and 1.53 µm, respectively.

6.3.2. Milling-depth optimization

Initial experiments focused on achieving high milling depths in $KGd_xLu_{1-x}(WO_4)_2:Yb^{3+}$ within a short fabrication time to minimize potential drifts of the ion beam. Based on our previous work [ay08], ion beam scanning parallel to the grating structures was employed. Two ion beam currents of 93 pA and 280 pA were tested. The higher value allowed a shorter total milling duration of 20 minutes, which is within the stable duration of the ion beam. Keeping the 280 pA current, the ion dose was increased by increasing the number of loops and keeping the dwell time fixed at 0.005 ms. Increasing the ion dose per area increased the milling depth, as expected (see Table 6.1, experiment A). However, this increase was not linear, as the grating depth was strongly affected the by re-deposition of material during milling. Table 6.1 shows the results. A sample cross-sectional image of the experiment A1 is given in Fig. 6.3 (a).

The second part, involving experiments B and C of Table 6.1, focused on reducing the re-deposition effect during the milling process. The stream file contained the design of the pathway by which the gratings were milled on the waveguide. A re-distribution of the pixel locations and variation of dwell time was implemented along each grating period. The goal of experiment B was to reduce the re-deposition effect by varying the dwell time per pixel, without increasing the dose per area, in order to optimize the milling process for steep sidewalls. The dwell time and pixel resolution increment at the sidewalls was compensated by a loop repetition decrement. The dwell time was varied linearly from a maximum value at the grating sidewalls to a minimum value at the center. This procedure leads to a higher dose per area near the sidewalls. In an alternative approach, experiment C, the pixel location was linearly re-distributed such that the pixel density was larger near the sidewalls than in the center (see the schematics in Table 6.1).

Table 6.1. Overview of optimization experiments of the milling parameters. The figures indicate the pixel distribution and ion dose variation along the grating position for each experiment

Experiment	Ion current and dose variation	Dose/Area (pC/µm^2)	Depth (µm)
A1		7203	3.21
A2		15491	3.36
A3		36146	4.27

Experiment	Dwell time distribution	Dwell time variation (ms)	Depth (µm)
B1		0.003 – 0.007	4.07
B2		0.003 – 0.01	4.45
B3		0.003 – 0.7	4.06

Experiment	Pixel distribution	Pixel step size	Depth (µm)
C1		20	4.27
C2		10 -20	4.24
C3		1 – 20	4.37

Both, approaches B and C resulted in a reduced re-deposition effect and, therefore, steeper sidewalls compared to the initial dose distribution of experiment A. For these experiments the total dose per area was ~33000 pC/µm^2. Fig. 6.3 shows the cross-sectional SEM images of three samples with grating structures. The black holes are due to the gratings being incompletely filled with Pt. The grating structure of Fig. 6.3 (a) was milled with a standard stream file with constant dose distribution. For the grating structure depicted in Fig. 6.3 (b, c) we applied the optimization processes of experiments B and C, respectively.
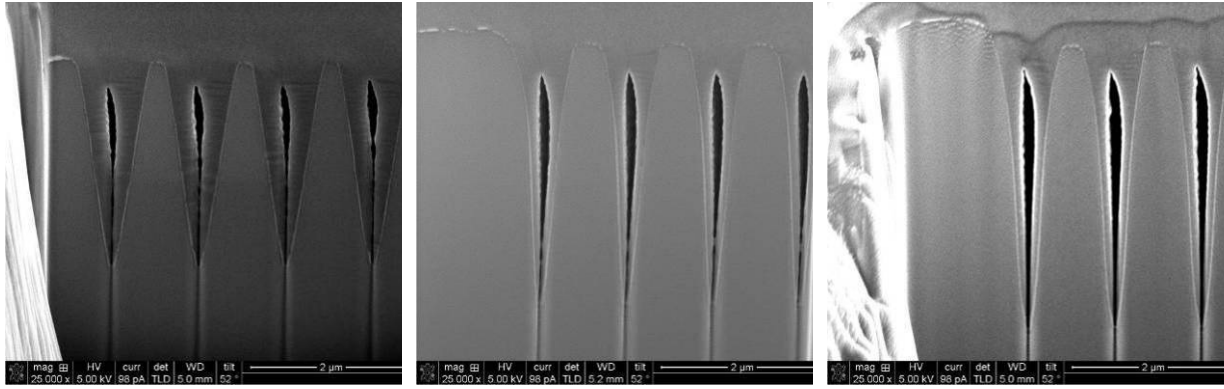
| (a) | (b) | (c) |

Fig. 6.3. SEM cross-sectional images of the grating structures defined in KGd$_x$Lu$_{1-x}$(WO$_4$)$_2$:Yb^{3+}: (a) experiment A1 with constant ion dose current; (b) experiment B2 with dwell-time distribution along the grating; (c) experiment C3 with pixel distribution variation along the grating.

6.3.3. *Effects of variation of the milling sequence and ion-dose distribution*

Compared to the flat-dose-distribution milling procedure, variation of dwell time or pixel distribution resulted in increased milling depths at the same constant total ion dose, therefore allowing for the milling of deep grating structures. The other desired property of the grating structures is straight sidewalls. The results of the variation of milling depth and obtained sidewall angle are summarized in Table 6.2. The angles are measured at the half depth of each grating structure.

Table 6.2. Variation of grating milling depth and sidewall angle as a function of dwell time and pixel distribution.

Experiment B: Dwell time distribution			Experiment C: Pixel distribution		
Dwell time variation(ms)	Depth (µm)	Angle (°)	Pixel step size	Depth (µm)	Angle (°)
0.003 – 0.007	4.07	7.3	20	4.27	9.0
0.003 – 0.01	4.45	5.4	10 – 20	4.24	7.2
0.003 – 0.7	4.06	7.0	1 – 20	4.37	6.6

From Table 6.2 it is evident that both approaches result in improved sidewall angle and total milling depth. The lowest sidewall angle of 5.4°, together with the largest milling depth of 4.45 µm, is obtained by varying the dwell time along the milling area of the grating. Although the results are similar, variation of the pixel distribution results in slightly lower depth values and higher sidewall angles. The reason is that the minimum inter-pixel distance is 1, which owing to the high current results in a less fine control of the dose around the sidewalls of the grating. Furthermore, procedure C results in deeper milling of the top part of the grating structures (the hills between the milled parts in the grating) by ~0.4 µm, see Fig. 6.3 (c). This is an undesired effect which can lead to extra optical losses in the device. Therefore, the dwell-time variation approach (experiment B2) was selected for implementing our device structures.

6.4. Optical characterization

Prior to defining grating structures in $KGd_xLu_{1-x}(WO_4)_2:Yb^{3+}$ waveguides for the realization of integrated waveguide lasers operating at $\lambda = 980$ nm, we characterized the optical properties of integrated cavity structures. This experiment was performed at $\lambda = 1530$ nm, where a widely tunable optical source was available. Hence, two sets of integrated cavities were fabricated, designed for operation around 1530 nm and 980 nm.

6.4.1. Optical cavities at 1530 nm

Fabry-Perot (F-P) microcavities with two identical gratings, see Fig. 6.4 (a, b), were defined using the optimized milling procedure reported in the previous section. The cavity length (L_C) was varied between 50-250 µm. The measured F-P transmission resonances in the wavelength range between 1503-1530 nm for transverse-electric (TE) and transverse-magnetic (TM) polarization are plotted in Fig. 6.5 (a, b), respectively. Using the values of finesse F and cavity length L_C obtained through a fit to the experimental data, for a given refractive index n_C and the relation [pru07, ay09]

$$F = \frac{\pi \exp\left(-\frac{1}{2}\alpha_T n_C L_C\right)}{1 - \exp\left(-\alpha_T n_C L_C\right)}, \tag{6.1}$$

the distributed-loss coefficient α_T was obtained. The observed reflectivity and loss values were strongly polarization dependent. For TE polarization, see Fig. 6.5 (a), the resulting resonator losses were found to be 5.0 dB, with a corresponding DBR reflectivity of 10% and finesse of 1.1. A better optical performance was observed for TM polarization, see Fig. 6.5 (b). The optical losses of the grating structures were found to be 2.2 dB, corresponding to a DBR reflectivity of 56% and resonator finesse of 3.0. This difference can be attributed to the different sensitivity of optical modes at different polarizations to the sidewall angle of the grating. The TM mode is expected to be less sensitive to these interfaces, resulting in lower out-of-plane losses [leew79].

(a)   **(b)**

(c)
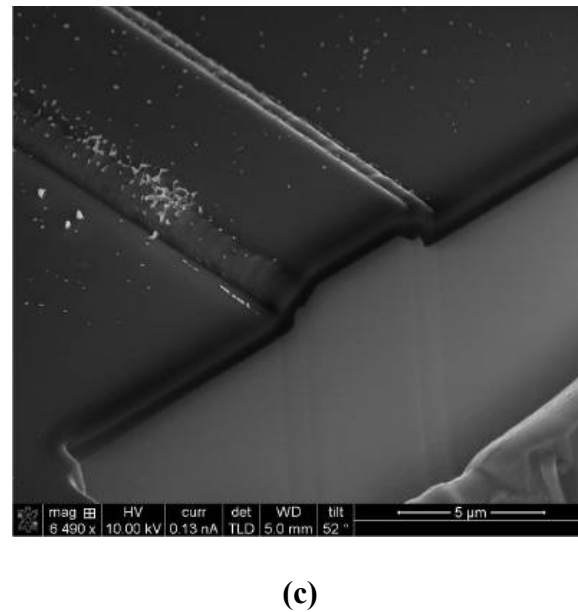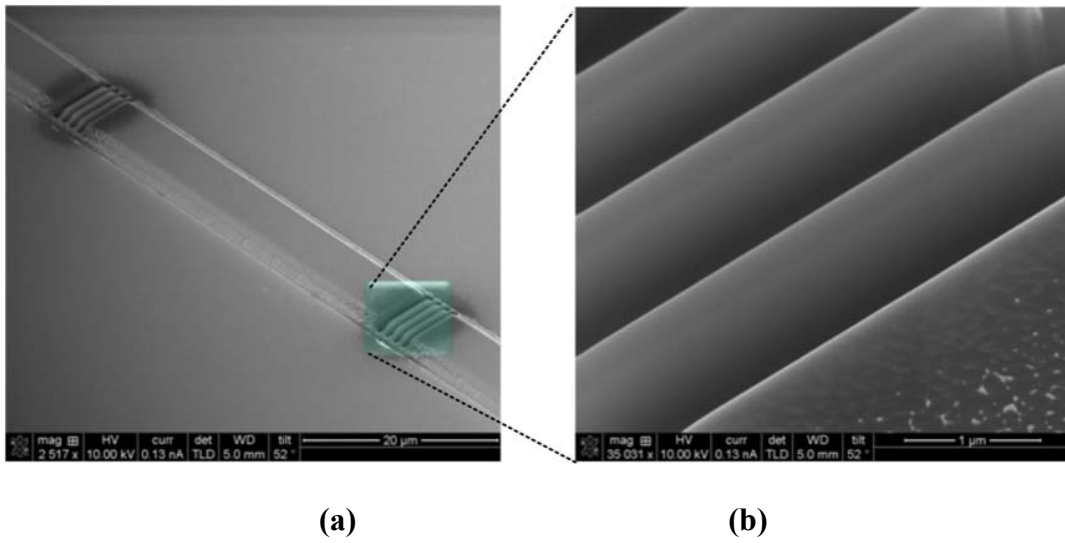
Fig. 6.4. (a) Integrated Fabry-Perot microcavity for optical investigation around 1550 nm; (b) SEM image of the grating structure forming the Fabry-Perot cavity; (c) SEM image of a FIB polished KGd$_x$Lu$_{1-x}$(WO$_4$)$_2$:Yb^{3+} waveguide end-facet.
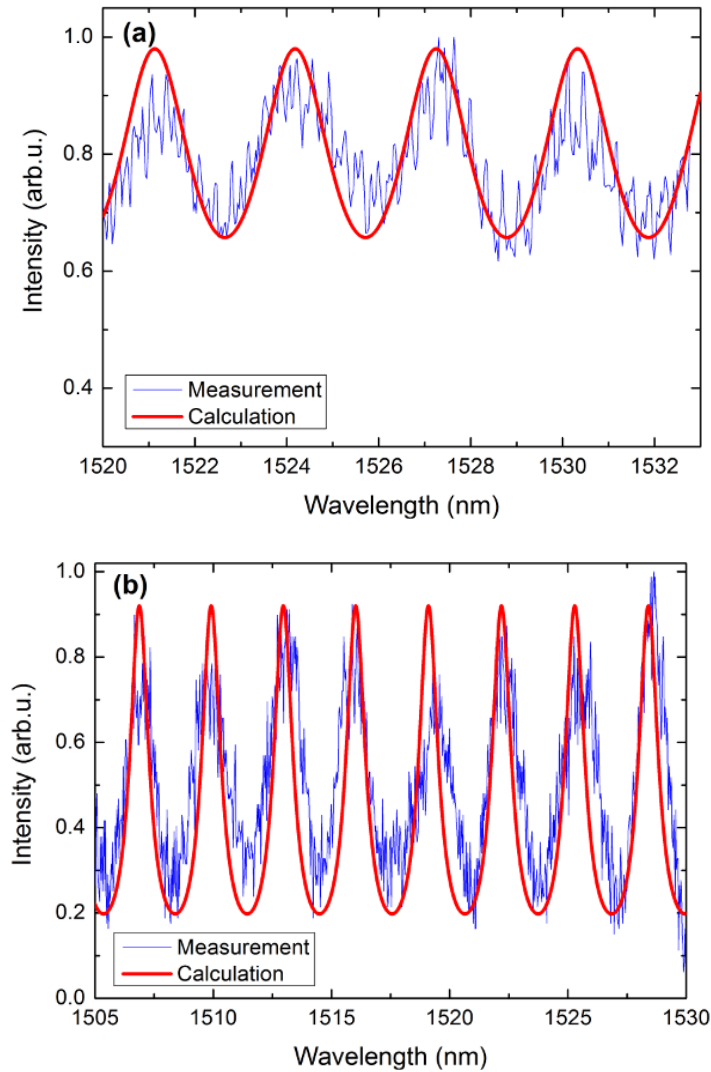
Fig. 6.5. Experimental and calculated Fabry-Perot transmission resonances for (a) TE and (b) TM polarization.

6.4.2. Laser performance

The ridge waveguides in the $KGd_{0.491}Lu_{0.509}(WO_4)_2$:(2.5%)$Yb^{3+}$ layers were aligned along the N_g optical axis of the material to make use of the large emission cross-section of the active ions when operated in TE polarization, shown in Fig. 3.6 [kule97]. In order to improve the low grating reflectivity for TE polarization the sample was tilted by the observed inclination angle of ~5° before milling the grating structure, such that the incoming optical mode enters the grating through a straight sidewall. Furthermore, the integrated cavities designed for laser operation consisted of a single grating on one side, while on the other side a polished waveguide facet was milled, as depicted in Fig. 6.4 (c). The total cavity length was ~4.5 mm. Laser investigations were performed using the optical setup depicted in Fig. 6.6. The active waveguide cavity was pumped via the polished facet by a Ti:Sapphire laser tuned to 932 nm in TE polarization. The pump laser was chopped with a 50% duty cycle at a frequency of 200 Hz. The laser emission at 980 nm was collected via a 20% beam splitter placed into the pump beam line, and a reflective grating was used to separate the residual pump light from the laser

emission.
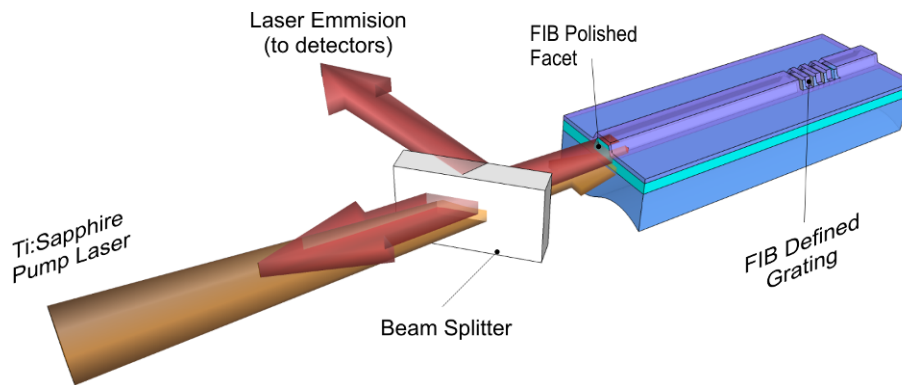
Fig. 6.6. Schematic of experimental setup used for laser experiments.

Lasing was observed for two different cavity configurations involving 12 μm wide and 8 μm wide grating structures. The slope efficiencies of the two lasers are 33% and 15% versus launched pump power and demonstrated laser thresholds of 13 mW and 10 mW, respectively (Fig. 6.7).
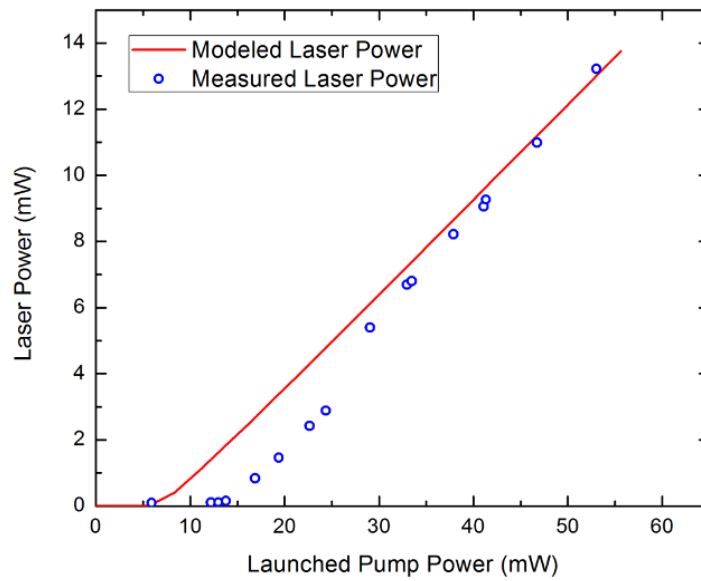
(a)
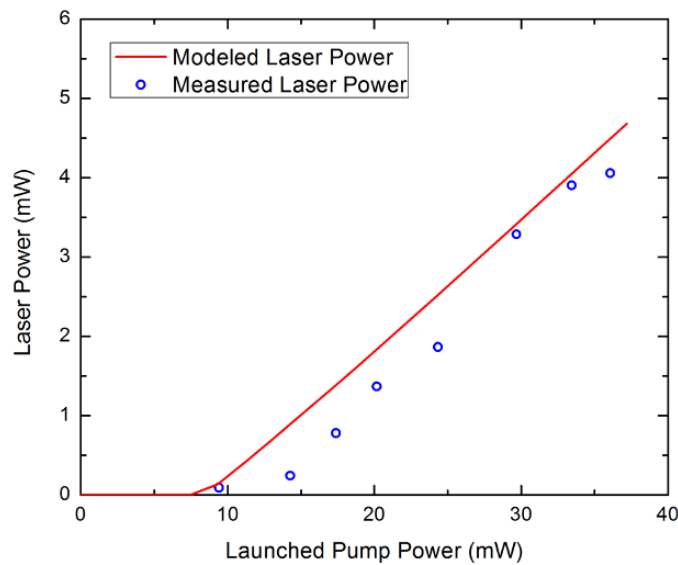
(b)

Fig. 6.7. Measured (dots) and modeled (line) performance of laser cavities involving (a) 12 μm wide and (b) 8 μm wide grating structures.

Modeling of the laser emission from these on-chip cavities was performed with a spatially resolved, steady state rate equation model, discussed in Section 3.3. The theoretical model was fitted to the measured results to obtain the relevant parameters. The used input data for this simulation, providing the best agreement with the experimentally observed performance is given in Table 6.3.

Table 6.3. Input parameters for the spatially resolved rate equation model, discussed in Section 3.3, to calculate the laser performance of channel waveguide lasers with two different grating types; a grating structure with horizontal width of 12 µm and a grating with a width of 8 µm, having a reflection of 40% and 18% respectively.

Parameter	Best matching input parameters for laser performance of Bragg-cavities	
Grating width (µm)	12	8
λ_p (nm)	932	
λ_l (nm)	981	
σ_p^{em} (m^2)	0.8×10^{-24}	
σ_p^{abs} (m^2)	3.0×10^{-24}	
σ_l^{em} (m^2)	15.9×10^{-24}	
σ_l^{abs} (m^2)	13.1×10^{-24}	
R_{1l}	0.09	
R_{1p}	0.09	
R_{2l}	0.4	0.18
R_{2p}	0.4	0.18
α_{loss} (m^{-1})	7.8[*]	
Cross-sectional information and mode profile		
N_T (m^{-3})	1.58×10^{26}	
L (mm)	4.5	
Δz (mm)	0.045	
End-facet aperture	0.8	0.7

[*]**Corresponding to a propagation loss of 0.34 dB/cm, as measured in Section 5.2**

The laser performance of these devices is poor compared to the laser performance of the devices discussed in Chapter 5, especially compared to a similar laser operating at the zero phonon line in a half open cavity presented as sample A in Section 5.3 having a slope efficiency of 76% versus absorbed pump power. This reduced performance is largely caused by too large intracavity losses. These losses are caused by the lower reflectivity of the Bragg reflector, possibly having some additional absorption of the light by implanted Gallium ions near these Fib-milled regions. But also an slightly increased propagation loss is expected by the Si$_3$N$_4$ cladding having a lower index compared to the KYW cladding. In addition the deposition of the Si$_3$N$_4$ cladding is a non thermal equilibrium process, while the deposition of a KYW cladding occurs using LPE, which possibly smoothens the sidewall roughness. Moreover, prior to FIB milling the end-facets of the waveguides were diced perpendicular to the waveguides, causing severe chipping of the Si$_3$N$_4$ cladding layer. In order to manufacture the FIB-polished outcoupling facet, an approximately 50 µm long trench with a depth of 5-10 µm was milled using FIB to overcome this chipped area, prior to the FIB polishing of the end-facet. However, due to clipping of the diverging laser beam in the trench, a part of the emission is not detected. This clipping effect was taken into account to fit the model to the

experimental data by defining the efficiency of the aperture formed by the trench, indicated as *end-facet aperture* in Table 6.3. Hence improved laser emission compared to the results presented here is expected when improving the design of the trench. For both lasers the reflectivity of the FIB-polished in-coupling facet was estimated from the model to be 9%. This value is 2% lower than the ideal Fresnel reflection of 11% from such a facet, which can be explained by a small fraction of the laser mode laterally extending outside the polished facet and/or a slight misalignment/tilt of the facet. The reflectivity of the grating structure of the first laser is estimated to be 40%, while for the second one the reflectivity is 18%. The higher reflectivity was obtained for the grating structure with increased horizontal width of 12 μm compared to the grating with a width of 8 μm.

The obtained results indicate that an increase in the overlap between the grating area and the optical mode increases the reflectivity of the grating structure. Further improvement of the mode confinement in the active waveguide is expected to significantly improve the laser performance. Reflectivities of more than 80% are expected for optimized waveguide geometries with larger etch depth and width to obtain a perfect overlap between the optical mode profile and the grating geometry and steeper sidewalls to obtain minimal out of plain loss.

In FIB-defined microstructures the implanted Ga^+ ions are known to give rise to strong additional optical losses [rid07] through absorption and/or resulting local amorphization of the crystalline material [bas03]. In this study the interaction of the optical mode with the implanted region was decreased and only a small percentage of the mode intensity was exposed to the heavily Ga^+-implanted region, below each trench. When the optical mode is confined to the initial 4 μm of the structure, in optimized waveguide geometry this implantation-related loss can be almost completely avoided. This approach also reduces the optical losses arising from the local amorphization.

6.5. Conclusions

FIB milling of deep grating structures in $KGd_xLu_{1-x}(WO_4)_2:Yb^{3+}$ has been developed. Re-deposition effects were significantly reduced and grating structures more than 4 μm in depth with an improved sidewall angle of about 5° were achieved by varying dwell time and pixel resolution distribution for the same dose per area. F-P microcavities were defined and used to assess the optical performance of the grating structures at ~1530 nm. Based on the optical results, a new geometry was applied for optical cavities at ~980 nm. An on-chip integrated laser cavity was achieved by defining a FIB reflective grating and a FIB polished waveguide end-facet. With this cavity, an integrated waveguide laser with 33% slope efficiency was demonstrated in $KGd_{0.491}Lu_{0.509}(WO_4)_2:(2.5\%)Yb^{3+}$. Possibilities for further performance increase for these on-chip waveguide lasers have been identified.

Semiconductor optical amplifier waveguide devices deliver high gain per unit length (reaching ~1000 dB/cm) [leu01, dou94] and over 10000 dB/cm in vertical-cavity semiconductor optical amplifiers (VCSOAs) [bjo03, bjo04, col05], enabling light amplification over short distances in photonic integrated circuits [roe07]. In contrast, rare earth ions are regarded as impurities providing low gain (reaching ~10 dB/cm) [pat04, tho10, yang10, kah08], because electronic transitions within their 4f subshell are parity forbidden, dictating low transition probabilities and cross-sections. Nevertheless, devices such as fiber amplifiers and solid-state lasers profit from accordingly long excited-state lifetimes – hence increased excitation densities – in rare earth-ion-doped materials, combined with large device lengths.

In this Chapter, the very high cross-section at the ZPL of Yb^{3+} ions, when doped into the KG$_x$Lu$_{1-x}$(WO$_4$)$_2$ host material, is exploited. The large cross-section, combined with the large doping concentration, in the vicinity of 50 %, that is attainable in co-doped layers, is efficiently excited in a microstructured channel waveguide, resulting in large population inversions. Hence a gain of 935 dB/cm was demonstrated, comparable to the best values reported for optically active waveguide devices in semiconductors. Further improvement seems feasible with larger dopant concentrations.

7.1.   Introduction

Amplification of optical signals is required whenever the optical losses per unit length times the total distance (e.g. in long-haul optical communication or plasmonic waveguides) or the losses per unit device element times the number of device elements (e.g. in very-large-scale-integrated optical circuits) requires periodic recovery of the signal strength.

Among the available amplifier types, fiber amplifiers doped with trivalent rare earth ions (specifically Er^{3+}) are a standard in optical communication systems due to their low insertion loss, low noise, negligible non-linearities, superior characteristics at high-speed amplification, and high overall gain (30-50 dB). However, this high gain comes at the expense of employing several meters of fiber length, making this solution unsuitable for on-chip integration. The amplifier length can be shortened to typically a few centimeters by increasing the dopant concentration of rare earth ions accordingly, but this approach is ultimately limited by the solubility of rare earth ions in the chosen host material as well as the scattering losses and spectroscopic quenching processes induced by these high dopant concentrations. The typical gain per unit length reported for rare earth-ion-doped integrated waveguides has hardly exceeded a few dB/cm [pat04, tho10, yang10, kah08].

Semiconductor optical amplifiers (SOAs), including organic semiconductors [ama06, goo05] and III-V semiconductors [cor90, sto01, bak03, koo01, nag10] with different gain structures, such as quantum wells (QW) [cor90, sto01], multiple quantum wells (MWQ) [koo01, bjo03, bjo04, col05], and quantum dots (QD) [bak03], deliver high gain over short distances, which in combination with heterogeneous integration techniques, make SOAs suitable for providing

on-chip gain. However, due to the short carrier lifetime in these materials and significant refractive index changes, which is assumed to be larger compared to the refractive index changes in rare earth doped double tungstates [sou10], accompanied with the excitation of electron-hole pairs, temporal and spatial gain patterning effects limit their performance. Also optically pumped dye-doped optical amplifiers (DOAs) can deliver high gain per unit length [law02, lam03].

The enormous difference in gain per unit length provided by these materials originates in their physical properties, as exemplified in Table 7.1. The relevant performance parameter, their modal gain (dB/cm),

$$g_{\mathrm{mod}} = \Gamma g_{mat} = 4.34 \, \Gamma [\sigma_{em} N_2 - \sigma_{abs} N_1] \,, \tag{7.1}$$

is given by the fractional overlap (or mode-confinement factor) Γ of the signal beam at wavelength λ_S with the gain structure exhibiting a material gain g_{mat} (dB/cm). The mode-confinement factor Γ can be split into a lateral overlap with the active medium Γ_{xy} and a longitudinal overlap with the active medium Γ_z according to

$$\Gamma = \Gamma_{xy} \Gamma_z \,. \tag{7.2}$$

Here $\Gamma_z = 1$ for most amplifier devices, except for resonant amplifiers having sub-wavelength sized interaction lengths with the active medium, such as in VCSOAs. In these resonant devices the standing wave pattern enhances the interaction of the light with the thin film(s) of active material, allowing Γ_z to reach a value of 2 for perfect overlap between a thin gain medium and the resonance peak of the electric field, while if the gain medium sits at a null of the resonant electric field, Γ_z approaches zero. To estimate the single pass gain from these resonant amplifiers, not only the average number of roundtrips, but also this longitudinal enhancement of interaction between the light and the gain medium has to be taken into account. However defining a gain coefficient (dB/cm) of vertical emitter gain media by is not completely appropriate and defining the gain per QW is preferred [blo00], but in order to make the comparison with other device geometries the current representation is used, indicating a maximum attainable gain coefficient for devices with vertical-cavity geometry.

The material gain g_{mat} (dB/cm) is derived as the product of 4.343 with the difference between the stimulated emission processes, given by the density of charge carriers in the excited state N_2 (cm^{-3}) times the emission cross-section σ_{em} (cm^2), and the material absorption, given by the density of charge carriers in the ground state N_1 (cm^{-3}) times the absorption cross-section σ_{abs} (cm^2), as depicted in Eq. 7.1. This relation is commonly used to determine gain in rare earth doped materials. In semiconductors, one commonly finds a relation stating only the emission cross-section times the inversion of the material ($N_{inv} = N_2 - N_t$). Here no absorption coefficient is given, but only transparency excitation N_t. These different notations represent the same underlying physics. The net modal gain (dB/cm) is $g_{net} = g_{mod} - L$; the propagation losses L are usually small compared to the modal gain and can be neglected.

A material gain of several $\times 10^3$ dB/cm is achieved in the recombination region of III-V semiconductors [leu00, cor90, sto01] due to the large stimulated emission cross-sections of

the excited carriers of several $\times$ 10^{-16} cm^2, while N_{inv} is in the range of a few $\times$ 10^{18} cm^{-3}. However, in QW and MQW SOAs, the usually μm-sized signal mode exhibits a poor overlap Γ with the few-nm-thin active gain region, reducing accordingly the modal gain of QW and MQW SOAs to several $\times$ 10^2 dB/cm [cor90, sto01, koo01, nag10]. The small mode overlap with the active material is strongly improved in VCSOAs. Here the light propagates

Table 7.1. Properties of various representative gain materials, including typical values of the stimulated emission cross-section σ_{em}, carrier densities N_2 and N_{tr}, mode confinement factor Γ, as well as resulting material gain g_{mat} and modal gain g_{mod}. In order to compensate for the resonant property of the VECSOAs the experimental gain values are re-evaluated to obtain the gain of a single pass of these devices. However, due to standing wave effects the mode confinement factor Γ exceeds 1, resulting in a larger modal gain compared to the material gain. In true single pass experiments, no standing wave pattern is expected, hence limiting the modal gain to the material gain.

		Material	λ (µm)	σ_{em} (cm²)	N_2 (cm⁻³)	N_{tr} (cm⁻³)	Γ	g_{mat} (dB/cm)	g_{mod} (dB/cm)
Semiconductors		InGaAsP bulk	1.50-1.55	1.2-2.5×10⁻¹⁶ [sve98]	3.25×10¹⁸ [leu00]	1×10¹⁸ [sve98]	0.3 [leu00] [c]	3440 [leu00] [e]	1032 [leu00] [e]
				1.2-2.5×10⁻¹⁶ [sve98]	--	1×10¹⁸ [sve98]	--	--	775-1192 [dou94] [e]
		AlInGaAs/InP MQW	1.28	--	--	2×10¹⁸ [koo01]	--	--	220 [koo01]
	VECSOA`s	InGaAsP/InP	1.31	--	--	--	1.75 [bjo03]	7800 [bjo03]	13650 [bjo03]
		AlInGaAs/InP	~1.5	--	--	--	1.7 [bjo04]	7790 [bjo04]	13250 [bjo04]
		AlInGaAs/InP	~1.5	--	--	--	1.6 [col05]	6550 [col05]	10480 [col05]
		InGaAs/AlGaAsP-InP	1.55	--	--	--	--	--	250 [nag10]
		GaAs/AlGaAs QW	0.83	7×10⁻¹⁶ [sve98]	14.6-19.6×10¹⁸ [sto01] [c*]	2×10¹⁸ [sve98]	0.0133 [sto01] [c]	22556 [sto01] [c**]	300 [sto01] [e]
		Strained InGaAs/AlGaAs QW	0.98	7-22×10⁻¹⁶ [cor90]	8.4×10¹⁸-11.1x10¹⁸ [sto01] [c*]	0.5-1×10¹⁸ [sve98]	0.0174 [sto01] [c]	15300 [sto01] [c**]	266 [sto01] [e]
	Organic semi-conductors	F8BT/Dow Red-F	0.66	2×10⁻¹⁶ [goo05]	--	--	--	--	775 [goo05] [e]
		MEH-PPV	0.63	4x10⁻¹⁷ [ama06]	--	--	--	--	290 [ama06] [e]
Laser Dyes		OC₁C₁₀PPV	0.60	3-5.3×10⁻¹⁷ [law02] [c]	4×10¹⁷ [law02] [c]	--	1 [law02]	44 [law02]	44 [law02] [e]
		Poly (9,9-dioctyfluorene) PFO	0.466	0.3-4×10⁻¹⁶ [sve98]	0.1-10×10¹⁸ [sve98]	--	1 [lam03]	318 [lam03]	318 [lam03] [e]
		PM650 in PMMA	0.616	3.7×10⁻¹⁶ [lam03]	0,24×10¹⁸ cm⁻³ [lam03]	--	1 [lam03]	385 [lam03]	385 [lam03] [e]
Rare earths		Er (8wt%)-Yb (12wt%) co-doped phosphate glass	1.534	2x10⁻²¹ [pat04] [c***]	7.5×10²⁰ [pat04]	--	1 [pat04]	13.6 [pat04]	13.6 [pat04] [e]
		Nd-complex-doped polymer	1.064	3.78 x10⁻²⁰ [yang10]	4.1×10¹⁹ [yang10]	--	0.83 [yang10]	6.9 [yang10]	5.7 [yang10] [e]
		KGd$_{0.447}$Lu$_{0.553}$(WO₄)₂:(0.475)Yb³⁺	0.9806	1.5×10⁻¹⁹ [kule97]	2.4×10²¹ [this work]	1.8×10²¹ [this work]	0.88 [this work]	up to 1170 [this work]	935 [this work] [e]

[*] Value derived when dividing the reported [sto01] sheet density (cm⁻²) by the corresponding well width. The sheet resistance values were selected [sto01] to explain the gain values measured experimentally as a function of injection current density.

[**] Value calculated from g_{mod}, assuming the reported [sto01] calculated optical confinement value.

[***] Value calculated from Fig. 7.1 of [pat04], considering full inversion.

[e] experimental.

[c] calculated.

perpendicularly through the active medium, resulting in a transverse mode overlap of $\Gamma_{xy} = 1$. On the other hand, in these VCSOAs the single pass gain is not large due to the extremely short interaction length; therefore, resonant multilayer structures are commonly used to extract the gain from the few nm thin active gain region. Due to the resonance in these devices a longitudinal mode overlap of typically $\Gamma_z = 1.7\text{-}1.8$ is observed [cor89, bjo02], providing a modal gain up to 13650 dB/cm, exceeding the material gain of 7800 dB/cm [bjo03, bjo04, col05]. However, true single pass amplification in these structures results in a $\Gamma_z = 1$, as no standing wave pattern is formed in a single pass amplification, resulting in a modal gain equal to the material gain.

Dyes can provide similarly high stimulated emission cross-sections as semiconductor amplifiers. However, their inversion density is an order of magnitude lower, resulting in values of the material gain up to a few $\times\ 10^2$ dB/cm; due to an excellent overlap Γ, DOAs can, nevertheless, provide a modal gain of a few $\times\ 10^2$ dB/cm.

Rare earth ions doped into amorphous materials, such as Al_2O_3, silica, and phosphate glass or polymers, suffer from stimulated emission cross-sections whose values are typically four to five orders of magnitude smaller than in semiconductors, namely several $\times\ 10^{-21}$ cm^2. The larger density of excited ions of several $\times\ 10^{20}$ cm^{-3}, combined with an excellent overlap Γ, cannot compensate this disadvantage, resulting in the modal gain hardly exceeding 10 dB/cm, which is two and three orders of magnitude lower than the best values reported in SOAs and VCSOAs, respectively.

In this Chapter, we show that an appropriate choice of host material, dopant concentration, and geometry can enhance the modal gain of rare earth ion doped waveguide amplifiers to values at which they can easily compete with waveguide SOAs and DOAs, while simultaneously providing the desirable gain characteristics present in rare earth ion doped fibers, holding promise for a new generation of highly efficient optical gain materials.

This approach utilizes the large transition cross-sections of Yb^{3+} ions doped into the $KG_xLu_{1-x}(WO_4)_2$ host material, exceeding by more than an order of magnitude the cross-sections observed in amorphous materials (Table 7.1). Furthermore, large doping concentrations are applied without introducing significant spectroscopic quenching effects, as the active ions are incorporated in lattice sites with large ion separation. Combination with a long excited state lifetime, tight pump and signal light confinement, and excellent pump mode overlap with the active region allows us to achieve extremely large excitation densities.

The emission and absorption cross-sections of the used composition for these experiments, namely $KGd_{0.447}Lu_{0.553}(WO_4)_2:(47.5\%)Yb^{3+}$ are shown in Fig. 7.1. The spectroscopic data were derived using the convolution of the available spectroscopic data of the stoichiometric compositions of KYbW, KLuW, and KGdW, with respect to the specific composition as presented in Section 3.2.
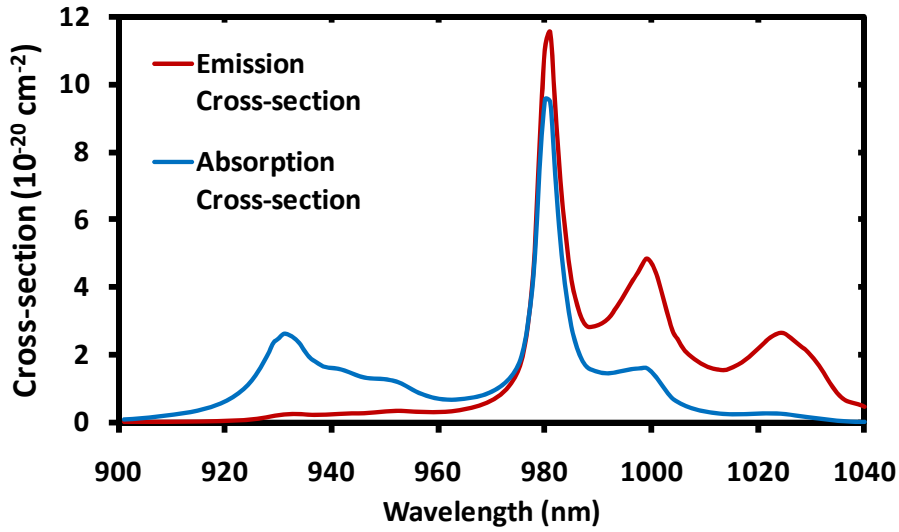
Fig. 7.1 The emission and absorption cross-sections of KGd$_{0.447}$Lu$_{0.553}$(WO$_4$)$_2$:(47.5%)Yb^{3+}, derived using the convolution of spectroscopic data from several sources, see Section 3.2. The peak emission and absorption cross-sections at a wavelength of 980.6 nm are σ_{em} = 1.15×10^{-19} cm^2 and σ_{abs} = 9.45×10^{20} cm^2, respectively.

By improving the relevant parameters in Eq. (7.1), maximization of the overlap $\Gamma \approx 088$, Increasing the excitation density N_2 ensures optimal emission by the large emission cross-section σ_{em} while the low ground state density N_1 reduces the reabsorption cross-section originating from the absorption cross-section σ_{abs}, we demonstrate a modal gain of 935 dB/cm, thereby increasing the small-signal gain achieved in rare earth ion doped microstructures [pat04, tho10, yang10, kah08] by two orders of magnitude. Fig. 7.2 visualizes the differences in the relevant parameters between SOAs and rare earth ion doped amplifiers.

(a)   (b)
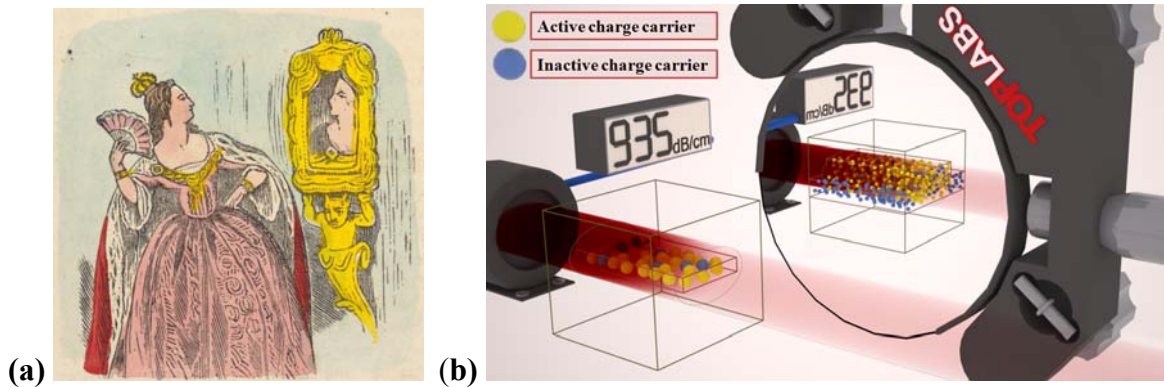
Fig. 7.2. "Mirror, mirror on the wall, who..." has the highest gain of all? (a) Like in the fairytale *Snow White and the Seven Dwarfs* [gri57], (b) the magic mirror tells the SOA its new competitor, a rare earth ion doped dielectric waveguide, delivering comparable modal gain of 935 dB/cm (visualized by the color strength of the amplified beam and the power meter display), despite orders of magnitude difference in the underlying physical parameters. On the left, the state of the art semiconductor amplifier (InGaAsP) exhibits a large transition cross-section of several × 10^{-16} cm^2 (visualized by the large-size gain elements), small carrier density of ~1 × 10^{18} cm^{-3} (visualized by their low number), and weak overlap of signal light with the gain structure of ~30 % (visualized by the sizes of optical mode and gain structure). The mirror image shows the presented Yb^{3+} doped potassium double tungstate waveguide amplifier exhibiting a

comparatively small transition cross-section of 1.5×10^{-19} cm^2, large inversion of 60% of the dopant concentration of 3.0×10^{21} cm^{-3}, and strong overlap of signal light with the gain structure of 88%.

7.2. Waveguide fabrication

For these experiments a crack-free KGd$_{0.447}$Lu$_{0.553}$(WO$_4$)$_2$:(47.5%)Yb^{3+} (with the Yb^{3+} ions replacing the Lu^{3+} ions) layer with a thickness of 2.2 µm was grown onto a pure KYW substrate and patterned by IBE, creating 1.4 µm deep, 6 µm wide ridge waveguides along the N_g optical axis. Further details of the device fabrication are found in Chapters 2 and 4 of this thesis. The channel structures were overgrown by undoped KY(WO$_4$)$_2$, to create buried channel waveguides having an enhanced refractive index difference between layer and substrate of ~1.7 × 10^{-2}, see Fig. 2.7. This refractive index contrast results in a tight confinement of pump and signal light, ensuring enhanced pump intensity and modal overlap of pump and signal beam with the active waveguide region. The device length was restricted to 180 µm of which the end-facets were diced to an wedge, to prevent parasitic laser oscillation. An optical micrograph of the channel waveguide devices is presented in Fig. 7.3.
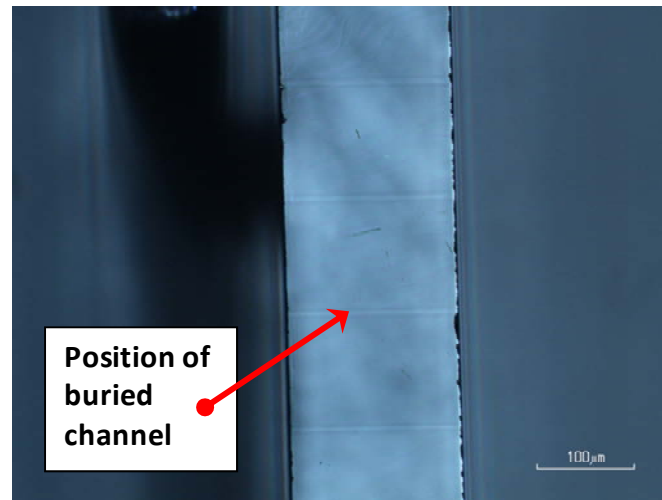
Fig. 7.3. Optical micrograph (top view) of the amplifier channels after dicing. Channels are hard to observe, since they are overgrown.

For perpendicular gain measurements, a 25 µm thick layer of the same material composition was prepared.

7.3. Gain calculation

The maximum attainable excitation density of Yb^{3+} ions is reached when the medium becomes transparent for the pump wavelength. With room-temperature Boltzmann factors b_{11} = 0.605 and b_{23} = 0.065 of the Stark levels [assuming KY(WO$_4$)$_2$] involved when pumping at 932 nm, maximum inversion obtains at transparency for the pump photons:

$$b_{11}\left(N_d - N_2\right) = b_{23}N_2 \Rightarrow b_{11}/\left(b_{23} + b_{11}\right) = N_2/N_d = 90\% . \qquad (7.3)$$

The used emission cross-section[2] of $\sigma_{em} = 1.15 \times 10^{-19}$ cm^2 and absorption cross-section of $\sigma_{abs} = 0.945 \times 10^{-19}$ cm^2 at the signal wavelength of $\lambda_S = 980.6$ nm are related to the used composition of the host material, see Fig. 7.1. With a dopant concentration of $N_d = 3.0 \times 10^{21}$ cm^{-3} (= 47.5 at.%), a material gain of $g_{mat} = 1230$ dB/cm can be achieved according Eq. 7.1. Using the spatially resolved rate equation model described in Section 3.3, a modal gain of $g_{mod} = 950$ dB/cm is calculated for the highest pump power (solid line in Fig. 7.4).
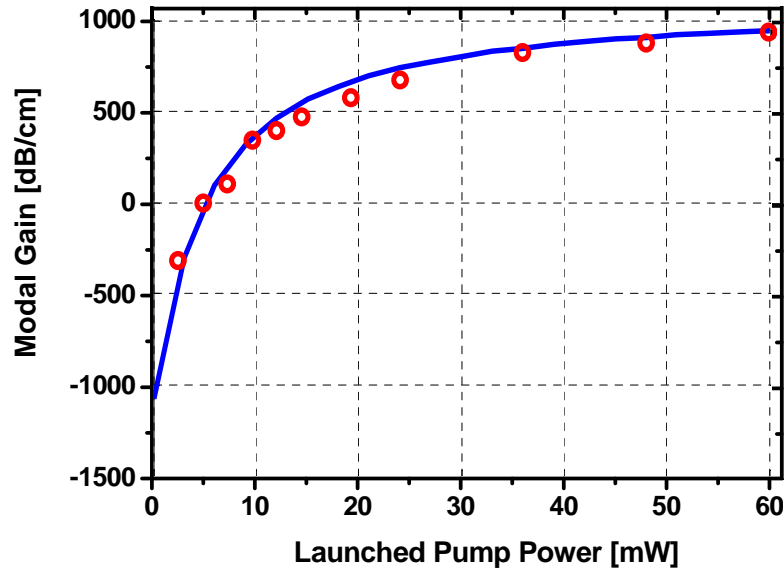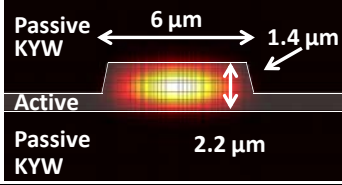
Fig. 7.4. Modal gain per unit length predicted (solid line) and measured (dots) in a 47.5 at.% Yb^{3+} doped potassium double tungstate channel waveguide versus launched pump power. The predicted gain reaches 950 dB/cm. The highest measured gain of 935 dB/cm exceeds values previously reported in the literature for rare earth ion doped waveguide amplifiers by two orders of magnitude.

The input parameters, corresponding to the tested amplifier, for this simulation are given in Table 7.2.

---

[2] Despite the mentioned Boltzmann factors in Eq. 7.3, here the effective cross-sections are used. The effective cross-section is the product between the atomic cross-section with the Boltzmann factor of the initial state that corresponding to the related transition. This makes the Boltzmann factors irrelevant in Eq. 7.1.

Table 7.2. Input parameters for the spatially resolved rate equation model to calculate performance of the waveguide amplifier operating at 980.6 nm.

Parameter	Waveguide amplifier
λ_p (nm)	932
λ_l (nm)	980.6
σ_p^{em} (cm^2)	0.2×10^{-20}
σ_p^{abs} (cm^2)	2.6×10^{-20}
σ_l^{em} (cm^2)	1.15×10^{-19}
σ_l^{abs} (cm^2)	0.945×10^{-19}
N_d (cm^{-3})	3.0×10^{21}
l (mm)	0.180
Δz (mm)	3.6×10^{-3}
Structural and modal information	

The confinement factor of the light in the waveguide has been estimated to be $\Gamma = 0.88$ using Phoenix FieldDesigner mode solver software. Using Eq. 7.1 the excitation density of the active region is found to be $N_2 / N_d = \sim 84\%$, which corresponds well with the spatially distributed excitation density found by the spatially resolved rate equation model, presented in Fig. 7.5. The maximum population inversion observed in Fig. 7.5 is nearly 90%, which corresponds to the maximum theoretical inversion of 90% at transparency for the pump photons given in Eq. 7.3.
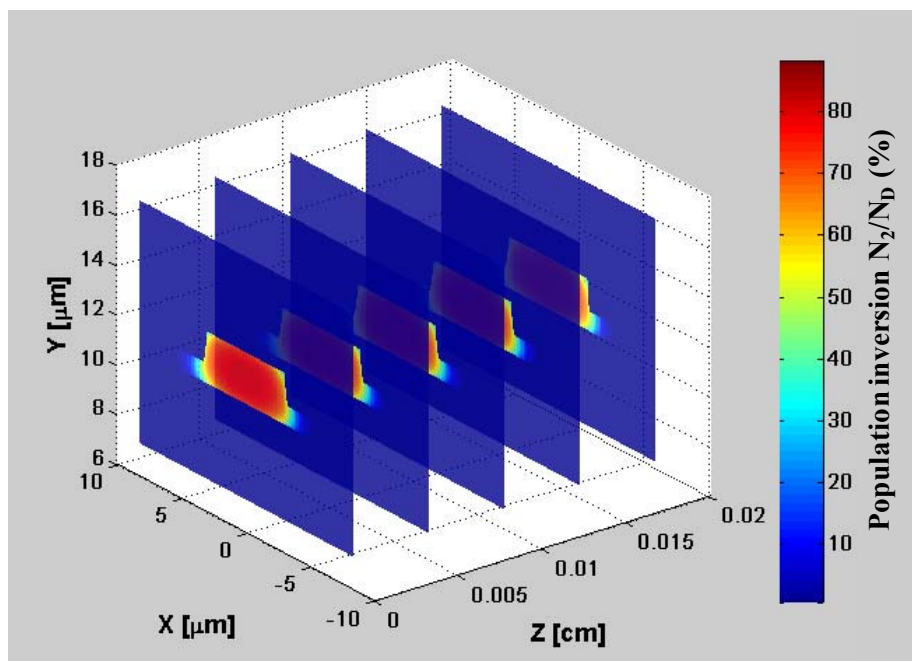
Fig. 7.5. Estimated population inversion using the spatially resolved rate equation model of Section 3.3.

Using the spectroscopic data provided for a stoichiometric KYb(WO$_4$)$_2$ waveguide having a

doping concentration $N_d = 6.3 \times 10^{21}$ cm^{-3}, emission cross-section of $\sigma_{em} = 1.36 \times 10^{-19}$ cm^2 and absorption cross-section of $\sigma_{em} = 1.17 \times 10^{-19}$ cm^2 [pujo02] in a similar waveguide configuration having a confinement factor of $\Gamma = 0.88$, pumped to an inversion of $N_2 / N_d = \sim$ 84%, results in an predicted modal gain of $g_{mod} = 2270$ dB/cm.

7.4. Experiment

7.4.1. Setup

Small-signal-gain measurements were performed using a Ti:Sapphire pump laser operating at 932 nm, a variable pump-beam expander, a broadband source (Fianium) polarized parallel to the N_m optical axis, mechanically modulated with a frequency of 142 Hz, and a monochromator selecting the signal wavelength $\lambda_S = 980.6$ nm. Pump and signal light were combined and coupled into the channel waveguide by a ×20 objective lens (numerical aperture NA = 0.4). The variable pump-beam expander was used to optimize the coupling of pump light to the channel waveguide that has an NA = 0.3. A schematic of the used setup is depicted in Fig. 7.6. Identical signal enhancement was obtained for various incident signal powers between 50-250 nW, hence confirming operation in the small-signal-gain regime. However, use of the monochromator resulted in a non-Gaussian signal beam profile, hence resulting in a low coupling efficiency. Light emitted from the opposite waveguide end is collimated by a ×40 objective lens. Residual pump light is suppressed by a dichroic filter and a spectrometer at 980.6 nm (0.14 nm resolution). The amplified signal is detected by an InGaAs detector and discriminated from luminescence at this wavelength by lock-in amplification.
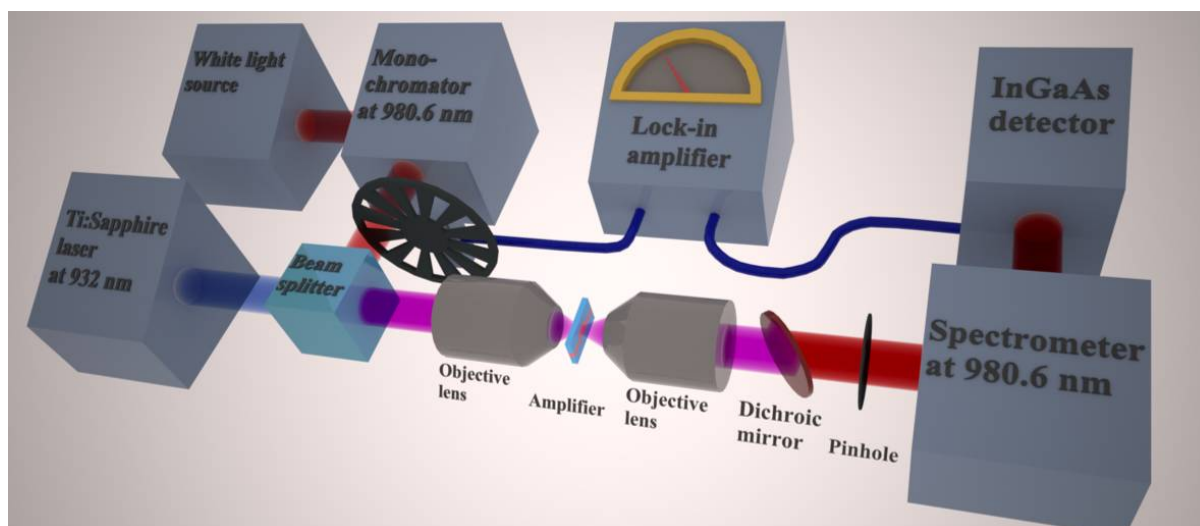
Fig. 7.6. Schematic of experimental setup for optical gain measurements. As gain medium either a planar thin film aligned perpendicular to the pump and signal beam or a microstructured channel waveguide (as displayed) has been investigated.

7.4.2. Data analysis of waveguide experiment

The spatially resolved rate equation model, described in Section 3.3, is used to determine the pump power establishing transparency at λ_S. The used input parameters to this model are provided in Table 7.2. Relative to this 0-dB transmitted signal intensity I_t, transmitted signal

intensities I_S at other pump powers are investigated. A fraction of incident signal light remains uncoupled, hence neither amplified nor attenuated, but is spatially insufficiently discriminated from guided signal light along the short waveguide. At I_t it amounts to $\rho \approx 50\%$ of the detected intensity. This fairly large fraction of uncoupled light is caused by the poor coupling efficiency of the signal light to the waveguide due to its non-Gaussian beam profile. The fraction of uncoupled light is chosen to be constant for all wavelengths and powers, such that the best agreement is found of the measured data with the modeled values. It must be noted that this stray light strongly deteriorates the measurement at low pump power, whereas at high pump power its influence is small compared to the strongly amplified guided fraction, hence reducing the influence of the value of ρ. These considerations yield a modal gain of

$$ g_{\text{mod}}\left(dB/cm\right)=\frac{1}{\ell}10\log_{10}\frac{I_S-\rho I_t}{\left(1-\rho\right)I_t} \ . \tag{7.4}$$

The modal gain measured in the waveguide at the maximum pump power is 935 dB/cm (Fig. 7.4).

In addition, gain in the channel was measured at other wavelengths and compared to the expected gain using the spatially resolved rate equation model, discussed in Section 3.3, and the spectroscopic data according to the used composite host material (Section 3.2), presented in Fig. 7.1. This resulted in an experimentally obtained modal gain of more than 150 dB/cm over a wavelength range from 980 nm to 1023 nm. Both the experimental and modeled data are presented in Fig. 7.7.
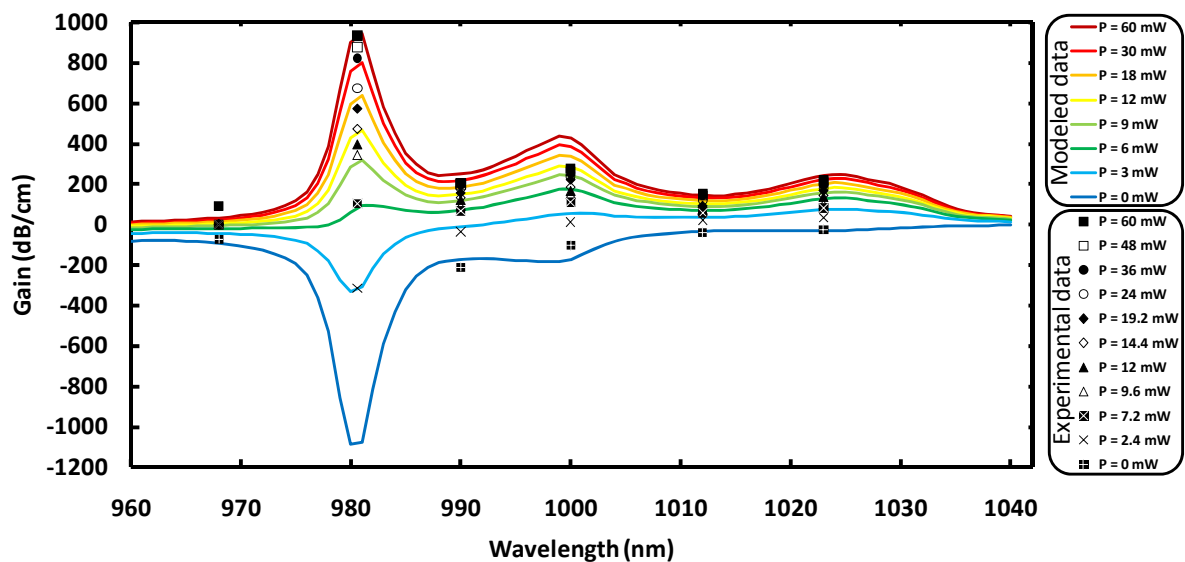
Fig. 7.7. Modal gain in a rare earth ion doped waveguide. The continuous line presents the outcome of the rate equation model using the spectroscopic information of the composite material according to the used composition. The experimentally obtained values, interpreted using Eq. 7.3, are presented as icons.

A significant difference between the modeled and the measured gain is found at a wavelength of 1000 nm. This discrepancy can be explained by an experimental error such as misalignment, hence reducing the excitation of the waveguide, or increasing the fraction of

non coupled signal light reaching the detector. The values measured at a wavelength of 968 nm show larger gain with respect to the modeled values. The measured increase of signal on the detector after switching off the pump is about 1.5 dB, which is close to the noise of the complete setup. The measured signals and their interpreted values are presented in Table 7.3. Here the intensity at the transparency point I_t is estimated for each measurement by firstly estimating the pump intensity required to reach transparency of the sample by using the spatially resolved rate equation model, and using this pump intensity the transparency intensity I_t is obtained by interpolation of the measured data. Each value of I_t is provided in Table 7.3.

Table 7.3. Experimental results and the interpretation of these results by making use of Eq. 7.3, with ρ = 0.5 and l = 0.018 cm.

Signal Wavelength	968 nm		980.6 nm		990 nm		1000 nm		1012 nm		1023 nm	
I_t	7.00		0.47		26.79		32.14		165.49		39.88	
Launched Pump Power	M	G	M	G	M	G	M	G	M	G	M	G
P = 0 mW	6.1	-72	0.1		19	-210	26.6	-102	153	-39	38	-24
P = 2.4 mW			0.3	-314	25	-35	33	13	174	24	43	35
P = 4.8 mW			0.47	-2	29	37	37	64	182	44	45	55
P = 7.2 mW			0.6	105	31.2	69	41.5	111	188.5	59	48	82
P = 9.6 mW			1.22	345	33	92	46	150	193	69	50	99
P = 12 mW			1.46	397	35.5	121	48	166	195	74	55	136
P = 14.4 mW			1.9	471	36.5	132	50.5	184	200	84	56	143
P = 19.2 mW			2.8	576	39	156	56.5	223	204	92	60	168
P = 24 mW			4.1	675	42	183	59	237	220	122	62	180
P = 36 mW			7.4	824	43.8	198	62	253	231	141	65	197
P = 48 mW			9.2	878	44	199	64	264	234	146	68	212
P = 60 mW	8.6	91	11.6	935	45	207	67	278	240	155	70	222

M = Measured signal (arb. units), G = Gain (dB/cm)

Due to the short length of the tested waveguide a fairly large influence of experimental errors, such as the detection of un-coupled light, on the evaluated gain is expected, hence reducing the accuracy of the presented pump-probe measurement. Therefore Hakki-Paoli (H-P) measurements are recommended to increase the accuracy of the gain measurement [hak73]. The H-P method is commonly used to measure the gain of SOAs and is based on the amplification spontaneous emission within a weak etalon, such that no lasing is obtained. In the H-P method the weak etalon is formed between the Fresnel reflections of the end facets of the active waveguide. The separation between the minima and maxima of the etalon fringes is an indication of the available gain inside the etalon, i.e. the active waveguide. The H-P method is therefore not influenced by the launch and detection efficiency, resulting in an improved accuracy.

7.4.3.   Perpendicular "bulk" measurement.

In perpendicular gain measurements stray light is inexistent and a 100% mode overlap is expected, but diverging pump and signal foci and signal-light reabsorption in the pump-beam wings do not allow long interaction lengths. In this experiment the co-propagating pump and signal light are focused perpendicularly through a planar active layer of thickness $\ell = 25$ μm. Without pumping all ions are assumed to be in ground state; $N_2 = 0$ and $N_1 = N_d = 3.0 \times 10^{21}$ cm^{-3}. Hence the absorption cross-section of $\sigma_{abs} = 9.45 \times 10^{-20}$ cm^2 at λ_S leads to a small signal light absorption of 4.34 σ_{abs} N_d ℓ = 3.08 dB. Under pumping, we measure 5.65 dB enhancement of the transmitted signal light. The net gain of 2.57 dB over the layer thickness results in a modal gain of 1030 dB/cm. This corresponds to a population inversion of 83 % according Eq. 7.1, with the emission cross-section of $\sigma_{em} = 1.15 \times 10^{-20}$ cm^2, which is in good agreement with the estimated population inversion of 84% obtained in the channel waveguide amplifier.

7.5.   Conclusions

The long excited state lifetimes of rare earth ions provide temporal and spatial stability to the optical gain. This is essential for achieving crucial performance parameters, such as high-bit-rate transmission of wavelength-division-multiplexed signals through optical amplifiers without cross-channel patterning effects [brad09] or ultra-narrow-linewidth lasers without the linewidth-broadening effect of spatial gain modulation [ber10]. The demonstration of over 150 dB/cm modal gain for a wavelength range from 980 nm to 1023 nm makes the double tungstate host material interesting for the development of micro-sized optical amplifiers in applications that require large bandwidths, such as multi-channel data communication, spectroscopy or applications involving ultra short pulses. The extraordinarily high gain value of 935 dB/cm demonstrated here make rare earth-ion-doped materials interesting candidates for providing gain in nano-photonic devices, such as nano-amplifiers and nano-lasers, and may enable loss-less propagation in plasmonic nano-structures [hol10, oul08].

8   Conclusions

This project started with the realization of a fully furnished crystal growth lab, having computer controlled LPE furnaces, polishing equipment, an optical interference contrast microscope and all the peripheral equipment. This enabled the fabrication of optically active potassium double tungstate waveguides on KYW substrates. In addition, a laser lab has been realized with a tunable Ti:Sapphire laser system, alignment stages and optical measurement tools to perform the optical investigations on the active waveguides.

8.1.   Material-related results

On the material side growth of heavily co-doped, lattice matched layers onto pure KYW using LPE was demonstrated by Dr. Shanmugam Aravazhi. By using the lattice information of the stoichiometric crystals KLuW, KGdW, KYbW and KYW we succeeded to grow lattice matched layers of the composition $KY_{1-x-y}Gd_xLu_y(WO_4)_2:Yb^{3+}$ and design the refractive index contrast with respect to the KYW substrate up to 1.5×10^{-2} for various concentrations of the active Yb^{3+} doping up to a demonstrated level of 47.5%. Structural investigations using XRD confirm the single-crystalline structure of these active layers, and LA-ICP-MS measurements show that the composition of the grown layer is close to that of the initial solution, which reveals that the segregation coefficients of all incorporated ions are close to unity. The large co-doping concentrations do not strongly affect the fluorescent lifetime of the Yb^{3+} ions. Hence, no adverse effects on laser related properties of the Yb^{3+} ions, when doped into a heavily co-doped host material, was observed.

A model has been developed to approximate the emission and absorption spectra of Yb^{3+} ions doped into the composite host materials of any composition. A spatially resolved rate equation model was developed and used in combination with mode solver software (Phoenix FieldDesigner) [pho] to design the waveguide lasers for optimal laser performance. The outcome of this model agrees well with the experimentally observed laser performance of these co-doped planar waveguide devices.

Lasers with low laser threshold of 18 mW, record-high slope efficiency of 82.3%, and maximum output power of 195 mW were demonstrated in a buried planar waveguide laser using a butt-coupled mirror configuration. The same device operated at the ZPL at 981 nm in a half-open cavity configuration when pumping at a shorter wavelength near 932 nm. These experimentally obtained laser performance confirm the excellent quality of the active co-doped waveguides.

8.2. Micro-structuring

After full characterization of the optically active planar waveguides, an etchin process was developed to fabricate micro-structured channel waveguides in KYW. First a RIE system (Oxford Plasmalabs 100) was tested to etch the KYW with a chlorine chemistry and inert argon plasma. Two types of photoresist, i.e. Olin 907-17 and SU-8, and Al_2O_3 were used as etching mask materials. Unfortunately, this approach resulted in rough waveguide structures with unacceptably large propagation losses. Secondly, micro-patterning of the KYW was tested using an IBE system using photoresists Olin 907-17 and SU-8. Smooth waveguide structures were obtained when using photoresist Olin 907-17. This etching recipe was adapted to the active waveguides described in this thesis, resulting in 1.4 µm deep etched ridge waveguide structures in co-doped crystalline waveguides. All these devices were overgrown by pure KYW to obtain buried channel waveguides.

8.3. Channel waveguide lasers and giant modal gain

Optical laser experiments, using the fabricated channel waveguides resulted in the following laser results:

The first microstructured channel waveguide laser in Gd^{3+}, Lu^{3+} co-doped KYW:(1.7%)Yb^{3+} is demonstrated using end-face-coupled mirror substrates to form the laser cavity. Various outcoupling efficiencies have been tested from 2% up to 23% outcoupling efficiency, all having a low laser threshold of around 5 mW absorbed pump power and a slope efficiency of 62% versus absorbed pump power and a maximum output power of 76 mW.

A $KGd_{0.49}Lu_{0.51}(WO_4)_2$:(2.5%)$Yb^{3+}$ layer having no Y^{3+} incorporated, reaching the maximal refractive index contrast of 1.5×10^{-2} between layer and substrate was used to create an improved channel waveguide structure. Laser emission at 1023 nm with a slope efficiency of 72% versus absorbed pump power at 981 nm was demonstrated from this channel waveguide using an outcoupling efficiency of 70%. Furthermore, an impressive output power of 418 mW was obtained in this configuration. The large outcoupling efficiency raises the laser threshold to 40 mW of launched pump power. The large outcoupling efficiency also demonstrates the impressive available gain in such microstructured Gd^{3+}, Lu^{3+} co-doped channel waveguide lasers.

By removal of the outcoupling mirror and changing of the pump excitation to a shorter wavelength of about 932 nm, the emission wavelength was tuned from 980 nm to 1045 nm using a reflective grating in Littrow configuration. This wide gain bandwidth of 65 nm provides an excellent basis for the generation of ultrashort pulses. In addition, laser operation with a low quantum defect of 0.7% was demonstrated. In order to achieve this, the mirror at the incoupling side was removed, while a mirror with a reflectivity of 97% at 980 nm was butt-coupled to the other waveguide facet. In this situation, laser emission at a wavelength of 980 nm was extracted from the pumped side. The laser continuously oscillated at 980 nm while tuning the excitation wavelength from 910 nm to 973 nm, resulting in a record-low quantum defect of only 0.7%.

Removal of both mirrors from the channel waveguide resulted in laser emission from both sides at the ZPL at 981 nm. Taking both emissions into account, a total emission power of 650 mW was demonstrated.

Laser emission from on-chip cavities has been demonstrated with 5 μm deep Bragg structures in channel waveguides having a silicon nitride cladding. The 5 μm deep Bragg trenches have been fabricated by Dr. Feridun Ay using an optimized FIB-milling procedure. Complete cross-sectioning of the active waveguide is achieved in this approach; the large refractive index modulation by air filled trenches in the active waveguide requires only 5 trenches to obtain sufficient reflection for the initiation of laser oscillations. The end-facets were polished using the same FIB-milling technology.

Giant optical gain of 935 dB/cm has been demonstrated in a 47.5% Yb^{3+}-doped, 180 μm long buried channel waveguide. This experiment opens the direct competition with state of the art semiconductor optical amplifiers. Up to this result rare earth ion doping was regarded as an optically active impurity resulting in modest gain figures hardly exceeding a few dB/cm. The record gain is possible due to the extreme doping concentration, the large emission cross-section compared to rare earth ions in other host materials, and the lack of spectroscopic quenching, which is secured by the fairly large inter ionic distance. These outcomes highlight the unique properties of KYW as host material for rare earth ions.

8.4. Final remark and prospects

In this work we have exploited the advantageous properties of KYW as host material for Yb^{3+} ions. The laser emission and absorption cross-sections allow efficient laser operation. Fabrication of Gd^{3+} and Lu^{3+} co-doped waveguides on pure KYW substrates reveals small-sized waveguide laser devices, and when using large Yb^{3+} doping concentration the high gain competes with that observed in semiconductor gain materials.

In the near future, on-chip mode locked lasers are expected to be demonstrated, and output powers exceeding the Watt level could be achieved by using a side-pump configuration. Devices for side-pumped experiments have been fabricated. These devices have orthogonal passive planar waveguides directing the pump light from high power multimode diode bars to highly Yb^{3+}-doped tapered waveguides, to achieve single mode multi-Watt laser emission. These devices will exploit the obtained freedom of independently designing of the refractive index and active doping concentration of multi layered structures.

Moreover the high gain property of these channel waveguides may allow for lossless propagation of light in nano-sized circuitry based on plasmonic waveguides and may result in nano-sized laser devices.

References

[ack11]   B. I. Akca, V. D. Nguyen, J. Kalkman, T. G. van Leeuwen, K. Wörhoff, R. M. de Ridder and M. Pollnau, "Arrayed waveguide-grating spectrometers for spectral-domain optical coherence tomography", submitted (2011)

[ama06]   D. Amarasinghe, A. Ruseckas, A. E. Vasdekis, M. Goossens, G. A. Turnbull and I. D. W. Samuel, "Broadband solid state optical amplifier based on a semiconducting polymer", *Appl. Phys. Lett.* **89**, 201119 (2006)

[auc81]   O. Auciello, "Ion interaction with solids: Surface texturing, some bulk effects, and their possible applications", *J. Vac. Sci. Technol.,* **19**, 841 (1981)

[aul82]   B. F. Aull and H. P. Jenssen, "Vibronic interactions in Nd:YAG resulting in nonreciprocity of absorption and stimulated emission cross sections", *IEEE J. Quantum Elect.*, **18**, 925 (1982)

[ay08]   F. Ay, A. Uranga, J. D. B. Bradley, K. Wörhoff, R. M. de Ridder and M. Pollnau, "Focused ion beam nano-structuring of Bragg gratings in Al_2O_3 channel waveguides", in *Proceedings of the first international workshop on FIB for photonics*, Eindhoven, The Netherlands, 48 (2008)

[ay09]   F. Ay, L. J. Kauppinen, J. D. B. Bradley, K. Wörhoff, R. M. de Ridder and M. Pollnau, "Bragg gratings in Al_2O_3 channel waveguides by focused ion beam milling", in *LEOS annual meeting conference proceedings*, Enschede, The Netherlands, 379 (2009)

[ay11]   F. Ay, I. Iñurrategui, D. Geskus, S. Aravazhi and M. Pollnau, "Deep Bragg grating cavities in $KY(WO_4)_2$ waveguides fabricated by focused-ion-beam milling", *Laser Phys. Lett.*, **8**, 423 (2011)

[bai09]   F. M. Bain, A. A. Lagatsky, R. R. Thomson, N. D. Psaila, N. V. Kuleshov, A. K. Kar, W. Sibbett and C. T. A. Brown, "Ultrafast laser inscribed $Yb:KGd(WO_4)_2$ and $Yb:KY(WO_4)_2$ channel waveguide lasers", *Opt. Express*, **17**, 22417 (2009)

[bain09]   F. M. Bain, A. A. Lagatsky, S. V. Kurilchik, V. E. Kisel, S. A. Guretsky, A. M. Luginets, N. A. Kalanda, I. M. Kolesova, N. V. Kuleshov, W. Sibbett and C. T. A. Brown, "Continuous-wave and Q-switched operation of a compact, diode-pumped $Yb^{3+}:KY(WO_4)_2$ planar waveguide laser", *Opt. Express*, **17**, 1666 (2009)

[bak03]   Z. Bakonyi, H. Su, G. Onishchukov, L. F. Lester, A. L. Gray, T. C. Newell, A. Tünnermann, "High-gain quantum-dot semiconductor optical amplifier for 1300 nm", *IEEE J. Quantum Elect.*, **39**, 1409 (2003)

[bas03]   B. Basnar, A. Lugstein, H. Wanzenboeck, H. Langfischer, E. Bertagnolli and E. Gornik, "Focused ion beam induced surface amorphization and sputter processes", *J. Vac. Sci. Technol. B*, **21**, 927 (2003)

[ber10]   E. H. Bernhardi, H. A. G. M. van Wolferen, L. Agazzi, M. R. H. Khan, C. G. H. Roeloffzen, K. Wörhoff, M. Pollnau and R. M. de Ridder, "Ultra-narrow-linewidth, single-frequency distributed feedback waveguide laser in Al_2O_3:Er^{3+} on silicon", *Opt. Lett.*, **35**, 2394 (2010)

[bis05]   S. Biswal, S. P. O'Connor and S. R. Bowman, "Thermo-optical parameters measured in ytterbium-doped potassium gadolinium tungstate", *Appl. Opt.*, **44**, 3093 (2005)

[bjo03]   E. S. Björlin, T. Kimura and J. E. Bowers, "Carrier-confined vertical-cavity semiconductor optical amplifiers for higher gain and efficiency", *IEEE J. Sel. Top. Quant.*, **9**, 1374 (2003)

[bjo04]   E. S. Björlin, T. Kimura, Q. Chen, C. Wang and J. E. Bowers, "High output power 1540 nm vertical cavity semiconductor optical amplifiers", *Electron. Lett.*, **40**, 121 (2004)

[blo00]   P. Blood, "On the dimensionality of optical absorption, gain, and recombination in quantum-confined structures", *IEEE J. Quantum Elect.*, **36**, 354 (2000)

[bog04]   W. Bogaerts, D. Taillaert, B. Luyssaert, P. Dumon, J. Van Campenhout, P. Bienstman, D. Van Thourhout, R. Baets, V. Wiaux and S. Beckx, "Basic structures for photonic integrated circuits in Silicon-on-insulator", *Opt. Express*, **12**, 1583 (2004)

[bol09]   W. Bolaños, J. J. Carvajal, M. C. Pujol, X. Mateos, G. Lifante, M. Aguiló and F. Díaz, "Epitaxial growth of lattice matched $KY_{1-x-y}Gd_xLu_y(WO_4)_2$ thin films on $KY(WO_4)_2$ substrates for waveguiding applications", *Cryst. Growth Des.*, **9**, 3525 (2009)

[bol10]   W. Bolaños, J. J. Carvajal, X. Mateos, G. S. Murugan, A. Z. Subramanian, J. S. Wilkinson, E. Cantelar, D. Jaque, G. Lifante, M. Aguiló and F. Díaz, "Mirrorless buried waveguide laser in monoclinic double tungstates fabricated by a novel combination of ion milling and liquid phase epitaxy", *Opt. Express*, **18**, 26937 (2010)

[ham64]   G. Hamilton, H. Saltzman, A. R. Broccoli and I. Fleming, "James Bond: Goldfinger", United Artists, Danjaq, LCC, EON Productions, United Kingdom, (1964)

[bor05]   C. N. Borca, F. Zäh, C. Schnider, R. P. Salathé, M. Pollnau and P. Moretti, "Fabrication of optical planar waveguides in $KY(WO_4)_2$ by He-ion implantation", in *Conference on lasers and electro-optics Europe*, Conference Digest, Munich, Germany, Optical Society of America, CE6-3-FRI (2005)

[bor06]   C. N. Borca, Y. E. Romanyuk, F. Gardillou, M. Pollnau, M. P. Bernal and P. Moretti, "Optical channel waveguides in $KY(WO_4)_2$:Yb^{3+}", in *Conference on lasers and electro-optics*, Technical Digest, Long Beach, CA, United Stated of America, CMFF3 (2006)

[bor07]   C. N. Borca, V. Apostolopoulos, F. Gardillou, H. Limberger, M. Pollnau and R. P. Salathé, "Buried channel waveguides in Yb-doped $KY(WO_4)_2$ crystals fabricated by femtosecond laser irradiation", *Appl. Surf. Sci.*, **19**, 8300 (2007)

[bor68]   S. V. Borisov and R. F. Klevtsova, "Crystal structure of $KY(WO_4)_2$", *Sov. Phys. Crystallogr.*, **13**, 420 (1968)

[bou05]   A. Bouchier, G. Lucas-Leclin, F. Balembois and P. Georges, "Intense laser emission at 981 nm in an ytterbium-doped $KY(WO_4)_2$ crystal", in *Advanced solid-state photonics*, Vienna, Austria, **98**, 157 (2005)

[bra09]   J. D. B. Bradley, "$Al_2O_3{:}Er^{3+}$ as a gain platform for integrated optics", Ph.D. dissertation, University of Twente, Netherlands, (2009)

[bra10]   J. D. B. Bradley, R. Stoffer, L. Agazzi, F. Ay, K. Wörhoff and M. Pollnau, "Integrated $Al_2O_3{:}Er^{3+}$ ring laser on silicon with wide wavelength selectivity", *Opt. Lett.*, **35**, 73 (2010)

[bra11]   J. D. B. Bradley and M. Pollnau, "Erbium-doped integrated waveguide amplifiers and lasers", *Laser Photonics Rev.*, **5**, 368 (2011)

[brad09]   J. D. B. Bradley, M. Costa e Silva, M. Gay, L. Bramerie, A. Driessen, K. Wörhoff, J.-C. Simon and M. Pollnau, "170 Gbit/s transmission in an erbium-doped waveguide amplifier on silicon", *Opt. Express*, **17**, 22201 (2009)

[bre01]   A. Brenier and G. Boulon, "Overview of the best Yb^{3+}-doped laser crystals, Journal of Alloys and Compounds", *J. Alloy. Compd.*, **323**, 210 (2001)

[chu93]   D. D. L. Chung, P. W. DeHaven and H. Arnold, "X-ray diffraction at elevated temperatures. A method for in situ process analysis", Debashis Ghosh VCH, New York, United States of America (1993)

[col05]   G. D. Cole, E. S. Björlin, C. S. Wang, N. C. MacDonald and J. E. Bowers, "Widely tunable bottom-emitting vertical-cavity SOAs", *IEEE Photonic. Tech. L.*, **17**, 2526 (2005)

[cor90]   S. W. Corzine, R. H. Yan and L. A. Coldren, "Theoretical gain in strained InGaAs/AlGaAs quantum wells including valence-band mixing effects", *Appl. Phys. Lett.*, **57**, 2835 (1990)

[cru02]   A. Crunteanu, M. Pollnau, G. Jänchen, C. Hibert, P. Hoffmann, R. P. Salathé, R. W. Eason, C. Grivas and D. P. Shepherd, "Ti:sapphire rib channel waveguide fabricated by reactive ion etching of a planar waveguide", *Appl. Phys. B-lasers O.*, **75**, 15 (2002)

[cum64]   D. E. McCumber, "Einstein relations connecting broadband emission and absorption spectra", *Phys. Rev.*, **136**, 954 (1964)

[dal11]   K. van Dalfsen, S. Aravazhi, D. Geskus, K. Wörhoff and M. Pollnau, "Efficient $KY_{1-x-y}Gd_xLu_y(WO_4)_2{:}Tm^{3+}$ channel waveguide lasers", *Opt. Express,* **19**, 5277 (2011)

[die63]   G. H. Dieke and H. M. Crosswhite, "The spectra of the doubly and triply ionized rare earths", *Appl. Optics*, **2**, 675 (1963)

[doc10]   B. Docter, J. Pozo, S. Beri, I. V. Ermakov, J. Danckaert, M. K. Smit and F. Karouta, "Discretely tunable laser based on filtered feedback for telecommunication applications", *IEEE J. Sel. Top. Quant.*, **16**, 1405 (2010)

[don10]   C. Dongre, J. van Weerd, G. A. J. Besselink, R. Osellame, R. Martínez Vázquez, G. Cerullo, R. van Weeghel, H. H. van den Vlekkert, H. J. W. M. Hoekstra and M. Pollnau, "Modulation-frequency encoded multi-colorfluorescent DNA analysis in an optofluidic chip", Lab Chip, **11**, 679 (2011)

[dou94]   P. Doussiere, P. Garabedian, C. Graver, D. Bonnevie, T. Fillion, E. Derouin, M. Monnot, J. G. Provost, D. Leclerc and M. Klenk, "1.55 μm polarization independent semiconductor optical amplifier with 25 dB fiber to fiber gain", *IEEE Photon. Technol. L.,* **6**, 170 (1994)

[ein17]   A. Einstein, "On the quantum theory of radiation", *Phys. Z.*, **18**, 121 (1917)

[eks]   http://www.eksmaoptics.com/

[fer99]   B. Ferrand, B. Chambaz and M. Couchaud, "Liquid phase epitaxy: a versatile technique for the development of miniature optical components in single crystal dielectric media", *Opt. Mater.*, **11**, 101 (1999).

[fuj]   http://www.fujifilm-ffem.com/

[gal98]   E. Gallucci, C. Goutaudier, G. Boulon and M.T. Cohen-Adad, "Growth of $KY(WO_4)_2$ single crystal: Investigation of the WO_3 rich region in the K_2O-Y_2O_3-WO_3 ternary system. 2 – The $KY(WO_4)_2$ crystallization field", *Eur. J. Sol. State Inor.*, Chem., **35**, 433 (1998)

[gar07]   F. Gardillou, Y. E. Romanyuk, C. N. Borca, R. P. Salathé and M. Pollnau, "Lu, Gd co-doped $KY(WO_4)_2$:Yb epitaxial layers: Towards integrated optics based on $KY(WO_4)_2$", *Opt. Lett.*, **32**, 488 (2007)

[ger01]   R. Gerhardt, "Channel waveguide lasers in epitaxial garnet films", Ph.D. dissertation, Universität Osnabrück, Germany, (2001)

[ger05]   D. Gerace, M. Galli, D. Bajoni, G. Guizzetti, L. C. Andreani, F. Riboli, M. Melchiorri, N. Daldosso, L. Pavesi, G. Pucker, S. Cabrini, L. Businaro and Di Fabrizio, "Wide-band transmittance of one-dimensional photonic crystals carved in Si_3N_4/SiO_2 channel waveguides", *Appl. Phys. Lett.*, **87** 211116 (2005)

[gie07]   A. Giesen, J. Speiser, "Fifteen years of work on thin-disk lasers: Results and scaling laws", *IEEE J. Sel. Top. Quant.*, **13**, 598 (2007)

[goo05]   M. Goosens, G. Heliotis, G. A. Turnbull, A. Ruseckas, J. R. Lawrence, R. Xia, D. D. C. Bradley and I. D. W. Samuel, "Semiconducting polymer optical amplifiers", in *Proceedings SPIE*, San Diego, California, United States of America, **5937**, 593706-1 (2005)

[gri03]   C. Grivas, D. P. Shepherd, T. C. May-Smith, R. W. Eason, M. Pollnau, A. Crunteanu and M. Jelinek, "Performance of Ar^+-milled Ti:Sapphire rib waveguides as single transverse mode broadband fluorescence sources", *IEEE J. Quantum Elect.*, **39**, 501 (2003)

[gri05]	U. Griebner, S. Rivier, J. Liu, R. Grunwald, V. Petrov, A. Aznar, R. Sole, M. Aguilo and F. Diaz, "Continuous-wave and mode-locked laser operation of epitaxially grown Yb:KLu(WO$_4$)$_2$ composites", in *Conference on lasers and electro-optics*, Baltimore, Maryland, United States of America, CtuQ4 (2005)
[gri11]	C. Grivas and M. Pollnau, "Polymer integrated amplifiers and lasers", *Laser Photon. Rev.*, submitted (2011)
[gri57]	J. Grimm and W. Grimm, "Kinder- und Hausmärchen **1**", *Dieterich*, 7th ed., Göttingen, Germany, 264 (1857)
[gue70]	R. Guerin and P. Caillet, "Phases of system K$_2$WO$_4$-WO$_3$ and their reduction by potassium vapor", *Cr. Acad. Sci. C. Chim.*, **271**, 815 (1970)
[gun08]	T. Gün, A. Kahn, B. İleri, K. Petermann and G. Huber, "Two-dimensional growth of lattice matched Nd-doped (Gd,Lu)$_2$O$_3$ films on Y$_2$O$_3$ by pulsed laser deposition", *Appl. Phys. Lett.*, **93**, 053108 (2008)
[gun99]	D. Günther and C.A. Heinrich, "Enhanced sensitivity in laser ablation-ICP mass spectrometry using helium-argon mixtures as aerosol carrier", *J. Anal. Atom. Spectrom.*, **14**, 1363 (1999)
[ham]	http://www.math.utwente.nl/_hammerm/Metric/
[hol10]	T. Holmgaard, J. Gosciniak and S. I. Bozhevolnyi, "Long-range dielectric-loaded surface plasmon-polariton waveguides", *Opt. Express,* **18**, 23009 (2010)
[hop07]	W. C. L. Hopman, F. Ay, W. B. Hu, V. J. Gadgil, L. Kuipers, M. Pollnau and R. M. de Ridder, "Focused ion beam scan routine, dwell time and dose optimizations for submicrometer period planar photonic crystal components and stamps in silicon", *Nanotechnology*, **18,** 195305 (2007)
[ino65]	M. Inokuti and F. Hirayama, "Influence of energy transfer by the exchange mechanism on donor luminescence", *J. Chem. Phys.*, **43**, 1978 (1965)
[ism11]	N. Ismail, F. Sun, K. Wörhoff, A. Driessen, R. M. de Ridder and M. Pollnau, "Integrated arrayed waveguide grating spectrometer for measuring Raman spectra", submitted (2011)
[jac07]	B. Jacobsson, J. E. Hellström, V. Pasiskevicius and F. Laurell, "Widely tunable Yb:KYW laser with a volume Bragg grating", *Opt. Express,* **15**, 1003 (2007)
[jac08]	B. Jacobsson, "Experimental and theoretical investigation of a volume-Bragg-grating-locked Yb:KYW laser at selected wavelengths", *Opt. Express,* **16**, 6443 (2008)
[jeo03]	C. H. Jeong, D. W. Kim, H. Y. Lee, H. S. Kim, Y. J. Sung and G. Y. Yeom, "Sapphire etching with BCL$_3$/HBr/Ar plasma", *Surf. Coat. Tech.*, **171**, 280 (2003)
[kah08]	A. Kahn, H. Kühn, S. Heinrich, K. Petermann, J. D. B. Bradley, K. Wörhoff, M. Pollnau, Y. Kuzminykh and G. Huber, "Amplification in epitaxially grown Er:(Gd, Lu)$_2$O$_3$ waveguides for active integrated optical devices", *J. Opt. Soc. Am. B*, **25**, 1850 (2008)

[kah09]   A. Kahn, S. Heinrich, H. Kühn, K. Petermann, J. Bradley, K. Wörhoff, M. Pollnau and G. Huber, "Low threshold monocrystalline Nd:(Gd, Lu)$_2$O$_3$ channel waveguide laser", *Opt. Express,* **17**, 4412 (2009)

[kam01]   A. A. Kaminskii, A. F. Konstantinova, V. P. Orekhova, A. V. Butashin, R. F. Klevtsova and A. A. Pavlyuk, "Optical and nonlinear laser properties of the χ(3)-active monoclinic α-KY(WO$_4$)$_2$ crystals", *Crystallogr. Rep.*, **46**, 665 (2001)

[kim03]   D. W. Kimm, C. H. Jeong, K. N. Kim, H. Y. Lee, H. S. Kim, Y. J. Sung and G. Y. Yeom, "High rate sapphire (Al$_2$O$_3$) etching in inductively coupled plasmas using axial external magnetic field", *Thin Solid Films*, **435**, 242 (2003)

[kle68]   P. V. Klevtsov, L. P. Kozeeva and R. F. Klevtsova, "Crystallographic study of potassium-yttrium tungstate and molybdate", *Izv. Akad. Nauk SSSR, Neorgan. Mater.*, **4**, 1147 (1968)

[kle69]   P. V. Klevtsov and L. P. Kozeeva, "Synthesis and X-ray and thermal studies of potassium rare-earth tungstates, KLn(WO$_4$)$_2$, Ln = rare-earth element", *Dokl. Akad. Nauk SSSR, Crystallography*, **185**, 571 (1969)

[kog90]   H. Kogelnik, "Theory of optical waveguides", *Guided-wave optoelectronics, Electronics and Photonics*, **26**, 2 (1990)

[koo01]   P. Koonath, S. Kim, W-J. Cho and A. Gopinath, "Polarization-insensitive optical amplifiers in AlInGaAs", *IEEE Photon. Technol. L.*, **13**, 779 (2001)

[kry02]   I. M. Krygin, A. D. Prokhorov, V. P. D'yakonov, M. T. Borowiec and H. Szymczak, "Spin-spin interaction of Dy^{3+} ions in KY(WO$_4$)$_2$", *Phys. Solid State*, **44**, 1513 (2002)

[kuh09]   H. Kühn, S. Heinrich, A. Kahn, K. Petermann, J. D. B. Bradley, K. Wörhoff, M. Pollnau and G. Huber, "Monocrystalline Yb^{3+}:(Gd,Lu)$_2$O$_3$ channel waveguide laser at 976.8 nm", *Opt. Lett.*, **34**, 18 (2009)

[kul97]   N. V. Kuleshov, A. A. Lagatsky, V. G. Shcherbitsky, V. P. Mikhailov, E. Heumann, T. Jensen, A. Diening and G. Huber, "CW laser performance of Yb and Er, Yb doped tungstates", *Appl. Phys. B-Lasers O.*, **64**, 409 (1997)

[kule97]   N. V. Kuleshov, A. A. Lagatsky, A. V. Podlipensky, V. P. Mikhailov and G. Huber, "Pulsed laser operation of Yb-doped KY(WO$_4$)$_2$ and KGd(WO$_4$)$_2$", *Opt. Lett.*, **22**, 1317 (1997)

[kus73]   T. Kushida, "Energy transfer and cooperative optical transitions in rare-earth doped inorganic materials. I. Transition probability calculation", *J. Phys. Soc. Jpn.,* **34**, 1318 (1973)

[lag99]   A. A. Lagatsky, N. V. Kuleshov and V. P. Mikhailov, "Diode-pumped CW lasing of Yb:KYW and Yb:KGW", *Opt. Commun.*, **165**, 71 (1999)

[lam03]   S. Y. Lam and M. J. Damzen, "Characterization of solid-state dyes and their use as tunable laser amplifiers", *Appl. Phys. B-Lasers O.*, **77**, 577 (2003)

[law02]	J. R. Lawrence, G. A. Turnbull and D. W. Samuel, "Broadband optical amplifier based on a conjugated polymer", *Appl. Phys. Lett.*, **80**, 3036 (2002)
[lee02]	J. R. Lee, H. J. Baker, G. J. Friel, G. J. Hilton and D. R. Hall, "High-average-power Nd:YAG planar waveguide laser that is face pumped by 10 laser diode bars", *Opt. Lett.*, **27**, 524 (2002)
[leew79]	W. H. Lee and W. Streifer, "Radiation loss calculations for corrugated dielectric waveguides. II. TM polarization", *J. Opt. Soc. Am.*, **69**, 1671 (1979)
[lee79]	R. E. Lee, "Microfabrication by ion-beam etching", *J. Vac. Sci. Technol.*, **16**, 164 (1979)
[leu00]	J. Leuthold, M. Mayer, J. Eckner, G. Guekos, H. Melchior and Ch. Zellweger, "Material gain of bulk 1.55 μm InGaAsP/InP semiconductor optical amplifiers approximated by a polynomial model", *J. Appl. Phys.*, **87**, 618 (2000)
[liu01]	H. Liu, J. Nees and G. Mourou, "Diode-pumped Kerr-lens mode-locked Yb:KY(WO$_4$)$_2$ laser", *Opt. Lett.*, **26**, 21 (2001)
[log]	http://www.logitech.uk.com/
[mad]	M. J. Madou, "Fundamentals of microfabrication", CRC press, Boka Raton, Florida, United States of America, 2nd edition (2002)
[mai60]	T. H. Maiman, "Stimulated optical radiation in Ruby", *Nature*, **187**, 493 (1960)
[maj03]	A. Major, I. Nikolakakos, J. S. Aitchison, A. I. Ferguson, N. Langford and P. W. E. Smith, "Characterization of the nonlinear refractive index of the laser crystal Yb : KGd(WO$_4$)$_2$", *Appl. Phys. B-Lasers O.*, **77**, 433 (2003)
[maj09]	A. Major, D. Sandkuijl and V. Barzda, "A diode-pumped continuous-wave Yb:KGW laser with N$_g$-axis polarized output", *Laser Phys. Lett.*, **6**, 779 (2009)
[majo09]	A. Major, R. Cisek, D. Sandkuijl and V. Barzda, "Femtosecond Yb:KGd(WO$_4$)$_2$ laser with >100 nJ of pulse energy", *Laser Phys. Lett.*, **6**, 272 (2009)
[mat06]	X. Mateos, R. Solé, J. Gavaldà, M. Aguiló, J. Massons, F. Díaz, V. Petrov and U. Griebner, "Crystal growth, spectroscopic studies and laser operation of Yb^{3+}-doped potassium lutetium tungstate", *Opt. Mater.*, **28**, 519 (2006)
[mat72]	J. W. Matthews and E. Klokholm, "Fracture of brittle epitaxial films under the influence of misfit stress", *Mater. Res. Bull.*, **7**, 213 (1972)
[mem]	http://www.memsnet.org/
[mic]	http://www.microchem.com/
[mic81]	A. A. Michelson, "The relative motion of the earth and the luminiferous ether", *Am. J. Sci.*, **22,** 120 (1881)
[mog79]	C. J. Mogab, "Ion beam, plasma and reactive ion etching", *Inst. Phys. Conf. Ser.*, **53**, 37 (1980)

[nag10] R. Nagarajan, M. Kato, J. Pleumeekers, P. Evans, S. Corzine, S. Hurtt, A. Dentai, S. Murthy, M. Missey, R. Muthiah, R. A. Salvatore, C. Joyner, R. Schneider, M. Ziari, F. Kish and D. Welch, "InP photonic integrated circuits", *IEEE J. Sel. Top. Quant.*, **16**, 11135 (2010)

[oka96] M. Okai, I. F. Lealman, L. J. Rivers, C. Dix and M. J. Robertson, "In-line Fabry-Perot optical waveguide filter with quasi-chirped gratings", *Electron. Lett.*, **32**, 108 (1996)

[oul08] R. F. Oulton, V. J. Sorger, D. A. Genov, F. P. Pile and X. Zhang, "A hybrid plasmonic waveguide for subwavelength confinement and long-range propagation", *Nat. Photonics*, **2**, 496 (2008).

[pat04] F. D. Patel, S. DiCarolis, P. Lum, S. Venkatesh and J. N. Miller, "A compact high-performance optical waveguide amplifier", *IEEE Photonic. Tech. L.*, **16**, 2607 (2004)

[pek10] S. Pekarek, C. Fiebig, M. C. Stumpf, A. E. H. Oehler, K. Paschke, G. Erbert, T. Südmeyer and U. Keller, "Diode-pumped gigahertz femtosecond Yb:KGW laser with a peak power of 3.9 kW", *Opt. Express*, **18**, 16320 (2010)

[pen11] C. H. Peng, H. T. Liu, K. T. Wu, Y. F. Chen, H. Chou, I. M. Jiang and W. S. Tse, "Structural properties of host laser single crystal Yb:YAG", *Optics Communications*, In press, corrected proof (2011)

[per] http://www.perkinelmer.com/

[pet05] K. Petermann, D. Fagundes-Peters, J. Johannsen, M. Mond, V. Peters, J. J. Romero, S. Kutovoi, J. Speiser and A. Giesen, "Highly Yb-doped oxides for thin disc lasers", *J. Cryst. Growth*, **275**, 135 (2005)

[pet07] V. Petrov, M. C. Pujol, X. Mateos, Ò. Silvestre, S. Rivier, M. Aguiló , R. M. Solé, J. Liu, U. Griebner and F. Díaz, "Growth and properties of $KLu(WO_4)_2$, and novel ytterbium and thulium lasers based on this monoclinic crystalline host", *Laser Photonics Rev.*, **1**, 179 (2007)

[pho] http://www.phoenixbv.com/

[pol00] M. Pollnau, D. R. Gamelin, S. R. Lüthi, H. U. Güdel and M. P. Hehlen, "Power dependence of upconversion luminescence in lanthanide and transition-metal-ion systems", *Phys. Rev. B.*, **61**, 3337 (2000)

[pol07] M. Pollnau, Y. E. Romanyuk, F. Gardillou, C. N. Borca, U. Griebner, S. Rivier and V. Petrov, "Double tungstate lasers: From bulk toward on-chip integrated waveguide devices", *IEEE J. Sel. Top. Quant.*, **13**, 661 (2007)

[pru07] M. W. Pruessner, T. H. Stievater and W. S. Rabinovich, "Integrated waveguide Fabry-Perot microcavities with silicon/air Bragg mirrors", *Opt. Lett.*, **32**, 533 (2007)

[pud08] D. Pudo, H. Byun, J. Chen, J. Sickler, F. X. Kärtner and E. P. Ippen, "Scaling of passively mode-locked soliton erbium waveguide lasers based on slow saturable absorbers", *Opt. Express*, **16**, 19221 (2008)

[puj01]   M. C. Pujol, X. Mateos, R. Solé, J. Massons, J. Gavaldà, X. Solans, F. Díaz and M. Aguiló, "Structure, crystal growth and physical anisotropy of KYb(WO$_4$)$_2$, a new layer matrix", *J. Appl. Cryst.*, **35**, 108 (2002)

[puj06]   M. Pujol, X. Mateos, A. Aznar, X. Solans, S. S. Nach, J. Massons, F. Díaz and M. Aguiló, "Structural redetermination, thermal expansion and refractive indices of KLu(WO$_4$)$_2$", *J. Appl. Crystallogr.*, **39**, 230 (2006)

[pujo01]   M. C. Pujol, X. Mateos, R. Solé, J. Massons, J. Gavaldà, F. Díaz and M. Aguiló, "Linear thermal expansion tensor in KRE(WO$_4$)$_2$ (RE=Gd, Y, Er, Yb) monoclinic crystals", *Mater. Sci. Forum,* **378-381**, 710 (2001)

[pujo02]   M. C. Pujol, M. A. Bursukova, F. Güell, X. Mateos, R. Sole, J. Gavaldà, M. Aguiló, J. Massons, F. Díaz, P. Klopp, U. Griebner and V. Petrov, "Growth, optical characterization, and laser operation of a stoichiometric crystal KYb(WO$_4$)$_2$", *Phys. Rev. B*, **65**, 165121 (2002)

[pujo99]   M. C. Pujol, R. Solé, J. Gavaldà, J. Massons, M. Aguiló, F. Díaz, V. Nikolov, C.Zaldo, "Growth and ultraviolet optical properties of KGd$_{1-x}$RE$_x$(WO$_4$)$_2$ single crystals", *J. Mater. Res.*, **14**, 3739 (1999)

[pujol01]   M. Pujol, R. Solé, J. Massons, J. Gavaldà, X. Solans, C. Zaldo, F. Dìaz and M. Aguiló, "Structural study of monoclinic KGd(WO$_4$)$_2$ and effects of lanthanide substitution", *J. Appl. Crystallogr.*, **34**, 1 (2001)

[rei98]   J. P. Reithmaier and A. Forchel, "Focused ion-beam implantation induced thermal quantum-well intermixing for monolithic optoelectronic device integration", *IEEE J. Sel. Top. Quant.*, **4,** 595 (1998)

[rid07]   R. M. de Ridder, W. C. Hopman and F. Ay, "Focused-ion-beam processing for photonics", in *Proceedings international conference on transparent optical networks*, Rome, Italy, 212 (2007)

[ris88]   W. P. Risk, "Modeling of longitudinally pumped solid-state lasers exhibiting reabsorption losses", *J. Opt. Soc. Am. B*, **5**, 1412 (1988)

[riv07]   S. Rivier, X. Mateos, V. Petrov, U. Griebner, Y. E. Romanyuk, C. N. Borca, F. Gardillou and M. Pollnau, "Tm:KY(WO$_4$)$_2$ waveguide laser", *Opt. Express*, **15**, 5885 (2007)

[riv08]   S. Rivier, X. Mateos, Ò. Silvestre, V. Petrov, U. Griebner, M. C. Pujol, M. Aguiló, F. Díaz, S. Vernay and D. Rytz, "Thin-disk Yb:KLu(WO$_4$)$_2$ laser with single-pass pumping", *Opt. Lett.*, **33**, 735 (2008)

[rivi08]   S. Rivier, V. Petrov, A. Gross, S. Vernay, V. Wesemann, D. Rytz and U. Griebner, "Diffusion bonding of monoclinic Yb:KY(WO$_4$)$_2$/KY(WO$_4$)$_2$ and its continuous-wave and mode-locked laser performance", *Appl. Phys. Express*, **1,** 112601 (2008)

[roe07]   G. Roelkens, J. Campenhout, J. Brouckaert, D. Thourhout, R. Baets, P. Romeo, P. Regreny, A. Kazmierczak, C. Seassal, X. Letartre, G. Hollinger, J. M. Fedeli, L. Di Cioccio, C. Lagahe-Blanchard, "III-V/Si photonics by die to wafer bonding", *Mater. Today*, **10**, 36 (2007)

[rom04]   Y. E. Romanyuk, D. Ehrentraut, M. Pollnau, S. García-Revilla, R. Valiente, "Low temperature flux growth of sulfates, molybdates, and tungstates of Ca, Sr, and Ba and investigation of doping with Mn^{6+}", *Appl. Phys. A*, **79**, 613 (2004)

[rom05]   Y. Romanyuk, "Liquid-phase epitaxy of doped $KY(WO_4)_2$ layers for waveguide lasers", Ph.D. dissertation, Ecole Polytechnique Fédérale de Lausanne, Switserland, (2005)

[rom06]   Y. E. Romanyuk, C. N. Borca, M. Pollnau, S. Rivier, V. Petrov and U. Griebner, "Yb-doped $KY(WO_4)_2$ planar waveguide laser", *Opt. Lett.*, **31**, 53 (2006)

[roma04] Y. E. Romanyuk, I. Utke, D. Ehrentraut, V. Apostolopoulos, M. Pollnau, S. García-Revilla and R. Valiente, "Low-temperature liquid phase epitaxy and optical waveguiding of rare-earth-ion doped $KY(WO_4)_2$ thin layers", *J. Cryst. Growth*, **269**, 377 (2004)

[ros08]   F. Röser, C. Jauregui, J. Limpert and A. Tünnermann, "94 W 980 nm high brightness Yb-doped fiber laser", *Opt. Express*, **16**, 17310 (2008)

[sie10]   J. Siebenmorgen, T. Calmano, K. Petermann and G. Huber, "Highly efficient Yb:YAG channel waveguide laser written with a femtosecond-laser", *Opt. Express*, **18**, 16035 (2010)

[sil04]   W. T. Silfvast, "*Laser fundamentals*", 2th ed., Cambridge University Press, Cambridge, United Kingdom, (2004)

[sil07]   Ò. Silvestre, M. Pujol, F. Güell, M. Aguiló, F. Díaz, A. Brenier and G. Boulon, "Crystal growth and spectroscopic analysis of co-doped (Ho,Tm):$KGd(WO_4)_2$", *Appl. Phys.B*, **87**, 111 (2007)

[sil08]   Ò. Silvestre, A. Aznar, R. Solé, M. C. Pujol, F. Díaz and M. Aguiló, "Lattice mismatch and crystal growth of monoclinic $KY_{1-x}Yb_x(WO_4)_2$ / $KY(WO_4)_2$ layers by liquid phase epitaxy", *J. Phys.: Condens. Matter*, **20**, 225004 (2008)

[sol96]   R. Solé, V. Nikolov, X. Ruiz, J. Gavaldà, X. Solans, M. Aguiló and F. Diaz, "Growth of beta-$KGd_{1-x}Nd_x(WO_4)_2$ single crystals in $K_2W_2O_7$ solvents", *J. Cryst. Growth*, **169**, 600 (1996)

[sou10]   R. Soulard, A. Zinoviev, J. L. Doualan, E. Ivakin, O. Antipov and R. Moncorgé, "Detailed characterization of pump-induced refractive index changes observed in Nd:YVO_4, Nd:$GdVO_4$ and Nd:KGW", *Opt. Expr.*, **18**, 1553 (2010)

[sri07]   M. Sridharan, M. Sillassen, J. Bøttiger, J. Chevallier and H. Birkedal, "Pulsed DC magnetron sputtered Al_2O_3 films and their hardness", *Surf. Coat. Tech.*, **202**, 920 (2007)

[sto01]   J. Stohs, D. J. Bossert, D. Gallant and S. R. J. Brueck, "Gain, refractive index change and linewidth enhancement factor in broad-area GaAs and InGaAs quantum-well lasers", *IEEE J. Quantum Elect.*, **37**, 1449 (2001)

[sve98]   O. Svelto, "*Principles of lasers*", D.C. Hanna, 4th ed., Plenum Press, New York, United States of America, (1998)

[tho10]   R. R. Thomson, N. D. Psaila, S. J. Beecher and A. K. Kar, "Ultrafast laser inscription of a high-gain Er-doped bismuthate glass waveguide amplifier", *Opt. Express* **18**, 13212 (2010)

[uit61]   L. G. Van Uitert and R. R. Soden, "Enhancement of Eu^{3+} emission by Tb^{3+}", *J. Chem. Phys.*, **36**, 1289 (1961)

[uqg]   http://www.uqgoptics.com/

[yan10]   J. Yang, M. B. J. Diemeer, C. Grivas, G. Sengo, A. Driessen and M. Pollnau, "Steady-state lasing in a solid polymer", *Laser Phys. Lett.*, **7**, 650 (2010)

[yang10]   J. Yang, M. B. J. Diemeer, G. Sengo, M. Pollnau and A. Driessen, "Nd-doped polymer waveguide amplifiers", *IEEE J. Quantum Electr.*, **46**, 1043 (2010)

Acknowledgements

Although it seems like some people are solely responsible for major scientific breakthroughs, in the past, in reality it is impossible to conduct research without the help of excellent colleagues, friends and family.

Five years ago, I was granted the possibility of performing my PhD at the IOMS group under the supervision of Markus Pollnau. I will never forget his enthusiastic reaction when I reported my first research results to him. He has been the driving force behind our many publications, for which I am grateful.

After 2 years, experiencing the standard PhD-dip, having had weak results and having another person in the world (Fiona Bain) publishing much better results [bain09], we decided to change the material composition, which turned out to be a golden decision. Kerstin Wörhoff advised me to develop more organization in my research. So, I decided to start from blank by making a new directory "H:/Systematical Research/" with a folder structure that made much more sense than the mess I had beforehand. From that moment on, I seriously started to plan tasks and forced myself to stay on the red research line with her words in my head. At about the same time Christos Grivas visited our group, teaching me the practical aspects of performing well organized experiments.

With infinite patience Shanmugam Aravazhi grew the crystals (his *precious*). I was honored by his confidence in me to let me polish and structure his *precious* samples. I certainly was reluctant in telling him that I again had broken one, or in asking him to grow an overlay over the heavily blackened horrible looking etched samples.

Then there is Anton Hollink, a person providing advice in any aspect. He can be considered as any of the following, namely a, technician, relation therapist, career advisor, etc. When I asked for "The Anton" in ETH Zurich, and explained who Anton is, I discovered there was none; they then realized that they heavily missed an Anton ;-).

Few experiments took place at other locations; I started with a 4 months internship at EPFL Lausanne in the group of René Salathé, where I had the opportunity of working together with Patrick Hoffman, Yun Luo and Gerard Harbach. Later on, many attempts to mode-lock the waveguide laser were undertaken in the group of Ursula Keller at the ETH Zurich. Here Martin Hoffman demonstrated lasing of the "undoped" substrate. A few years later mode-locking of channel waveguide lasers was attempted together with Selina Pekarek, who was charmed by these sweet little channels since they always seemed to lase. Together with Thomas Südmeyer we developed an approach that might lead to mode-locking of these devices in the future.

I thank you all for giving me a warm welcome!

The small sample size and funny composition always drew the attention in the cleanroom, especially when taking apart the mask aligner for exposure or taking apart the wet bench when a "holy" sample was launched through the cleanroom. I would like to thank all of the cleanroom people as I always received the full support from them when asking the impossible things. I want to name a few: Peter Linders the mask-men, Hans Mertens trusting me to repair the IBE and providing a great support in using the machine, "DJ" Mark Smithers, the singing SEMer took most of the SEM micrographs in this thesis. Meint de Boer and Erwin Berenschot from TST, providing the advice towards a successful etch procedure, which I did not manage in 2 years, during a single coffee break.

The FIB (Focussed Ion Beam) project was largely lead by Feridun Ay (Teşekkür Ederim!). Our Spanish master student Ion Iñurategui (having a perfect name for the job) spend most of the hours in the cleanroom with Vishwas Gadkil to test all the FIB milling methods and found an optimal method. Later structures were made together with "pirate" Henk van Wolferen (Har Har!).

Then there are the closest colleagues with whom I shared the office over the longest period of time in the Hogekamp building: Chaitanya Dongre the travel guide, Laura Agazzi besides being a luminescent life time expert taking away doubts about healthy lifetimes but also initiated many PIOMS meetings by bringing Italian coffee with "Salame di Cioccolata" and Edward Bernhardi with whom I had endless discussions how to improve the lasers, cheat online poker games, and making "baie" good simulations. Thank you party people!

 I especially enjoyed working with Marko van Dalfsen who is a direct successor in the work of KYW and who has to deal with all of the frustrating parts that are connected with working with the brittle KYW. Happily he already discovered that all the efforts that has been put into this squared centimeter will be rewarded with new, fancy results. In addition I would like to thank Sonia Garcia Blanco. She is a fairly new "spark of the group" and I wish her good luck in fabricating lossless or lasing plasmonic nano-devices (James Bond`s watch laser etc.) in KYW.

Besides the people I had intensive contact with, I would like to gratefully acknowledged the rest of the old and new colleagues for numerous things that keeps it all fun! I always dialed 1022 from the cleanroom to ask Meindert Dijkstra which buttons I had to push when things went wrong. Also I would like to thank and name: Gabriel Sengo, Hugo Hoekstra, Manfred Hammer, René de Ridder, Alfred Driessen, Marcel Hoekman, Imran Acka, Fehmi Civici, Nur Ismail, So Van Pham, Rita ter Weele-Stokkers, Annitta David, Birgit Binkhorst-Reinshagen, Jonathan Bradley (Johnny B), Mart Dimeer, Wico Hopman, Lasse kauppinen (one of the constant

factors in the PIOMS outings: "Kippis"!), Henry Kelderman, Paul Lambeck, Arne Leinse, Gerwin Steen, Fei Sun, Jing Yang (plastic is fantastic!), Berker Mogulkoc (AFM specialist). When being in need of a spectrophotometer I only needed to say: Kees van der Werf and Liesbeth Hartsuiker and I could enter the labs of the medical cell biophysics group. My old colleagues from the laser physics department provided me of infinite support on laser related stuff. In the free hours I could completely forget the daily "gelazer" together with close friends: AAA-3, DDD, the HTS-guys or the "UT-angels" from the motor sports group (MSG).

I would like to thank my colleagues at Xio photonics and Lionix; they have always been very encouraging towards me to finalize my PhD, which is remarkable since I know they preferred me working for them instead: Hans v.d. Vlekkert saying: "Just start writing it!". Willem Hoving who provided me with a flexible job and all the other colleagues creating a comfortable atmosphere! I certainly do not want to forget the daily PhD support team (old IOMS-ers): Douwe Geuzebroek, Edwin Klein and Ronald Dekker.

I greatly thank the committee members, Carsten Fallnich, Uwe Griebner, Anne Tropper, Klaus Boller, Pepijn Pinkse, Kerstin Wörhoff, and Markus Pollnau, who took the time to examine the work and find the flexibility to adapt to sudden changes in the defense date.

Then there is the loyal support of family, providing long term lodging: Coby, Barend, Jos and Tim. Herewith I would like to express my pleasure to be fully adopted in the warm, sometimes slightly chaotic (that`s my favorite style) family in law: Arthur, Marketta, Petri, Ilmari and Renske.

The longest support I received from my brother and sister: Rens and Iris. They always encouraged me to postpone working (;-)) and to keep on studying, even when expensive journeys could be made they always stand in for the financial risks. Now they encourage their kids to do the same as uncle Dimitri. Oups! ...this is where I start worrying. Now I have to give an example of having a well organized life. Happily I find myself blessed with my loving and caring wife, Saara-Maarit, who is the only person making sure that I keep organized (still wondering from whom she inherited that quality ;-)). She makes sure that I go to bed in time and set my priorities straight. Without her love and support I think it would have been impossible to write this thesis.

Lieve Saara-Maarit, ik vind het fantastisch om met jou dit avontuurlijke leven te mogen delen en beleven, bedankt voor jou onvoorwaardelijke support!

Dimitri

Journal publications

In direct relation to the content of this thesis

1   F. Ay, I. Iñurrategui, D. Geskus, S. Aravazhi and M. Pollnau, "Deep Bragg grating cavities in $KY(WO_4)_2$ waveguides fabricated by focused-ion-beam milling", *Laser Phys. Lett.*, **8**, 423 (2011)

2   D. Geskus, S. Aravazhi, E. Bernhardi, C. Grivas, S. Harkema, K. Hametner, D. Günther, K. Wörhoff and M. Pollnau, "Low-threshold, highly efficient Gd^{3+}, Lu^{3+} co-doped $KY(WO_4)_2:Yb^{3+}$ planar waveguide lasers", *Laser Phys. Lett.*, **6**, 800 (2009)

3   D. Geskus, S. Aravazhi, C. Grivas, K. Wörhoff and M. Pollnau, "Microstructured $KY(WO_4)_2:Gd^{3+}$, Lu^{3+}, Yb^{3+} channel waveguide laser", *Opt. Express,* **18**, 8853 (2010)

4   D. Geskus, S. Aravazhi, K. Wörhoff and M. Pollnau, "High-power, broadly tunable, and low-quantum-defect $KGd_{1-x}Lu_x(WO_4)_2:Yb^{3+}$ channel waveguide lasers", *Opt. Express,* **18**, 26107 (2010)

5   D. Geskus, S. Aravazhi, S. M. García-Blanco and M. Pollnau, "Giant optical gain in a rare-earth-ion-doped microstructure", *Adv. Mater*, DOI: 10.1002/adma.201101781 (2011)

6   D. Geskus, E. H. Bernhardi, K. van Dalfsen, S. Aravazhi, and M. Pollnau, "Highly efficient channel waveguide laser at the zero-phonon line of Yb^{3+}", *In preparation*

Contributions to other work

7   J. D. B. Bradley, L. Agazzi, D. Geskus, F. Ay, K. Wörhoff and M. Pollnau, "Gain bandwidth of 80 nm and 2 dB/cm peak gain in $Al_2O_3:Er^{3+}$ optical amplifiers on silicon", *J. Opt. Soc. Am. B*, **27**, 187, (2010)

8   K. van Dalfsen, S. Aravazhi, D. Geskus, K. Wörhoff and M. Pollnau, "Efficient
$KY_{1-x-y}Gd_xLu_y(WO_4)_2:Tm^{3+}$ channel waveguide lasers", *Opt. Express*, **19**, 5277 (2011)

9   K. Wörhoff, J. D. B. Bradley, F. Ay, D. Geskus, T. P. Blauwendraat and M. Pollnau, "Reliable low-cost fabrication of low-loss $Al_2O_3:Er^{3+}$ waveguides with 5.4-dB optical gain", in *IEEE journal of quantum electronics*, **45**, 454 (2009)

10   J. Yang, M. B. J. Diemeer, D. Geskus, G. Sengo, M. Pollnau and A. Driessen, "Neodymium-complex-doped, photo-defined polymer channel waveguide ampliers", *Optics letters*, **34**, 473 (2009)

Conference contributions

In direct relation to the content of this thesis

11   S. Aravazhi, D. Geskus, K. Wörhoff and M. Pollnau, "Growth of Yb^{3+}, Lu^{3+}, Gd^{3+} co-doped $KY(WO_4)_2$ thin layers", in *Proceedings of the 13th annual symposium of the IEEE LEOS Benelux chapter*, Enschede, The Netherlands, 219 (2008) *Poster presentation*

12   S. Aravazhi, D. Geskus, K. Wörhoff and M. Pollnau, "Improved-index-contrast $KY(WO_4)_2$:Gd, Lu, Yb epitaxial waveguides suitable for highly efficient waveguide lasing", in *Proceedings of the 2009 annual symposium of the IEEE photonics Benelux chapter*, Brussels, Belgium, 133 (2009)

13   S. Aravazhi, D. Geskus, D. Günther, K. Wörhoff and M. Pollnau, "Growth, characterization, and waveguide lasing of Yb^{3+}, Lu^{3+}, Gd^{3+} co-doped $KY(WO_4)_2$ thin layers", in *International commission for optics (ICO) topical meeting on emerging trends and novel materials in photonics*, Delphi, Greece, 142 (2009) *Oral presentation*

14   S. Aravazhi, D. Geskus, K. Wörhoff and M. Pollnau, "Thin film crystal growth of $KY(WO_4)_2$", in *Dutch association for crystal growth (DACG) annuals symposium, Almelo*, The Netherlands, (2009) *Invited*

15   S. Aravazhi, D. Geskus, K. Wörhoff and M. Pollnau, "Gd^{3+}, Lu^{3+} co-doped $KY(WO_4)_2$:Yb^{3+} planar waveguide lasers at 1025 and 980 nm", in *European materials research society*, *Symposium K: Rare earth doped materials for optical based technologies*, Strasbourg, France, 52 (2010)

16   S. Aravazhi, D. Geskus, K. van Dalfsen, D. Günther and M. Pollnau, "Growth and characterization of highly Yb^{3+}-doped $KY(WO_4)_2$ thin layers", in *Conference on lasers and electro-optics Europe*, Munich, Germany, CE3.2 (2011) *Oral presentation*

17   F. Ay, D. Geskus, I. Iñurrategui, S. Aravazhi, V. J. Gadgil, K. Wörhoff and M. Pollnau, "Focused Ion Beam Nanostructured Gratings in Crystalline KYW:Yb^{3+} Channel Waveguides", in *Proceedings of the 2010 annual symposium of the IEEE photonics Benelux chapter*, Delft, The Netherlands, 265 (2010)

18   F. Ay, D. Geskus, I. Iñurrategui, S. Aravazhi and M. Pollnau, "Focused-ion-beam nanostructured photonic cavities for integrated lasers in crystalline double tungstate channel waveguides", *Conference on lasers and electro-optics Europe*, Munich, Germany, CK8.3 (2011) *Oral presentation*

19   S. M. García-Blanco, D. Geskus, K. van Dalfsen, F. Ay, S. Aravazhi, M. Pollnau, "Monoclinic double tungstate waveguide amplifiers and microlasers", in *13th International conference on transparent optical networks*, Stockholm, Sweden (2011) *Invited*

20   S. M. García-Blanco, D. Geskus, K. van Dalfsen, S. Aravazhi, and M. Pollnau, "Rare-earth-ion-doped double tungstates: A promising gain material for integrated optics", in *International symposium on modern optics and its applications*, Bandung, Indonesia, (2011) *Invited*

21   D. Geskus, J. D. B. Bradley, S. Aravazhi, K. Wörhoff and M. Pollnau, "Progress on micro-structured $KY(WO_4)_2$ waveguides for optically active devices", in *12th annual symposium IEEE/LEOS Benelux*, Brussels, Belgium, 103 (2007) *Poster presentation*

22   D. Geskus, J. D. B. Bradley, S. Aravazhi, K. Wörhoff and M. Pollnau, "Poor man's channel waveguide laser: $KY(WO_4)_2$:Yb", in *Conference on lasers and electro-optics*, *OSA Technical Digest (CD)*, San Jose, California, United States of America, CTuS4 (2008) *Oral presentation*

23   D. Geskus, J. D. B. Bradley, S. Aravazhi, K. Wörhoff and M. Pollnau, "Fibre-top-loaded channel waveguide laser in $KY(WO_4)_2$:Yb^{3+}", in *Annual workshop of the IEEE LEOS Benelux chapter materials*, *devices and systems in optics and photonics*, Brussels, Belgium, 13 (2008) *Oral presentation*

24   D. Geskus, S. Aravazhi, E. H. Bernhardi, C. Grivas, K. Wörhoff and M. Pollnau, "Highly efficient Gd, Lu co-doped $KY(WO_4)_2$:Yb^{3+} planar waveguide laser", in *Proceedings of the European Optical Society*, *1st EOS Topical Meeting on Lasers 2009*, Capri, Italy (2009) *Oral presentation*

25   D. Geskus, S. Aravazhi, K. Wörhoff and M. Pollnau, "Low-threshold laser in a high-index-contrast double tungstate waveguide", in *Lasers and electro-optics and the European quantum electronics conference*, Munich, Germany, CE4.1 TUE (2009) *Oral presentation*

26   D. Geskus, S. Aravazhi, C. Grivas, K. Wörhoff and M. Pollnau, "Highly efficient $KY(WO_4)_2$:Gd^{3+}, Lu^{3+}, Yb^{3+} channel waveguide laser", in *Europhoton conference*, Hamburg, Germany, **34C**, WeP12 (2010) *Poster presentation (2nd poster price)*

27   D. Geskus, S. Aravazhi, C. Grivas, K. Wörhoff and M. Pollnau, "Microstructured channel waveguide lasers in $KY(WO_4)_2$:Gd^{3+},Lu^{3+},Yb^{3+}", in *Frontiers in optics*, *novel hybrid integration II*, Rochester, New York, United States of America, FWD3 (2010) *Oral presentation*

28   D. Geskus, S. Aravazhi, E. H. Bernhardi, C. Grivas, K. Wörhoff and M. Pollnau, "Low-Threshold and highly efficient Gd^{3+}, Lu^{3+} co-doped $KY(WO_4)_2$:Yb^{3+} planar waveguide lasers", in *Advanced solid state photonics (ASSP) Technical digest*, San Diego, California, United States of America, ATuB2 (2010) *Oral presentation*

29   D. Geskus, S. Aravazhi, K. Wörhoff and M. Pollnau, "High-gain $KY(WO_4)_2$:Yb^{3+} planar waveguide laser at the zero-phonon line", in *Conference on lasers and electro-optics*, San Jose, California, United States of America, CTuU3 (2010) *Oral presentation*

30   D. Geskus, S. Aravazhi, K. Wörhoff and M. Pollnau, "High-power $KY(WO_4)_2$:Yb^{3+} channel waveguide lasers", in *European workshop on double tungstate lasers*, Hamburg, Germany, 10 (2010) *Invited*

31   D. Geskus, S. Aravazhi, K. Wörhoff and M. Pollnau, "Highly efficient Gd, Lu co-doped KYW:Yb^{3+} planar and channel waveguide lasers", in *IV International workshop on photonic and electronic materials, scientific program and workshop abstracts*, San Sebastian, Spain, 50 (2010) *Invited*

32   D. Geskus, S. Aravazhi, K. Wörhoff and M. Pollnau, "Broadly tunable and low-quantum-defect Yb^{3+}-doped double tungstate channel waveguide lasers", in *Conference on lasers and electro-optics Europe*, Munich, Germany, CA7.4 (2011) *Oral presentation*

33   D. Geskus, S. Aravazhi, K. Wörhoff and M. Pollnau, "High-power, broadly tunable, and low-quantum-defect Yb^{3+}-doped double tungstate channel waveguide lasers", in *Advanced solid-state photonics*, Istanbul, Turkey, ATuD6(1) (2011) *Oral presentation*

34   D. Geskus, S. Aravazhi, S. M. García Blanco and M. Pollnau, "Giant optical gain in a rare-earth-ion-doped waveguide", in *Conference on lasers and electro-optics*, Baltimore, Maryland, United States of America, PDPA12 (2011) *Post deadline*

35   D. Geskus, S. Aravazhi, S. M. García Blanco and M. Pollnau, "Giant gain in a rare-earth-ion-doped waveguide", in *Conference on lasers and electro-optics Europe*, Munich, Germany, CJ2.5 (2011) *Oral presentation*

36   D. Geskus, K. van Dalfsen, S. Aravazhi, K. Wörhoff and M. Pollnau, "Yb^{3+} and Tm^{3+} doped $KGd_xLu_yY_{1-x-y}(WO_4)_2$ channel waveguide lasers", in *Conference on lasers and electro-optics*, Baltimore, Maryland, United States of America, CWP4 (2011) *Oral presentation*

37   D. Geskus, S. Aravazhi, S.M. García-Blanco and M. Pollnau, "Ultra-high gain in an Yb^{3+}-doped dielectric waveguide", in *International conference on luminescence*, Ann Arbor, Michigan, United States of America, ThDD6 (2011) *Oral presentation*

38   D. Geskus, S. Aravazhi, S.M. García-Blanco and M. Pollnau, "Wavelength-dependent optical gain in a $KGd_xLu_{1-x}(WO^4)^2$:Yb^{3+} waveguide amplifier", in *IEEE photonics conference*, Arlington, Virginia United States of America (2011) *Submitted*

39   D. Geskus, S. Aravazhi, S.M. García-Blanco, M. Pollnau, "Giant optical gain in rare-earth-ion-doped thin films and waveguides", in *Conference on lasers and electro-optics: integrated and guided-wave optics and thin film optics*, Sidney, Australia, 170 (2011) *Oral presentation*

40   D. Geskus, S. Aravazhi, S.M. García-Blanco, and M. Pollnau, "Giant optical gain in a rare-earth-ion-doped waveguide amplifier", in *The twentieth annual international laser physics workshop*, Sarajevo, Bosnia and Herzegovina, 4.2.4 (2011) *Invited*

41   I. Iñurrategui, F. Ay, D. Geskus, S. Aravazhi, V. J. Gadgil, K. Wörhoff and M. Pollnau, "Bragg Gratings in Crystalline Waveguides Fabricated by Focused Ion Beam Milling", in *Proceedings of the 2ⁿᵈ international workshop on FIB for photonics*, Cambridge, United Kingdom, 8 (2010) *Oral presentation*

42   M. Pollnau, K. Wörhoff, F. Ay, D. Geskus, L. Agazzi and J. D. B. Bradley, "Higher gain in 977-nm-pumped Al_2O_3:Er^{3+} integrated optical amplifiers", in *Lasers and electro-optics and the European quantum electronics conference*, Munich, Germany, CE1.4 MON (2009)

43   M. Pollnau, D. Geskus, K. van Dalfsen, S. M. García Blanco and S. Aravazhi, "Highly efficient lasers and amplifiers in double tungstates", in *Joint annual meeting of the Swiss physical society and the Austrian physical society*, Lausanne, Switzerland, **28**, 627 (2011) *Oral presentation*

44   M. Pollnau, D. Geskus, E.H. Bernhardi, K. van Dalfsen, K. Wörhoff, and R.M. de Ridder, "Highly efficient solid-state waveguide lasers", in *Advanced solid-state photonics conference*, San Diego, California, (2012) *Invited*

45   K. van Dalfsen, S. Aravazhi, D. Geskus, K. Wörhoff and M. Pollnau, "Lattice matching and microstructuring of Gd^{3+}, Lu^{3+} co-doped $KY(WO_4)_2$:Tm^{3+} channel waveguide lasers", in *European workshop on double tungstate lasers*, Hamburg, Germany, 9 (2010) *Invited*

46   K. van Dalfsen, S. Aravazhi, D. Geskus, K. Wörhoff and M. Pollnau, "Efficient Gd^{3+}, Lu^{3+} co-doped $KY(WO_4)_2$:Tm^{3+} channel waveguide lasers", in *Conference on lasers and electro-optics Europe*, Munich, Germany, CA1.5 (2011) *Oral presentation*

47   K. van Dalfsen, S. Aravazhi, D. Geskus, K. Wörhoff and M. Pollnau, "Efficient Tm^{3+} lasers in double tungstate channel waveguides", in *International conference on luminescence*, Ann Arbor, Michigan, United States of America, ThII2 (2011) *Oral presentation*

48   K. van Dalfsen, D. Geskus, F. Ay, K. Wörhoff, S. Aravazhi and M. Pollnau, "High-power Yb- and Tm-doped double tungstate channel waveguide lasers", in *The twentieth annual international laser physics workshop*, Sarajevo, Bosnia and Herzegovina, 4.4.4 (2011) *Oral presentation*

49   K. van Dalfsen, D. Geskus, F. Ay, K. Wörhoff, S. Aravazhi and M. Pollnau, "High-power Yb- and Tm-doped double tungstate channel waveguide lasers", in *Conference on lasers and electro-optics: solid-state laser and other lasers, and laser materials*, Sidney, Australia, 168 (2011) *Oral presentation*

Contributions related to other work outside this thesis

50   J. D. B. Bradley, D. Geskus, T. P. Blauwendraat, F. Ay, K. Wörhoff and M. Pollnau, "Optimized deposition and structuring of reactively co-sputtered Al_2O_3:Er waveguide layers with net optical gain", in *12th Annual symposium IEEE/LEOS Benelux*, Brussels, Belgium, 107 (2007)

51   J. D. B. Bradley, L. Agazzi, D. Geskus, F. Ay, K. Wörhoff and M. Pollnau, "Reactively co-sputtered Al_2O_3:Er^{3+} for active photonic devices", in *2008 Annual workshop of the IEEE LEOS Benelux chapter materials, devices and systems in optics and photonics*, Brussels, Belgium, 9 (2008)

52   J. D. B. Bradley, L. Agazzi, D. Geskus, F. Ay, K. Wörhoff, M. Pollnau and W. M. Arnoldbik, "Enhanced gain in Er-doped Al_2O_3 channel waveguide amplifiers", in *Proceedings of the 13th annual symposium of the IEEE LEOS Benelux chapter*, Enschede, The Netherlands, 131 (2008)

53   J. D. B. Bradley, L. Agazzi, D. Geskus, T. P. Blauwendraat, F. Ay, K. Wörhoff and M. Pollnau, "Investigation of optical gain in Al_2O_3:Er channel waveguide amplifiers", in *Technical digest conference on lasers and electro-optics*, San Jose, California, United States of America, JTuA30 (2008)

54   J. D. B. Bradley, D. Geskus, T. P. Blauwendraat, F. Ay, K. Wörhoff, M. Pollnau, A. Kahn, H. Scheife, K. Petermann and G. Huber, "Growth, micro-structuring, spectroscopy, and optical gain in as-deposited Al_2O_3:Er waveguides", in *Conference program and technical digest, advanced solid-state photonics: topical meeting and tabletop exhibit*, Nara, Japan, WB10 (2008) *Poster presentation*

55   J. D. B. Bradley, L. Agazzi, D. Geskus, F. Ay, K. Wörhoff and M. Pollnau, "2.0 dB/cm gain in an Al_2O_3:Er^{3+} waveguide on silicon", in *Conference on lasers and electro-optics*, Baltimore, Maryland, United states of America, CThCC2 (2009)

56   K. Wörhoff, J.D.B. Bradley, F. Ay, D. Geskus, S. Aravazhi and M. Pollnau, "Actively doped dielectric materials for on-chip integrated light sources", in *Fotonica evenement*, Den Haag, The Netherlands, (2007)

57   K. Wörhoff, J. D. B. Bradley, L. Agazzi, D. Geskus, F. Ay, A. Kahn, H. Scheife, K. Petermann, G. Huber and M. Pollnau, "Energy-transfer upconversion in Al_2O_3:Er^{3+} thin layers", in *Second international workshop on advanced spectroscopy and optical materials*, Gdansk, Poland, 6-O (2008)

58   K. Wörhoff, J. D. B. Bradley, F. Ay, D. Geskus, T. P. Blauwendraat and M. Pollnau, "Optimization of Al_2O_3:Er^{3+} waveguide technology for active integrated optical devices", in *Proceedings of SPIE*, Strasbourg, France, **6996**, 699618 (2008)

59   J. Yang, M. B. J. Diemeer, D. Geskus, G. Sengo, M. Pollnau and A. Driessen, "Demonstration of net gain at 1060 nm in a Nd-complex-doped, photo-defined polymer channel waveguide", in *3rd EPS-QEOD Europhoton conference*, Paris, France, TUoE.4 (2008) *Oral presentation*

60   J. Yang, M. B. J. Diemeer, D. Geskus, G. Sengo, M. Pollnau and A. Driessen, "Neodymium-complex-doped, photo-defined polymer channel waveguide amplifiers", in *Proceedings of the 13th annual symposium of the IEEE LEOS Benelux chapter*, Enschede, The Netherlands, 123 (2008) *Poster presentation*

CURRICULUM VITAE OF DIMITRI GESKUS

PERSONALIA
Name	Dimitri Geskus
Telephone	+31(0)616436756
E-mail	d.geskus@alumnus.utwente.nl
Birth date	19 November 1979
Birth place	Hardenberg, The Netherlands

PROFESSIONAL
2010-2011 Product engineer: XiO Photonics BV, The Netherlands
Assembly, characterization and durability testing of integrated laserbeam combiners

2010-2011 Process engineer: LioniX BV, The Netherlands
Assembly, characterization and packaging of integrated optical devices

EDUCATION
2006-2011 PhD: Integrated Optical Micro Systems (IOMS), University of Twente, The Netherlands
Fabrication of integrated laser devices in Yb^{3+} doped $KY(WO_4)_2$

2003-2006 Master applied physics: University of Twente, The Netherlands
Specialization: Laser physics

1998-2003 Bachelor applied physics: Saxion Hogescholen Enschede, The Netherlands

TRAINEESHIPS
2006-2007 Internship: Advanced Photonics Laboratory (APL) Ecole Polytechnique Fédérale de Lausanne (EPFL), Lausanne, Switzerland
Migration of knowledge concerning development of integrated devices in crystalline material required for my PhD project

2005-2006 Master assignment: Laser Physics department, University of Twente, The Netherlands
Design, construction and characterization of a chirped laser pulse amplifier

2002-2003 Bachelors assignment: Forschungszentrum Jülich (FZJ) Institut für Plasmaphysik IPP, Jülich, Germany
Design, construction and characterization of an instrument to measure the Doppler shifted H-alpha emission lines of a hydrogen beam

2002-2002 Internship: CERN, Geneva, Switzerland
Endurance measurements on super conducting magnets

2000-2001 Internship: ASTRON, Dwingeloo, The Netherlands
Characterization of low noise amplifiers

SIDE ACTIVITIES
2007-2010 Treasurer of IEEE photonics Benelux student chapter
This organization is the link for students in the field of photonics and electro-optics, within the Benelux. It organizes workshops, company visits and various activities

2004-2006 Vice president of the physics study committee
This committee consists of staff as well as students, which plays an advisory role in the organisation of the physics department

2005-2006 Member of physics promotion team
This organization provides information about the study to attract more students

SKILLS
Cleanroom Lithography with positive and negative resist (SU-8), microstructuring (RIE, IBE, FIB, dicing, polishing), analysis with prism coupling and various microscopes (optical, SEM, AFM)

Laboratory Assembly, characterisation and packaging of integrated optical devices. Managing and setting up polishing- and optical device characterisation lab

Software Mode solver tools, mask designer software (Phoenix) and Matlab

Language Dutch (native language), English (fluent), German (advanced) and French (basic)

Hobby Driving old-timer motorcycles and performing the maintenance and overhaul of these machines. Swimming is my favourite sport